Politecnico di Milano
Department of Chemistry, Materials and
Chemical Engineering "Giulio Natta"
Doctoral Programme In Materials Engineering

---

# Investigation of collimator materials for the High Luminosity Large Hadron Collider

Doctoral Dissertation of:
**Elena QUARANTA**

Supervisor:
**Stefano REDAELLI (CERN)**

Advisor:
**Alessandro BERTARELLI (CERN)**

Tutor:
**Prof. Marco BEGHI**

The Chair of the Doctoral Program:
**Prof.ssa Chiara CASTIGLIONI**

Year 2017 – XXIX cycle

The research leading to these results has received funding from the European Commission under the FP7 Research Infrastructures project EuCARD-2 (grant agreement no.312453), from the European Union's Horizon 2020 Research and Innovation programme under Grant Agreement No 730871, and from the High Luminosity LHC project. The financial support of CERN and Politecnico of Milan is also acknowledged.

*A coloro che mi hanno insegnato che*
*nella vita bisogna lottare, stringere i denti,*
*cadere e rialzarsi sulle proprie gambe*
*se si vuole raggiungere la meta.*

# Abstract

THIS PhD thesis work has been carried out at the European Organisation for Nuclear Research (CERN), Geneva, Switzerland), in the framework of the High Luminosity (HL) upgrade of the Large Hadron Collider (LHC). The HL-LHC upgrade will bring the accelerator beyond the nominal performance: it is planning to reach higher stored beam energy up to 700 MJ, through more intense proton beams. The present multi-stage LHC collimation system was designed to handle 360 MJ stored beam energy and withstand realistic losses only for this nominal beam. Therefore, the challenging HL-LHC beam parameters pose strong concerns for beam collimation, which call for important upgrades of the present system.

The objective of this thesis is to provide solid basis for optimum choices of materials for the different collimators that will be upgraded for the baseline layout of the HL-LHC collimation system.

To achieve this goal, material-related limitations of the present system are identified and novel advanced composite materials are selected as candidates for the new collimators. A series of experimental activities are performed to characterise the material properties, both in normal operation or in conditions of extreme exposure to beam losses, in particular high irradiation doses similar to what could be induced by high-intensity LHC operation. The results provided important feedback to the material production.

Numerical simulations are also carried out to evaluate the achievable performance of the HL-LHC collimation system with new collimator materials. To this purpose, dedicated simulation tools are developed and successfully benchmarked to adequately simulate the new HL-LHC collimation layout. By means of these tools, cleaning performance of the upgraded system are assessed in standard operation and beam failure scenarios. Simulation results are being used to refine the material requirements needed to achieve the HL-LHC beam parameters.

Keywords: accelerator physics, material science, HL-LHC, collimator, irradiation, XRD, simulations, SixTrack.

# Riassunto

IL presente lavoro di tesi di dottorato è stato svolto presso l'Organizzazione Europea per la Ricerca Nucleare (CERN, Ginevra, Svizzera), nell'ambito del progetto di potenziamento High Luminosity (HL) dell'acceleratore di particelle Large Hadron Collider (LHC). Tale potenziamento porterà l'acceleratore al di là delle sue prestazioni nominali: il programma, infatti, prevedere di raggiungere una energia di fascio di 700 MJ, attraverso fasci di protoni più intensi. L'attuale sistema di collimazione di LHC è stato progettato per gestire un'energia di 360 MJ e resistere a scenari realistici di perdite per questo fascio nominale. Pertanto, tale sistema deve essere ugualmente potenziato per garantire il raggiungimento dei parametri HL-LHC.

L'obiettivo di questa tesi è fornire basi solide per scelte ottimali di materiali per i nuovi collimatori del sistema HL-LHC.

Una parte importante di questo lavoro di dottorato è quella di identificare le limitazioni relative ai materiali nel presente sistema di collimazione e selezionare nuovi materiali avanzati per i futuri collimatori. Sono state eseguite una serie di attività sperimentali per caratterizzare le proprietà di tali materiali, sia in normale funzionamento della macchina sia in condizioni di fascio più estreme. In particolare, esposizioni a dosi elevate di irraggiamento hanno permesso di studiare gli effetti sui collimatori indotti dai fasci HL-LHC in fase operativa. I risultati di tali attività hanno consentito di intervenire adeguatamente sul ciclo di produzione dei materiali per migliorarne le proprietà finali.

Sono stati svolti studi computazionali per valutare le prestazioni del sistema di collimazione HL-LHC con nuovi materiali. A questo scopo, sono stati sviluppati specifici strumenti di simulazione per studiare il nuovo layout. Attraverso questi strumenti, le prestazioni del sistema sono state simulate per normale operazione della macchina e per situazioni accidentali. I risultati delle simulazioni hanno permesso di perfezionare i requisiti richiesti ai materiali dei collimatori dai parametri di fascio HL-LHC.

Parole chiave: fisica degli acceleratori, scienza dei materiali, HL-LHC, collimatore, irraggiamento, XRD, simulazioni, SixTrack.

# Contents

# List of Figures

# List of Tables

# Nomenclature

| | |
|---|---|
| **ABD** | Asynchronous Beam Dump |
| **ALICE** | A Large Ion Collider Experiment |
| **ATLAS** | A Toroidal LHC Apparatus |
| **ATS** | Achromatic Telescopic Squeezing |
| **BLIP** | Brookhaven Linear Isotope Producer |
| **BLM** | Beam Loss Monitor |
| **BNL** | Brookhaven National Laboratory, USA |
| **BPM** | Beam Position Monitor |
| **CEI** | Cleaning Efficiency Index |
| **CERN** | European Organisation for Nuclear Research |
| **CFC** | Carbon Fiber Carbon composite, AC-150Ks |
| **CMS** | Compact Muon Solenoid |
| **CTE** | Coefficient of thermal Expansion |
| **CuCD** | Copper-Diamond composite |
| **dpa** | Displacements Per Atoms |
| **DSC** | Differential Scanning Calorimeter |
| **DS** | Dispersion Suppressor |
| **EBSD** | Electron Backscatter Diffraction |
| **EDS** | Energy-Dispersive X-Ray Spectroscopy |
| **GSI** | GSI Helmholtzzentrum for Heavy Ion Research, Germany |
| **HL-LHC** | High Luminosity LHC |
| **IAEA** | International Atomic Energy Agency |
| **IP1** | Interaction Point 1, ATLAS |
| **IP2** | Interaction Point 2, ALICE, and LHC beam injection |
| **IP5** | Interaction Point 5, CMS |

| | |
|---|---|
| **IP8** | Interaction Point 8, LHCb, and LHC beam injection |
| **IP** | Interaction Point |
| **IR3** | Insertion Region 3, Momentum Cleaning collimation |
| **IR4** | Insertion Region 4, RF cavity system |
| **IR6** | Insertion Region 6, Beam Dump |
| **IR7** | Insertion Region 7, Betatron Cleaning collimation |
| **IR** | Insertion Region |
| **IT-180** | Inermet-180 |
| **KP** | Kinchin-Pease model |
| **LEIR** | Low-Energy Ion Ring |
| **LFA** | Laser Flash Apparatus |
| **LHCb** | Large Hadron Collider beauty |
| **LHC** | Large Hadron Collider |
| **LINAC** | Linear Accelerator |
| **LIU** | LHC Injectors Upgrade |
| **LSS** | Long Straight Section |
| **LS** | Long Shutdown |
| **LVDT** | Linear Variable Displacement Transducer |
| **MCS** | Multiple Coulomb Scattering |
| **MKD** | Extraction kicker magnets |
| **MoGr** | Molybdenum-Graphite composite |
| **MS** | Matching Section |
| **NRT** | Norgett, Robinson and Torrens model |
| **NSLS** | National Synchrotron Light Source |
| **PECS** | Pulsed Electric Current Sintering |
| **PKA** | Primary Knock-on Atom |
| **PSB** | Proton Synchrotron Booster |
| **PS** | Proton Synchrotron |
| **RDI** | Radiation Damage Index |
| **RFI** | RF impedance Index |
| **RFQ** | Radio Frequency Quadrupole |
| **RF** | Radio Frequency |
| **SC** | Superconducting magnet |
| **SD** | Single-Diffractive event |
| **SEM** | Scanning Electron Microscopy |
| **SMPF** | Single Module Pre-Firing |
| **SPS** | Super Proton Synchrotron |
| **TCDD** | Target Collimator Dump for D1 protection |

| | |
|---|---|
| **TCDQ** | Target Collimator Dump Quadruple (Diluter) |
| **TCLA** | Target Collimator Long Absorber |
| **TCLD** | Target Collimator Long absorbers in Dispersion suppressor region |
| **TCLI** | Target Collimator Long Injection |
| **TCLP5** | Target Collimator Long with Pick-up |
| **TCL** | Target Collimator Long |
| **TCPPM** | Target Collimator Primary with Pick-up and “Metallic” (low-impedance) jaws |
| **TCP** | Target Collimator Primary |
| **TCSG** | Target Collimator Secondary Graphite |
| **TCSPM** | Target Collimator Secondary with Pick-up and “Metallic” (low-impedance) jaws |
| **TCSP** | Target Collimator Secondary with Pick-up |
| **TCTPM** | Target Collimator Tertiary with Pick-up and new (more robust) Material jaws |
| **TCTPX** | Target Collimator Tertiary with Pick-up and beam-beam compensation wire |
| **TCTP** | Target Collimator Tertiary with Pick-up |
| **TCT** | Target Collimator Tertiary |
| **TDI** | Target Dump Injection |
| **TRI** | Thermo-mechanical Robustness Index |
| **TSI** | Thermal Stability Index |
| **XRD** | X-ray Diffraction |

# Introduction

HIGH-ENERGY particle colliders are major experimental machines to investigate matter at the smallest scales. Over decades, accelerators have been developed to achieve ever increasing particle energies and beam intensities. Such development implies the need of handling higher and higher particle fluxes and stored energies. Despite the improvement in techniques to control the beams, a fraction of the particles circulating in the machine deviates from the ideal trajectory and "leaks", eventually impacting on accelerator components and devices. Due to their high energy, these "leaking" particles can be highly dangerous for the machine. Collimators are therefore installed along the accelerator to safely intercept such particles, thus cleaning the beam and protecting the machine. Apart from this continuous cleaning provided during normal operation, the collimators must also protect the machine in case of much more severe accidental conditions, in which the control of the main beam is lost. This poses extremely challenging constraints to the properties of collimator materials.

The CERN Large Hadron Collider (LHC) was designed to accelerate proton and lead ion beams to provide collisions with centre-of-mass energies of 14 TeV and 1.15 PeV respectively [1]. The proton operation started at 3.5 TeV in 2010-2011 and the beam energy was raised to 4 TeV in 2012. After two years of shutdown, the accelerator resumed operation in 2015 at 6.5 TeV, with the aim of achieving the design 7 TeV and stored energy of 360 MJ. Furthermore, the High-Luminosity project (HL-LHC) [2] aims at an upgraded accelerator with smaller beam emittance and doubled beam current, i.e., a stored beam energy of about 700 MJ.

The present LHC machine works extremely well. Indeed, in 2016 the nominal peak luminosity was surpassed. On the other hand, the challenging parameters of the HL-LHC beams are beyond the values foreseen by the original design of the accelerator [1, 2]. Therefore, an upgrade of numerous accelerator systems, including the collimation system [1,3], is required. The first years of operation at the LHC showed some aspects related to beam collimation that might become limiting factors for HL-LHC:

- Materials and shapes of the devices surrounding a charged beam might induced an image current that act back on the beam. Beam coupling impedance can thus be at the origin of beam instabilities. The LHC impedance budget is dominated by the contribution of non-metallic collimators. Therefore, HL-LHC beam cannot be stable with sufficient operational margins unless the wall-impedance from those collimators is reduced [4].

- Some metallic collimators used to protect locally critical elements, like inner triplet magnets around the experiments, might not withstand direct impact from the primary beam. During standard operation, this should never be the case, however, in certain accident scenarios parts of the main beam risk to directly impact these collimators. Improving the collimator robustness against beam impacts, while preserving their protection functionality, could improve the performance of HL-LHC.
- Off-momentum proton leakage in the dispersion suppressor (DS) magnets downstream of the IR7 betatron cleaning insertion (see Chap. 2) turns out to be the location of highest losses from collimation. The factor 2 increase in total stored beam energy for HL-LHC requires an improvement of collimation cleaning efficiency in operation in order to maintain the same relative beam loss tolerances as in the LHC [5].

Also note that HL-LHC foresees to change significantly the layouts of some LHC insertion regions, and several new collimators need to be built for these new layouts.

An R&D program has been launched to develop new collimator materials that can improve the performance of the present system. Materials of future collimators must ideally optimise different thermo-mechanical properties:

- Density, to guarantee cleaning efficiency;
- Electrical conductivity, to reduce beam coupling impedance;
- Mechanical strength, to withstand shock impacts from beam losses;
- Thermal expansion and diffusivity, to withstand thermal loads, preserving geometrical stability of the device;
- Radiation hardness, to withstand high cumulated doses before property degradation occurs due to radiation exposure.

It is difficult to achieve high performance on all fronts with standard materials: for example, metals generally feature high density, which might be in conflict with the mechanical robustness required for collimators. The choice of optimum materials for collimators is a very complex problem, which also depends on the collimator type.

The objective of this PhD thesis work is to propose, based on the results of experimental activities and numerical simulations, optimum materials for different collimation types for the HL-LHC upgrades.

One key element to ensure that next-generation collimators meet their challenging requirements lies in the development and use of novel advanced materials for the collimators, as no existing metal-based or carbon-based material possesses the combination of physical, thermal, electrical and mechanical properties that is required. In the frame of FP7 EU programs, in particular EuCARD and EuCARD2, several families of novel composite materials have been developed over the last ten years. To date, two materials have been considered as the most promising candidates for LHC collimators, i.e., Molybdenum carbide-Graphite composite (MoGr) and Copper-Diamond composite (CuCD). The outstanding thermal and electrical properties of MoGr makes it promising for primary and secondary collimators. On the other hand, CuCD is appealing for the final collimation stages, owing to its high mechanical robustness together with low thermal expansion coefficient and electrical resistivity. This development generates a broad international interest, which goes beyond the applications for accelerators. Other research studies triggered by CERN involve collaboration with different laboratory experts in material science, like Brookhaven National Laboratory (USA), GSI Helmholtz Centre for Heavy Ion Research (Germany) and Kurchatov Institute (Russia), which participated to the irradiation studies.

In this thesis, recent experimental activities towards the optimisation of physical and thermo-mechanical properties of the novel materials are discussed. As collimators are the most exposed components to beam losses, modifications of the material properties are expected as a consequence of high radiation doses. For this reason, several irradiation campaigns were performed in partner laboratories to study the consequences of high radiation doses, i.e. with protons, neutrons and ions at different energies, on collimator materials. The main goal of these activities was to evaluate the response of collimator materials under irradiation and ultimately to define a threshold for radiation damage above which collimators might need to be replaced. In this thesis work, the unique chance to gather results from different institutes, and to put them together as inputs for the final material choices for HL-LHC, was made available.

The performance of the upgraded LHC collimation system has been also evaluated by simulations for different machine configurations. To this purpose, the SixTrack code [6–8], a standard tool for collimation studies at CERN, was used. As a part of this PhD work, a new collimator material implementation has been added to the existing code with a new approach to model composite materials. The benchmark of this tool with other simulation codes based on different material models is discussed. Moreover, a dedicated routine, already implemented in SixTrack, to simulate fast beam loss scenarios on collimators, has been validated in this work, by comparing simulation results with measurements in the LHC at top beam energy. This was used to assess in all relevant conditions, beam loads on collimators that might be exposed to fast loss scenarios.

Based on these tools, the effects of novel composite materials on the cleaning performance of the upgraded collimation system has been evaluated in simulation. A new method to reliably calculate the onset of beam-induced damage in the material of accelerator components has been also developed as part of this work. It is a three-step approach which bring together competences of different teams. Simulation studies, performed in the frame of this thesis, to determine beam impact conditions on collimators for design failure cases, provided initial inputs to the following steps of the method, i.e. energy deposition studies, and thermo-mechanical analysis of the dynamic material response to the impact. Although the specific case of LHC tungsten collimators is discussed here, the proposed method is generic and can be applied to other future accelerators with a very high stored beam energy, such as the Future Circular Collider (FCC) [9, 10]. The same methods and tools are applied to all relevant cases, and have been used to define final material choices for the three new types of collimators that address the three main challenges listed above: low impedance, improved robustness and cleaning of DS losses.

To summarise, this PhD thesis aims at offering important contributions towards the final choices of collimator materials and layout for the future HL-LHC collimation system. This ambitious goal involves a wide spectrum of expertise, which have been gathered by interacting with various teams involved in the upgrade of the collider.

To have a better understanding of the topics covered in the thesis, the first three chapters are dedicated to the introduction of some important concepts. Given the different background of the readers, i.e. material scientists and accelerator physicists, **Chapter 1** summarises basic topics not common to both communities. A brief introduction of the CERN accelerator complex, the LHC and the program for the HL-LHC upgrade is given in **Chapter 2**, together with a description of beam collimation at the LHC and collimator design. **Chapter 3** recalls the main performance limitations of the present collimation system and how they are being addressed by the future upgrade. Present collimator materials and novel composite materials for the next generation of collimators are presented in **Chapter 4**. Macroscopic characterization of thermo-physical properties and studies of the microscopic structure of these materials in normal operation conditions as well as under high-dose exposure are addressed in **Chapter 5** and **Chapter 6**, respectively. In **Chapter 7**, new simulation tools for collimation studies and their validation strategy are presented. The results of simulations, performed by means of the new tools, which finalise the material choice of the upgraded collimators are discussed in **Chapter 8**. Finally, **Chapter 9** proposes a baseline layout for the HL-LHC collimation layout: the main novelties of the upgrade are discussed and the performance of the new system is evaluated.

# CHAPTER 1

# Relevant concepts of beam dynamics and radiation damage in materials

The present thesis might be read in different communities, namely the materials scientists and the experts of accelerators, who have different backgrounds. In order to facilitate the understanding of the successive discussions, some basic, textbook level, topics, which might not be common to both communities, are summarised in this Chapter for reference purposes.

## 1.1 Concepts of beam dynamics for circular particle accelerators

The electrical and magnetic fields are the essential ingredients that allow particles to move inside an accelerator. The former is generated by a Radio Frequency (RF) system, in which a sinusoidal potential is applied to resonant cavities. This system provides the energy to accelerate the particles. Since the RF cavity is a resonating structure at a specific RF frequency, there will be standing waves generated within this cavity. These standing wave “pockets” are the RF buckets. When beam is captured by the RF system, it is contained in the buckets, inside which particles are grouped in bunches.

Several orders of magnetic fields are needed to steer particles: dipoles, quadrupoles, sextupoles, octupoles and so on. Dipole magnets bend charged particles and define the ideal closed orbit for a particle with the reference energy. The quadrupoles instead, focus the circulating beam around the closed orbit, as an optical lens does with the rays of light. The energy and the arrival point of the protons inside these magnets have a strong impact on the particle focusing, defocusing and deflection: there are the cromaticity effect. Higher order magnets, like sextupoles and octupoles, are installed in the accelerator to correct these effects.

On a particle circulating in the ring, an electromagnetic force acts, given by:

$$\frac{d\vec{p}}{dt} = q(\vec{E} + \vec{v} \wedge \vec{B}), \tag{1.1}$$

where $\vec{p}$ is the relativistic momentum, $q$ and $\vec{v}$ are the charge and the velocity of the particle, $\vec{E}$ and $\vec{B}$ refer respectively to the electrical and the magnetic fields acting on the proton. The Lorentz force is applied as bending force to guide the particle along the design orbit which in principle all particles should follow but from which most of them will unavoidably deviate.

### 1.1.1 Betatron oscillations

We now discuss the transverse motion [11–14] of a charged particle in a circular accelerator in steady state, that means not in injecting, extracting or accelerating conditions. Using a fixed and right-handed Cartesian reference system [11], it would be difficult to express deviations of individual particle trajectories from the design orbit. Because of that, it is more useful to introduce a right-handed orthogonal and co-rotating system ($x$, $y$, $s$), as Figure 1.1 shows, that follows an ideal particle travelling along the design orbit. The blue line represents the ideal orbit and the black arrow $r_0$ shows the orbital radius. By convention, the local axis $x$ points outwards and the axis $y$ points upwards. The local longitudinal axis $s$ is tangent to the propagation direction of the reference particle.

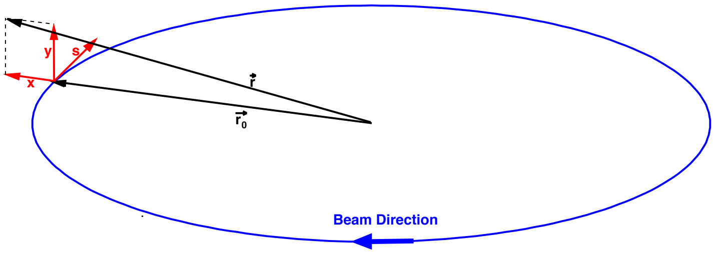

**Figure 1.1:** *Right-handed moving reference system of the accelerator.*

In transverse linear dynamics, $\vec{E} = 0$ and, in the following discussion only the magnetic field $\vec{B}$ will be taken into account in Eq. 1.1. Vertical and orthogonal dipoles force protons to curve in the horizontal plane with a local bending radius equal to:

$$\rho = \frac{p}{qB}. \tag{1.2}$$

From that, the definition of the *magnetic rigidity* $R$ can be derived:

$$R = B\rho = \frac{p}{q}. \tag{1.3}$$

The equations of transversal motion, whose full derivation can be found in Ref. [11], are expressed from the so called *Hill's equations*:

$$x'' + K_x(s)x = 0,\ K_x(s) = \frac{1}{\rho(s)^2} - \frac{B_1(s)}{B_0\rho(s)} = \frac{1}{\rho(s)^2} + K_y(s) \tag{1.4}$$

$$y'' - K_y(s)y = 0,\ K_y(s) = -\frac{B_1(s)}{B_0\rho(s)} \tag{1.5}$$

where $\rho$ is the local bending radius, $B_0$ and $B_1$ are the coefficients of dipole and quadrupole respectively Within a magnetic element, $\rho$(s) and $K_y(s)$ can be considered constant in s, so the solution of Eqs. 1.4 and 1.5 gives respectively a harmonic oscillator or an exponential function depending on the sign of $K_y$. The general solution of Hill's equation along $x$, assuming $\rho(s)$ and $K_y(s)$ piecewise constant functions with the same periodicity as the piecewise constant with appropriate boundary conditions and neglecting dispersion, is [13]:

$$x(s) = \sqrt{\epsilon_x\beta_x(s)}\,\cos(\varphi_x(s) + \varphi_0). \tag{1.6}$$

$\beta_x(s)$ is a periodic function, known as *betatron function*, that modulates the amplitude of the oscillation in the transversal plane, referred to as betatron oscillations. $\beta$ is determined by the quadrupole magnet arrangement and powering. $\varphi_0$ is an arbitrary constant phase, which can be considered as an integration constant, and $\varphi_x(s)$ is the phase advance, given by:

$$\varphi(s) = \int_{s_0}^{s} \frac{1}{\beta(s')ds'}, \tag{1.7}$$

with $s_0 \leq s$ being an arbitrary reference location in the ring. According to the equation 1.7, $\varphi_x(s)$ is positive and monotonic increasing quantity. $\epsilon_x^i$ is called the single-particle emittance and, as detailed below, determines the particle's oscillation amplitude. Emittance is the property of a particle beam that characterizes its size and unlike the physical dimensions of the beam, which vary with location in an accelerator, emittance is invariant. For the full set of particles composing the beam, a statistical quantity $\epsilon_x$ can be defined: it represents the so-called geometrical beam emittance, i.e. the rms value of the single-particle emittances.

Therefore, as a particle travels around a ring, its motion is a pseudo-harmonic oscillation with amplitude modulated by the periodic function beta and with a phase $\varphi_x(s) + \varphi_0$, which advances with $s$ at a varying rate proportional to $1/\beta$.

At each $s$ position in the machine, the displacement $x$ of the circulating particle lies always below a limit value X(s) referred to as:

$$X(s) = \sqrt{\epsilon_x\beta_x(s)}. \tag{1.8}$$

The complete trajectory of a particle will fall within an envelope defined by $\pm X(s)$.

The rms betatronic beam size $\sigma(s)$ can be expressed as [11]:

$$\sigma(s) = \sqrt{\epsilon\beta(s)}. \tag{1.9}$$

It indicates that the 66.6% of the circulating particles stays within such a distance. With good approximation, the particle distribution is a Gaussian within $3\sigma(s)$ from the center of the distribution. Inside this range, we define the *core* of the beam, while the particles populating the tails of the distribution generate the beam *halo*.

If expressed in terms of $\sigma(s)$ and $\epsilon$, the $\beta$-function becomes:

$$\beta(s) = \frac{\pi\sigma(s)^2}{\epsilon} \tag{1.10}$$

So, at each s position, $\beta$ roughly corresponds to the width of the squared beam size divided by the emittance. If $\beta$ is low, the beam is narrower, "squeezed". If $\beta$ is high, the beam is wide and straight.

In a storage ring, the number of transverse oscillations of a particle in one revolution around the ring is defined as *betatron tune*. It mainly depends from the quadrupoles and is mathematically defined as:

$$Q_x = \frac{1}{2\pi}\varphi(C) = \frac{1}{2\pi}\int_{s_0}^{s_0+C}\frac{ds}{\beta(s)} \tag{1.11}$$

At some fixed value $s_0$, since $\beta(s)$ is periodic, the amplitude in Eq. 1.6 will be constant ($\sqrt{\epsilon_x\beta_x(s_o)}$). The only variable changing is the phase $\varphi_x$, which increases by $2\pi Q_x$ on every turn. As said, the motion in $x$ resembles a harmonic oscillation. If $Q_x$ were an integer, x($s_0$) would have the same value on every revolution. In that case, any imperfections in the magnetic field around the ring act as perturbations, which are synchronous with the oscillation frequency. This will excite resonances, causing an increasing amplitude and unstable motion provoking a consequent loss of the beam. Therefore, integer values of the tune must be avoided. Similarly, resonances appear also for rational fractions. Thus, it is preferred that the tune is an irrational number to stay far from the resonances that would make the machine unstable. In circular colliders, high brightness beams may cause a notable shift and spread of the single particle tunes, which may move the particles onto tune resonances. Several effects in the machine, such as the beam coupling impedance (see Section 1.1.4), may lead particles circulating in a ring to move away from the reference betatron tune of the machine, $Q_0$. This is commonly referred to as *tune shift*, $\Delta Q_i = Q_i - Q_{i,0}$, where $i$ can be calculated in the horizontal plane, $i = x$ or in the vertical one, $i = y$.

### 1.1.2 Particle momentum and dispersion

The *momentum offset* of a particle is related to the energy deviation by:

$$\delta = \frac{\Delta p}{p} = \frac{1}{\beta^2}\frac{\Delta E}{E} \tag{1.12}$$

where $\beta = v/c$ is the relativistic beta.

In the transverse plane, an energy offset is manifested by a new distorted closed orbit, around which the particles can perform betatron oscillations. For small deviations in momentum, Eq. 1.4 becomes:

$$x'' + K(s)x = \frac{\delta}{\rho(s)} \tag{1.13}$$

The solution of this equation is:

$$x(s) = x_\beta(s) + x_\delta(s) \tag{1.14}$$

where $x_\beta$ is the betatron oscillation around the off-momentum orbit and $x_\delta(s)$ is the displacement due to the energy error. $x_\delta(s)$ is the particular solution of the inhomogeneous equation ( 1.13) and it is generally expressed as:

$$x_d(s) = D(s)\delta \tag{1.15}$$

where $D(s)$ is called *dispersion function*. For most accelerators, the dispersion function has values in the range from few centimeters up to meters.

### 1.1.3 Machine aperture

The physical space set by the vacuum chamber in which the particle beam moves and by the equipments installed all along the ring (e.g., magnets, screens, collimators, other diagnostic instrumentation) is called *geometrical aperture* $A_{geo}$. The aperture is expressed in units of the standard deviation of the beam size in a certain plane, which in plane $i$ is derived by:

$$\sigma_i(s) = \sqrt{\beta_i(s) \cdot \epsilon + (D_i(s) \cdot \delta)^2} \tag{1.16}$$

However, as the contribution of the dispersion is much smaller than the betatronic one, the aperture is normally defined by the betatronic part only. At any location of the machine, the geometric aperture must be larger than the maximum oscillation amplitude of the particles to avoid that particles hit the opening. However, in a real accelerator the presence of non-linear elements (i.e. sextupole magnets, used for machine chromaticity correction, or higher order correctors), introduce unavoidable non-linearities in the magnetic fields that act on all the beam particles. Therefore, a particle with an oscillation amplitude larger than a certain value, called *dynamic aperture* $A_{dyn}$, will no longer perform stable oscillation but be lost after some turns.

### 1.1.4 Beam coupling impedance

A particle beam travelling through an accelerator interacts with its surroundings (vacuum chambers, magnets, collimators, etc.) generating a scattered electromagnetic field, known as *wake field* (Fig. 1.2), that acts back on the beam and may eventually perturb its motion [15] . The coupling between the field generated by the beam and their effect on beam itself through the environment can be described by the *beam coupling impedance*. This parameter relates the beam-induced voltage $V(\omega)$ on the structure and the particle beam current $I(\omega)$ as [13]:

$$V(\omega) = -Z(\omega)I(\omega), \tag{1.17}$$

indicating by the minus sign that the induced voltage leads to an energy loss for beam particles. The impedance $Z(\omega)$, expressed in Ohm in the longitudinal plane and in Ohm/m in the transversal plane, is in general complex function of the frequency $\omega$:

$$Z(\omega) = Z_{Re}(\omega) + iZ_{Im}(\omega), \tag{1.18}$$

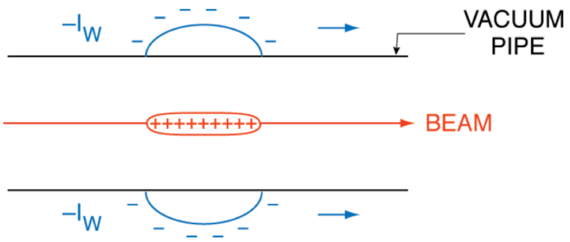

**Figure 1.2:** *Schematic example of the effect generated by the beam while circulating in a beam pipe.*

The longitudinal coupling impedance, determined by the scattered longitudinal electrical field seen by the particle beam, may lead to device heating and instabilities as well. On the transverse plane, the imaginary part of the impedance can lead to a shift in the betatron oscillation frequency of the particles, while the real part may cause damping or antidamping [13]. Therefore, impedance can be at the origin of strong beam instabilities, which may limit the achievable intensity in an accelerating machine. The transverse impedance indicates the transverse force deflecting the beam during its betatron motion and does not affect particle energy.

One of the main contributor to impedance is the resistive wall impedance of the devices surrounding the beam. A relativistic point charge travelling through a vacuum chamber with perfectly conducting walls leaves behind no wake fields, since the fields do not penetrate the chamber and no energy is dissipated in the walls. However, if the vacuum chamber walls have a finite conductivity, then energy will be dissipated by the beam's induced currents, and a wake field will be produced. The transversal resistive wall impedance $Z_{RW}^{\perp}$ of a cylindrical beam pipe (resistive object) is given by [15, 16]:

$$Z_{RW}^{\perp}(\omega) = \frac{2cZ_{RW}^{\parallel}}{b^2\omega} = \frac{2cR}{b^3\omega\delta_c\sigma_c} \tag{1.19}$$

where $\omega$ is the revolution frequency of the particle, $c$ is the speed of light, $R$ is the radius of the accelerator (the LHC ring in our case), $b$ is the radius of the beam pipe, $Z_{RW}^{\parallel}$ is the longitudinal resistive wall resistivity, $\sigma_{el}$ is the electrical conductivity of the material, $\delta_c$ is the skin depth, defined as $\delta_c = \sqrt{\frac{2}{\mu_r\mu_0\omega\sigma_{el}}}$, with $\mu_r$ and $\mu_0$ the relative and free-space permeability, respectively, and. Based on Eq. 1.19, the better the electrical properties of the materials used, i.e. the highest the conductivity, the lower is the risk of beam instabilities induced by impedance. This issue strongly concerns beam intercepting devices, such as collimators, owing to their proximity to the circulating beam.

## 1.2 Concepts of radiation damage in materials

Radiation damage is commonly defined as the unfavourable consequences of the radiation interaction with the materials. In high-power accelerators, it is a threat particularly to those components exposed to beam losses. These components include targets, beam dumps, and highly exposed collimators. There is renewed interest in the topic of radiation damage owing to new projects and initiatives which require high-power accelerators, and therefore materials which will withstand the high power for sufficiently long times.

Besides the fundamental importance for the LHC collimators and their future upgrades, there are several other projects in which the radiation damage is an issue that must be taken into strong consideration. At the European Spallation Source (ESS) [17], a rotating wheel made of tungsten with a tantalum cladding is proposed for the target, which will be irradiated with 5 MW of 2.5 GeV protons. The Facility for Rare Ion Beams (FRIB) at the National Superconducting Cyclotron Laboratory (NSCL) at Michigan State University will deliver heavy ions with a high power density of 20-60 MW/cm$^3$ [18]. In the framework of the Daedalus project [19] at the Deep Underground Science and Engineering Laboratory (DUSEL) in South Dakota, a neutrino beam is produced by three cyclotrons, each delivering a proton beam with an energy of about 800 MeV with a power on the target of 1, 2, and 5 MW for the first, second, and third cyclotron, respectively. An upgrade to higher beam power is already foreseen. At PSI, a 1.3 MW proton beam is routinely available, which is currently the most intense proton source in the world and will be upgraded to 1.8 MW in the future.

It is therefore essential to know how long heavily irradiated components will survive. Improvement of the lifetime of components needs knowledge about the underlying mechanisms of radiation damage and its relation to the changes in material properties. One issue is that the components cannot be tested under the same conditions as the ones they will be exposed to when the facility is in operation. This aspects is particularly important for accelerators like LHC (or FCC in the future) where beam energies are much higher than what available facilities can provide. Therefore, the correlations between data obtained under different conditions need to be understood.

### 1.2.1 Types of radiation

According to the electric charge of the particle, radiations are usually categorised into two categories [20, 21]:

- Charged radiation (directly ionising):
  - Heavy charged particles
  - Fast electrons
- Uncharged radiation (indirectly ionising):
  - Electromagnetic radiation
  - Neutrons

The behaviour of charged particles passing through matter is fundamentally different from that of the neutral ones. Charged particles strongly interact with the orbital electrons of the material. If sufficiently energetic, any charged particle can directly ionise the atoms by Coulomb force interaction. Among the charged radiation, there are protons, ions, alpha particles (two protons and two neutrons, identical to a helium nucleus), fission products, and also light electrons, which positive and negative beta particles emitted in nuclear decay and energetic electrons produced in other processes.

Indirectly ionizing radiations consists of particles electrically neutral, thus they do not interact strongly with the matter and can travel longer distances before an interaction occurs. In this case, ionisation is produced by the secondary charged particles generated as a consequence of the interaction. Electromagnetic radiation includes X-ray, emitted in the re-arrrangement of atomic electron shells, and gamma-rays emitted by excited nuclei in their transition to lower-lying nuclear levels. Neutrons, either thermal (eV) or fast (MeV), are mainly generated during nuclear interactions.

### 1.2.2 Effects of radiation interaction with matter

To understand the mechanism of radiation damage, we have to consider the various interactions of particles with the atoms of a material. Effects of radiation on materials can be classified in [21, 22]:

- **Atom displacement**: atoms are knocked out from their position in the lattice, leaving vacancies and relocating in interstitial locations or causing interchange of different species in the lattice.
- **Impurity production**: transmutation of nuclei in other nuclei, ex. generation of gas, such as hydrogen and helium.
- **Energy release**: a large amount of energy may be released in a small volume, which can result in heating of the material.
- **Ionization**: electrons are removed from the atomic shells of the target material and ion pairs are generated in the path of the incoming charged particles.

Table 1.1 summarises the damage produced by different types of radiation. The table is intended to give a relative extent of the effect induced by different particles.

**Table 1.1:** *Qualitative description of radiation damage to materials of various types of radiation, adapted from Ref. [22].*

| Damage<br>Radiation | **Atomic displacement** | **Impurity production** | **Energy release** | **Ionization** |
|---|---|---|---|---|
| **Alpha** | yes | He production | very short range | substantial |
| **Proton** | yes | H production | short range | direct |
| **Fission fragment and heavy ions** | multiple (via scattering) | become impurities themselves | short range | direct |
| **Electron/Positrons** | some | - | medium range | direct |
| **Photon** | rarely | - | low exponential attenuation | indirect |
| **Thermal neutron (eV)** | indirect | by absorption | indirect | indirect |
| **Fast neutron (MeV)** | multiple (via scattering) | by absorption (during thermalization) | indirect | indirect |

**Atomic Displacement (Damage)**

Atomic displacement occurs through kinetic energy transfer between the incoming particle and the material, by conversion of radiation-induced excitation of the matter into atom motion (i.e., formation of recoil atoms) [23]. Particles producing displacement damage include protons of all energies, heavy ions with energies below 1 MeV, fission products with very high energies (>100 MeV), electrons with energies above 150 keV, and neutrons. When one of these particle traverses the matter, the energy is dissipated by exciting orbital electrons and by elastic collisions with the material nuclei. An elastic collision can eject an atom from its normal lattice position. The ejected atom is known as a primary knock-on atom (PKA), which, in turn, may cause a cascade of atomic displacements before eventually coming to rest. The collision between an incoming particle and a lattice atom subsequently displaces the atom from its original lattice position, as shown in Figure 1.3: the displaced atom becomes an interstitial, and the position that the atom formerly occupied becomes a vacancy. Together the interstitial and vacancy are called Frenkel pair. Some displaced atoms can lead to secondary, tertiary, etc displacements: for example, the displaced atom may collide with and replace another atom in the material. Displacement damage is therefore the result of multiple nuclear interactions, typically scattering, which cause lattice defects.

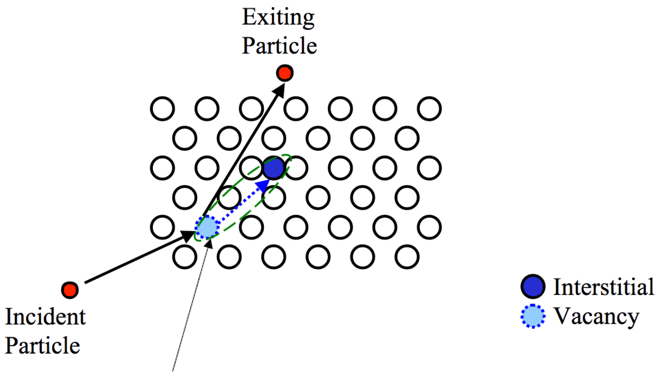

**Figure 1.3:** *Scheme of the atomic displacement damage, from Ref. [21]. A Frenkel pair consists of a vacancy and an interstitial atom.*

The role of the temperature is also important. When vacancies and interstitials are produced, the process involves the transfer of particle kinetic energy to potential energy stored in the crystal lattice. Both vacancies and, even more, interstitials are mobile at sufficiently high temperature, which helps the recombination. At high temperature, indeed, the vibration of the atoms in the lattice increases, providing a mechanism by which an interstitial atom can migrate to a vacancy, and they anneal themselves out.

The number of displacements per atoms (dpa) is a useful quantity commonly used to estimate the severity of the primary damage from radiation. A theory for calculating this parameter was proposed by Norgett, Robinson and Torrens (NRT model) in 1955 [24]. The NRT is based on a previous model, rather simpler, called Kinchin-Pease (KP) model [25], and is recommended as standard by the International Atomic Energy Agency (IAEA) [26]. The NRT evaluates the number of Frenkel pairs formed for a given energy transferred to the PKA, thus the number of atoms displaced over a certain volume. If $E_i$ is the energy of the incoming particle, dpa can be expressed as:

$$dpa = \int_0^E \sigma_{\text{disp}}(E_i)\, \phi(E_i)\, dE_i = \int_0^E \phi(E_i) dE_i \int_0^T \sigma_{dam}(E_i, E_R)\, \nu(E_R)\, dE_R \tag{1.20}$$

where $\sigma_{\text{disp}}(E_i)$ is the displacement cross-section, which gives the number of displacements per primary (bombarding) particle or secondary particle (neutrons, protons, etc.), and $\phi(E_i)$ the energy-dependent particle fluence (in units of cm$^{-2}$). The displacement cross-section is obtained from the damage cross-section $\sigma_{\text{dam}}$(E, E$_R$), function of E$_i$ and the recoil energy E$_R$ of the PKA. The damage function $\nu(E_R)$ indicates how many atoms are displaced after the collision. The energy available for the displacement cascade is called the damage energy, T$_{\text{dam}}$, equal to the recoil energy minus the energy dissipated in ionization and excitation of the atom.

The dpa concept and KP/NRT equations are widely used in estimating the amounts of radiation damage in materials [26]. It is appealing as it is easy to understand, and gives an order-of-magnitude estimate of which fraction of atoms are displaced during an irradiation process. For instance, a total radiation dose of 10 kJ/cm$^3$ does not tell a non-expert anything about how many defects such a dose can be expected to cause, whereas a value of 0.01 dpa would tell that one atom in a hundred has been displaced and likely become a defect. Dpa is a quantity that depends on the irradiation conditions (energy, doses, etc) and combines the irradiation conditions into a single global indicator, which characterises the amount of primary damage. Therefore, it is the most appropriate parameter for scaling radiation doses or fluences between different kinds of irradiations. For instance, if damage has been produced in a material by a given fluence of 50 keV Ne ions, and one wants to compare with Ar ions, a dpa calculation can tell what energy and fluence for the Ar ions can be expected to produce about the same damage as the 50 keV Ne irradiation did. For cases where the measured accumulated damage does not follow the dpa scaling, this indicates nonlinear behaviour in the damage production, as demonstrated in Refs [27, 28] for some cases of ion beams irradiation. However, it should be emphasized that the NRT approach is a simplified method that neglects the details of the process of the displacement cascade. No interactions of the struck atom with the remaining lattice atoms are taken into account.

### Impurity production

Among the impurities produced during irradiation, helium and hydrogen are the most important. When interacting with matter, protons may generate hydrogen and alpha particles. In both cases, the neutral atom is a gas at room temperature, and hence, will induce “pressure” on its neighbouring atoms. In solids, this internal pressurisation has been observed to cause swelling. However, impurity production becomes more relevant when dealing with neutron and ion irradiation. Incident ions will eventually slow and capture the necessary electrons to become neutral. On the other hand, inelastic reactions from neutron and ion irradiation may also lead to transmutation of the nuclei, which become radioactive. Neutron capture by a nucleus does not necessarily change the chemical element present, but create a different isotope that can eventually be radioactive and, decaying, can emit additional radiation. In contrast, ion absorption by a nucleus, a nuclear fusion process that is relatively improbable since it must overcome coulomb repulsion, immediately changes the chemical element present. Conventionally, presence of radiation-induced impurities in the lattice is measured in appm (atomic parts per million) and the ratio of transmutations to displacements in appm/dpa.

Bombarding isotopes with particles leads to a change in their proton and neutron numbers, i.e. transmutation inelastic reactions and production of transmutation nuclei of which H and He are the most important in radiation damage.

#### Ionization

Ionization is the process of removing or adding an electron to a neutral atom, which becomes an ion. The term is also often used in connection with the removal of a further electron from a partially ionized atom. A closely related process is the excitation, in which an electron is raised to a higher energy state. However, the amount of energy required for an excitation is lower than that for ionization. Charged radiations can directly ionise matter; however, neutral radiations indirectly cause ionization. Ionizing radiation tends to be increasingly damaging the material according to the localization of atomic bonds in the material structure [23]: the strongest metallic bond (metal + metal) will be the least damaged by radiation, then comes the ionic bond (metal + non-metal) and the most affected by damage will be the covalent bond (non-metal + non-metal) in which the bonding electrons are strictly localized.

#### Energy deposition

All radiation types cause energy (and charge) deposition within the absorbing material through the ionization process. In water and organics, most of the absorbed ionization energy breaks chemical bonds. In metals, the kinetic energy deposition from ionization generally manifests itself as thermal heating of the material. The corresponding temperature raise can change a number of material properties. In the case of direct heating due to the radiation, the product of the absorbed dose rate $\dot{D}$ and the material density $\rho$ gives the energy deposition rate per unit volume $\dot{Q}$.

The effects of a particle travelling through matter depend on its nature and the environment encountered. Under irradiation, defects can develop in a crystalline lattice. According to the topology of the defect formation, they are distinguished in:

- Points defects, i.e. defects that occur only at or around a single lattice point:
  - **Vacancy defects**: lattice sites which would be occupied in a perfect crystal, but are vacant because atoms have been knocked out.
  - **(Self)-interstitial defects**: atoms from the lattice which have left their lattice site for a site not provided in the lattice. The influence on its surroundings is a shift of neighbouring atoms away from the interstitial to make space for it.
  - **Interstitial impurity or extrinsic interstitial**: atoms much smaller than the atoms in the bulk matrix that fit into the open space between the bulk atoms of the lattice structure.
- 1D or line defects:

  - **Dislocation lines**: areas around which the atoms are out of position in the crystal structure.

- 2D or planar defects:
  - **Dislocation loops**: part of a lattice plane is missing or has been added. There are two types of dislocation loops: in the vacancy-type, part of a plane of lattice sites is missing, while in the interstitial-type, part of a plane of additional atoms has been incorporated into the lattice structure. Dislocations move under the influence of external forces, which cause internal stresses in a crystal.
  - **Grain boundaries**: the crystallographic direction of the lattice abruptly changes. This usually occurs when two crystals begin growing separately and then meet.
  - **Stacking faults**: local deviation of the stacking sequence of layers in a crystal (it is common in close-packed structures).

- 3D or volume defects:
  - **Voids**: several vacancy loops join and form three dimensional cavities of a few nm diameter.
  - **Bubbles**: originally voids later filled by insoluble gases formed by radiation-induced transmutation (ex: helium formation from transmutation of nickel atoms).
  - **Precipitates**: agglomeration of impurity atoms replacing neighbouring lattice sites on more than one plane. Owing to their different sizes and properties, the neighbouring atoms are slightly shifted from their original positions, which generates stresses.

Defects in a crystal lattice are summarised in Figure 1.4.

### 1.2.3 Macroscopic effects of radiation damage in materials

Radiation tends to alter the structure of the material, introducing imperfections in the lattice [30]. The production of defects in the microstructure can change the mechanical and thermo-physical properties of the irradiate materials. Such changes are a synergistic effects of atomic displacement, irradiation temperature, stress, etc. Radiation-induced damage takes place at different irradiation temperatures and dpa levels depending on the considered process (Figure 1.5). External stress conditions on the material during irradiation may also induce or catalyse some phenomena more than others.

*Swelling* is an isotropic volume expansion of the irradiated material due to void formation, which, in metals, typically occurs at fraction of the melting temperature ($T_m$) of $T/T_m = 0.3-0.6$ and for dpa $>10$. In the incubation period, swelling increases slowly with increasing irradiation dose, then swelling increases at a higher rate until the saturation [32]. Owing to the swelling, the material density may decrease. Pure metals may swell at low doses, even for dpa $<1$, while complex alloys require about 10-100 dpa and higher. Figure 1.6 shows the history of the swelling occurring in tungsten

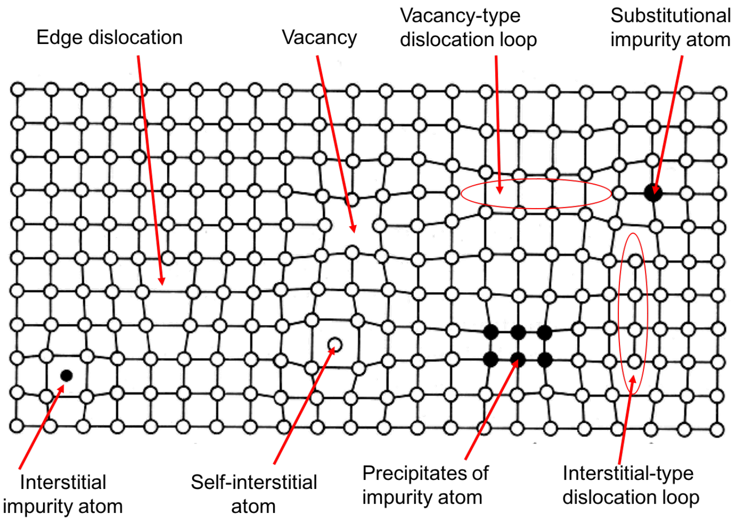

**Figure 1.4:** *Defects in a crystal lattice. The picture was modified from the original version of Ref. [29].*

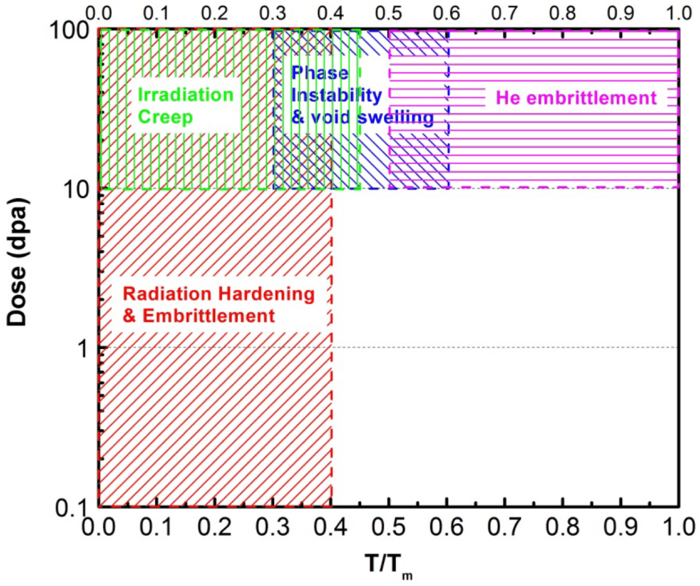

**Figure 1.5:** *Correlation of radiation-induced effects with dose (in terms of dpa) and irradiation temperature (expressed as fraction of the melting temperature of the material, $T_m$). From Ref. [31].*

compression specimens, exposed to increasing irradiation with 800 MeV protons and compression tested to 20% strain at room temperature [33].

*Radiation hardening* consists in an increase of both the yield and the tensile strength, with a consequent reduction of ductility (plastic strain). The large density of defect loops generated during irradiation fixes the dislocations and inhibits slip processes of the crystalline planes, which contributes to determine mechanical properties of the material. More energy is therefore required to start a slipping process. Radiation hardening occurs after a few tenths of a dpa at temperatures $T/T_m \leq 0.4$, and then saturates.

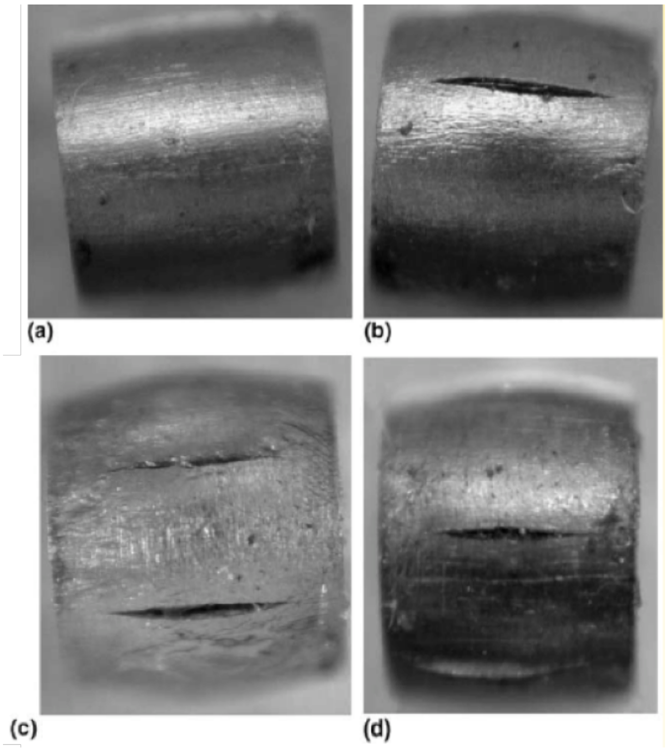

**Figure 1.6:** *Swelling in tungsten compression specimens, exposed to increasing irradiation with 800 MeV protons and compression tested to 20% strain at room temperature: (a) before irradiation, (b) after 3.2 dpa, (c) after 14.9 dpa, and (d) after 23.3 dpa. Picture from Ref. [33].*

This process is usually accompanied by *embrittlement*, i.e. a reduction of the energy to fracture, which causes a fast crack propagation. The ductile-brittle transition temperature (DBTT) is the temperature which determine the transition of a material exhibiting ductile behaviour at higher temperatures and brittle behaviour at lower temperatures; it increases significantly with irradiation. *Thermal creep* is the time-dependent component of the plastic strain and refers to a permanent deformation under constant load and at temperature $T/T_m \geq 0.5$. Thermal creep is also a temperature-dependent process requiring the thermal formation and mobility of vacancies. Irradiation can accelerate creep due the production of defects. *Irradiation creep* is not strongly dependent on temperature because formation of vacancies and interstitials is mainly driven by energetic atomic displacement rather than by thermal processes. Indeed, it occurs at low temperatures ($T/T_m \leq 0.45$) when thermal creep is still negligible, and dpa >10 [30, 34]. In low symmetry crystalline structures, radiation can induce changes in dimensions, in the absence of applied stress: this process is called *growth*. It can occur at low temperatures ($T/T_m = 0.1 - 0.3$) and is usually accompanied by embrittlement.

Heat conduction in materials can occur by electrons, phonons or other excitations, and thermal conductivity is a function of the velocity and mean free path of the heat carriers [35]. In metals, thermal current is carried by both electrons and phonons, while in insulators, only phonons can be carriers. Irradiation generates defects in the materials that become obstacles to the heat carriers. A change of the mean free path of phonons or electrons due to interaction with lattice defects is the main cause of irradiation-induced degradation of thermal conductivity. In a similar way, radiation also affect the electrical properties. Any radiation that introduces irregularities into the crystal structure causes an increase in the electrical resistivity since the lattice imperfections decrease the mobility of the charge carriers. An example of the reduction in thermal conductivity in graphite after neutron irradiation is depicted in Figure 1.7.

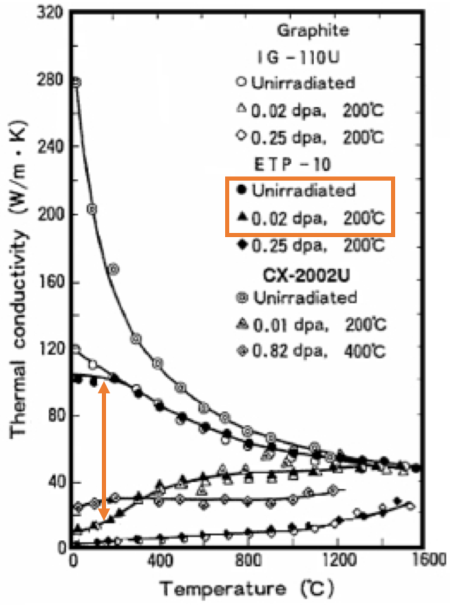

**Figure 1.7:** *Change in thermal conductivity of different types of graphite as a function of irradiation temperature and dose. About a factor 10 in reduction of thermal conductivity is visible already after 0.02 dpa. Picture from Ref. [36].*

Helium and hydrogen gas atoms are produced as transmutation products in the material during irradiation and may have negative effects on the mechanical properties. Helium atoms migrates into vacancies, forming bubbles at the grain boundaries, which grow with increasing temperature. The results are the void swelling (Figure 1.8) or the high-temperature embrittlement of the irradiated material, in which cracks can develop [37]. Hydrogen is even more mobile than helium and it does not depend as much from the temperature. High concentration of hydrogen can cause ductility loss by hydrogen bubble formation, or formation of hydrides [39]. The production rates of helium and hydrogen can be quite different in different irradiation environments (see Table 1.2). For example, since spallation reactions are often accompanied by helium emission, He production rate per dpa is much larger in these reactions than during fission. In fission reactors, about 0.5 appm He/dpa is produced, almost negligible compared with 100 appm He/dpa which will be produced on the steel window of the target at the European Spallation Source, once operating with 2.5 GeV protons [17]. Furthermore, about 10 times more hydrogen than helium is formed during the irradiation. In particle accelerators handling GeV protons, the helium and hydrogen transmutation rate is respectively 100 appm He/dpa and 500 appm H/dpa [41].

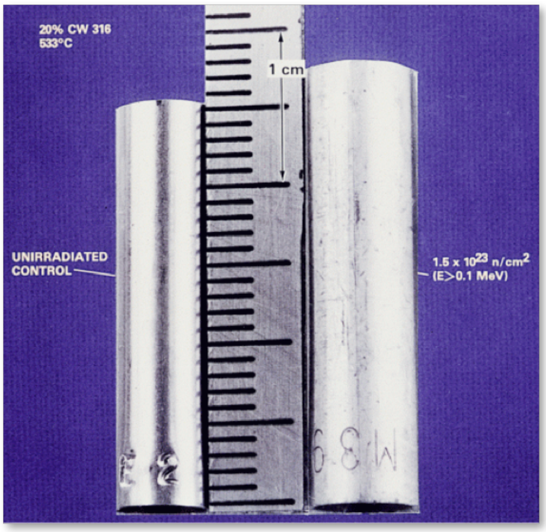

**Figure 1.8:** *Void swelling in 316-stainless steel tube exposed to reactor dose of* $1.5 \times 10^{23}$ *n/cm*$^2$*: (left) before irradiation, (right) after irradiation. Picture from Ref. [38].*

**Table 1.2:** *Typical parameters of different irradiation sources. From Ref. [40].*

| **Irradiation source** | **Displacement rate** (dpa/s) | **He/H production** (appm/dpa) | **Irrad. temperature** (° C) |
|---|---|---|---|
| Mixed spectrum fission reactors | $3 \times 10^{-7}$ | $10^{-1}$ | 200-600 |
| Fusion reactor | $1 \times 10^{-6}$ | $10^{1}$ | 400-1000 |
| High-energy proton beam | $6 \times 10^{-3}$ | $10^{2}$ | 100-800 |

An overview of the different mechanisms contributing to the material damage at various irradiation temperature regimes is given in Table 1.3.

Damage correlation between different types of irradiations should consider various parameters, such as the irradiation temperature, the displacement dose rate, the He/H production rates, etc. Reliable damage correlation requires integration of theoretical, computational and experimental activities to make predictions of radiation damage for any specific case. In particular, for high-energy accelerator particles not many experimental data are currently available, while much has been studied in the past concerning neutron irradiation in fission reactors. However, effects from low energy neutron irradiations do not equal effects from high energy proton irradiations. High energy protons cause displacement cascades and transmutation production of helium and hydrogen and solid impurities. Both displacement damage and production of helium and hydrogen must be considered in correlating damage between neutron and high energy proton irradiations in order to evaluate the entity of the micro/macroscopic property changes in the device subject to irradiation.

**Table 1.3:** *Irradiation temperature regimes. Note that $V$ and $I$ stand for vacancies and interstitials respectively, $A$ is referred to as the atoms of one of the material components in the lattice, $GB$ are the grain boundaries, $T_m$ is the melting temperature of the material and $T_{irr}$ the irradiation temperature.*

| **Temperature regime** | **Irradiation temperature** | **Microscopic process** | **Macroscopic effect** |
|---|---|---|---|
| Low | $T_{irr} \geq 0.2\,T_m$ | Non-equilibrium phases due to microchemical changes | Segregation and precipitates |
| | $0.1\,T_m \leq T_{irr} \leq 0.3\,T_m$ | • Hardening by dislocation loops and precipitates.<br>• Anisotropic nucleation and growth of dislocation loops. | • Low temperature embrittlement<br>• Irradiation growth |
| | $T_{irr} \leq 0.3\,T_m$ | Pinning of mobile dislocations by point defect clusters | Hardening, Embrittlement |
| | $0.2\,T_m \leq T_{irr} \leq 0.4\,T_m$ | Under load, I and V are absorbed at preferred oriented dislocations | Irradiation creep under load |
| Intermediate | $0.3\,T_m \leq T_{irr} \leq 0.5\,T_m$ | • Preferential absorption of I at dislocation, surplus of vacancies flowing to voids.<br>• Defects move to sinks (surface, dislocations, GB), preferred association of A with defect flux, enrichment or depletion of A in a certain area.<br>• Precipitation of defects and impurities. | • Void swelling<br>• Segragation<br>• Irradiation creep |
| | $T_{irr} \leq 0.45\,T_m$ | Nucleation and growth of He bubbles on GB leading to premature intergranular failure | He embrittlement |
| High | $T_{irr} \geq 0.5\,T_m$ | Increased dislocation probability | Thermal creep |

CHAPTER 2

# The Large Hadron Collider and its collimation system

Particle accelerators are nowadays among the most powerful instruments for scientists in different branches of science. Many examples can be listed: in the high energy physics, a new research path has been traced after the discovery of the theorised Higgs Boson at CERN (European Organisation for Nuclear Research) in 2012, or several studies in biological, chemical, material science performed in synchrotron radiation facilities, as well as the the new hadron therapies for medical purpose, pursued in other research laboratories. CERN is currently the world's leading laboratory for particle physics, whose mission is to push the frontiers of the human knowledge through the fundamental research in physics. In the first part of this Chapter, a brief introduction to the CERN accelerator complex, the Large Hadron Collider (LHC) and the program for its future upgrade is given. The high energy and intensity reached in the LHC and the use of superconducting technologies require a sophisticated collimation system for beam cleaning and machine protection. Beam collimation at the LHC is presented in the second part of the Chapter, where different design and collimator functions are described.

## 2.1 The LHC: scope and layout

The CERN Large Hadron Collider (LHC) is the largest and most powerful accelerator for research ever designed, built and operated. The construction of such machine has been a project spanning almost 15 years and involving scientists and engineers from all over the world. It consists of two-rings, and can accelerate and collide two opposite hadrons beams. It is installed in a 27 km long circular tunnel at a depth ranging from 50 to 175 m, between France and Switzerland, as shown in Figure 2.1. It is a synchrotron, where two counter rotating hadron beams are guided around their circular orbit by powerful superconducting magnets (8.3 T) cooled in a bath of superfluid helium at a temperature of 1.9 K. Particles are accelerated and brought into collision in four large detectors.

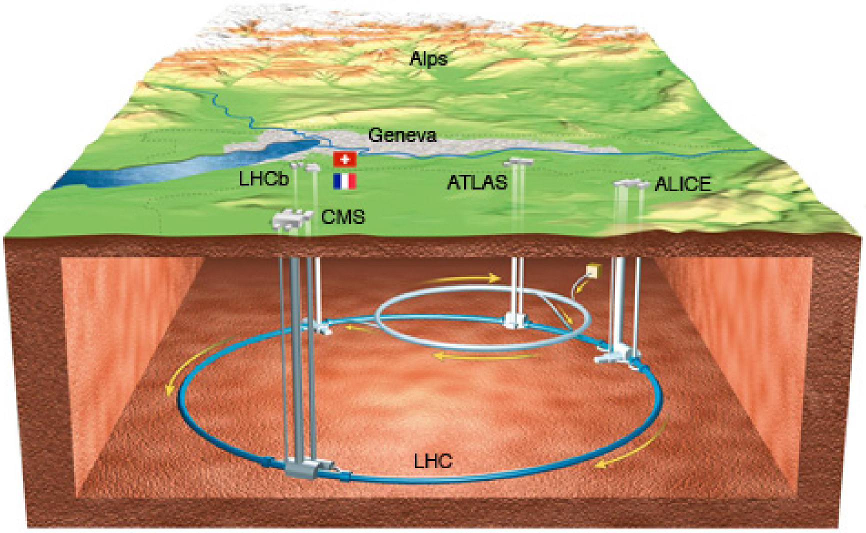

**Figure 2.1:** *Position of the CERN LHC inside Geneva area.*

### 2.1.1 The accelerator chain

The LHC has been designed to collide protons with a center-of-mass energy of 7 TeV per beam and heavy ion beams up to the design energy of 574 TeV [1]. However, one single machine cannot reach all alone such energies but it needs support from an accelerator chain behind. This is also the case at the LHC (Figure 2.2).

Everything starts from a bottle containing hydrogen from which protons are taken by stripping out the orbiting electrons with a process called Duoplasmatron. After being generated at approximately 100 keV, particles pass a radio frequency quadrupole (RFQ), which focusses, bunches and accelerates at the same time a continuous beam of charged particles with high efficiency. After the RFQ, the protons are accelerated in the LINAC 2 to the kinetic energy of 50 MeV. The extracted beam is injected in the PSB (Proton Synchrotron Booster), a piled-ring accelerator, built in 1972, which provides high intensity beams up to 1.4 GeV, then delivered to the PS (Protron Synchrotron). The PS is one of the oldest machine at CERN, built in 1959: here the particles are grouped into trains of bunches with 25 or 50 ns spacing and receive a further acceleration up to 26 GeV. Particles are injected in the SPS (Super Protron Synchrotron), built in 1976, where they are further accelerated to 450 GeV. Before reaching the LHC, the beam is sent through two different transfer lines: TI2 (clockwise, for Beam 1) or TI8 (counter-clockwise, for Beam 2).

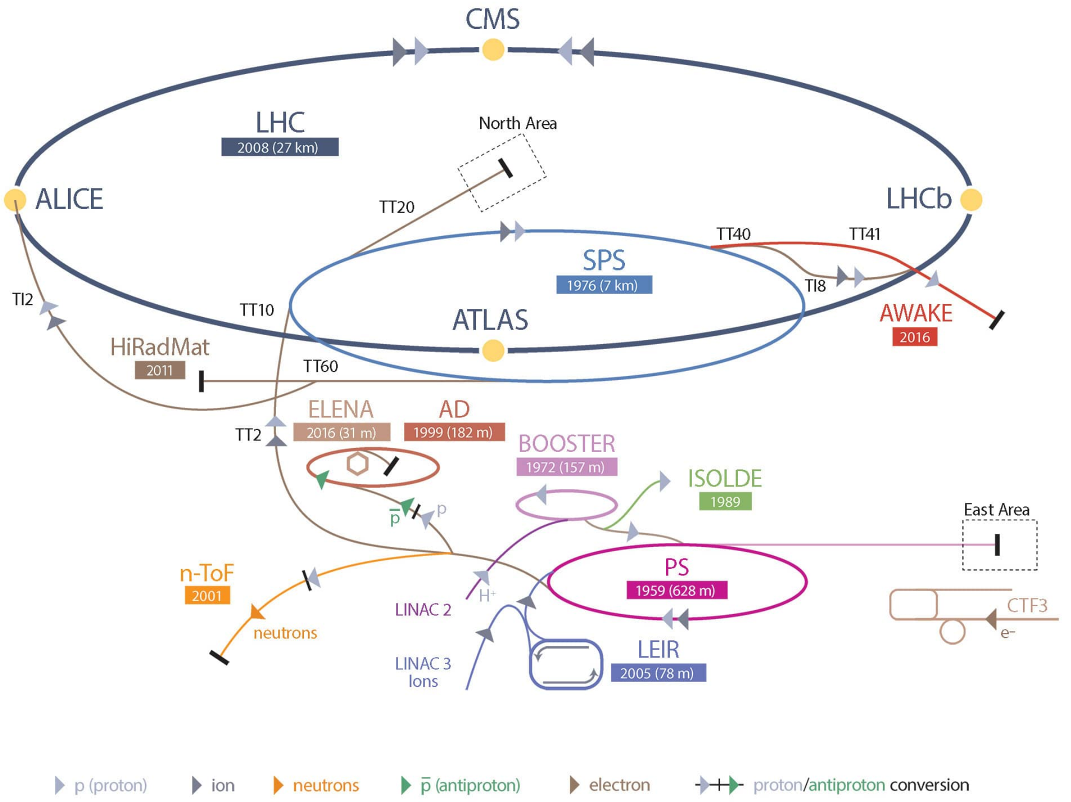

**Figure 2.2:** *Scheme of the LHC accelerator chain.*

The LHC can also operate with heavy ion beams. In this case, they are first accelerated by a dedicated linear accelerator, called LINAC 3, then go into the Low-Energy Ion Ring (LEIR) before being injected in the PS, SPS and finally in LHC, as for the protons.

### 2.1.2 An insight into the LHC accelerator ring

Figure 2.3 gives a schematic reproduction of the LHC ring [1]. It is segmented in eight arcs that keep the beams on the circular orbit, and eight Long Straight Sections (LSSs), where devices with dedicated functions are installed. The part of each LSS hosting devices with specific tasks is called Insertion Region (IR), and it is surrounded by Matching Sections (MSs), responsible for the smooth transition between the specialised optics of the IR and the regular one of the arc. Finally, Dispersion Suppressors (DS) identify an area at each end of the arcs aimed at reducing dispersion onto the IRs (see Chap. 1).

During the normal operation of the machine [42], the beams are injected through transfer lines from the SPS to the LHC located close to IP2 (from Beam 1) and IP8 (for Beam 2). Then, they are accelerated by a radio frequency cavities (located in IR4) and simultaneously the magnetic field of the LHC is ramped up to keep them in the center of the beam pipe. The beams are stored and kept colliding for many hours and once the "Physics" period ends or in case of any failure, the beams are extracted from the ring by

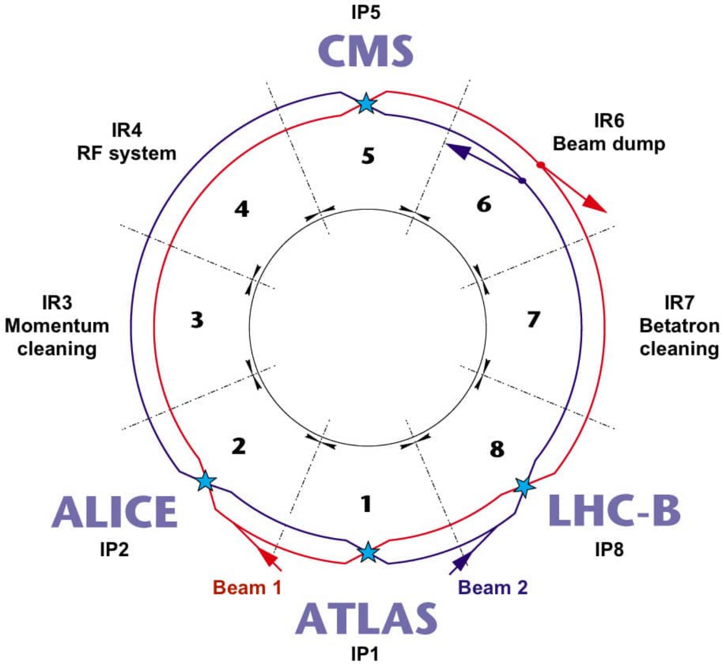

**Figure 2.3:** *Schematic layout of the LHC ring. Beam 1 circulates clockwise, while Beam 2 counter-clockwise.*

the dump system located in IR6. IR3 and IR7 are two collimation insertions dedicated to beam cleaning. This topic is treated in more detail in Chap. 2.2.

### 2.1.3 The superconducting magnets in the LHC

In order to steer, bend and focus the particle beams at top energy on the circular orbit, more than 6500 magnets are installed in the LHC ring, 1232 of which are superconducting (SC) magnets. They provide a magnetic field of 8.3 T, which is much higher than the maximum magnetic field provided by warm dipoles. The arcs of LHC are formed by 15 m long modules; each of them contains a superconducting dipole. A transversal section of such module is shown in Figure 2.4. Superconductivity is a property that some materials have when cooled to very low temperatures, and it enables the flow of currents with no dissipation by the Joule effect [43]. The material chosen for LHC SC dipoles is a Niobium-Tin alloy ($Ni_3Sn$). To work in superconducting conditions, the coils are kept at cryogenic temperatures of 1.9 K. However, SC magnets are sensitive to heating from beam losses or other sources. If a local increase in temperature brings the working point above the critical point, the coil locally loses the SC state and transits to the normal conducting one. This phenomenon is known as magnet *quench*. Quenches should be avoided during LHC operation also because recovery is a lengthy process that may reduce the availability of the machine.

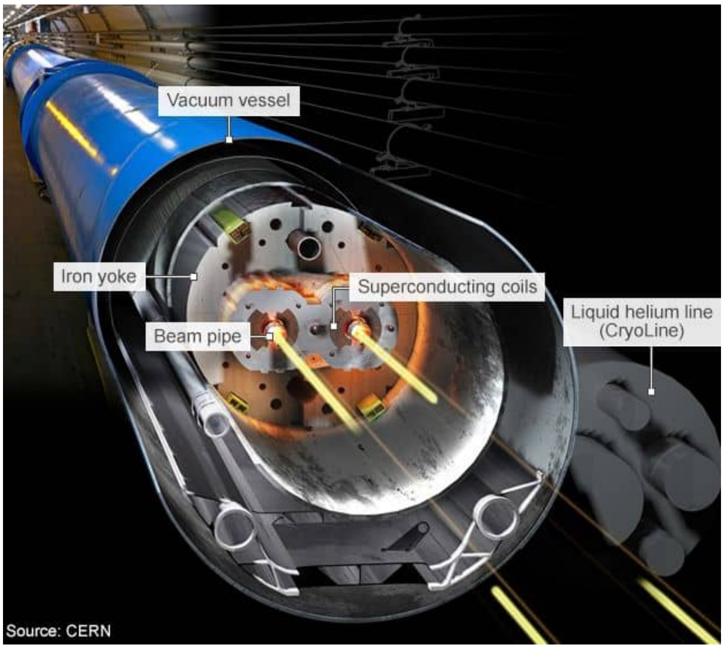

**Figure 2.4:** *Transversal section of 15 m long superconducting dipole in the LHC.*

### 2.1.4 The luminosity and the LHC experiments

The LHC provides extraordinary opportunities in particle physics thanks to its high beam energies and high beam intensities. However, a large amount of collisions has to be accumulated before reaching a statistically sound conclusion from the data. The rate of useful events generated from particle collisions in a high energy experiment is given by:

$$\frac{dN_{event}}{dt} = \mathcal{L}\,\sigma_{event} \tag{2.1}$$

where $N_{event}$ is the number of collisions, $\sigma_{event}$ is the cross section of the event under study, which represents the probability for a reaction to happen starting from the given collision, and $\mathcal{L}$ is the instantaneous luminosity. $\mathcal{L}$ is a fundamental parameter for a particle collider and represents the collision frequency per interaction cross section. For two head-on colliding beams with an identical Gaussian beam distribution (ideal case), the luminosity can be expressed as:

$$\mathcal{L} = \frac{N_b^2 n_b f_{rev} \gamma_{rel}}{4\pi\epsilon_n\beta^*}F \tag{2.2}$$

where $N_b$ is the number of particles per bunch, $n_b$ the number of bunches per beam, $f_{rev}$ revolution frequency, $\gamma_{rel}$ the relativistic gamma factor, $\beta^*$ the $\beta$-function at the collision points, $\epsilon_n = \epsilon\beta_{rel}\gamma_{rel}$ the normalised transverse beam emittance (see Chap. 1.1.1), $\beta$-function and $\epsilon_n$ determine the transversal beam size. If $\beta_{rel}$ is close to one (that is the case of the LHC where particles are very close to the speed of light), the emittance is approximately inversely proportional to the energy and so the physical width of the beam will vary inversely to the square root of the energy. Finally, $F$ is the geometric luminosity reduction factor that tells how the bunches cross because of the crossing angle that is imposed to the colliding bunches to avoid parasitic collisions at the interaction points.

About 1 billion proton-proton interactions per second are expected with the nominal LHC design luminosity $\mathcal{L} = 10^{34}\,\mathrm{cm}^{-2}\mathrm{s}^{-1}$. Summary of the main parameters for the proton beam operation for the nominal LHC machine is given in Table 2.1, together with the values expected in 2017 operation and the ones foreseen for the High Luminosity LHC (HL-LHC) upgrade.

As the integral of the collision rate over time gives the statistics available to the analysis of experimental data, the integral over time of the instantaneous luminosity, called integrated luminosity $\mathcal{L}_{int}$, gives an indication of the useful collisions collected during a certain running period $\Delta$T:

$$\mathcal{L}_{int} = \int_0^{\Delta T} \mathcal{L}(t)dt \tag{2.3}$$

For a given configuration, the machine availability significantly contributes to the integrated luminosity performance.

The beam collisions at the LHC occur at four Interaction Points (IPs) which host huge particle detectors. The two high luminosity experiments are *ATLAS* (A Toroidal LHC Apparatus) [44] (IP1) and *CMS* (Compact Muon Solenoid) [45] (IP5). They are multi-purpose detectors and explore the frontiers of high energy physics; they brought on July $12^{\mathrm{th}}$ to the discovery of the Higgs Boson, a boson of a mass of approximately 125 GeV/c$^2$ [46, 47]. The experiment *LHCb* (Large Hadron Collider beauty) [48] (IP8) is dedicated to study the decay of B mesons and *ALICE* (A Large Ion Collider Experiment) [49] (IP2) is optimized for heavy ions collisions. All IPs are also equipped with special magnets (that sit on both sides of each detector) that provide final focus of the beams before going into collision: they are three quadrupoles in a row, and as such they are called the “inner triplet".

The value of the beta function at the interaction points is called $\beta^*$. The machine optics is typically adjusted to have a local minimum at such points, in order to minimize the beam size and thus maximise the interaction rate. Assuming that this point is in a drift space, one can show that the evolution of the beta function around the minimum point is given by:

$$\beta(z) = \beta^* + \frac{z^2}{\beta^*} \tag{2.4}$$

where $z$ is the distance along the nominal beam direction from the minimum point. This implies that the smaller the beam size at the interaction point, the faster the rise of the beta function, and thus the beam size, when going away from the interaction point. In practice, the aperture of the beam line elements (e.g. focusing magnets) around the interaction point limit how small $\beta^*$ can be made.

### 2.1.5 The challenges of the High Luminosity LHC upgrade

Since the first circulating beam at 450 GeV in 2010, the LHC performance has been continuously improved in terms of both beam energy and peak luminosity. However, in order to extend its discovery potential, the LHC will need a major upgrade in the

**Table 2.1:** *The table shows the values for the nominal LHC according to Ref. [1], the values for 2017 operation and the ones expected for the HL-LHC upgrade.*

| **Parameter** | **Nominal LHC** (design) | **Expected in 2017** | **HL-LHC** (baseline) |
|---|---|---|---|
| Beam energy in collision [TeV] | 7 | 6.5 | 7 |
| Bunch spacing [ns] | 25 | 25 | 25 |
| Number of bunches | 2808 | 2760 | 2748 |
| Maximum number of bunches per injection | 288 | 144 | 288 |
| Number of particles per bunch [$10^{11}$ p] | 1.15 | $1.15 - 1.3$ | 2.2 |
| Maximum stored energy per beam [MJ] | 362 | $330 - 373$ | 678 |
| Minimum $\beta^*$ [cm] | 55 | $30 - 40$ | 15 |
| Transversal normalised emittance [$\mu$m rad] | 3.75 | 3.5 | 2.5 |
| Maximum peak luminosity [$10^{34}\,\mathrm{cm}^{-2}\mathrm{s}^{-1}$] | 1.0 | 1.63 | 5 (levelled) |
| Ring circumference [m] | 26658.883 | | |
| Number of SC dipoles | 1232 | | |
| Length of SC dipoles [m] | 14.3 | | |
| Field of SC dipoles [T] | 8.33 | | |
| Bending radius [m] | 2803.95 | | |
| Revolution frequency [kHz] | 11.25 | | |
| RF frequency [MHz] | 400.79 | | |

2020s, which will increase its integrated luminosity by a factor of 5 beyond the design value (see Table 2.1). As a highly complex and optimised machine, such an upgrade will involve several operational aspects and machine devices, and about 10 years will be required to prototype, test and realise the necessary developments.

The baseline programme of the LHC until 2037 is schematically shown in Figure 2.5. The first Long Shutdown (LS1) in 2013-2014 allowed to remove limitations on

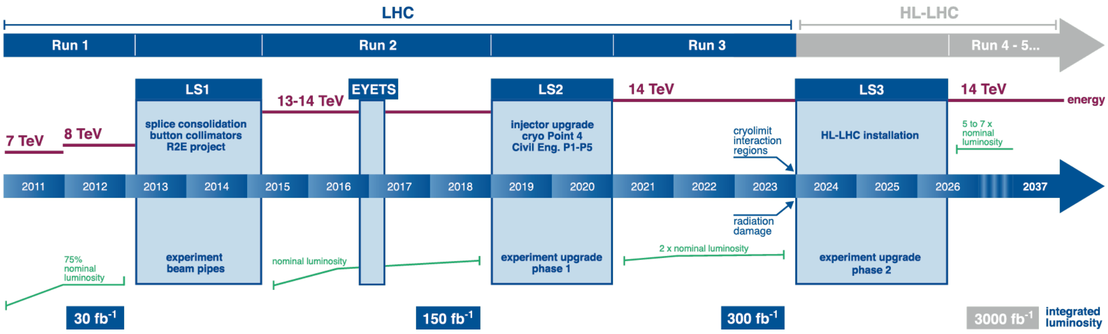

**Figure 2.5:** *Planning of the activities foreseen for LHC and the HL-LHC upgrade. The center of mass energies are shown, i.e. the double of the energies of the single beam.*

beam energy and to reach an integrated luminosity of about $40\,\mathrm{fb}^{-1}$. The second Long Shutdown (LS2), expected for the period 2018-2019, should bring the machine to reach an integrated luminosity of $300\,\mathrm{fb}^{-1}$.

The High Luminosity LHC (HL-LHC) project [2] will aim at a total integrated luminosity of more than $3000\,\mathrm{fb}^{-1}$ over approximately 12 years of operation after the upgrade. By definition, the instantaneous luminosity can be pushed forward by acting on the beam parameters, such as by increasing the number of circulating protons, i.e. the product of the bunch intensity and the number of injected bunches per beam, and by reducing the normalised beam emittance. The baseline beam parameters foreseen for HL-LHC are listed in the last column of Table 2.1. The achievements of such values will require several upgrades at the level of the LHC injector chain, which will be managed in the framework of the LHC Injectors Upgrade (LIU) program [50]. On the other hand, significant improvement of the machine optics can act positively on the luminosity by reducing the $\beta^*$ at the IPs. For this reason, a new LHC optics has been recently proposed, based on the novel Achromatic Telescopic Squeezing (ATS) scheme [51].

In view of the HL-LHC upgrade, several systems will need to be changed and improved, because they may become vulnerable to breakdown and aging, or a bottleneck for operation in a high radiation environment. In particular, the challenges of the HL-LHC upgrade pose various demanding requests for the beam collimation, limitations which will be discussed in Chap. 3.

## 2.2 Beam collimation at the LHC

In a large machine, like the LHC, several processes can increase the number of particles that drift away from the beam core and populate the tails (beam halo), which ultimately cause beam losses. Some of these processes are induced by normal machine operation, e.g. collision in the interaction points (beam burn up), dynamics changes during the operational cycle (orbit drifts, optics changes, beam-beam effects...) and dynamic instabilities. These are commonly referred to as *regular beam losses*. On the other hand, when the beam is suddenly lost due to a failure of a machine device or an operational error, *abnormal losses* are generated. Beam losses are continuously monitored by about 4000 dedicated Beam Loss Monitors (BLMs) [52,53] installed all around the LHC ring, close to the most sensitive equipment (collimators, magnets, etc). They trigger a beam dump within few turns if dangerous losses above a certain threshold are detected.

At the LHC, the energy stored in the beams in nominal operation would be sufficient to melt about 500 kg of copper and approximately $10^{-9}$ of the total beam energy would be enough to quench a SC magnet. Such destructive potential must be carefully controlled by an appropriate collimation system [1, 54]. At this energy, cross sections are very small, therefore large devices are needed to intercept the halo beam particles. LHC collimators are indeed massive devices of about 0.6-1 m length. Additional details on the collimator design are discussed in Chap. 2.2.5.

The LHC collimation system [1, 54] has to fulfil a number of different functions. First, there is the beam cleaning functionality: the system must efficiently intercept the unavoidable losses due to the continuous repopulation of the beam halo. Passive machine protection is another priority, protecting sensitive equipment from losses following a device failure or wrong operation of the machine. Finally, it has to minimise the collimation-related background to the experiments in order to ensure clean data acquisition. For these reasons, a sophisticated multi-stage collimation system has been designed, based on different collimator families.

### 2.2.1 Regular (slow) beam losses

In a particle accelerator, the beam lifetime has a finite and time-dependent duration characterised by different loss mechanisms that occur during the machine operation. Consequently, the beam intensity evolves as a function of the time and can be expressed by:

$$I(t) = I_0 \exp\left(-\frac{t}{\tau_b}\right) \tag{2.5}$$

where $I_0$ is the initial beam population, $\tau_b$ is called *beam lifetime*, which indicates the time needed to reduce the number of particles to a fraction 1/e of the initial intensity.

The range of acceptable beam lifetimes for LHC was defined based on the operational experience with other colliders (LEP, RHIC, TEVATRON and HERA), but it must be large enough to allow commissioning of the machine and performance tuning in operation. The lifetime of a non-colliding LHC beam could exceed 100 h [55]. Such a lifetime corresponds to a power deposition due to lost particles of about 1 kW distributed over the LHC circumference. However, during colliding beam operation, collision losses may significantly reduce the lifetime of the beam, giving raise to a power load of several kilowatts. In normal LHC working conditions, collimators are continuously exposed to "steady-state" loss condition, i.e. particle from the external beam halo are continuously lost in the collimators, giving raise to a steady-state thermal load deposited in the jaws. According to Ref. [56], for continuous losses a minimum possible lifetime of 1 h at injection and top energy is specified. Furthermore, a "transient loss scenario" may also happen in which, starting from normal loss condition, an increase of beam loss occurs over a short time. For this case, a beam lifetime of 0.1 h at injection and 0.2 h at top energy has been specified and collimators are designed to withstand such lifetime drop for a period of 10 seconds. In all cases, the adeguate management of beam losses on collimators is of primary importance for machine protection: leakage of particles from the collimation system may be intercepted by the elements downstream, such as the cold magnets. Therefore, high beam cleaning efficiency is required to avoid the risk of magnet quench.

In linear approximation, the proton loss rate $R_{loss}$ is given by the total beam intensity divided by $\tau_b$. The power deposited in the collimation system, $P_{loss}$, is derived from the beam stored energy divided by the beam lifetime. Tables 2.2 and 2.3 summarises beam lifetime, proton loss rate and power deposition in the cleaning insertion in the case of nominal LHC and HL-LHC for regular loss scenarios.

**Table 2.2:** *Loss duration, minimum beam lifetimes, maximum proton loss rates and power deposition in the LHC collimators in case of regular beam losses for Nominal LHC machine. Values are calculated assuming a total of 2808 bunches with a bunch intensity of* $1.15 \times 10^{11}$ *p/b.*

| **Energy** | **Loss scenario** | | $R_{loss}$ | $P_{loss}$ |
|---|---|---|---|---|
| (GeV) | $\Delta t$ (s) | $\tau_b$ (h) | ($\times 10^{11}$ p s$^{-1}$) | (kW) |
| 450 | continuous | 1 | 0.90 | 6.5 |
| | 10 | 0.1 | 8.97 | 64.6 |
| 7000 | continuous | 1 | 0.90 | 100 |
| | 10 | 0.2 | 4.49 | 503 |

**Table 2.3:** *Loss duration, minimum beam lifetimes, maximum proton loss rates and power deposition in the LHC collimators in case of regular beam losses for HL-LHC machine. Values are calculated assuming a total of 2748 bunches with a bunch intensity of* $2.2 \times 10^{11}$ *p/b.*

| **Energy** (GeV) | **Loss scenario** $\Delta t$ (s) | $\tau_b$ (h) | $R_{loss}$ ($\times 10^{11}$ p s$^{-1}$) | $P_{loss}$ (kW) |
|---|---|---|---|---|
| 450 | continuous | 1 | 1.679 | 12 |
| | 10 | 0.1 | 16.793 | 120 |
| 7000 | continuous | 1 | 1.679 | 188 |
| | 10 | 0.2 | 8.397 | 942 |

## 2.2.2 Abnormal (fast) beam losses

If any irregularity occurs during either the injection or the extraction process of the beam, single turn losses may be generated, also called *fast losses*. Single turn losses on collimators for various failure scenarios are reported in Table 2.4 and Table 2.5 for the case of Nominal LHC and HL-LHC machine respectively.

**Table 2.4:** *Beam load on collimators for design failure scenarios during beam injection and dump for Nominal LHC. The values are calculated for a bunch intensity of* $1.15 \times 10^{11}$ *p/b. SMPF: Single Module Pre-Firing, ABD: Asynchronous Beam Dump.*

| **Failure scenario** | **Energy** (GeV) | **Impacting bunches** | **Deposited intensity** (p) | **Deposited energy** (kJ) | **Beam size** (mm × mm) | **Affected planes** |
|---|---|---|---|---|---|---|
| Injection error | 450 | 288 | $3.3 \times 10^{13}$ | 2376 | $1 \times 1$ | V |
| SMPF | 7000 | 8 | $9.2 \times 10^{11}$ | 1030 | $1 \times 0.2$ | H |

**Table 2.5:** *Beam load on collimators for design failure during beam injection and dump. Calculation are done by scaling the values in Table 2.4 with the bunch intensity for HL-LHC (*$2.2 \times 10^{11}$ *p/b).*

| **Failure scenario** | **Energy** (GeV) | **Impacting bunches** | **Deposited intensity** (p) | **Deposited energy** (kJ) | **Beam size** (mm × mm) | **Affected planes** |
|---|---|---|---|---|---|---|
| Injection error | 450 | 288 | $6.3 \times 10^{13}$ | 7056 | $1 \times 1$ | V |
| SMPF | 7000 | 8 | $1.8 \times 10^{12}$ | 2016 | $1 \times 0.2$ | H |

#### Failures during beam injection

Beam injection into LHC is performed in the combined experimental and injection insertions IP2 and IP8. In both insertions, the beam is directed by a series of dipoles towards five septum magnets, which deflect the beam horizontally. A series of four kicker magnet (MKI[1]), instead, deflect the beam vertically. An injection beam stopper (TDI[2]), movable shielding devices and collimators (TCDD[3] and TCLI[4]) are installed

---

[1] Magnet Kicker Injection

[2] Target Dump Injection

[3] Target Collimator Dump for D1 protection

[4] Target Collimator Long Injection

to protect the superconducting magnets located downstream. However, during the injection of the beam from the SPS to the LHC ring, possible errors in triggering of one or more MKI can occur: in this case, the incoming beam is not injected correctly in the ring but starts to oscillate around the reference orbit, with the risk to hit the downstream aperture and eventually the collimators. Generally, the worse scenario, when a full injected batch of 288 bunches from the SPS receives a mismatched kick and hits the collimators, is referred to as “injection error". It can also happen that the MKI is not fully synchronised and may kick not only the injected batch but also the circulating beam.

#### Failures during beam dump

In the current operation at the LHC, there is an abort gap of about 3 $\mu$s without beam in the filling scheme to allow the 15 horizontal extraction kicker magnets (MKD) to rise up to full field during a standard beam dump. In normal operation mode, the 15 modules fire all at the same time, synchronised with the abort gap, in order to correctly dump the beam out from the ring. However, two major failure scenarios might occur during a beam abort [57]: one is the simultaneous firing of the 15 kicker modules, but outside the abort gap (*asynchronous beam dump*). In this case some bunches are affected by the kicker field when it is still rising. A *single-module pre-fire* (SMPF), instead, happens when a single kicker spontaneously misfires, out of phase with the abort gap, followed within a short delay by the re-triggering of the remaining 14 modules. This case is the most critical one [57]: the slower rise time of the total kick seen by the beam exposes more bunches to smaller kicks. Some miskicked particles cannot reach the dump line at the first turn and could be instead deviated towards the aperture. The requirement for collimators is to withstand 8 nominal bunches impacting simultaneously on one collimator jaw, at a distance from 5 to 10 $\sigma$ from the center of the beam. It was assumed that above 10 $\sigma$, local dump protection devices should intercept all the beam. This requirement is based on a particularly pessimistic design, as of Ref. [1], which assumed parallel beam impacting in any collimator of IR7. In this thesis, this requirement will be reviewed thanks to refined simulations. Note that abnormal dumps have effects on horizontal collimators, as the MKDs kick only on the horizontal plane. However, if a failure of any upstream components occur, vertical and skew collimators can also be hit [1].

### 2.2.3 Cleaning inefficiency

Different parameters are used to quantify the cleaning performance of the collimation system. One of them is the *Global Cleaning Inefficiency* $\eta_g$ [1] given by:

$$\eta_g(A_i) = \frac{N_p(A > A_i)}{N_{abs}} \tag{2.6}$$

where $N_p$ is the number of particle escaping the cleaning insertion with a betatron oscillation amplitude $A$ bigger than a certain amplitude $A_i$ and $N_{abs}$ is the total number of particles absorbed in the collimation system. Inefficiency $\eta_g(A_i)$ should be below quench limits.

However, it is also important to know the distribution of the losses along the ring, because the surviving particles not stopped in the collimator material are lost locally in the machine and could cause quenches in the magnets. For this reason, a second parameter must be introduced, the *Local Cleaning Inefficiency* $\eta_c$:

$$\eta_c = \frac{N_{loss}}{\Delta s \cdot N_{abs}} \tag{2.7}$$

where $N_{loss}$ is the number of particles lost in a $\Delta s$ length. The local cleaning inefficiency plays an important role in the estimation of the maximum circulating beam intensity $I_{max}$ (in number of protons) allowed in the machine that can ensure safe operation without magnet quenches. This parameter can be expressed as:

$$I_{max} \leq \frac{R_q \tau_{min}}{\eta_c} \tag{2.8}$$

where $R_q$ is the maximum allowed loss rate (in protons per second) on the LHC superconducting magnets, $\tau_{min}$ is the minimum beam lifetime, estimated at 0.2 h and $\eta_c$ is the cleaning inefficiency. The higher the local cleaning inefficiency, the lower is the number of particles that can circulate in the accelerator without inducing quenches, for a given beam lifetime. Eventually, this may limit the achievable beam parameters with respect to the design values, which would translate ultimately in severe limitations for the luminosity. It is for this reason that having an efficient collimation system is an important asset for the LHC as well as for its future upgrades.

### 2.2.4 The multi-stage collimation system at the LHC

The present LHC collimation layout includes about hundred collimators (see complete list in Table 2.6), distributed around the ring as shown in Figure 2.6. Collimators devoted to beam cleaning are mainly located in two dedicated insertions, i.e. IR3, for momentum cleaning, and IR7, for betatron cleaning. The Betatron Cleaning insertion (IR7) is characterised by low dispersion value, where the particles with large distance from the beam center feature high betatronic amplitude, while the transversal displacement due to the momentum offset is negligible. On the other hand, the dispersion is higher in the Momentum Cleaning insertion (IR3), where the halo particles are characterised by a high momentum offset.

The layout in these two insertions is quite similar and it is schematically reproduced in Figure 2.7. Primary (TCP[5]) and secondary (TCSG[6]) collimators are the closest to the beam. The active part of their jaws, 0.6 and 1 m long, respectively, is made of a Carbon Fiber Carbon (CFC) composite (see Chap. 4 for more details) that is designed to withstand without significant permanent damage beam impacts for the worst failure cases [1], such as impacts of a full injected batch of $288 \times 1.15 \times 10^{11}$ protons at 450 GeV and up to $8 \times 1.15 \times 10^{11}$ protons at 7 TeV. Other collimators made of a heavy tungsten alloy (Inermet180, or IT-180, see Chap. 4) do not have the same robustness and operate at larger distances from the circulating beam. Among those, there are the

---

[5] TCP: Target Collimator Primary

[6] TCSG: Target Collimator Secondary Graphite

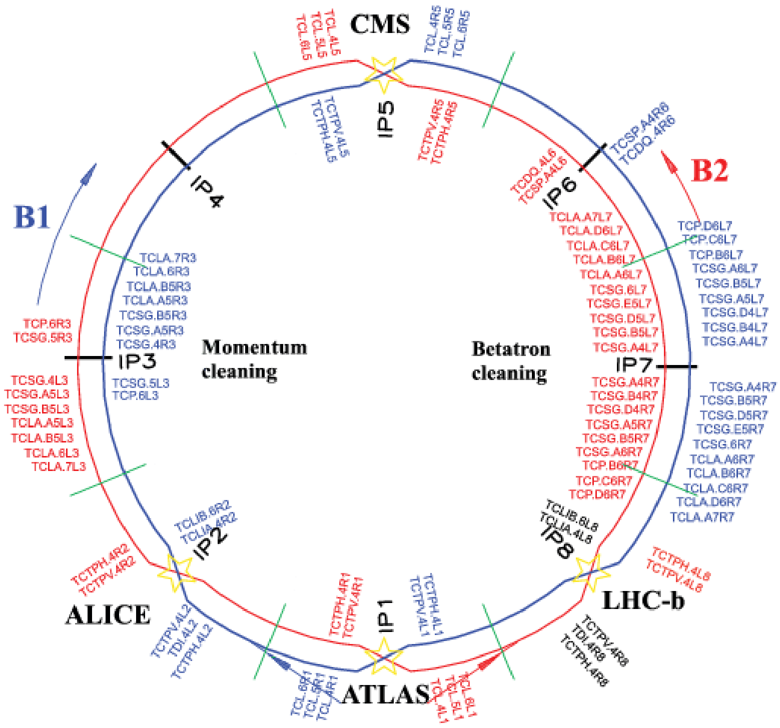

**Figure 2.6:** *Collimator locations around the LHC ring.*

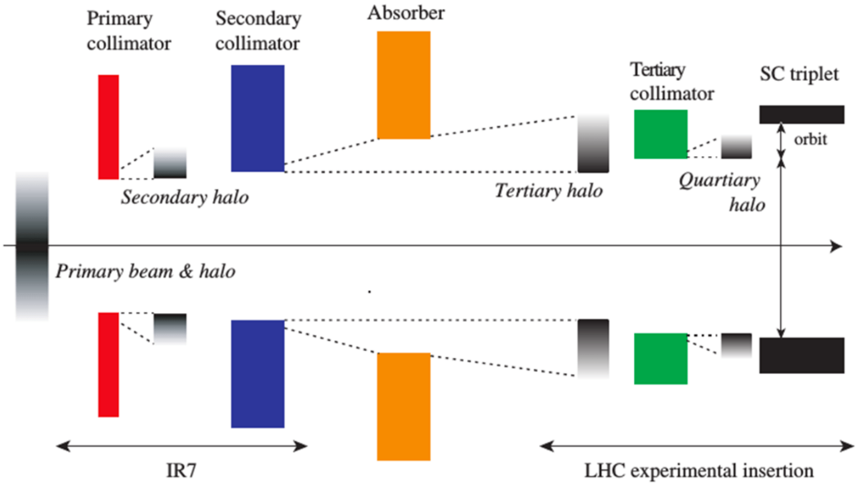

**Figure 2.7:** *Scheme of the collimation hierarchy at the LHC.*

absorbers (TCLA[7]), which catch particles that have been scattered out from the previous collimation stages and protect the superconducting magnets downstream of the warm insertions.

Tertiary collimators (TCT[8]) of 1 m long jaws are installed in the LSSs hosting the

---

[7] TCLA: Target Collimator Long Absorber

[8] TCT: Target Collimator Tertiary

detectors, and provide local protection around the interaction points (IP1/2/5/8). Their tungsten-based jaws ensure high particle stopping power. Copper absorbers (TCL[9]), instead, protect the Dispersion Suppressor magnets from particle showers (debris) coming from the collisions in the high luminosity points IP1 and IP5.

Additional collimators protect sensitive equipment in the injection and extraction regions. The injector beam stoppers (TDI) are 4.2 m long graphite jaws. They are installed in IP2 and IP8 to ensure a correct beam injection setup even in case some of the injector kickers fails. A one-jaw graphite collimator (TCDQ[10]) and a secondary collimator (we will call it TCSP6[11] to distinguish from those in the cleaning insertions) are used to protect the LHC beam dump lines.

**Table 2.6:** *List of LHC collimators, location and material used for each collimator family. Table refers to collimation layout for Beam 1, which is injected in IP2. For Beam 2, the configuration of IP2 and IP8 is reverted.*

| **Location** | **Collimator family** | **Collimator acronyms** | **Collimator material** | **Length** (m) | **N. of units** |
|---|---|---|---|---|---|
| IR 7 | Primary | TCP | CFC | 0.6 | 3 |
| | Secondary | TCSG | CFC | 1.0 | 11 |
| | Shower absorber | TCLA | IT-180 | 1.0 | 5 |
| IR 3 | Primary | TCP | CFC | 0.6 | 1 |
| | Secondary | TCSG | CFC | 1.0 | 4 |
| | Shower absorber | TCLA | IT-180 | 1.0 | 4 |
| IR 6 | Secondary | TCSP | CFC | 1.0 | 1 |
| | Diluiter | TCDQ | graphite | 9.0 | 1 |
| IP 1/5 | Tertiary | TCT | IT-180 | 1.0 | 2 |
| | Debris absorbers | TCL | Cu | 1.0 | 3 |
| IP 2 | Tertiary | TCT | IT-180 | 1.0 | 2 |
| | Debris absorbers | TCLI | graphite | 1.0 | 2 |
| | Injection stoppers | TDI/TCDD | graphite | 4.0 | 2 |
| IP 8 | Tertiary | TCT | IT-180 | 1.0 | 2 |
| **Total n. collimators per beam** | | | | | 48 |

### 2.2.5 The LHC and HL-LHC collimator design

Most of the LHC collimators consist of a support on which a vacuum tank and an actuation mechanism are positioned thanks to a plug-in system. Particle beam enters longitudinally into the vacuum tank through the connections at the extremities, as illustrated in Figure 2.8(left). Inside the vacuum tank, there are the two parallel collimation jaw assemblies, which have direct interaction with the beams. In nominal working con-

---

[9] TCL: Target Collimator Long

[10] TCDQ: Target Collimator Dump Quadruple (Diluter): Collimator for Q4 protection

[11] TCSP: Target Collimator Secondary with Pick-up

dition, particles only graze the assembly with its external halo and the “active” part of the jaw (0.6-1 m length, 65 mm height and 25 mm depth) is the one most exposed to the beam.

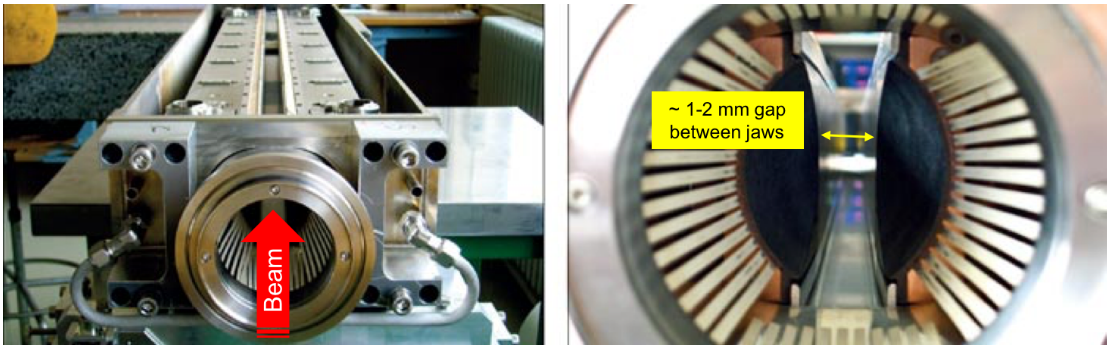

**Figure 2.8:** *View of two parallel jaws inside an open vacuum tank of a LHC collimator.*

The azimuthal rotation of the vacuum tank where the two jaws are enclosed is used to define a horizontal, vertical or skew collimator (see Figure 2.9).

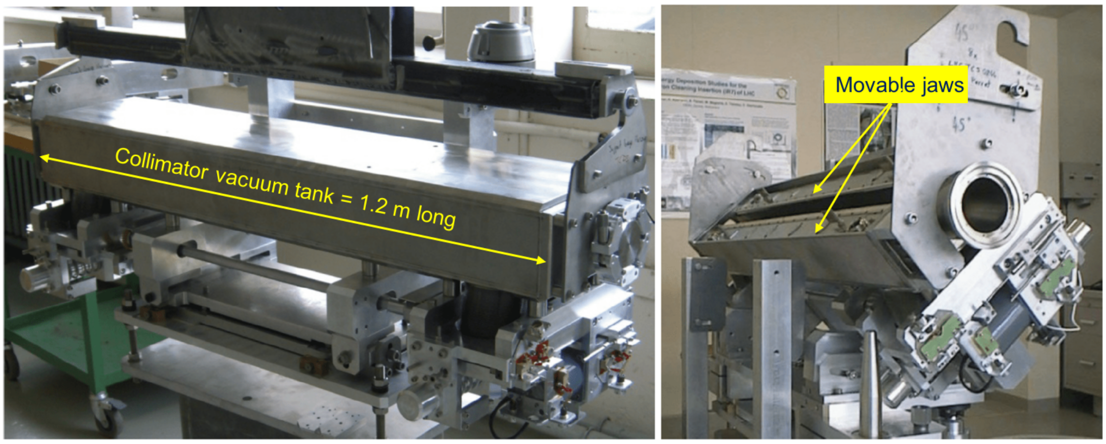

**Figure 2.9:** *Horizontal (left) and a skew (right) LHC collimator. The latter has the vacuum tank open to show the two movable jaws.*

The surface of each collimator jaw is constituted by a flat part, determining the active length (different for each collimator type, as seen above) and by a 10 cm tapering part at both ends to minimise geometrical impedance effects. However, the requirements imposed by the machine upgrade partially modified the initial design. During LS1, two Beam Position Monitors (BPMs) have been installed on each tapering [58] in 18 collimators (16 tertiaries at the IPs and 2 secondaries in IR6) [59, 60]. The addition of these instruments is marked with a "P" at the end of the collimator acronym. The BPMs allow a fast collimator alignment as well as a constant monitoring of the beam orbit at the collimator. The BPM-embedded design is considered to be part of the baseline for the future collimator upgrades. The BPM design is equally applicable to all collimators regardless of the jaw material. The operation during Run II proved that they are reliable and fully operational [61]. By the end of LS2 in 2021, all new collimators installed in the machine will adopt the new design with embedded BPMs. An example of BPM installed in the tapering region of a CFC jaw is shown in Figure 2.10.

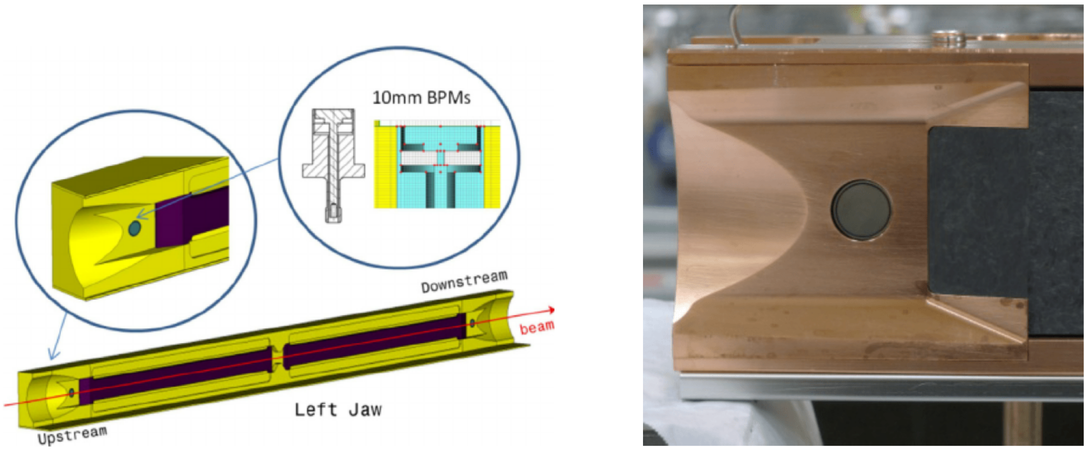

(a) Overview scheme.

(b) Detailed view.

**Figure 2.10:** *Beam Position Monitor (BPM) embedded in a collimator jaw, installed during LS1.*

In order to efficiently intercept the halo particles, collimator jaws must be able to move, to always be centred and aligned with respect to the beam envelope and the actual orbit, which changes during the ramp in energy. For this reason, independent stepping motors are located at the end of each jaw to allow precise movement (Figure 2.11). The four motors are also used to set the position and the tilt angle of the jaws. Excessive tilt is prevented by a rack and pinion system. The return springs ensure a semi-automatic back-driving of the jaw in case of motor failure.

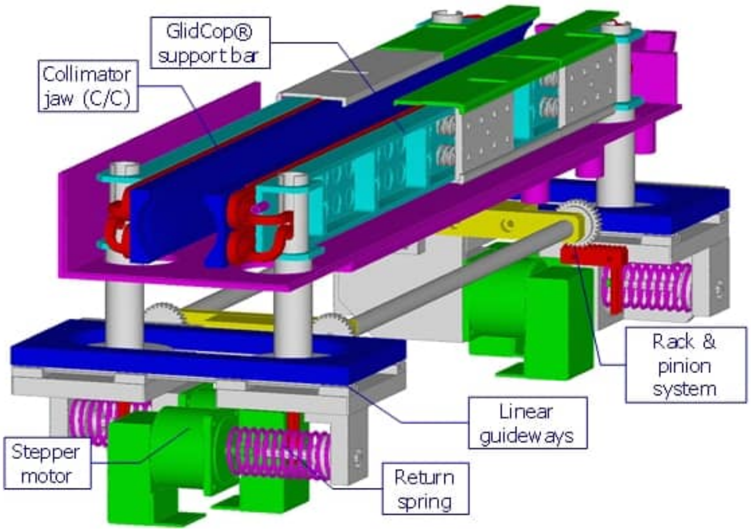

**Figure 2.11:** *Design of present LHC collimators.*

The cooling of collimator jaws and tank is provided by a cooling circuit with two Oxygen Free Electronic (OFE) copper pipes. A GlidCop (see Chap. 4) support bar presses the cooling pipes against the jaw material by means of clamping springs: this system avoids mechanical stress caused by the contact between materials (jaws and cooling pipes) having different thermal expansion coefficient and, at the same time, it enhances the thermal contact between them.

In view of the HL-LHC operation, collimator design must be compatible with larger beam stored beam intensities. The increased bunch intensity by a factor of 2 and smaller emittance are more demanding in terms of high robustness and low impedance. To that end, a new design of primary/secondary collimators accommodating novel materials was studied.

The HL-LHC collimator design, illustrated in Figure 2.12, is flexible and multi-purpose, and can be used for primary, secondary and tertiary collimators by simply replacing the absorber material, e.g. Molybdenum-Graphite (MoGr) or Copper-Diamond (CuCD) (see Chap. 4 for additional details on the materials), without modifying the rest of the structure [62]. The 1 m long active jaw consists of 8 MoGr (or 10 CuCD) blocks, clamped against a Glidcop (see Chap. 4) housing by means of screws, which provide higher contact pressure between the jaw and the housing: therefore, better thermal conductance at the interface guarantees efficient heat transfer of beam-induced thermal load. The cooling pipes are made in corrosion-resistant CuNi 90-10 alloy and are brazed against the housing. Thermal probes are added to the cooling circuit, to bet-

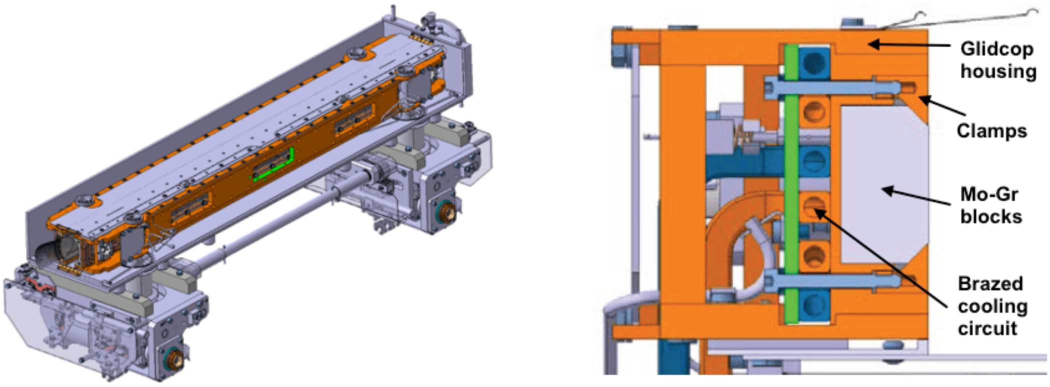

(a) Full HL-LHC collimator assembly.

(b) Jaw cross-section.

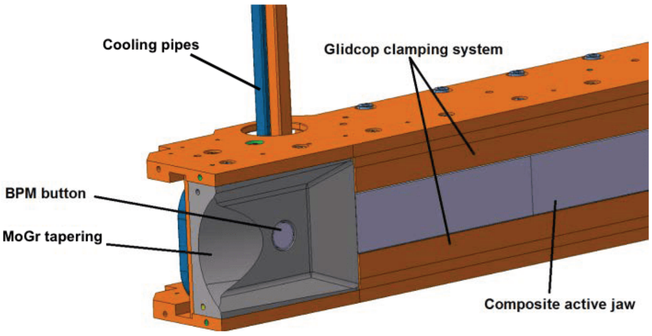

(c) 3D view of the jaw.

**Figure 2.12:** *New HL-LHC collimator design [62].*

ter monitor water heating in case of abnormal operation. The MoGr tapering minimizes the RF impedance of the component, increasing the robustness. One BPM at both ends of the jaw is also embedded, to speed up the alignment procedure and improve the efficiency of the machine.

The new collimator design and materials must be qualified for operation. Therefore, a rich program of validation is in progress, which includes:

- beam impact tests at the CERN HiRadMat facility [63], which will be discussed in Chap. 5
- mechanical engineering prototyping
- beam test at the LHC, planned during 2017-2018 operation (installation of collimator prototype scheduled for mid 2017)

### 2.2.6 Collimation settings

During operation, the collimator settings must be carefully adjusted in order to minimise the beam losses in the machine aperture. The aperture of the collimator, i.e. the distance of each jaw from the center of the beam (also called *halp-gap*), is expressed for the collimator $i$ as:

$$h = \pm n_i \cdot \sigma_i, \tag{2.9}$$

The collimator half-gap is conventionally expressed in units of the standard deviation $\sigma_i$ of the beam in the collimator plane, which is given by:

$$\sigma_i = \sqrt{\beta_{x,i}\epsilon \cos^2\theta_i + \beta_{y,i}\epsilon \sin^2\theta_i}, \tag{2.10}$$

where $\beta_{x,i}$ and $\beta_{y,i}$ are the betatron functions at collimator $i$ in the horizontal and vertical plane respectively (see Chap. 1.1.1), $\theta_i$ is the azimuthal angle of the $i$-th collimator and $\epsilon$ is the nominal geometrical emittance, given by $\epsilon = \epsilon_n/\gamma_{rel}$, with $\epsilon_n$ the normalised emittance. For the nominal 7 TeV machine, $\epsilon_n = 3.5\,\mu\text{m rad}$ is considered, while for HL-LHC $\epsilon_n = 2.5\,\mu\text{m rad}$. The opening $n_i$ is different for every collimator type according to the collimation hierarchy.

# CHAPTER 3

# Performance limitations and upgrade of the LHC collimation system

One of the hardest challenges in the design of the LHC collimators is to ensure safe disposal of halo particles in the available space (i.e. cleaning efficiency), while guaranteeing thermo-mechanical robustness of the device against beam impacts. While the former calls for materials with high density and atomic number, featured by high absorption capabilities and thus high levels of heat load, the latter calls for light materials that show the opposite trend.

The choice of present LHC collimator materials was done by favouring some specific aspects, depending on the role that the specific collimator holds in the hierarchy. Low-Z materials (carbon-based composite) is used in primary and secondary collimator jaws to guarantee sufficient mechanical robustness against large beam losses. However, such non-metallic collimators largely contribute to the machine impedance budget. This aspect might limit the maximum bunch intensity that can be kept stable in the machine. Metallic high-Z (tungsten alloy) jaws, used for absorbers and tertiary collimators, guarantee efficient cleaning of regular beam losses but might be severely damaged if hit by fast beam losses. To achieve high cleaning performance, collimator jaws must respect specific mechanical tolerances during the whole operation of a collimator. High doses from the continuous exposure of the collimators to beam losses may eventually degrade the properties of the jaw materials: collimators may need to be replaced if they do not comply with their standard anymore.

Each section of this Chapter reviews fundamental requirements of collimator materials, discussing the main constraints owing to the present system and how the HL-LHC collimation upgrade may comply with the more challenging beam parameters.

## 3.1 Beam coupling impedance

In the LHC collimators are the closest components to the circulating beam. As shown in Figure 3.1, collimator contribution to the accelerator transverse impedance (introduced in Chap. 1.1.4) is by far the highest, about 90% over the range 1 MHz - 1 GHz [64].

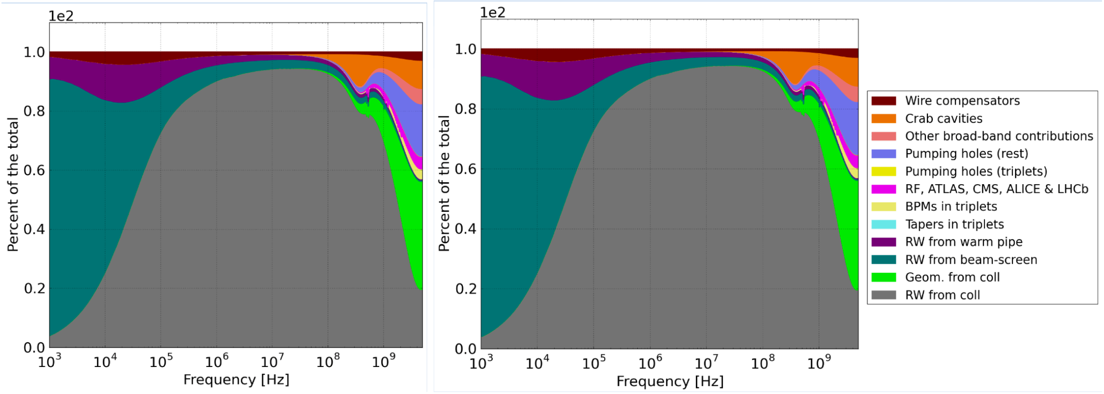

**Figure 3.1:** *Distribution of the various contributions (in percent) to the LHC resistive wall (RW) transverse impedance: real part (left) and imaginary part (right). Pictures from [65].*

However, collimators contribute differently to the impedance budget, depending on their jaw material and operational settings (see Figure 3.2). Among the various collimator families, the contribution of primary and secondary collimators is clearly dominant. The reason behind is that they are the closest to the beam, are made of a high resistivity material (CFC) and there is a large number of these types of collimators around the ring.

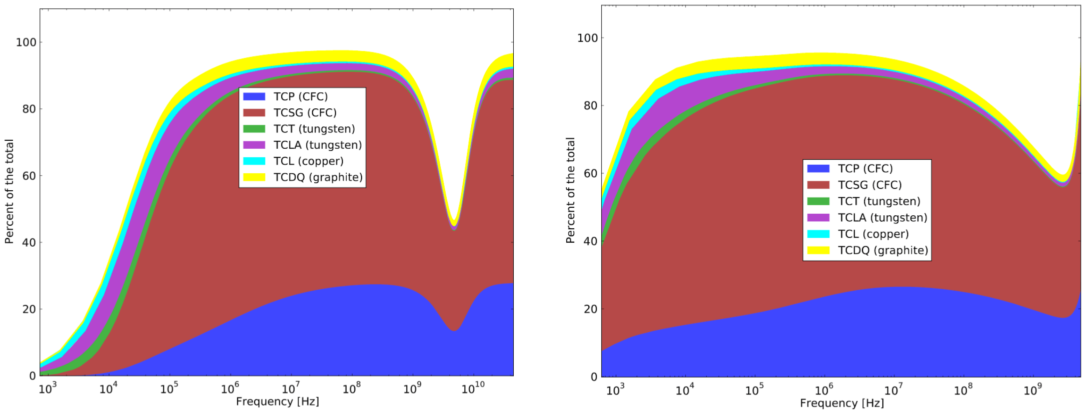

**Figure 3.2:** *Contributions (in percent) of collimator families to the total vertical impedance, (left) real part (right) imaginary part, at 4 TeV with collimator settings as in Ref. [66]. Pictures from Ref. [67].*

Based on the experience gained during Run I and Run II, the LHC was already operating at the limit of the transverse beam stability [4,64,68]. Transverse instabilities are expected to become more critical at higher beam intensity of HL-LHC [4]. With the present assumption, HL-LHC beam cannot be stable with sufficient margins with such collimator impedance. According to simulations, an octupole current of $\sim$350 A (500 A, if tighter collimator settings are used) would be needed to stabilise the HL-LHC beam, if the present CFC collimator configuration is adopted [69]. On the other hand, low-impedance secondary collimators, with jaws in molybdenum-graphite composite (see Chap. 4.3) and 5 $\mu$m coating in pure molybdenum, would allow a gain of 200 A in octupole current.

## 3.2 Mechanical tolerances and geometrical stability

Collimators are built as very precise beam intercepting devices, which at the LHC deal with beams of size as small as 200 $\mu$m. Their settings are remotely controlled and should be reproducible over several weeks or months. For this reason, mechanical tolerances (in the order of microns) are particular important for collimation production, that translate into very strict requirements for surface flatness, step size in jaw movements and reproducibility of jaw settings. Present specifications impose a 5 $\mu$m positioning resolution and an overall settings reproducibility below 20 $\mu$m. A surface roughness of collimator jaw below 2 $\mu$m must be guaranteed. Jaw roughness from production can be minimised with proper surface treatments and monitored by metrological control of pieces before assembling the complete device.

For their nature, collimators continuously interact with the beam halo. To guarantee the cleaning efficiency, collimators have to maintain their longitudinal straightness to a fraction of a transverse beam size and ensure parallel surface in operation. Turning that into numbers, a jaw flatness of 40 $\mu$m along the 1 m long active jaw surface can be tolerated. The choice of a jaw material with good properties for a high thermal range is therefore crucial. As an examples, Figure 3.3 shows operating temperatures and thermally-induced deflection of a LHC secondary collimator jaw in steady-state conditions. The length of the jaw is 1 m and its deflection $\sim 40\mu$m. A material with a low thermal expansion coefficient is therefore required for the material of the collimator jaw to contain deformations, which may affect the absorbance capability in operation. Moreover, collimators are designed in such a way that keep the jaw straight by placing the heat sink in between heated parts.

It is thus very important to control collimator's dynamic deformations during operation, and also to minimise permanent deformation of the jaws after standard operation and failure scenarios. For these matters, the factor of 2 in bunch intensity and the smaller emittance of the HL-LHC are big challenges, which require to revise the collimator design in light of the new beam parameters.

## 3.3 Mechanical robustness against beam impact

The first physics run at the LHC proved that the collimation hierarchy constrains the performance in terms of minimum achievable $\beta$-function at the collision points, $\beta$*, determined by the minimum normalized machine aperture that can be protected by the collimators [72]. In the present LHC, the aperture bottlenecks are the inner triplets

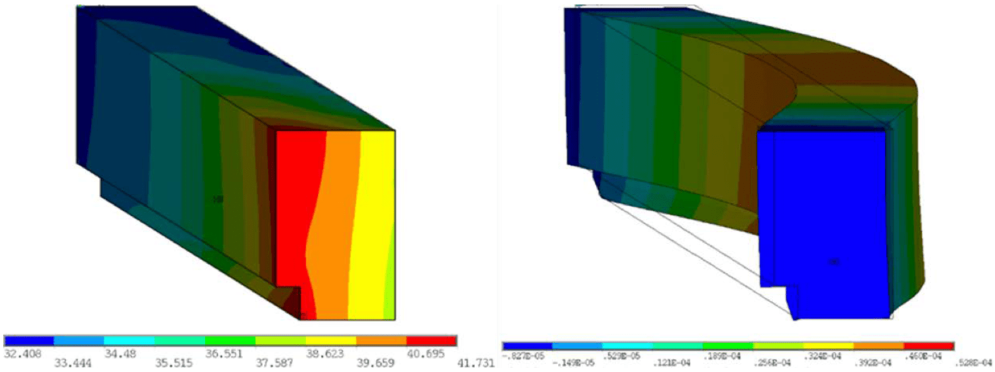

**Figure 3.3:** *Temperature, in Celsius degrees, and deformation, in meters, of a CFC secondary collimator jaw in steady-state loss operation conditions and 1 h beam lifetime. Pictures from [70, 71].*

upstream of the experiments that risk to be exposed to local beam losses if not sufficiently protected by the TCTs [72]. The small regular losses during standard operation at triplets and TCTs do not pose concerns for the material robustness. However, during fast failures, such as during an ABD and an SMPF (see Chap. 2.2.2), even a small fraction of beam loss might be sufficient to go beyond the damage limit in these collimators that are not designed to be robust. In such scenario, the TCT tungsten jaws can be severely damaged and the collimator operational functionalities compromised.

A series of experiments were performed at the CERN HiRadMat (High Radiation to Material) facility [63] to test the the robustness of the LHC collimators. In particular, a dedicated experiment, called HRMT-09, was set up to obtain a thorough integral assessment of beam accident scenarios relevant for 7 TeV LHC operation involving a full tertiary collimator. The extent of the damage on the jaws was quite massive and significant damage was observed, as shown in Figure 3.4.

The present system is designed to withstand without damage up to 500 kW from regular beam losses. The HL-LHC upgrade will almost double this value (see Table 2.3) and collimator robustness might become an important limitation to the achievable performance. Therefore, improved mechanical robustness is needed at all stages of collimation, which can be addressed by novel composite materials for collimator jaws. Furthermore, the calculation of damage limit for LHC collimators is crucial in the evaluation of the feasibility of the machine design: for example, to assess if HL-LHC collimator settings are compatible with the constraints imposed by the machine protection, or to choose optimum materials for the upgraded collimators [73].

## 3.4 Cleaning inefficiency

The limiting locations for collimation losses, both in the cleaning insertions and in the experimental regions, are the cold dispersion suppressor (DS) magnets immediately downstream of the straight sections. This is the first high dispersion location seen by the outgoing beam: here the particle experiences a momentum variation with a consequent change in its rigidity (see Eq. 1.3), due to interactions with collimator materials, mainly primary collimators, in the cleaning insertions or after collisions with the other beam

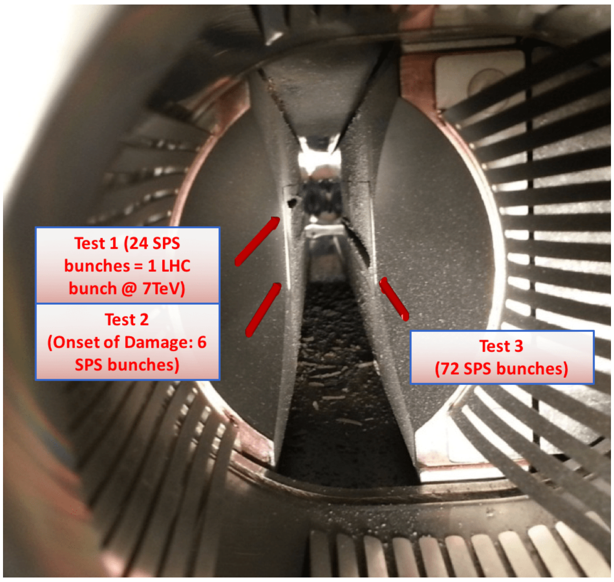

**Figure 3.4:** *Visual inspection of the TCT collimator after HRMT-09 experiment. There are clearly visible the groove left by the beam on the left jaw as well as the tungsten ejecta deposited at the bottom of the collimator tank.*

in the experimental insertions. Such "off-momentum" particles can be swept onto the cold magnets in the DSs before reaching the dedicated momentum cleaning insertion in IR3 and therefore magnet quench can occur.

The present LHC collimation system, indeed, does not efficiently catch such losses. Losses at the DS magnets downstream of IR7 are so far the highest in cold elements around the ring: they represent the main limitation for the collimation efficiency and it may prevent the accelerator from reaching the desired beam intensity. In addition, ion losses in the DS around the experiments may limit the achievable peak luminosity if the DS magnets are not adequately protected. The factor of 2 increase in total stored beam energy of HL-LHC requires a corresponding improvement of cleaning performance to maintain the same level of losses in the superconducting magnets.

The solution to this problem is the installation of additional particle absorbers upstream of the DS, where the dispersion function starts rising and consequently the particle orbit largely displaces, to locally clean such losses. However, this implementation requires an arrangement of the layout of the cold dipoles nearby. Even though the decision to add new DS collimators is already well established, this work is meant to give an important contribution to finalise the collimator design in the context of the material choice.

## 3.5 Radiation-induced effects

The position of collimators so close to the particle beams unavoidably exposes them to high radiation doses during their operational life. According to simulations [74], a total of about $10^{16}$ protons are expected to be lost in a primary collimator in IR7 over one year of operation. Such losses generally occur in relatively small volumes inside the collimator jaws. In a long term scale, beam losses on collimators can turn into detrimental effect on the jaws. In particular, radiation acts at the microscopic level on the material structure, either changing phases and breaking chemical bonds, that reflects on a modification of the macroscopic properties of the material itself.

For devices, such as the LHC collimators, built to operate in the machine for years assuring high performance over all time, a worsening of the active jaw material properties may turn into relevant effect for the entire machine performance. The exposure to radiation of a secondary collimator in CFC may increase its electrical resistivity, induce overall loss of robustness and possible change of dimensions. The increase in electrical resistivity, for example, would increase its contribution to the resistive impedance budget (that is already high, as discussed in Chap. 3.1) and the stability of the LHC beams would be even more challenged.

Looking at the future HL-LHC upgrade, an important asset will be to select materials for collimators able to withstand large radiation doses without affecting significantly their physical and thermo-mechanical properties. For this reason, several irradiation tests have been performed in various irradiation conditions on LHC collimator materials to assess their resistance to radiation damage. This topic will be treated in more detail in Chap. 6.

CHAPTER 4

# Materials for LHC collimators

The material choice for Beam Intercepting Devices, such as collimators, is driven by the performance of the material under various operational conditions and is based on a number of criteria, which are discussed at the beginning of this Chapter. Then, collimator materials currently used at the LHC are presented together with their properties. The HL-LHC upgrade imposes more compelling requirements for collimators. An intense material development campaign has been launched at CERN in the recent years in order to explore novel materials with excellent properties to accomplish the new challenges. Such newly developed composites are presented in this Chapter, with details on their production process and main properties. Finally, a comparison of present and promising candidate collimator materials is done.

## 4.1 Performance indicators for collimator materials

A large range of requirements must be taken into account in the choice of collimator materials for high energy accelerators, like the LHC. Besides general aspects of material availability, production feasibility, cost, production timeline etc, there are also aspects to account for to address the specific needs of LHC collimators: these aspects are particularly important as they determine the final design choice. Specific requirements for collimators are the mechanical robustness against high energy beam impacts, the geometrical stability to withstand thermal shocks, the electrical conductance for low resistive-wall impedance contribution, and the resistance to radiation damage. Due to the complexity of the problem, the optimization cannot be done by taking into account individual parameters. The challenging requirements of beam operation also impose contradictory requirements: for example, a reduction of the impedance calls for low-resistivity materials that are mostly high density materials, which are typically not a good choice to withstand high beam loads without damage.

A formalism, based on Figures of Merit (FoM), was proposed in Ref. [71, 75] to provide a comparative tool to orient the material choice for collimator devices. The indexes, which are briefly recalled below, allow to rank interesting materials against the most relevant requirements: they are built in such a way that a higher value indicates a better ability to withstand a specific challenge. In case of anisotropic materials, only the properties averaged over the three directions are used in the FoMs.

The *Thermo-mechanical Robustness Index* (TRI) is associated to the mechanical robustness of the material, which means the ability of the material to withstand the impact of a short particle pulse. With the assumptions and mathematical manipulation reported in Ref. [71], TRI is defined as:

$$\text{TRI} = \frac{R_M \, c_p \, X_g}{\bar{E}\,(1-\nu)\,\bar{\alpha}\,C_R\,\rho^n} \left( \frac{T_{melt}\,c_p\,X_g}{C_R\,\rho^n} \right)^m \tag{4.1}$$

where $R_M$ is the failure strength [MPa], $c_p$ is the specific heat [J/g/K], $X_g$ is the geometrical radiation length [m], given by the radiation length (i.e. a characteristic of the material, related to the energy loss by high energy, electromagnetic-interacting particles with the traversed material) divided by the density, $\bar{E}$ is the averaged Young's modulus [GPa], $\nu$ the Poisson ratio and $\bar{\alpha}$ the average coefficient of thermal expansion CTE [$\mu$m/K], $\rho$ is the material density [g/cm$^3$] and $T_{melt}$ the melting temperature [K]. $C_R$ is an arbitrary scaling factor and $n$ is a coefficient related to the effect of the material density on the energy distribution generated by the impact of the beam. It has been empirically observed that the coefficient $n$ for materials impacted by protons at several hundreds of GeV is $\sim$0.2. Finally, $m$ is a coefficient related to the material loss of strength with temperature increase.

The *Thermal Stability Index* (TSI) refers to the ability of the material to maintain the geometrical stability of a component (e.g. flatness of a collimator jaw) and minimise the deformation when exposed to steady-state beam losses. It is related to the inverse of the curvature of an elongated structure induced by a non-uniform temperature distribution. TSI is expressed as:

$$\text{TSI} = \frac{\bar{\lambda}\,X_g}{\bar{\alpha}\,C_s\,\rho^n} \tag{4.2}$$

where $\bar{\lambda}$ is the average thermal conductivity [W/m/K], and $C_s$ a scaling factor.

As already discussed in Chap. 3, the part of the beam coupling impedance related to the resistive losses in the materials close to the circulating beam is inversely proportional to the electrical conductivity of the material. The electrical properties are thus of paramount importance for LHC collimators. The *RF impedance Index* (RFI) is defined as the ability of the material to minimise the RF impedance and it is expressed as:

$$\text{RFI} = \sqrt{\frac{\gamma}{\mu_r}} \tag{4.3}$$

where $\gamma$ is the electrical conductivity of the material [MS/m] and $\mu_r$ its magnetic permeability [H/m], which for paramagnetic materials is considered to be practically equal to 1.

When materials are exposed to high energy particles radiation, microstructural defects occur, which can translate into a degradation of the thermo-physical and mechanical properties of the material. Radiation resistance is thus the ability of the material to minimise its degradation under irradiation. We define a *Radiation Damage Index* (RDI), for which a preliminary formula is given:

$$\mathrm{RDI} = \frac{\mathrm{dpa}_{adm}}{1 + \frac{\sigma_{gas}(E)}{\sigma_0(E)}} \cdot K_{adm}^{ion} \tag{4.4}$$

where $\mathrm{dpa}_{adm}$ is the admissible displacement per atom (for the definition of dpa, see Chap. 1), i.e. the integrated radiation load above which a given property undergoes an unacceptable degradation: generally a 30-50% change in the property of interest is considered as threshold. $\sigma_{gas}$ is the cross section of gas production (mainly H and He) at the irradiation energy $E$, $\sigma_0$ is a normalisation factor and $\mathrm{K}_{adm}^{ion}$ is a factor accounting for ion track formation (concept more extensively detailed in Chap. 1 and 6), which becomes very important to evaluate the damage induced by ions, as they create very few displacements per atom and the $\mathrm{dpa}_{adm}$ level is not reached.

Collimation cleaning performance are fundamental for LHC operation and are also related to collimator material properties. First of all, the density $\rho$ directly affects the cleaning of the system: the denser the material of the jaw, the higher is the fraction of the beam that is stopped in the collimator and the energy deposited in the volume. Low density materials ($< 5\,\mathrm{g/cm^3}$) are used in the first stages of collimation (i.e. primary and secondary collimators) to avoid a high energy deposition per unit of volume, which may cause the failure of the collimator. For tertiary collimators and absorbers high density ($> 10\,\mathrm{g/cm^3}$) are chosen to maximise the particle stopping. Radiation length ($\chi_0$) and nuclear interaction length ($\lambda_{\text{inel}}$) are also fundamental parameters for the collimator design (see Chap. 7.2), in particular to define the active length of the material needed for each specific stage of collimation. Therefore, we can propose a *Cleaning Efficiency Index* (CEI),

$$\mathrm{CEI} = f\,(\rho, \chi_0, \lambda_{\text{inel}}), \tag{4.5}$$

which correlates the cleaning performance of the system with specific material properties.

## 4.2 LHC collimator materials

In this section, the materials currently used for the active part of the LHC collimator jaws are discussed. Materials properties are presented and compared based on the indicators introduced in Section 4.1. Main properties and figures of merit of the materials are summarised in Table 4.5.

### 4.2.1 Carbon Fiber Carbon composite: AC-150K

Carbon Fiber Carbon (CFC) composite is based on a carbon fiber reinforcement in a graphite matrix (Figure 4.1).

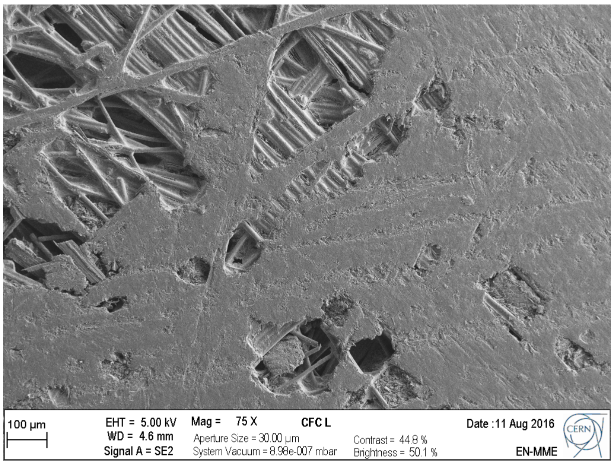

**Figure 4.1:** *Microstructure of Carbon Fiber Carbon composite. The picture clearly shows the presence of the carbon fibers sintered together with the graphite matrix.*

CFC composites are widely used in many fields: aerospace industry benefits of the excellent thermal shock resistance, high specific strength and modulus of elasticity of such composites. Their superior thermal resistance and their ability to maintain strength at high temperatures has made them suitable materials for heat-resistant components in high temperature furnaces. These composites found application also in very high temperature fission and fusion reactors due to the high sublimation temperature (about 3600 K), high thermal conductivity and low neutron absorption cross section.

The commercial type of CFC composite used in the LHC primary and secondary collimators is labelled AC-150K and is produced by the Japanese company Tatsuno: AC-150K is a graphite-based composite reinforced by 2D-oriented carbon fibres, treated at temperatures of around 2800 ° C to enhance graphitization and hence improve its thermal and electrical properties. The fibers are randomly disposed in the y-z plane and create several layers parallel to each other along x, as illustrated in Figure 4.2.

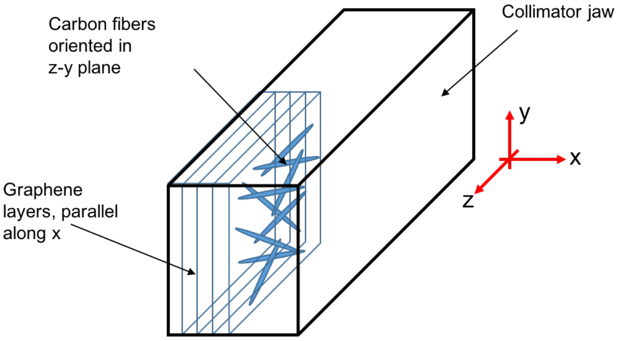

**Figure 4.2:** *Orientation of CFC's carbon fibers in collimator jaw.*

### 4.2.2 Tungsten Heavy Alloy: Inermet-180

Commercialised by Plansee, Tungsten Heavy Alloys are composite materials with high tungsten (W) content. As shown in Figure 4.3, the tungsten grains are surrounded by a NiCu phase, with a melting temperature of 1400 °C. This phase infiltrates in the voids between adjacent tungsten particles and provides good thermal and electrical continuity to the matrix. These alloys stand out for the high density (close to that of pure tungsten) but with a much better machinability compared to tungsten. The high Young's modulus and the very good mechanical properties make these composites suitable for a wide range of applications, such as the aerospace and the automotive industry, medical engineering and the construction industry.

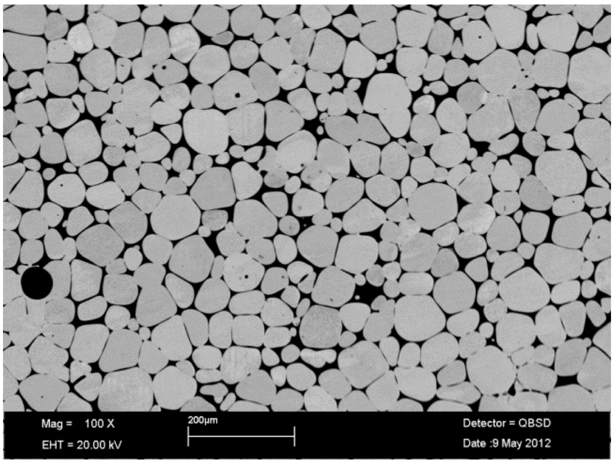

**Figure 4.3:** *Microstructure of Inermet-180, obtained with QBSD technique at low magnification. The tungsten particles look brighter than the Cu-Ni phase that appears black. Courtesy of N. Mariani, CERN [75].*

The alloy used for the LHC collimators is referred to as Inermet-180 (IT-180) and contains $95\%_{wt}$ W, $3.5\%_{wt}$ Ni and $1.5\%_{wt}$ Cu, where the numbers are fractions of the total weight. In the LHC, this material found its application in beam absorbers and tertiary collimators: these collimators, indeed, require an high Z-material to be able to efficiently stop the beams in order to prevent any possible damage in the downstream experimental regions.

### 4.2.3 Copper-based alloy: Glidcop AL-15

Glidcop AL-15, manufactured by North American Höganäs, belongs to a family of copper-based alloys strengthened by aluminium oxide ceramic particles $(0.3\%_{wt}\ \mathrm{Al_2O_3})$. In Figure 4.4(a), a micrograph of the composite is shown.

The addition of aluminum oxide in the allow greatly increases the resistance of oxygen-free (OFE) copper to thermal softening and its the mechanical strength at high temperature. Moreover, the precipitates increase the resistance of the material to radiation damage, especially from neutrons. As depicted in Figure 4.4(b), they obstacle the dislocation movement in the copper binder reducing thermal softening, retard recrystallization and prevent grain growth [77]. For this reason, an intensive use of Glidcop

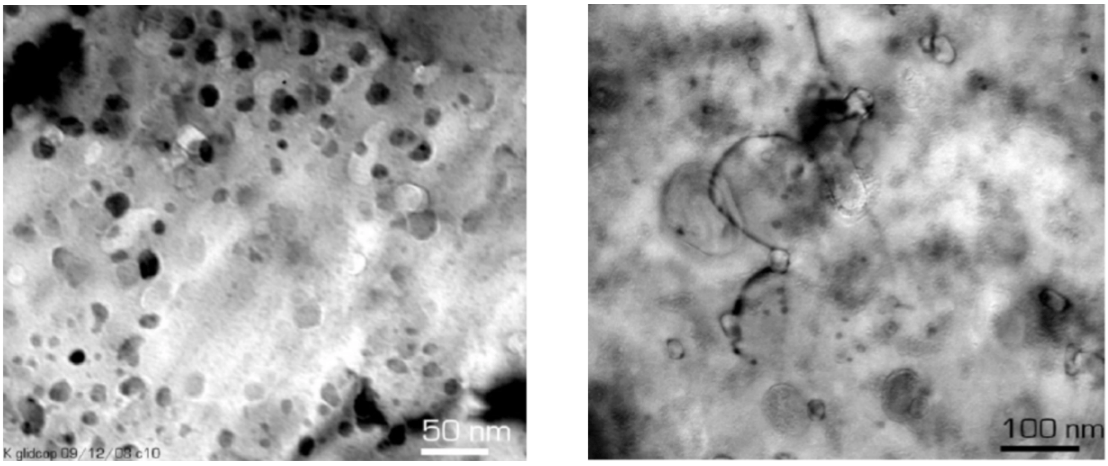

(a) Alumina particles dispersed in Glidcop AL-15.

(b) Dislocation movement obstacled by alumina particles.

**Figure 4.4:** *Transmission Electron micrograps of Glidcop AL-15 composite. Alumina particles of 5 to 12 nm are finely dispersed in the copper matrix (a) and their presence obstacle the propagation of dislocations (b). Images from Ref. [76].*

has been made in particle accelerator components, where the alloy can be subjected to high temperature and high radiation conditions simultaneously. Examples include Radio Frequency Quadrupoles (RFQs). In the LHC, Glidcop finds its use in the cooling system of collimators: the heat exchanger, in fact, is constituted by two copper-nickel pipes per jaw brazed on two sides to a Glidcop stiffener and a Glidcop plate, respectively. Furthermore, it is also used as active part of the jaws of the shower absorbers (TCLs) located downstream of the high luminosity experiments.

## 4.3 Newly developed composite materials

A material that fulfils all the requirements for HL-LHC collimators does not exists. An ambitious material R&D program has been launched at CERN in the last 10 years, which foresees a strong collaboration with external industrial companies, to develop novel composite materials to face the HL-LHC challenges. The main purpose was to explore composites ideally combining the properties of graphite or diamond (low density, high thermal properties) with those of metals and transition metal-based ceramics (low resistivity and high mechanical strength). Up to now, the outcome of this program has been the identification of the two most promising candidates: Molybdenum-graphite composite (MoGr) and Copper-Diamond composite (CuCD). The discussion of this thesis is therefore focus on these two materials. A more complete overview of all the materials developed within the program is treated in Ref. [75].

### 4.3.1 Molybdenum-graphite composite: MoGr

Molybdenum carbide - Graphite (MoGr) is a novel composite jointly developed by CERN and the Italian company Brevetti Bizz (Verona, Italy). It is produced by Pulsed Electric Current Sintering (PECS) technique, also known as Spark Plasma Sintering

(SPS) [75], from a cold pressed mixture, called “green", made of molybdenum powder, graphite flakes and, in some grades, carbon fibers, as illustrated in Fig. 4.5.

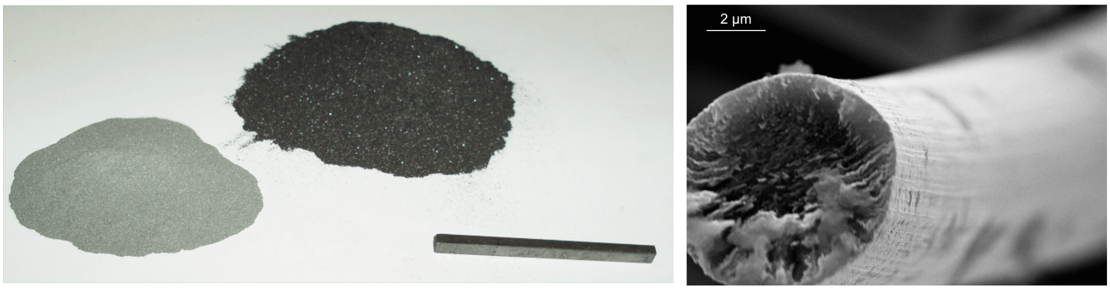

**Figure 4.5:** *Molybdenum powder, graphite flakes and an example of small MoGr bar (left). High magnification SEM observation of pitch-based carbon fibers used in the MoGr production (right). Radially oriented graphene planes are clearly visible in the internal structure of the fiber. Courtesy of N. Mariani, CERN [75].*

### Composition

Graphite is an allotropic form of carbon with a layered planar structure (Figure 4.6). The individual layers are called graphene and in each layer atoms are arranged hexagonally: atoms in the plane are bonded covalently with only three out of four potential bonding sites satisfied. The delocalised electrons are free to move in the plane, assuring good thermal and electrical conduction. The bonding between adjacent graphene layers is instead very weak due to feeble Van der Waals forces, which allows the graphene layers to easily slide one on top each other. Therefore, due to its structure, graphite features strongly different properties in the parallel (basal plane) and perpendicular direction of the graphene layers. Graphite is made commercially by electrical resistive heating to temperatures in excess of about 3100 °C, a process that can be very expensive and challenging [78]. Any process able to make graphite at lower temperature is referred to as catalytic graphitization. When a good level of graphitisation is achieved,

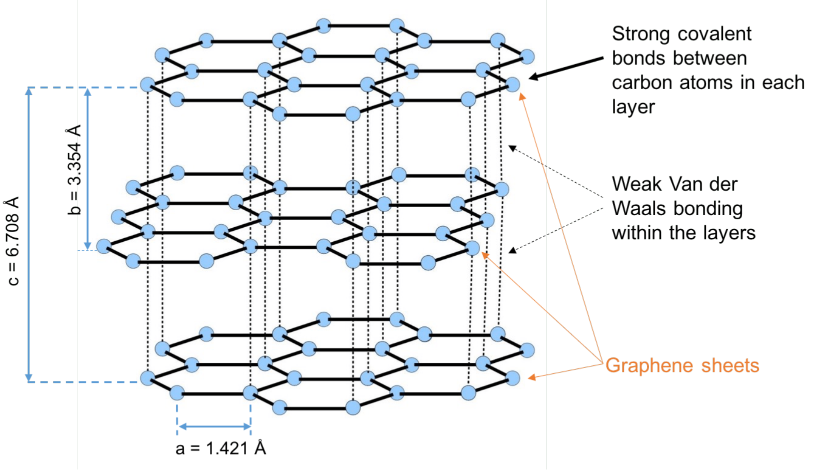

**Figure 4.6:** *Scheme of the graphite structure.*

graphitic materials feature low density, high operational temperature, large damping capacity (useful in attenuating shock waves), excellent thermal conductivity in the direction aligned with crystallite basal plane, and low CTE.

Spheroidal flakes of an average size of $45\,\mu$m in diameter of natural graphite (named Asbury 3260) were chosen for MoGr: the advantage of this graphite powder is that it shows the highest chemical purity and regular round shape which results in a higher compaction of the final composite.

Pure molybdenum has very high melting point and low CTE, as well as excellent mechanical strength and electrical conductivity. Molybdenum adopted in MoGr is a combination of powders that range from $5$ to $45\,\mu$m diameter. Graphite and molybdenum have a chemically affinity for each other. Figure 4.7 illustrates the phase diagram of the molybdenum-carbon system. The hexagonal $Mo_2C$ can be formed when the powders of graphite and molybdenum are heated up to 1000 °C. During the reaction process, carbon atoms diffuse inside the molybdenum cubic (bcc) lattice interstitials. When the amount of carbon reaches about $33\%$at, the molybdenum grain is totally transformed, according to the reaction:

$$2Mo + C \leftrightarrow Mo_2C \tag{4.6}$$

As the amount of carbon further increases, MoC carbide is formed. In MoGr, molybdenum carbides are dispersed in the graphite matrix and, under particular conditions of pressure and temperature, help the catalytic graphitization process of carbon. During hot-working process, in fact, graphite bodies containing a fine dispersion of carbide particles are compressed at temperatures above the carbon-carbide eutectic so that the carbide-bearing phase is in the liquid state. In the molybdenum-carbon system, the eutectic is reached at the temperature of 2589 °C. Under compression load, the liquid carbide is driven throughout the pore structure, thus assuring intimate contact of the matrix with the liquid medium and close the open porosity. The compression squeezes out the excess carbides, which appears as droplets on the surface of the plate. This process results in a dense, free of pores microstructure, which consists of fine carbide particles, generally of few microns, distributed uniformly in an oriented graphite matrix, featuring good density, impermeability, and strength [79].

In some grades, carbon fibres (CF) are added to the composite as a reinforcing phase due to their excellent physical and mechanical properties, such as high strength and high thermal conductivity. Moreover, CF's act as nucleation sites for enhanced graphitisation. For MoGr, mesophase pitch-derived carbon fibers has been used (as shown in Figure 4.8) of two different lengths, in the following called "long" (3 mm) and "short" fibers ($250\,\mu$m).

#### MoGr production cycle

MoGr is obtained by PECS, a pressure-assisted sintering process, in which the heating of the powders is obtained by the passage of an electrical current through the moulds by graphite electrodes (Figure 4.9). Before sintering, the powders are pre-cleaned in $H_2$ - $N_2$ atmosphere. A pressure of 35 MPa is applied during the heating ramp until the desired temperature is reached. The material to be sintered is maintained at the maximum temperature for about 20 min, then the cooling starts while pressure is progressively

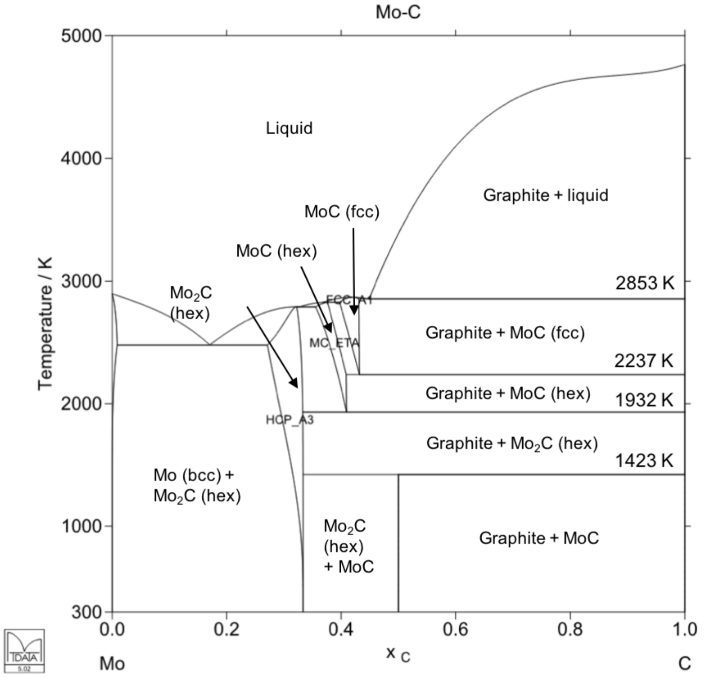

**Figure 4.7:** *Phase diagram of Mo-C system.*

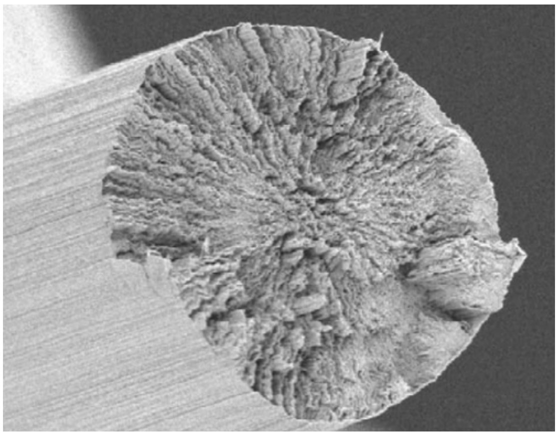

**Figure 4.8:** *Internal highly-oriented structure of a pitch-based carbon fiber. Courtesy of N. Mariani, CERN [75].*

released. The temperature is controlled by means of an optical pyrometer. In the used sintering setup, the temperature is read on the lower punch, to limit the issues related to the very high temperatures achieved. Since a non-negligible temperature gradient exists between that measuring point and the core, the actual temperature in the compact during the process can be inferred by recording the temperature at the moment of the eutectic reaction (2589 °C), which can be deduced by the change in compression speed due to the ongoing melting. The presence of droplets of molten material spilling out of the plates confirms that the eutectic point is reached. The sintering process is generally performed in a reductive atmosphere of $H_2$ - $N_2$ at $10^{-4}$ bar. A more recent

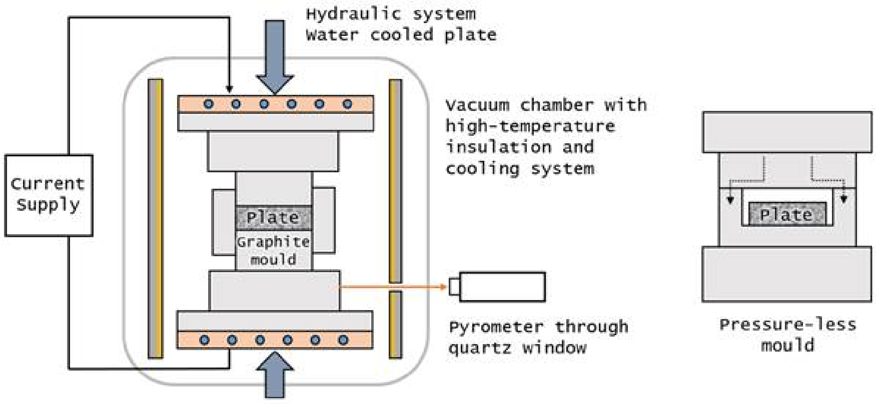

**Figure 4.9:** *Scheme of the production setup of MoGr (left). During post-production annealing, the plate is hosted in a slightly different setup (right), which is positioned inside the vacuum chamber. Courtesy of J. Guardia Valenzuela [80].*

grade, MG-6403Fc (see Table 4.4), was sintered and annealed in vacuum, to minimize the air absorption in the material and eventually reduce the outgassing rate during the operation in the LHC. A comprehensive vacuum characterization of MG-6403Fc grade was performed at CERN on various blocks of material in different conditions [81]. A difference of about one order of magnitude in the outgassing rate was observed between the batches and a factor of 10 above the acceptance limit in the worst case. Possible improvement of the vacuum performance of the material can be achieved by acting at the level of the production process, for example by compacting the "green" powders under vacuum instead of in a reductive atmosphere.

#### MoGr generations and classification

A broad range of composition and production cycle parameters were explored in order to improve the final properties of the material. More than 30 different grades of MoGr were produced in the last years and a clear nomenclature was needed to identify each grade uniquely. The nomenclature adopted is:

$$MG - \#\#\#\# - Aa \tag{4.7}$$

and contains information about:

- Composite acronym: e.g., "MG" stands for Molybdenum-Graphite.
- Material composition: 4 digits, each of them corresponds to the fraction in volume $\%_v$ of a certain component of the composite: respectively, molybdenum, graphite, carbon fibers and other possible elements.
- Sintering cycle: a uppercase letter (A...Z) is assigned to a different cycles. See Table 4.1 for additional details on the meaning of the most relevant grades.
- Annealing cycle: a lowercase letter (a...z) is assigned to a different post-sintering annealing treatment. See Table 4.1 for additional details on the most relevant grades.

**Table 4.1:** *Parameters of MoGr production and annealing cycles. Only the cycles related to MoGr grades treated in this work are listed in the table. The temperature was recorded by means of an optical pyrometer, reading the temperature on the outer surface of the graphite electrode. To account for the temperature difference between the plate and the electrode where the pyrometer is located, an additional* $\Delta T = \sim 300\,K$ *must be considered to know the real temperature of the plate. Note that* $\Delta T$ *value are obtained from simulations, and depends on several factors, such as the injected current, the material of the electrode, etc.*

| **Cod.** | **CYCLE** | | | **ATMOSPHERE** | |
|---|---|---|---|---|---|
| | **Temperature** (°C) | **Time** (s) | **Pressure** (MPa) | **Pressure** (mbar) | **Type** |
| E | < 2000 | 1200 | 35 | 0.1 | 100% $N_2$ |
| P | 2000 | 600 | 35 | 0.1 | 95% $N_2$, 5% $H_2$ |
| S | 2150 | 600 | 35 | 0.1 | 95% $N_2$, 5% $H_2$ |
| U | 2160 | 1300 | 35 | 0.1 | 95% $N_2$, 5% $H_2$ |
| A | 2210 | 1200 | 35 | 0.1 | 95% $N_2$, 5% $H_2$ |
| | cooling to 700 °C, pressure down to 35 MPa | | | | |
| | 2210 | 1200 | 35 | 0.1 | 95% $N_2$, 5% $H_2$ |
| | cooling to $T_{room}$, pressure down to 7.5 MPa | | | | |
| F | 2250 | 1200 | 35 | vacuum | |
| | cooling to 700 °C, pressure down to 7.5 MPa | | | | |
| | 2300 | 1200 | 35 | vacuum | |
| | cooling to $T_{room}$, pressure down to 7.5 MPa | | | | |
| G | 2400 | 1200 | 35 | vacuum | |
| | cooling to 700 °C, pressure down to 7.5 MPa | | | | |
| | 2400 | 1200 | 35 | 0.1 | 95% $N_2$, 5% $H_2$ |
| | cooling to $T_{room}$, pressure down to 7.5 MPa | | | | |
| **Post-production annealing cycle** (followed by natural cooling to $T_{room}$) | | | | | |
| a | 1900 | 3000 | 0 | 0.1 | 95% $N_2$, 5% $H_2$ |
| c | 2400 | 3000 | 0 | vacuum | |

Once assigned a label, the MoGr grades were grouped in "generation" (Table 4.2), which differ from each other mainly by the presence of CF's, the temperature used during the production cycle, the presence of other additive elements in the composition.

The density of the material tends to decrease with the generations. The reason is found in a combination of factors, e.g., the initial molybdenum content in the powders and the catalytic graphitization that takes place during the production cycle. In generations 1-3, the high density of the material is mainly owing to the high initial content of molybdenum and the limited removal of the liquid carbide phase during the process,

**Table 4.2:** *Generations of Molybdenum-Graphite grades. Note that the temperature values from generation 4 (G4) on are measured by means of a pyrometer on the outer surface of the graphite electrode. Therefore, same consideration of Table 4.1 applies.*

| **MG gener.** | **Period of development** | **Carbon fibers** | **Other elements** | **Sintering T** (°C) | **Annealing** (°C) | **Density** (g/cm$^3$) |
|---|---|---|---|---|---|---|
| G1 | 2011 - early 2012 | no | no | $\sim$1700 | no | $\sim$5.3 |
| G2 | 2012 - mid 2013 | no | no | $\sim$2200 | no | $\sim$3.8 |
| G3 | mid 2013 | yes | no | $\sim$2400 | no | $\sim$3.7 |
| G4 | late 2013 - mid 2014 | yes | no | $\sim$2000 (*) | no | $\sim$2.7 |
| G5 | mid 2014 | yes | no | $\sim$2150 (*) | 1150-1300 (*) | $\sim$2.6 |
| G6 | late 2014 - mid 2015 | yes | no | 2160-2210 (*) | $\sim$1900 (*) | $\sim$2.5 |
| G7 | late 2015 - early 2016 | yes/no | Ti | 2250-2400 (*) | 1900-2400 (*) | $\sim$2.5 |

which was constrained by the temperature. In generation 4-7, instead, the fraction of molybdenum in the “green” powders was progressively reduced, and the temperature of the cycle was increased: the latter enhanced the catalytic graphitization by the infiltration of liquid carbides in the pores of the graphite matrix and the spill out of the liquid in excess.

Post-production annealing cycle at high temperature introduced from generation 5 was beneficial to release the internal stresses accumulated in the material during the sintering. The issue of the residual stresses was indeed revealed by the results of the irradiation tests performed on collimator materials (topic discussed in detail in Chap. 6), and from there the need to reduce them by acting on the production process itself. The contribution to graphitisation and mechanical reinforcement from CF was also questioned by the results of the irradiation tests. For this reason, it was decided to produce some MoGr grades of generation 7 without CF. Finally, the addition of titanium, even a small amount, turned to make the cubic MoC carbide phase stable at room temperature (more details in Chap. 5) and to increase thermal and electrical properties. The composition and the main properties of those MoGr grades that will be recalled in the next chapters are summarised in Table 4.4.

### 4.3.2 Copper-Diamond composite: CuCD

Copper-Diamond (CuCD) is a novel material developed by the Austrian company RHP-Technology. It is produced by conventional Hot Pressing using cold pressed powders, which includes diamond particles, copper powder and a small addition of boron. The low chemical affinity between main components is overcome by the addition of boron particles: they form a stable boron carbide layer on the diamond surface and dissolve on the other side into the copper matrix, providing a good bonding to the material [75]. The "green" powders are heated at a constant pressure of 35 MPa up to slightly below the melting point of copper (1000-1050 °C) and kept in this condition for 1-4 hours. A controlled heating/cooling rate of 50 K/min is applied. The process is conducted

**Table 4.3:** *Chemical composition of MoGr grades. For each grade, the initial volumetric composition (of the "green" powders) is listed together with the final atomic composition after sintering. The latter takes into account possible spill out of the liquid carbide phase if the eutectic temperature is reached during the cycle. Abbreviations: Mo=Molybdenum powder, C = graphite flakes, cy =* $300\,\mu m$ *carbon fibers (from Cytec©), gra =* $3\,mm$ *carbon fibers (from Granoc©), Ti=Titanium.*

| **Gen.** | **Grade** | **Initial volumetric fraction** ($\%_{\mathrm{vol}}$) | | | | | **Final atomic fraction** ($\%_{\mathrm{at}}$) | | |
|---|---|---|---|---|---|---|---|---|---|
| | | Mo | C | cy | gr | Ti | Mo | C | Ti |
| G3 | MG-1110E | 20 | 40 | 20 | 20 | – | 12.45 | 87.55 | – |
| G4 | MG-3110P | 20 | 40 | 20 | 20 | – | 2.45 | 97.55 | – |
| G5 | MG-5220S | 7.2 | 46.4 | 23.2 | 23.2 | – | 2.61 | 97.39 | – |
| G6 | MG-6400U | 4.5 | 95.5 | – | – | – | 1.65 | 98.35 | – |
| | MG-6530Aa | 4.5 | 90.5 | – | 5 | – | 1.79 | 98.21 | – |
| G7 | MG-6541Aa | 4.28 | 90.91 | 4.76 | – | 0.05 | 1.68 | 98.30 | 0.02 |
| | MG-6403Ga | 4.5 | 95.3 | – | – | 0.2 | 1.54 | 98.40 | 0.06 |
| | MG-6403Fc | 4.5 | 95.3 | – | – | 0.2 | 1.87 | 98.06 | 0.07 |

under dry hydrogen gas atmosphere at $10^{-4}$ bar. Usually, CuCD composite is produced using a sandwich setup, composed by a metallic layer on the bottom, another metallic layer on the top and the diamond-containing composite mixture in between. A stress relieving heat treatment at 300-400 °C is performed for 1 h after the hot pressing cycle. A simplified scheme in Fig. 4.10 illustrates the different steps of the CuCD production.

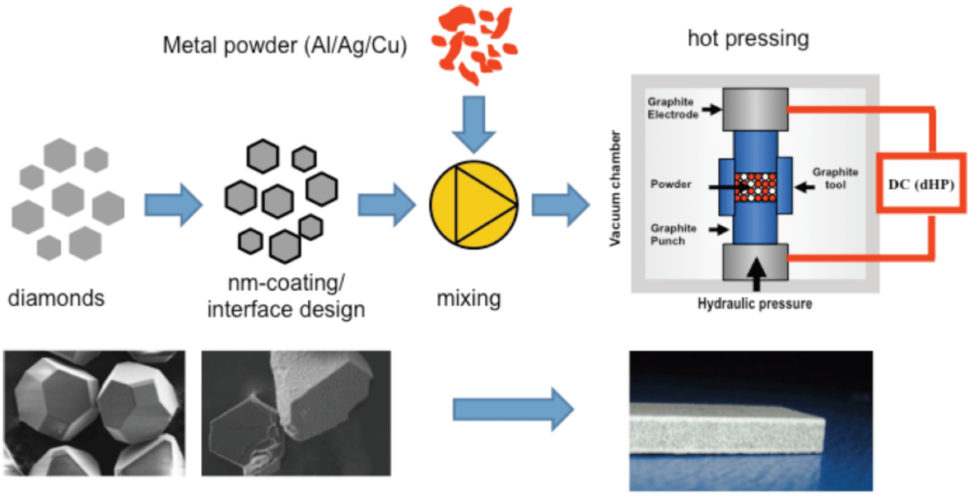

**Figure 4.10:** *Scheme of production cycle of CuCD.*

The volumetric composition of the current baseline CuCD grade is $60\%_v$ diamonds (90% of 100 $\mu$m size and 10% of 45 $\mu$m size to achieve a better compaction), $39\%_v$ of Cu powder (45 $\mu$m) and $1\%_v$ of B powder (5 $\mu$m). The addition of boron is of crucial importance: as shown in Fig. 4.11, the formation of boron carbides at the interface between copper and diamond balances the low chemical affinity of the other two ele-

**Table 4.4:** *Thermo-mechanical properties of MoGr grades. Properties are measured at room temperature (RT= $20\,^{\circ}\mathrm{C}$), except the coefficient of thermal expansion (CTE) that is averaged between RT and $1000\,^{\circ}\mathrm{C}$. Provided values refer to the stiffer direction of the material.*

| **Grade** | **Density** (g/cm$^3$) | **El. cond.** (MS/m) | **Th. cond.** (W/m/K) | **CTE** ($10^{-6}K^{-1}$) | **Flex strength** (MPa) | **Flex strain-to-rupture** ($\mu$m/m) |
|---|---|---|---|---|---|---|
| MG-1110E | 3.76 | $1.0 \pm 0.05$ | 320 | n.a. | n.a. | n.a. |
| MG-3110P | 2.59 | $1.1 \pm 0.06$ | 644.5 | n.a. | n.a. | n.a. |
| MG-5220S | 2.64 | $0.9 \pm 0.05$ | 677 | 5.70 | $64.5 \pm 13$ | $1905 \pm 52$ |
| MG-6400U | 2.48 | $0.9 \pm 0.05$ | 548.8 | 5.46 | $62.9 \pm 6$ | $1867 \pm 124$ |
| MG-6530Aa | 2.51 | $0.8 \pm 0.04$ | 489.9 | 6.26 | $70.9 \pm 3$ | $2501 \pm 547$ |
| MG-6541Aa | 2.49 | $1.0 \pm 0.05$ | 507 | 6.03 | $79.5 \pm 4$ | $1910 \pm 142$ |
| MG-6403Ga | 2.49 | $0.9 \pm 0.05$ | 547 | 5.66 | $73.5 \pm 7$ | $2643 \pm 279$ |
| MG-6403Fc | 2.54 | $0.9 \pm 0.05$ | 740 | 5.54 | $58.1 \pm 8$ | $2430 \pm 498$ |

ments. The lack of these carbides would impair the resulting mechanical strength as well as the thermal conductivity.

**Figure 4.11:** *CuCD samples (left) and high magnification SEM observation on a fracture surface of CuCD (right). Courtesy of N. Mariani, CERN.*

Diamond is a metastable allotrope of carbon, where each carbon atom is bonded covalently with other surrounding four carbon atoms and are arranged in a variation of the face centered cubic (fcc) crystal structure, called "diamond lattice", shown schematically in Figure 4.12. In standard conditions (i.e. room temperature and 1 atm), the structure of diamond is thermodynamically metastable and a sort of “graphitization” process can occur: the carbon atoms bonds tend to return to that of graphite. However, the kinetic of this process is not negligible only at high temperatures. Diamond stands out for its superlative physical qualities, most of which originate from the strong covalent bonding between the carbon atoms. In particular, it has the highest hardness and thermal conductivity (900-2320 W/mK) of any bulk material. Therefore, the presence of diamond particles in CuCD provides high thermal and electrical properties.

In CuCD, Copper is chosen for its excellent thermal and electrical conductivity, along with its good ductility, while diamond is added to reduce the density and the CTE, while contributing to the thermal conductivity. It is for the latter-mentioned property that the material may provide an effective solution to existing thermal management issues. Results of thermal measurements performed at CERN on CuCD samples are

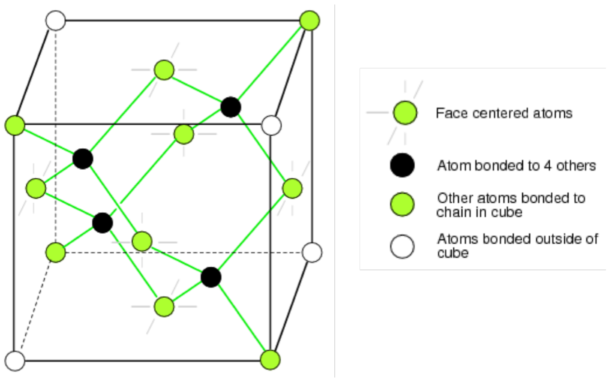

**Figure 4.12:** *Scheme of the structure of a diamond crystal.*

plotted in Fig. 4.13. The main limitation of CuCD is the low melting point due to the presence of the low-melting copper phase. Moreover, Figure 4.14 shows that the CTE significantly increases with the temperature, from $\sim 7 \times 10^{-6}\,\mathrm{K}^{-1}$ at 30° C up to $\sim 13 \times 10^{-6}\,\mathrm{K}^{-1}$ at 640° C, because of the high Cu content.

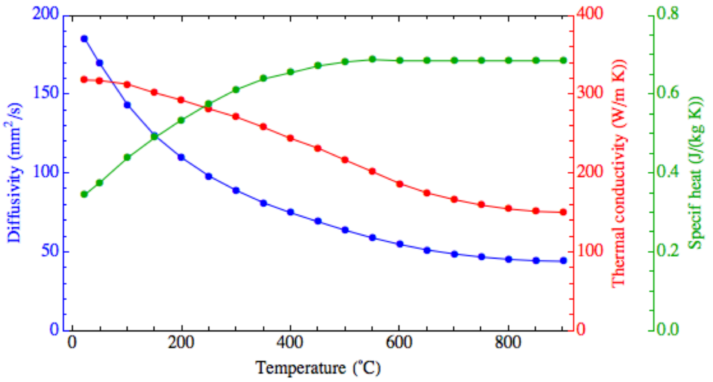

**Figure 4.13:** *Result of thermal measurements performed at CERN on CuCD, using a Netzsch LFA 427 analyser. The plot contains information about thermal diffusivity, thermal conductivity and specific heat.*

## 4.4 Comparison of collimator materials properties and performances

A comparison of the materials for LHC collimators presented in the previous Sections is shown in Table 4.5. The values of the figures of merit (FoM) are also listed for each material. Note that these indexes are derived assuming a linear elastic behaviour, while certain materials significantly depart from linearity: this is the case of CuCD and MoG. Therefore, FoMs must be considered as qualitative parameters, to be used for a relative comparison between the selected materials.

Carbon-based materials possess the highest TRI and TSI thanks to low-Z, low CTE, low density, high degradation temperature and high conductivity. CFC guarantees very

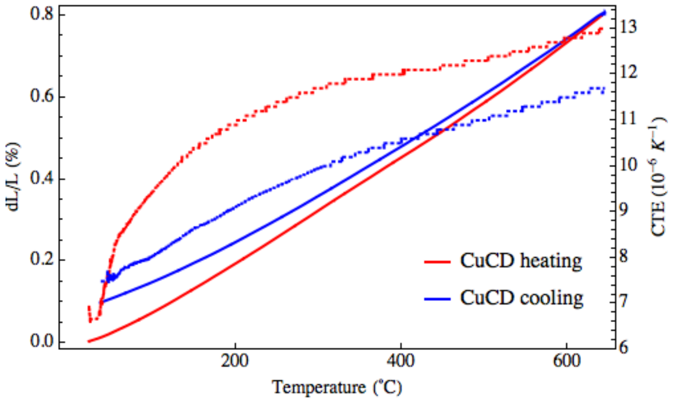

**Figure 4.14:** *Result of thermal expansion test performed at CERN on CuCD, using a Netzsch DIL 402E dilatometer. Full lines refer to the deformation of the sample as function of the temperature, while dotted lines show the evolution of the coefficient of thermal expansion (CTE). Red and blue curves indicate the heating and the cooling cycle, respectively. The sample is heated in the dilatometer furnace and it elongates under the effect of the temperature, then the cooling process brings the material back to room temperature, which should fully recover the deformation. If the two curves are not superposed, it means that a residual non-recovered elongation survived after the cycle, which in the case of CuCD can be quantified to 0.1%.*

high mechanical resistance to collimators as well as good heat removal. In case the beam coupling impedance becomes an issue (e.g. for HL-LHC), the low electrical conductivity penalises CFC, while MoGr can be a valid alternative. A thin coating layer of pure metals (e.g. Mo) or ceramics (e.g. TiN) on top of the bulk material (CFC or MoGr) could further improve the electrical conductivity with a consequent positive impact on the impedance reduction [82]. The poor performance of Inermet-180 in terms of thermo-mechanical robustness is due to the low melting temperature of the Ni-Cu matrix, which is used to bind the tungsten particles and to increase the ductility of the final material. CuCD features very good RFI, however its density and CTE, higher than MoGr, may be penalising in case of beam accidents.

None of the materials fully matches all the requirements for collimators in the LHC. The final material choice is therefore dependent on which performance aspects must be favoured, which is connected to the specific role of each collimator family in the collimation system hierarchy.

**Table 4.5:** *Properties and figures of merit of materials relevant for collimators. Values of thermo-mechanical properties are measured at room temperature (RT=20 °C), except for CTE that is averaged between RT and 1000°C. For anisotropic materials (e.g., CFC and MG), properties, such thermal and electrical conductivity, Young's modulus and ultimate strength, are listed for the stiffer direction. Note that the column "graphite" refers to a type of isostatic graphite, called R4550 (SGL Carbon), currently used at the LHC for injection protection collimators.*

| **Parameter** | **Unit** | **graphite** | **Mo** | **Cu** | **W** | **CFC** | **IT-180** | **Glidcop** | **MG-6403Fc** | **CuCD** |
|---|---|---|---|---|---|---|---|---|---|---|
| Density | g/cm$^3$ | 1.83 | 10.22 | 8.93 | 19.26 | 1.67 | 18.0 | 8.90 | 2.54 | 5.4 |
| Radiation length | cm | 25.8 | 0.96 | 1.44 | 0.35 | 25.8 | 0.42 | 1.48 | 15.8 | 4.8 |
| Melting temp. | °C | 3650 | 2623 | 1083 | 3422 | 3650 | $\sim 1400$ | 1085 | 2589 | 1083 |
| Thermal cond. | W/m/K | 105 | 142 | 398 | 163 | 197 | 109 | 379 | 508 | 319 |
| Specific heat | J/kgK | 600 | 251 | 385 | 130 | 712 | 140 | 385 | 624 | 340 |
| Volumetric CTE | $10^{-6}$ K$^{-1}$ | 4.2 | 5.5 | 17.3 | 4.3 | 3.9 | 5.5 | 21.1 | 5.5 | 10.6 |
| Electrical cond. | MS/m | 0.08 | 18.7 | 58.0 | 17.7 | 0.18 | 8.4 | 52.1 | 0.9 | 12.6 |
| Young's modulus | GPa | 11.5 | 330 | 115 | 410 | 61.5 | 360 | 120 | 61 | 146 |
| Ultimate strength | MPa | 60 | 560 | 210 | 980 | 121 | 690 | 375 | 58 | 100 |
| **TRI** | - | 2738 | 6.2 | 5.8 | 1.06 | 1626.3 | 0.5 | 5.3 | 231 | 8.5 |
| **TSI** | - | 24.3 | 0.74 | 0.96 | 0.34 | 54.8 | 0.14 | 0.78 | 55.9 | 5.0 |
| **RFI** | - | 0.22 | 4.3 | 7.6 | 4.2 | 0.34 | 2.9 | 7.2 | 1 | 3.5 |

CHAPTER 5

# Experimental characterisation of collimator materials

Several experimental activities to characterise thermo-physical, mechanical and electrical properties of collimator materials have been performed at CERN as well as in other research institutes. In addition, a unique beam impact test carried out at the CERN HiRadMat facility helped in assessing the ability of the materials to withstand high-energy beam impacts. A selection of the relevant results of materials characterization performed on LHC collimator materials is presented in this Chapter.

## 5.1 Methods of material properties measurements

In order to provide a systematic approach for material characterisation, this Section is structured such that the properties of interest for collimator materials are introduced, as well as the experimental tools used to measure such properties.

### 5.1.1 Thermal properties

**Laser Flash apparatus**

The Laser Flash apparatus (LFA) was firstly documented in 1961 [83]. Figure 5.1(a) shows the principle of LFA operation. The sample is placed in a vacuum-tight furnace. The device fires a short laser pulse at the surface of a thin disk specimen, the heat absorbed by the front face of the sample is transferred through the specimen, and it results in a temperature rise on the rear face. That is measured by temperature sensor and the analysis of this temperature change allows determination of thermal diffusivity.

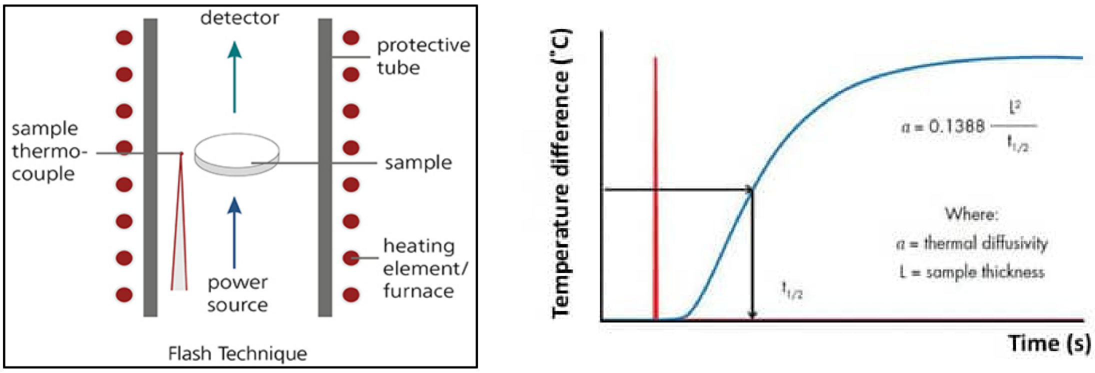

(a) Scheme of the apparatus.

(b) Typical measuring curve.

**Figure 5.1:** *Scheme of Laser Flash apparatus and its functioning principle.*

As shown in Figure 5.1(b), the relative increase of temperature on the rear side is then plotted as a function of time. In the adiabatic case, the thermal diffusivity $a$ (in mm$^2$/s) can be calculated as:

$$a = 0.1388 \frac{L^2}{t_{\frac{1}{2}}} \tag{5.1}$$

where $L$ represents the sample thickness (in millimetres) and $t_{\frac{1}{2}}$ is the time (in seconds) at 50% of the temperature increase. The thermal diffusivity is proportional to the square of the sample thickness, therefore this quantity must be measured very carefully (at room temperature) and must be corrected for thermal expansion at elevated temperatures. However, it has to be noted that Eq. 5.1 is strictly valid only if the duration of the laser pulse is much shorter compared to the halftime $t_{\frac{1}{2}}$. The thermogram in Figure 5.2 shows the response of three different materials according to their diffusivity behaviour. The blue curve corresponds to a “slow” behaviour of a ceramic material, which features a gradual increment of the temperature on the rear face of the specimen. On the other hand, red curve corresponds to a “fast” sample according to the steepness of the thermogram, e.i. graphite. In between we find most of the metals. Therefore, we can say that the higher the sample’s thermal diffusivity, the steeper the signal increase.

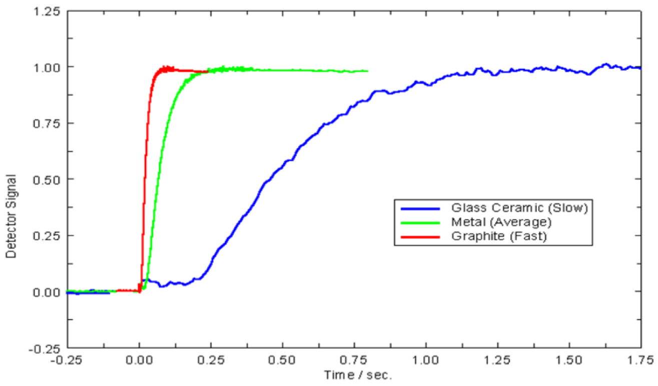

**Figure 5.2:** *Response of materials with different diffusivity behaviour.*

Once the thermal diffusivity is known, the thermal conductivity $\lambda$ can be computed through the formula:

$$\lambda(T) = a(T) \cdot c_p(T) \cdot \rho(T). \tag{5.2}$$

where $\rho$ is the material density and $c_p$ the specific heat.

By LFA, it is possible to measure 2 and 3-layers samples: this might be the case for a sample exposed to radiation with a penetration depth shorter than the thickness of the irradiated sample, which can be sees as an irradiated layer on top of the unirradiated bulk. If the thermal diffusivity of the pristine material is known, the thermal diffusivity of the irradiated sample (irradiated layer and unirradiated bulk) is measured using LFA and the diffusivity of the irradiated layer can be determinate analytically. After the measurement, the calculation can be also improved by non-linear regression analysis.

### Dilatometer

Dilatometry is a thermo-analytical technique for determining dimensional changes under negligible load while the material sample is subjected to a controlled thermal cycle. Figure 5.3 illustrates the scheme of a dilatometer. A sample is placed into a special holder inside a movable furnace. An alumina pushrod is positioned directly against the sample and transmits the length change to a linear variable displacement transducer sensor (LVDT). As the sample length changes during the thermal cycle, the LVDT core is moved and an output signal proportional to the displacement is recorded. Since the sample holder and the front part of the pushrod are being exposed to the same temperature program as the sample, they are also expanding. The resulting signal is therefore the sum of the length changes of sample, sample holder, and pushrod.

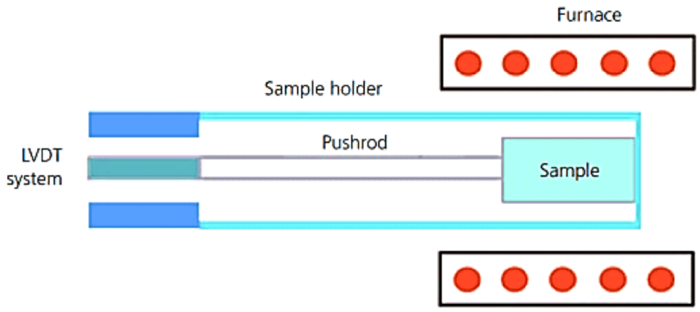

**Figure 5.3:** *Scheme of a pushrod dilatometer.*

The thermal expansion coefficient of the measured sample, expressed in $[K^{-1}]$ is then calculated as:

$$\text{CTE} = \frac{1}{L_0}\left(\frac{dL(T)}{dT}\right) \tag{5.3}$$

where $L_0$ is the initial length of the sample at room temperature, while $L$ and $T$ are respectively the length and the temperature at the time of the measurement. The contributions from sample holder and pushrod should be deduced by calibration.

### Differential Scanning Calorimeter

A Differential Scanning Calorimeter (DSC) allows the quantitative determination of caloric entities, such as the enthalpies for solids and liquids, by measuring the heat flows to both the sample and to a reference as a function of temperature and time. As depicted in Figure 5.4(a), it consists of a furnace containing an integrated sensor with designated positions for the sample and reference pans. The sensor areas are connected to thermocouples, which record both the temperature difference between the sample and reference side (DSC signal) and the absolute temperature of the sample or reference side. During heating of the DSC measuring cell, due to the heat capacity of the sample, the reference side (usually an empty pan) generally heats faster than the sample side. The two curves exhibit parallel behaviour during heating at a constant heating rate, until a sample reaction occurs. In the example shown in Figure 5.4(b), the sample starts to melt at temperature $t_1$. The temperature of the sample does not change during melting. The temperature of the reference side, however, remains unaffected and continues exhibiting a linear increase. When melting is completed (at $t_2$), the sample temperature begins to increase linearly again. The blue area is correlated with the heat content of the endothermic melting process (enthalpy in J/g).

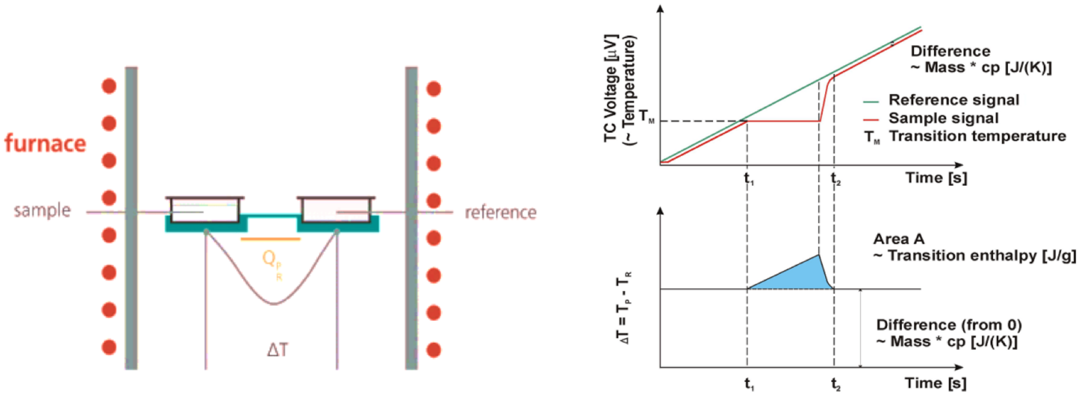

(a) Scheme of the apparatus.

(b) Typical measuring curve.

**Figure 5.4:** *Scheme of Laser Flash apparatus and its principle of operation.*

## 5.1.2 Mechanical properties

### Flexural test

The ultimate strength and the constants of the elastic matrix are the main mechanical properties of interest for collimators. Generally, the tensile test is used to derive the mechanical strength of metals. On the other hand, the extremely low ductility of brittle materials, which do not show almost any plastic deformation, does not allow the success of the test. Therefore, brittle materials (such as CFC, MoGr and CuCD of the LHC collimators) are measured by Flexural Test, according to the standard ASTM C1161-02c [84]. In this test, a bar-type specimens is placed on two parallel supporting pins (Figure 5.5). The loading force is applied by means of two loading pins with a distance

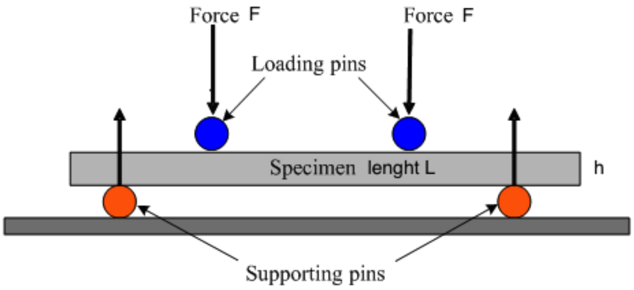

**Figure 5.5:** *Scheme of the 4-point bending flexural test.*

between them equal to a half of the distance between the supporting pins. As a result of the loading, the specimen bends, causing formation of tension stress in its convex side and compression stress in the concave one. The maximum stress and the corresponding maximum strain are calculated for every load value. The flexural strength is the maximum stress generated in the sample at its failure during the flexure test, multiplied by the area of the sample. For bar-type specimens, the flexural stress (in N/mm$^2$) is calculated by the formula:

$$\sigma_{fl} = \frac{3 \cdot L \cdot F}{4 \cdot w \cdot h^2} \tag{5.4}$$

where $F$ is the total force applied to the specimen by two loading pins, while $L$ ,$w$ and $h$ are respectively length, width, and height of the specimen. Ideally, the ultimate strength of materials should be measured with a tensile test; however, in the case of brittle materials, the specimen would typically break at the grips, in a triaxial stress state, invalidating the test results. For brittle materials, a four-point bending test is performed. Generally, the ultimate strength measured with a bending test is overestimated with respect to a tensile test, as in the first case the specimen reaches the maximum stress state only at the external surface. In the case of brittle failure, controlled by fracture mechanics and based on the generation and propagation of defects, the crack can originate internally, at a lower stress than that measured by strain gauges on the surface. Another issue of bending tests is that they are sensitive to the surface state, as a rough machining can ease the generation and propagation of defects under tensile load. It must also be noted that Eq. 5.4 implicitly assumes that the material has a linear elastic behaviour, meaning that a linear relationships exists between stresses and strains until failure. However, some materials can significantly depart from linearity. Examples are “soft” materials, such as annealed copper or aluminium and magnesium alloys, and, most interestingly for collimators, graphitic materials [71]. In this case, knowing the moment from the measurement and with the hypothesis of linear strain, we can calculate the equivalent stress.

#### Impulse excitation technique

Impulse excitation technique (IET) is used to determine the elastic properties of a material. By measuring the resonant frequencies, it is possible to calculate Young’s modulus, shear modulus, Poisson’s ratio. As shown in Figure 5.6, the sample is mechanically excited by a singular elastic strike with an impulse tool. A transducer (e.g., a microphone) senses the resulting mechanical vibrations of the specimen and transforms them into electric signals. The acoustic response is composed of the natural frequencies of vibration of the specimen that are proportional to the elastic modulus, and its amplitude is reduced according to the damping of the material. The signals are then analysed, and the fundamental resonant frequency is determined by dedicated software. A further simulation step may be necessary to reconstruct the elastic matrix.

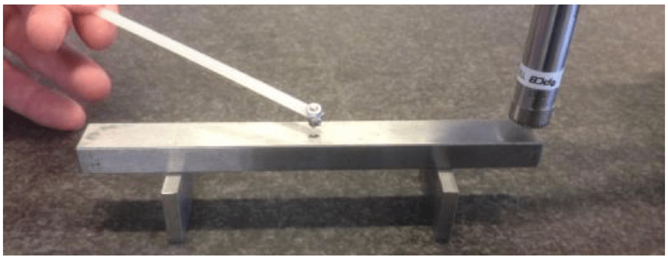

**Figure 5.6:** *Impulse excitation technique.*

### 5.1.3 Electrical properties

Electrical resistivity is an intrinsic property that quantifies how strongly a given material opposes the flow of electric current. It is expressed in ohm-metre (Ω m). The reciprocal of electrical resistivity is referred to as electrical conductivity (in unit of siemens per metre, S/m) and, conversely, it measures the ability of the material to conduct an electric current.

#### Four-wire method

It is a direct method to measure the electrical resistivity of a bulk material. Ohm's law defines resistance, $R$, as the ratio of voltage $V$ across a component, to the current $I$ passing through it, i.e. $R = V/I$. To measure $R$, we apply a test current to the sample and detect the resulting voltage drop. The voltmeter probes are two pins of $L$ width apart. However, several issues must be taken into account. The current must be applied between two parallel and opposite faces of the sample by electrodes with a certain contact pressure, which results in a current uniformly distributed on the faces. Therefore, a material with high electrical conductivity, such as copper, is required as electrode and the size should be at least as big as the faces of the sample. Figure 5.7 illustrates schematically the setup of the four-wire method.

The current through voltmeters always tends to zero, so in this setup the voltmeter is measuring only the voltage drop produced over the sample by the current from the power supply. The resistance measured between the two pins of the voltmeter includes also that of the contacts. However, in many cases the contact resistance is much lower than the resistance of the material we want to measure and therefore can be disregarded. Finally, the electrical resistivity is calculated as:

$$\rho = R\,\frac{A_{\text{sample}}}{L} = R\,\frac{d_1 \cdot d_2}{L} \tag{5.5}$$

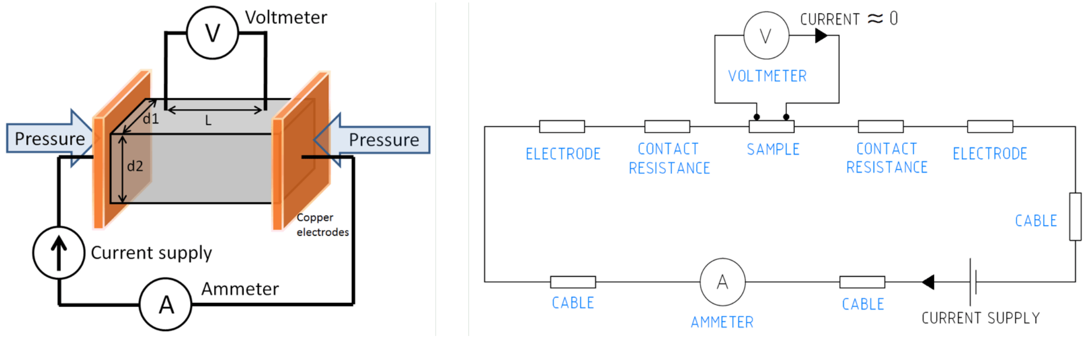

**Figure 5.7:** *Scheme of the four-wire method setup (left) and corresponding electrical circuit (right). Picture courtesy of J. Guardia Valenzuela.*

where $L$ is the distance between the voltmeter pins, $d_1$ and $d_2$ indicate the size of the sample face.

### 5.1.4 Microstructural analysis

**Raman spectroscopy**

Raman spectroscopy provides chemical and structural information that help understanding more about materials.

When light impinges a molecule, most photons are elastically scattered. The scattered photons have the same energy (frequency), and therefore wavelength, as the incident photons. However, a small fraction of light (approximately 1 out of $10^7$ photons) is scattered at optical frequencies different from, and usually lower than, the frequency of the incident photons. The process leading to this inelastic scatter is known as *Raman effect*. The difference in energy between the incident photon and the Raman scattered photon is equal to the vibration energy of the scattering molecule.

In practice (Figure 5.8(a)), a sample is illuminated with a laser beam. Electromagnetic radiation from the illuminated spot is collected with a lens and sent through a monochromator. Elastic scattered radiation at the wavelength corresponding to the laser line (Rayleigh scattering) is filtered out by either a notch filter, edge pass filter, or a band pass filter, while the rest of the collected light is dispersed onto a detector. A Raman spectrum reproduces the intensity of the scattered light versus the energy difference is then generated. Raman peaks (also called bands) are observed in those substances that have vibrational or rotational modes which change the polarizability (hence the inelastic scattering). Metals, for example, are not “Raman active” and they do not have Raman peaks. The Raman spectrum of crystals with a regular array of identical atoms, all in the same configuration (such as the carbon atoms in diamond) often shows just one dominant Raman band, because there is just one molecular environment of the crystal (Figure 5.8(b)). In the case of polystyrene, instead, the Raman spectrum is much more complex because the molecule is less symmetric and has hydrogen atoms in addition to carbon atoms. There are also different bond types connecting the atoms.

Vibrational frequencies are characteristic of chemical bonds in a molecule and are sensitive to the local environment of the molecule. Therefore, there might be shifts of

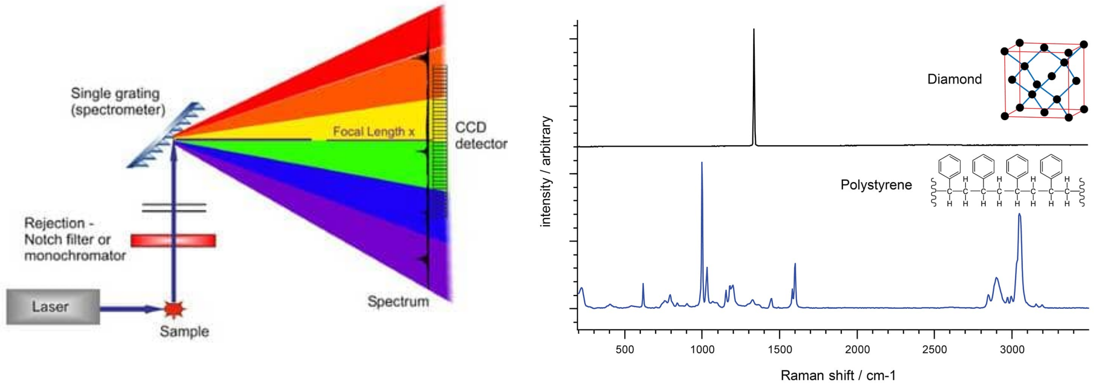

(a) Raman spectroscopy apparatus.

(b) Raman spectra of diamond (single band) and polystyrene (multiple bands).

**Figure 5.8:** *Raman spectroscopy: scheme of the basic operating principle (a) and an example of a resulting spectrum (b).*

the vibrational frequencies due to crystal phase, local strain or change in the degree of crystallinity. A Raman spectrum provides indeed a fingerprint representing the set of bonds presents in the material. The relative intensities within a spectrum can also quantify the concentration of a substance.

### Scanning Electron Microscopy

The Scanning Electron Microscope (SEM) operates in high vacuum, where a beam of electrons is generated by a tungsten filament or a field emission gun. The electron beam is accelerated through a high voltage (e.g.: 20 kV) and pass through a system of apertures and electromagnetic lenses to produce a thin beam of electrons, which scans the surface of the specimen by means of scan coils (see Figure 5.9(a)). When the electron beam hits the surface of the sample, it penetrates the sample to a depth of few microns, depending on the accelerating voltage and the density of the sample. As a consequence of their interaction with the sample, the incoming electrons produce secondary electrons, backscattered electrons and characteristic X-rays (see Figure 5.9(b)). These signals are collected by one or more detectors to form images which are then displayed on the computer screen. Secondary electrons are most valuable for showing morphology and topography on samples, while backscattered electrons are used for illustrating contrasts in the composition of multiphase samples. In most applications, data are collected over a selected area of the sample surface, and a 2-dimensional image is generated that displays spatial variations in these properties. Areas ranging from approximately 1 cm to 5 $\mu$m in width can be imaged in scanning mode using conventional SEM techniques (magnification ranging from 20X to approximately 30,000X, spatial resolution of 50 to 100 nm). The SEM is also capable of performing analyses of selected point locations on the sample: this approach is especially useful in qualitatively or semi-quantitatively determining chemical compositions (using Energy-Dispersive X-Ray Spectroscopy, EDS), crystalline structure, and crystal orientations (using Electron Backscatter Diffraction, EBSD).

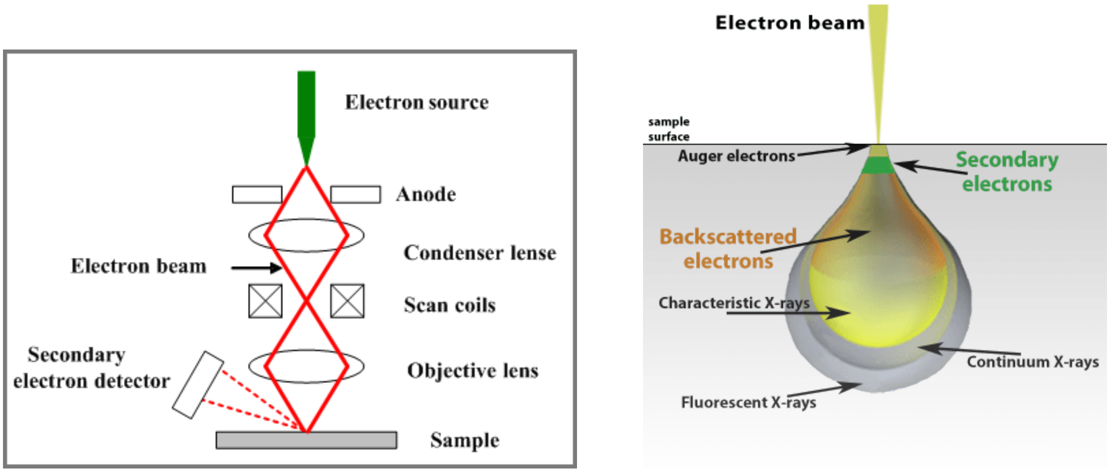

(a) Schematic illustration of SEM components.

(b) Effects of beam interaction on SEM sample.

**Figure 5.9:** *Scanning Electron Microscopy: basic scheme of an SEM apparatus (a) and comparison of penetration depths of the products of the interaction of the electrons with the sample (b).*

### X-Ray Diffraction

Besides Raman spectroscopy, X-ray diffraction (XRD) is a very useful technique to interpret the material internal structure. The basic principle behind X-ray diffraction is Bragg's Law (Eq. 5.6), illustrated in Figure 5.10. X-rays reflected from the adjacent crystal planes will undergo constructive interference only when the path difference between them is an integer multiple of the X-ray's wavelength:

$$n\lambda = 2d\sin\theta \tag{5.6}$$

where $n$ is an integer, $d$ is the spacing between the adjacent crystal planes, $\theta$ is the angle between incident X-ray beam and scattering plane, and $\lambda$ is the wavelength of the incident X-ray.

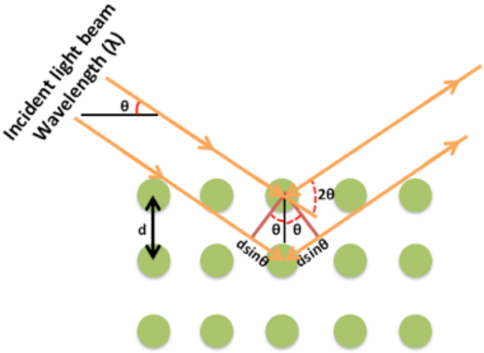

**Figure 5.10:** *Schematic illustration of Bragg's law.*

If viewed in three-dimensions, the reflected/diffracted X-rays form Debye-Scherrer cones that originate from the reflection point and expand to infinity (Figure 5.11(a)).

When a two-dimensional detector intersects these cones, spots tightly jointed in “rings” are observed on a two-dimensional detector image (Figure 5.11(b)). After the data have been collected, corrections for instrumental factors, polarization effects, X-ray absorption, etc are applied to the entire data set. The integration process along the $\gamma$ direction (as indicated in Figure 5.11(b)) converts the raw frame data to a set of individual integrated intensities, which then produce a standard “diffraction pattern”, i.e. a diagram of intensity counts versus $2\theta$ diffraction angles (or d-spacing, in Ångstrom). An example of a 2D diffraction frame and the resulting pattern after integration obtained at the BNL synchrotron light facility using 69 keV synchrotron x-ray beam on an as-received MG-6530Aa sample is shown in Figure 5.12.

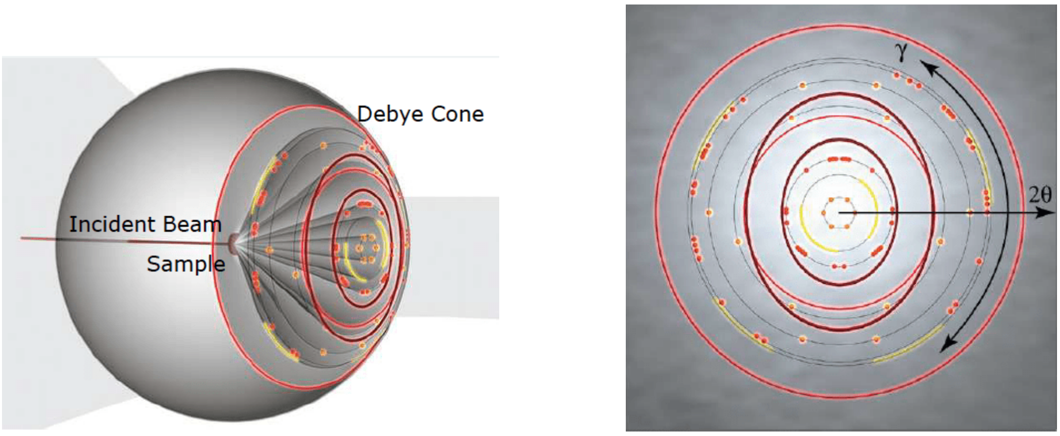

(a) 3D view.

(b) projection on a 2D screen.

**Figure 5.11:** *Illustration of Debye-Scherrer cones in X-ray diffraction, seen in 3D (left) and projected on a 2D screen (right).*

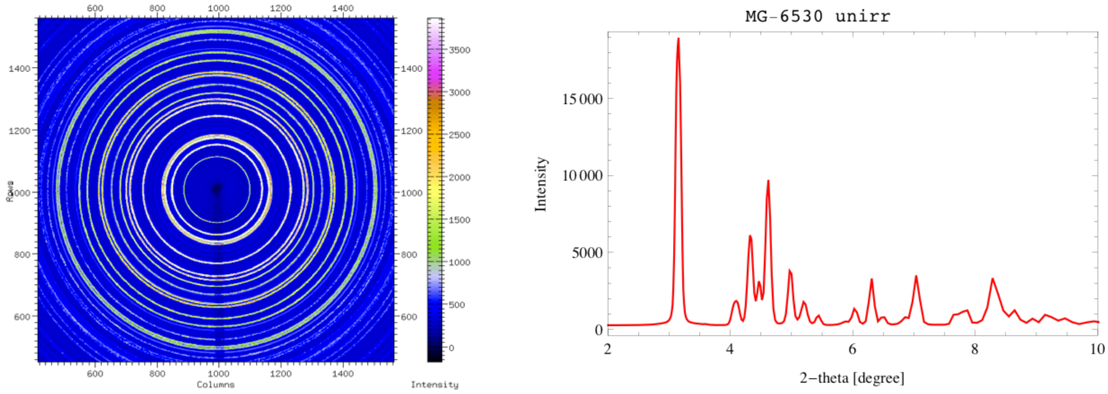

(a) 2D detector image.

(b) Diffraction pattern.

**Figure 5.12:** *XRD image of as received MG-6530Aa sample acquired by a 2D detector at the BNL synchrotron light facility (a), using 69 keV synchrotron x-ray beam, and the resulting diffraction pattern (d).*

From the analysis of the diffranction pattern, we can obtain information on the crystallography, phases, atomic arrangement, grain size, residual stresses and possible texture in the sample.

Most of the laboratory diffractometers employ as incident beam on the sample the Cu $K_\alpha$ radiation ($\lambda = 1.5406$ Å), emitted by a Cu target. XRD measurements can be also performed at synchrotron light source facilities by using x-rays with smaller wavelength. An example is the beamline of the NSLS synchrotron at BNL (Figure 5.13), which uses 69 keV monochromatic x-ray beam with a wavelength of $0.18465$ Å. The

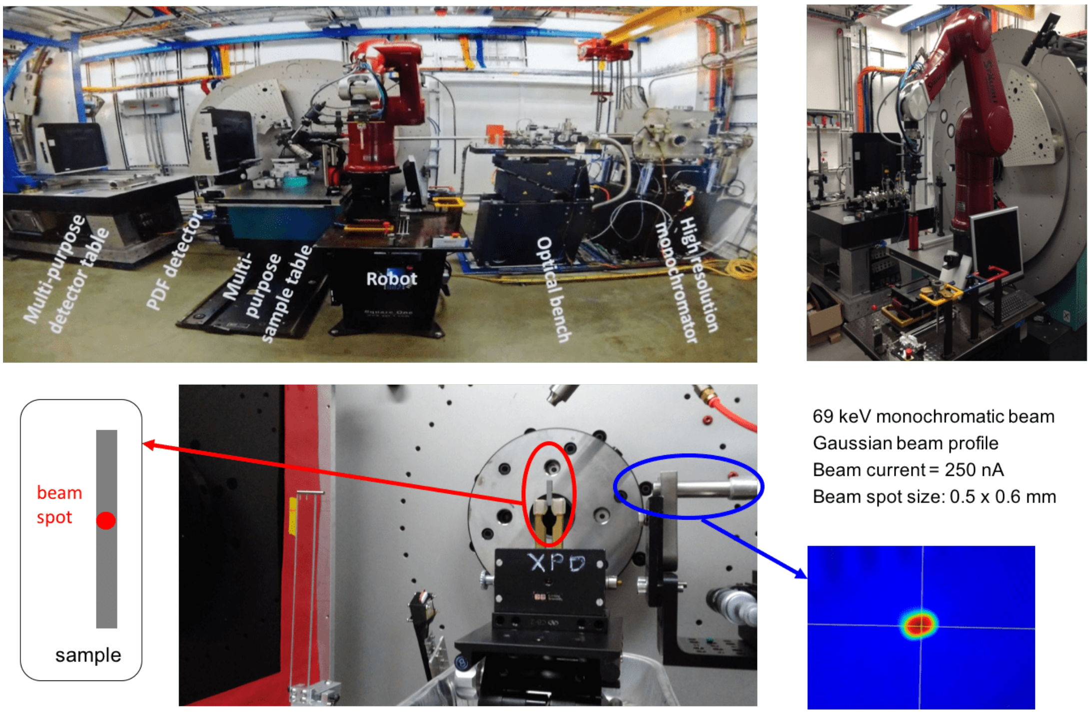

**Figure 5.13:** *Images of the NSLS's beam line for XRD studies.*

Synchrotron X-ray Diffraction allows the user to choose the operational mode (using either the monochromatic or the white beams) and the wavelength from a continuous x-ray spectrum, provides a more intense x-ray beam (which provides higher counting statistic and a better signal-to-noise ratio) and a better spatial precision of the incident/diffracted X-ray beams (i.e. higher resolution).

## 5.2 Experimental characterisation of collimator materials

A complete microscopical and macroscopical characterisation of collimator materials is of fundamental importance in order to understand the properties of the materials and predict the performance of the device in operation. Several experimental activities to characterise the collimator materials have been performed, in particular at the CERN mechanical laboratory, at the NanoLab at Politecnico of Milan, and at the synchrotron facility (NSLS) available at BNL. The study was particularly focused on MoGr and the evolution of its properties within the various generations of grades. Before going into the detail of the measurements, it is useful to remind that MoGr is a transversally isotropic material: in a coordinate system $xyz$, as shown in Figure 5.14, we can define two possible orientations of the samples. "Longitudinal" is referred to the sample that is cut along the x-y plane, therefore the carbon fibers are parallel to the largest surface of the sample. "Transversal" sample, instead, is cut along the z axis and fibers are perpendicular.

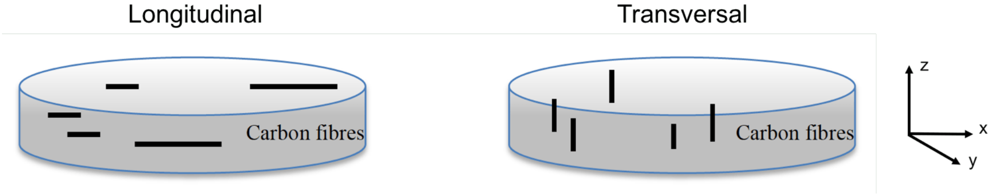

**Figure 5.14:** *Convention used to identify sample directions.*

### 5.2.1 Thermo-mechanical-electrical analysis

The equipment of the CERN mechanical laboratory was used to characterise the macroscopical properties of MoGr. Figure 5.15 illustrates the LFA's measurements of thermal diffusivity and conductivity at room temperature of the most recent grades of MoGr (MG-6530Aa, MG-6403Fc and MG-6403Ga) together with the CFC's. Measurements were performed on 2 mm thick samples, except for MG-6403Fc, for which 5 mm one were available. For materials with such high thermal diffusivity as MoGr, the length of the laser pulse may become comparable with the diffusion time. Therefore, if the thickness is too small and Eq.5.1 is applied, the calculation of the thermal properties might be underestimated. This may be the case for MG-6530Aa and MG-6403Ga samples, for which only smaller samples were available at the time of the measurement. However, the results show that all the measured MoGr grades perform better than CFC. The

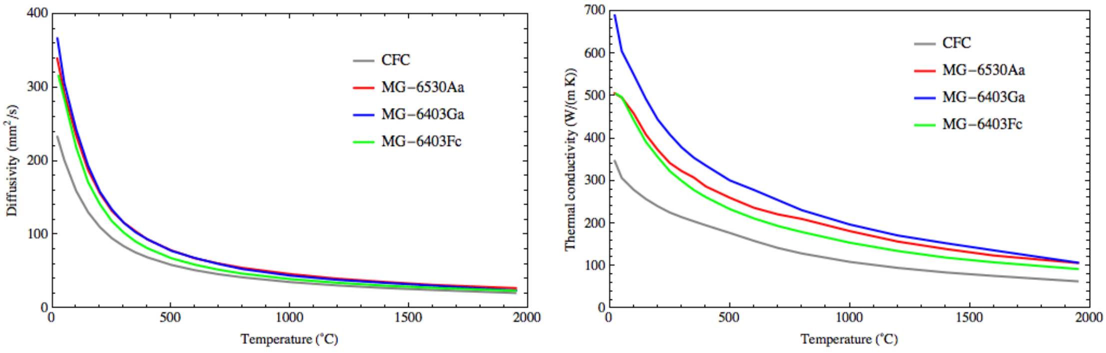

(a) Thermal diffusivity, full temperature range.

(b) Thermal conductivity.

**Figure 5.15:** *Thermal diffusivity and thermal conductivity, given as a function of temperature, of CFC and some MoGr grades, measured with LFA in the most favourable direction (i.e. transversally to the graphite planes), given as function of the temperature.*

specific heat, measured by the DSC apparatus, is shown in Figure 5.16 as a function of temperature up to 1000° C. By comparing the curves, MG-6403Ga and CFC have similar trendThe behaviour of MG-6530Aa and MG-6403Fc is also quite similar but the curves are shifted to smaller values than the others.

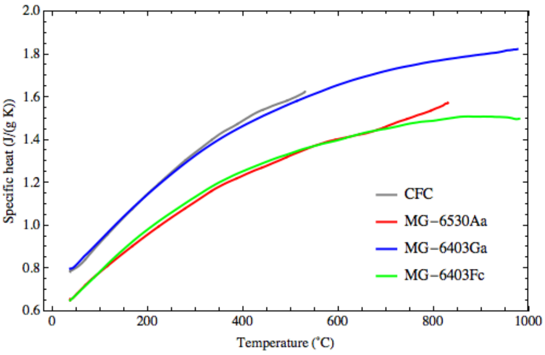

**Figure 5.16:** *Specific heat of CFC and some MoGr grades, measured with DSC in the most favourable direction (i.e. transversally to the basal plane), given as function of the temperature.*

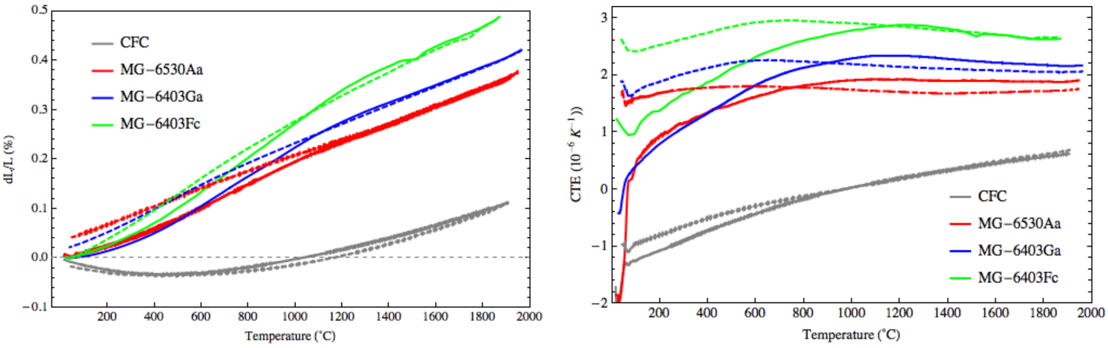

(a) Elongation.

(b) Coefficient of thermal expansion.

**Figure 5.17:** *Dilatometry measurements performed on CFC and MoGr grades. The elongation (a) and the coefficient of thermal expansion (b) of each measured materials are expressed as function of the temperature.*

Dilatometry results of thermal deformation in the longitudinal and transveral samples of CFC and MoGr are shown in Figure 5.17(a). Each color reproduced the elongation achieved by each sample during the heating segment of the thermal cycle (solid line) and the contraction due to the following cooling (dashed line). At the end of the full thermal cycle, CFC and MG-6403Fc almost fully recover their initial dimension, while MG-6403Ga shows a residual unrecovered deformation of 0.02% and MG-6530Aa of 0.04%. Similar differences in the behaviour between the MoGr grades are also expected during irradiation, as radiation acts on the material as a heating process. Therefore, if irradiated, MG-6530Aa should deform more than the others. This would explain the findings from heavy ion irradiation discussed in Chap. 6.3.1. In Figure 5.17(b), the profile of the coefficient of thermal expansion is reproduced during both heating and cooling phases of the thermal cycle .

Comparative results of the four-point bending tests performed on the three MoGr grades are shown in Figure 5.18. In the longitudinal direction (Figure 5.18(a)), MG-

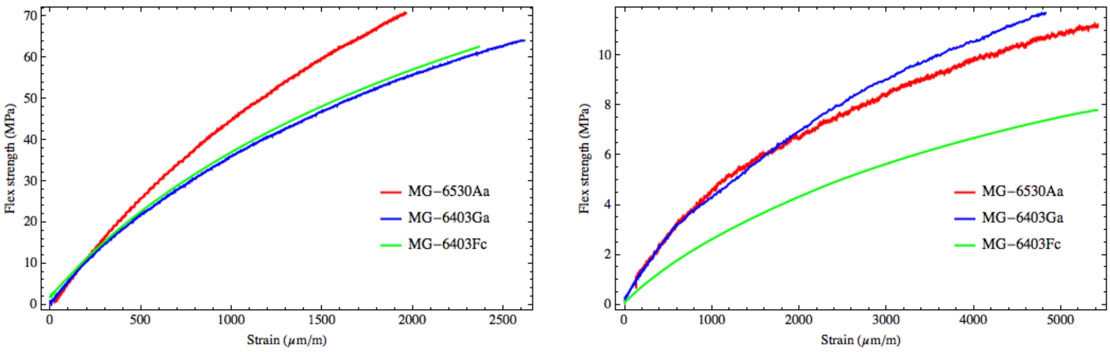

(a) Longitudinal orientation.

(b) Transversal orientation.

**Figure 5.18:** *Four-point bending test performed on three MoGr grades in different sample orientations, longitudinal (a) and transversal (b).*

6530Aa has the highest value of flexural strength but also highest Young's modulus, while MG-6403Fc and MG-6403Ga feature similar behaviours but lower stress than the other grade and larger strain to failure, which means lower elastic modulus. Transversally (Figure 5.18(b)), that is the weak direction from the mechanical point of view, MG-6403Ga shows the stiffest curve, closely followed by the MG-6530Aa one. In this direction, MG-6403Fc differs from MG-6403Ga, showing smaller failure strength but higher Young's modulus. Tables 5.1 and 5.2 summarise, respectively, the thermal and the mechanical properties of CFC and three MoGr grades. The values are listed for both sample orientations.

**Table 5.1:** *Summary of thermal properties of CFC and MoGr. Values of thermal conductivity, thermal diffusivity, and specific heat are measured at room temperature (RT= 20 °C), while CTE is averaged between RT and 1000 °C.*

| Material | Diffusivity ($mm^2/s$) | | Thermal cond. (W/mK) | | Specific heat (J/gK) | CTE $10^{-6}$ ($K^{-1}$) | |
|---|---|---|---|---|---|---|---|
| | $\parallel$ | $\perp$ | $\parallel$ | $\perp$ | - | $\parallel$ | $\perp$ |
| CFC | 226.8 | 40.4 | 304.4 | 54.2 | 0.785 | 0.03 | 11.64 |
| MG-6530Aa | 325.4 | 31.4 | 489.9 | 47.2 | 0.601 | 1.74 | 15.33 |
| MG-6403Ga | 363.7 | 37.0 | 547.0 | 55.7 | 0.604 | 2.24 | 12.49 |
| MG-6403Fc | 465.5 | 31.3 | 737.8 | 49.6 | 0.624 | 2.82 | 10.98 |

The electrical resistivity of CFC and MoGr grades have been measured by means of the four-wire method. The measurements have been carried out on bar-type specimens with face dimensions of 10 mm×5 mm. The results obtained in the longitudinal and transversal directions are summarised in Table 5.3. As expected for 2D-graphite-based materials, the electrical properties in the longitudinal direction are better than those in the transversal one, thanks to the delocalised carbon electrons that are free to move in the basal plane (see Chap. 4). About a factor 5 lower electrical resistivity, i.e. higher electrical conductivity, is measured in the MoGr grades with respect to CFC. In particular, the grade MG-6403Ga turns to perform better than the other ones, with an electrical

**Table 5.2:** *Summary of mechanical properties of CFC and MoGr, for both sample orientations.*

| Material | Flexual strength (MPa) | | Strain to failure ($\mu$m/m) | | Elastic modulus (GPa) | |
|---|---|---|---|---|---|---|
| | $\parallel$ | $\perp$ | $\parallel$ | $\perp$ | $\parallel$ | $\perp$ |
| CFC | $104.2 \pm 3$ | $10.3 \pm 0$ | $1995 \pm 406$ | $4287 \pm 312$ | 62 | - |
| MG-6530Aa | $70.9 \pm 3$ | $12.0 \pm 0$ | $2501 \pm 547$ | $7244 \pm 1771$ | 76.7 | 4.7 |
| MG-6403Ga | $73.5 \pm 7$ | $11.6 \pm 0$ | $2643 \pm 279$ | $4431 \pm 308$ | 74.2 | 3.8 |
| MG-6403Fc | $58.1 \pm 8$ | $10.0 \pm 1$ | $2430 \pm 498$ | $4344 \pm 1010$ | 60.4 | 4.0 |

conductivity in the best direction close to 1 MS/m.

**Table 5.3:** *Summary of electrical resistivity measurements of CFC and MoGr performed using the four-wire setup in both sample orientations.*

| Material | Electrical resistivity ($\mu\Omega$ m) | | Electrical conductivity (MS/m) | |
|---|---|---|---|---|
| | $\parallel$ | $\perp$ | $\parallel$ | $\perp$ |
| CFC | 5.43 | 29.10 | 0.18 | 0.03 |
| MG-6530Aa | 1.2 | 20.8 | 0.83 | 0.05 |
| MG-6403Ga | 1.1 | 12.7 | 0.88 | 0.08 |
| MG-6403Fc | 1.1 | 14.4 | 0.91 | 0.07 |

### 5.2.2 Microscopical characterisation

#### Scanning Electron Microscopy

Several observations of the microstructure of MoGr were performed at the CERN metallurgy laboratory, aiming at studying he morphology and the distribution of the phases inside the material. Figure 5.19 shows some images from the analysis carried out on MG-3110P grade. The bright spots on the darker background are molybdenum carbides precipitated on the graphite matrix. The distribution of the carbides appears quite regular. The presence of agglomerates of carbon fibers is visible in both the longitudinal and the transversal planes. In particular, the electron-backscattered image in Figure 5.19(d) shows clearly the agglomeration of partially sintered fibers surrounded by small carbide particles.

Grade MG-5220S was observed at the SEM and the images in Figure 5.20 show that no relevant inhomogeneity in the distribution of molybdenum carbides is found. The precipitates appear to be well melted in the matrix after the sintering. The length of the precipitate is between 5 and 10 $\mu$m. Cavities due to graphite detachment after sample cutting are also visible. EDS analysis was performed in a selected area of the sample in order to investigate the chemical composition of the compound. A chemical mapping is reproduced in Figure 5.21(a): the red color dominates and represents mainly the graphite matrix and the carbon component of the carbides, while in green the contribution of molybdenum is shown. The line scan of Figure 5.21(b) how the mass fraction of the two components, i.e. carbon and molybdenum, varies along the scan. As expected,

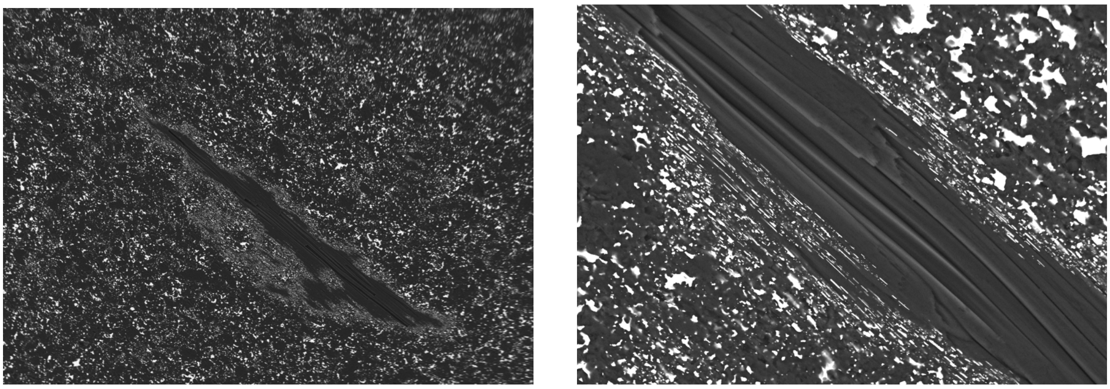

(a) Longitudinal sample, magnification 100x, SE detector.

(b) Longitudinal sample, magnification 550x, QBSD detector.

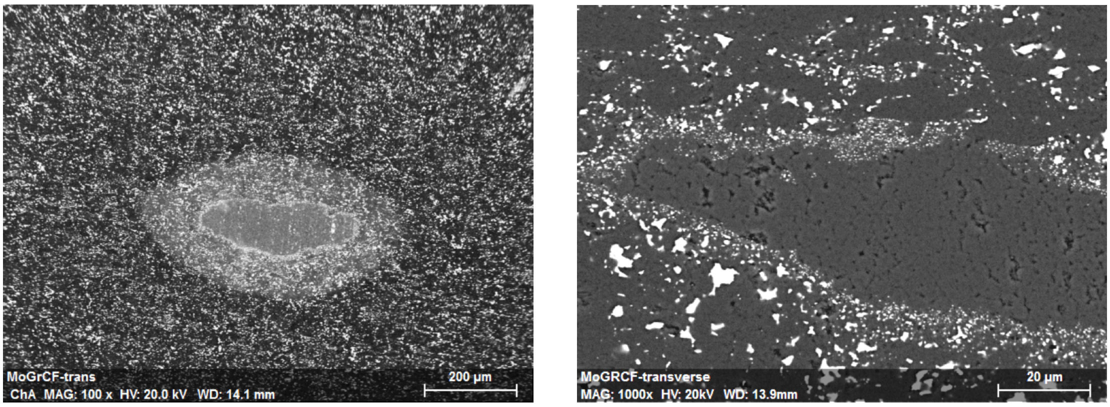

(c) Transversal sample, magnification 100x, SE detector.

(d) Transversal sample, magnification 100x, QBSD detector.

**Figure 5.19:** *Agglomeration of carbon fibers in grade MG-3110P observed with two different detectors in the longitudinal sample (a-b) and the transversal one (c-d).*

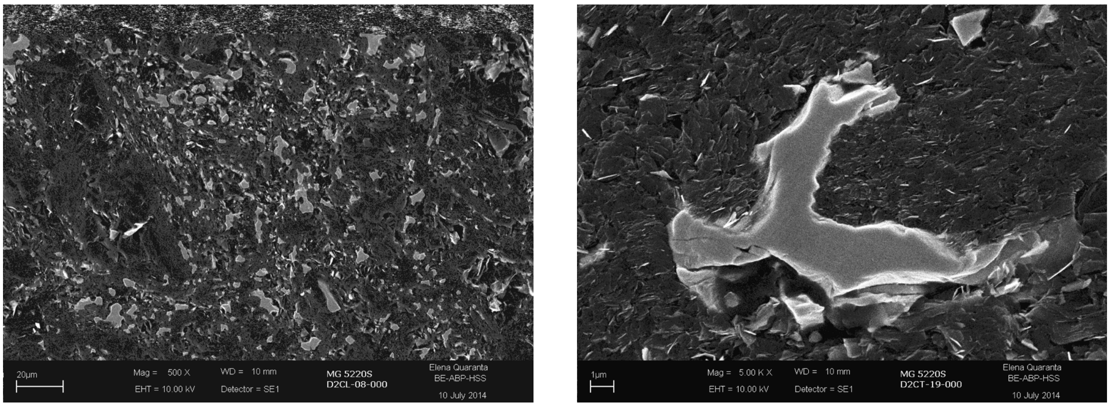

(a) Longitudinal direction, magnification 500x: distribution of $Mo_2C$ grains in the graphite matrix.

(b) Transversal direction, high magnification: Mo-carbide.

**Figure 5.20:** *SEM images with different magnification of grade MG-5220S: longitudinal sample with low magnification (a) and transversal sample with higher magnification.*

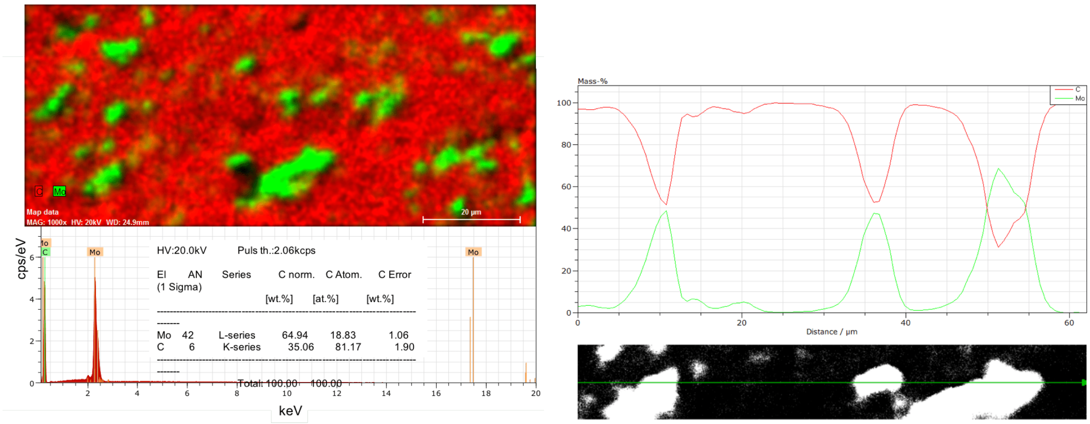

```
HV:20.0kV        Puls th.:2.06kcps

El      AN      Series        C norm.   C Atom.    C Error
(1 Sigma)
                              [wt.%]    [at.%]     [wt.%]
------------------------------------------------------------------
-------
Mo   42       L-series       64.94     18.83        1.06
C      6        K-series       35.06     81.17        1.90
------------------------------------------------------------------
-------
                    Total: 100.00    100.00
```

(a) Chemical element mapping.

(b) Line scan.

**Figure 5.21:** *EDS analysis of a transversal sample of MG-5220S grade.*

the peaks of molybdenum concentration stick out when the scan crosses the carbides, while the percentage of carbon is maximum in the matrix.

A comparison of the latest generation of MoGr grades is illustrated in Figure 5.22. In each row, the pictures belong to MG-6530Aa, MG-6403Fc and MG-6403Ga, respectively. In the top row, backscattered electron images show the distribution of the carbide particles in the graphite matrix, which appears quite homogeneous in all grades. The second and the third row of images are taken with the in-lens detector. Such detector is generally located inside the electron column of the microscope, where secondary electrons are collected with high efficiency due to a sophisticated magnetic field at the pole piece. In particular, at low voltages and small working distances, images with high contrast can be obtained. We used the information collected by this detector to look at the size of graphite crystallite, which can be estimated around 20$\mu$m. Thus, from a morphological and topological point of you, the three grades do not shown relevant differences. The EDS analysis confirms that MG-6403Fc and MG-6403Ga are very similar also from the chemical point of view, as expected as they have same composition. The analysis reveal the presence of the small fraction of titanium content added at the composition of MoGr grades from the $6^{th}$ generation on (Figures 5.23(b) and 5.23(c)), while in the case of MG-6530Aa such element do not appear in the spectrum of Figures 5.23(a).

### Raman spectroscopy

Optical microscopy and Raman spectroscopy measurements were performed in the NanoLab (Politecnico of Milan) on MG-6530Aa in order to take a closer look to the crystalline structure in the as-received material. The tests were carried out by means of a Renishaw spectrometer with optical microscope. A preliminary observation with low magnification of a larger portion of the sample surface is reproduced in Figure 5.24. Black and bright areas are determined by the more or less absorption of the incoming light beam: porosity, cracks or grain borders, for example, give rise to black zones, while crystal phase appear usually brighter. The analysis of Raman spectra in different

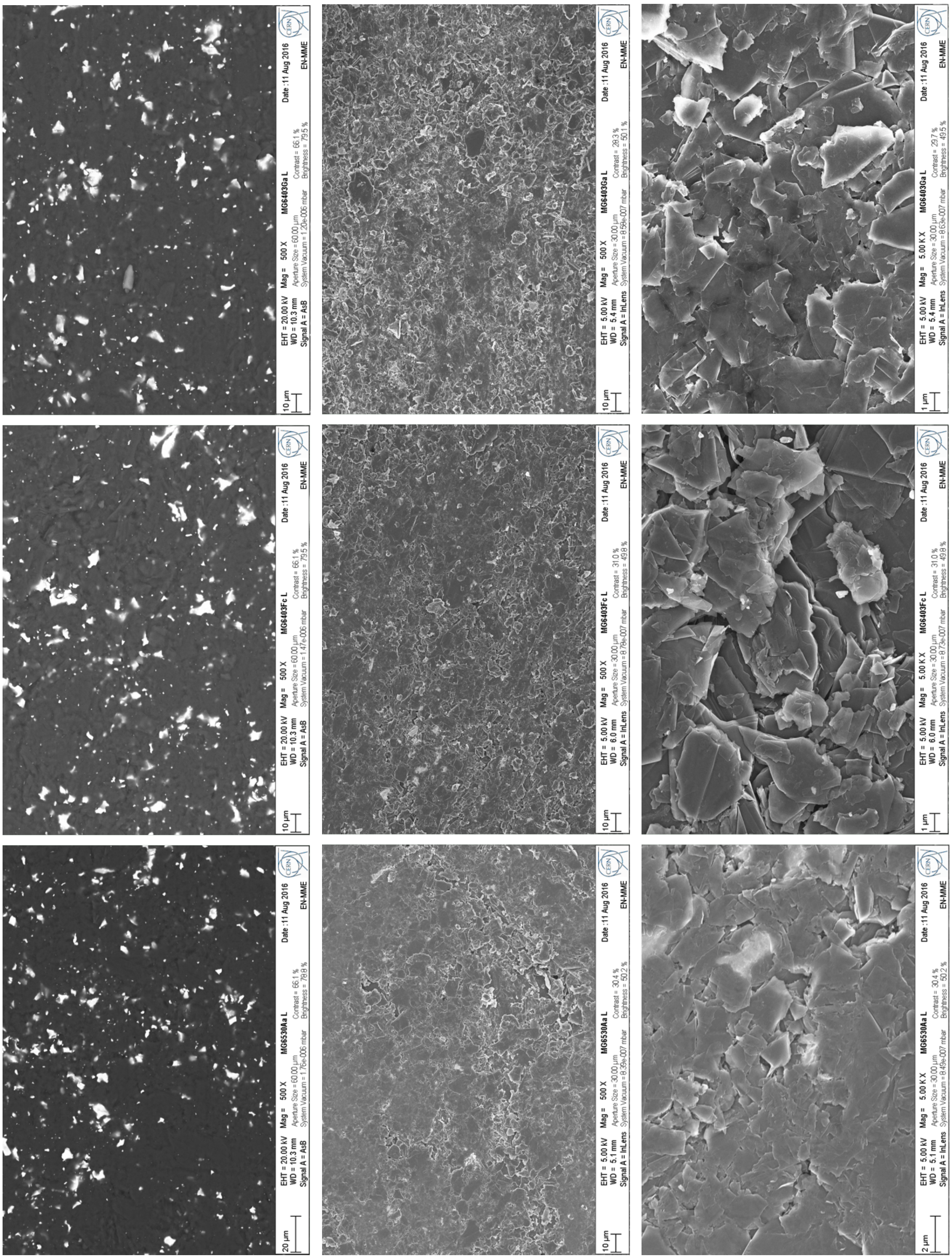

(a) (b) (c)

**Figure 5.22:** *QBSD images (a) and InLens (b-c) images of different MoGr grades. In each row, from left to right: MG-6530Aa, MG-6403Fc and MG-6403Ga.*

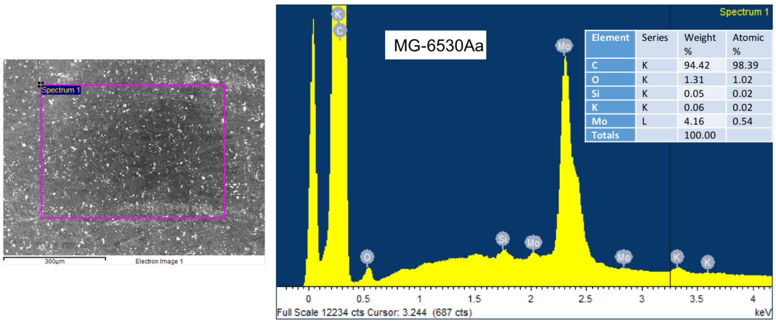

| Element | Series | Weight % | Atomic % |
|---|---|---|---|
| C | K | 94.42 | 98.39 |
| O | K | 1.31 | 1.02 |
| Si | K | 0.05 | 0.02 |
| K | K | 0.06 | 0.02 |
| Mo | L | 4.16 | 0.54 |
| Totals | | 100.00 | |

(a) EDS spectrum of MG-6530Aa.

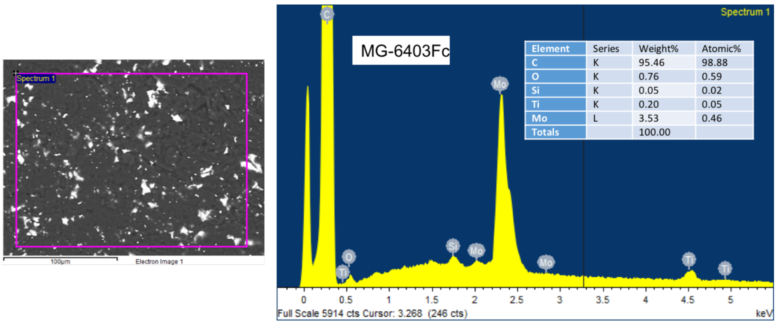

| Element | Series | Weight% | Atomic% |
|---|---|---|---|
| C | K | 95.46 | 98.88 |
| O | K | 0.76 | 0.59 |
| Si | K | 0.05 | 0.02 |
| Ti | K | 0.20 | 0.05 |
| Mo | L | 3.53 | 0.46 |
| Totals | | 100.00 | |

(b) EDS spectrum of MG-6403Fc.

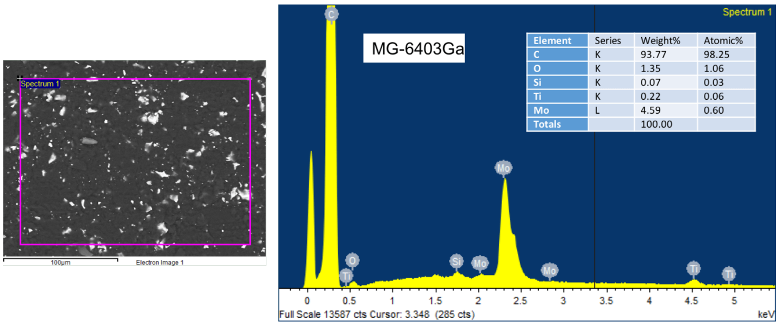

| Element | Series | Weight% | Atomic% |
|---|---|---|---|
| C | K | 93.77 | 98.25 |
| O | K | 1.35 | 1.06 |
| Si | K | 0.07 | 0.03 |
| Ti | K | 0.22 | 0.06 |
| Mo | L | 4.59 | 0.60 |
| Totals | | 100.00 | |

(c) EDS spectrum of MG-6403Ga.

**Figure 5.23:** *EDS analysis of different MoGr grades.*

position inside the sample reveals the presence of “all grades” of graphite in the sample of MG-6530Aa:

- Perfect graphite, due to the presence of the G (”Graphite”) first-order peak and the 2D peaks of the higher vibrational orders (intensity ratio of 1:2). Figure 5.25.
- Polycrystalline graphite, where D and D’ (”Defect”) peaks appear, and the intensity ratio of the 2D peaks differs from 1:2. Figure 5.26.
- Polycrystalline graphite and disorder, which induces a broadening of the peaks. Figure 5.27.
- Polycrystalline graphite, disorder and metal-carbide (Figure 5.28): the presence of a metallic component in the Mo-carbides produces a further broadening and modification of the peak shape. New peaks that can be associated to Mo-carbides

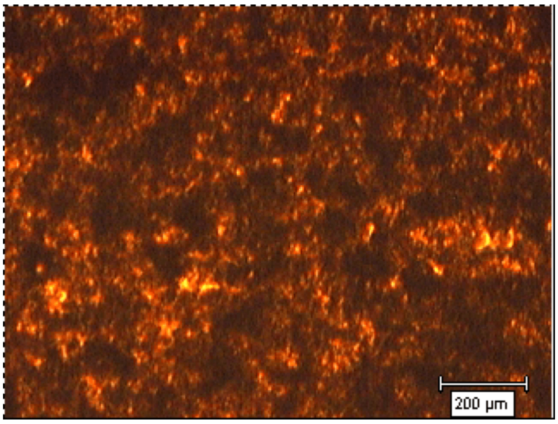

**Figure 5.24:** *Optical microscope image of MG-6530Aa*

are visible. Note that, metals are not Raman active, as well as most of carbides. Therefore, it was not possible to retrieve Raman spectra from MoC and $Mo_2C$ in order to fully identify the new peaks.

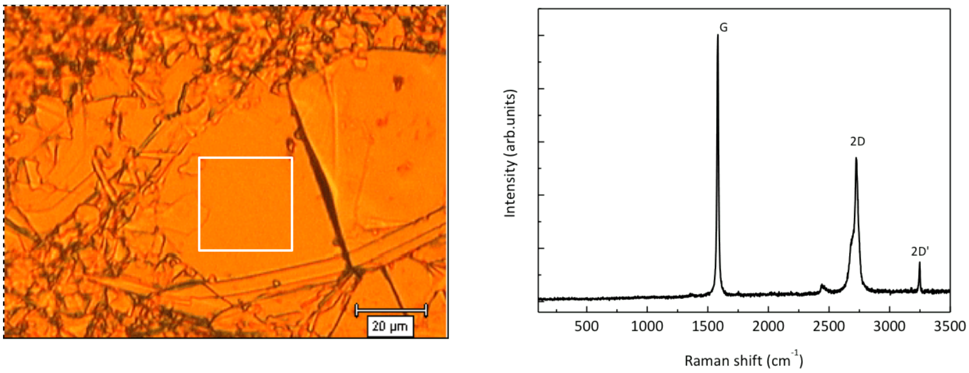

**Figure 5.25:** *Optical microscope image (left) and Raman spectrum (right) of perfect graphite in MG-6530Aa.*

#### X-ray Diffraction

One of the most challenging part of the MoGr characterisation was the identification of the different phases present in the compound, especially those of the carbides. First XRD measurements on MG-6530Aa were carried out at the NanoLab (Politecnico of Milan) with the Panalytical X'Pert PRO X-Ray diffractometer, which uses the $K_\alpha$ line of Cu. As shown in Figure 5.29, the most intense peaks are attributable to crystalline graphite, while less intense peaks correspond to molybdenum carbides. In particular, hexagonal MoC and hexagonal $Mo_2C$ were identified, however the relative intensities of the peaks attributed to carbides are different from literature. No traces of metallic Mo were found.

A comparative diffraction analysis of different MoGr grades was performed at the

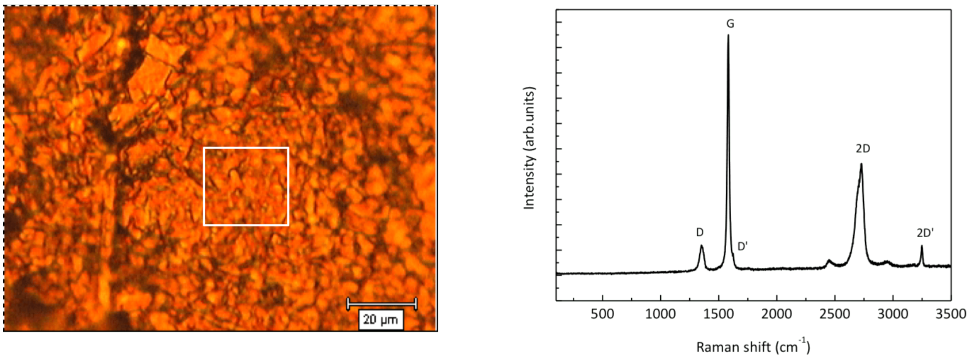

**Figure 5.26:** *Optical microscope image (left) and Raman spectrum (right) of polycrystalline graphite in MG-6530Aa.*

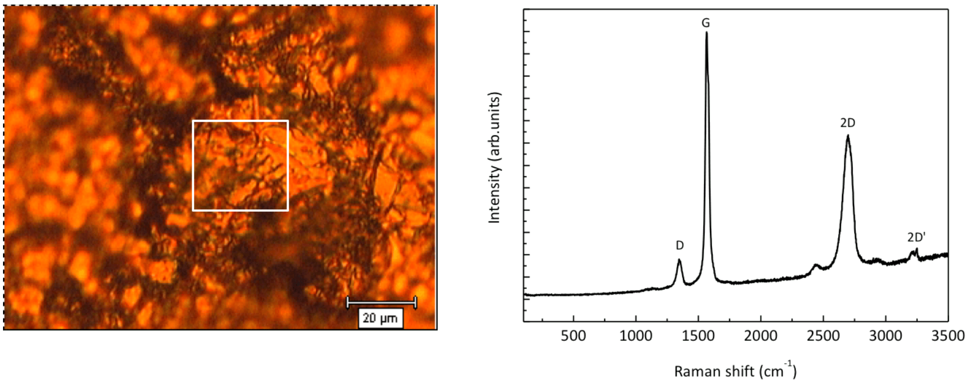

**Figure 5.27:** *Optical microscope image (left) and Raman spectrum (right) of polycrystalline graphite with disorder feature in MG-6530Aa.*

dedicated beamline 28ID of the NSLS II synchrotron at BNL for 2D-XRD technique, and the resulting patterns are compared in Figure 5.30. As expected, graphite peaks are visible in all the samples, but the carbide phases present are not the same for all the grade. In the first two patterns (grade MG-1110E and MG-6530Aa), there is the evidence of $Mo_2C$ and MoC phases, both with hexagonal crystal structure. On the other hand, the patterns of more recent grades (MG-6403Ga and Fc) show peaks related only to the cubic MoC carbide (or $MoC_{1-x}$). The addition of a small quantity of titanium in the composition of these grades stabilises the cubic MoC carbide phase until room temperature, conversely from the case of the binary Mo-C phase diagram, where MoC phase is not stable below 2237 K. This finding has important implications: if MG-6403 grades are exposed to temperature increase, e.g. during irradiation, phases initially present in the component are not expected to change as consequence of heating.

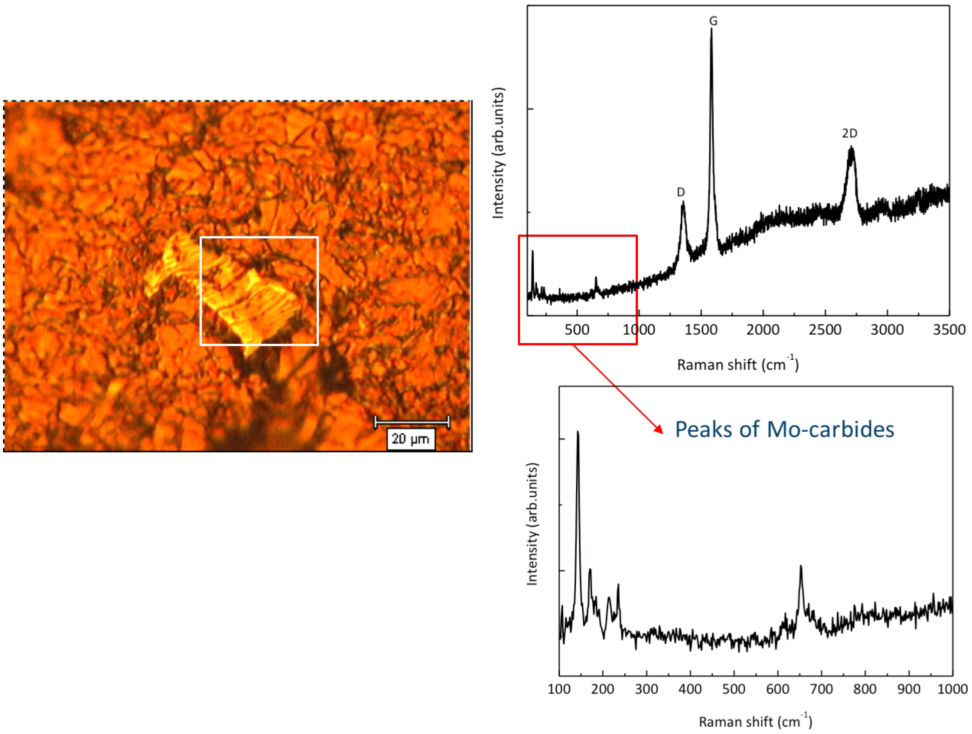

**Figure 5.28:** *Optical microscope image (left) and Raman spectrum (right) of disordered polycrystalline graphite and Mo-carbides in MG-6530Aa.*

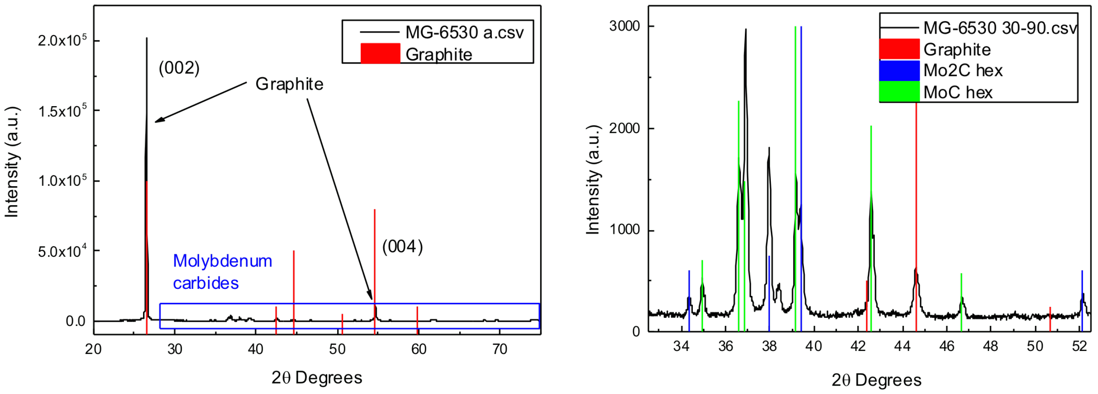

(a) Full interval of $2\theta$ angles.

(b) Zoom in a shorter $2\theta$ interval.

**Figure 5.29:** *XRD spectrum of MG-6530Aa grade performed at NanoLab (Politecnico of Milan).*

### Effect of MoGr sample cutting orientation on XRD spectra

The effect of different cutting orientations of MoGr samples was studied with the diffraction technique using synchrotron X-rays. Specimens of various MoGr grades were tested with x-ray beam impacting on either of the three directions $L_1$, $L_2$, $T$, and the resulting diffraction patterns were compared. Figures 5.32 and 5.33 show the

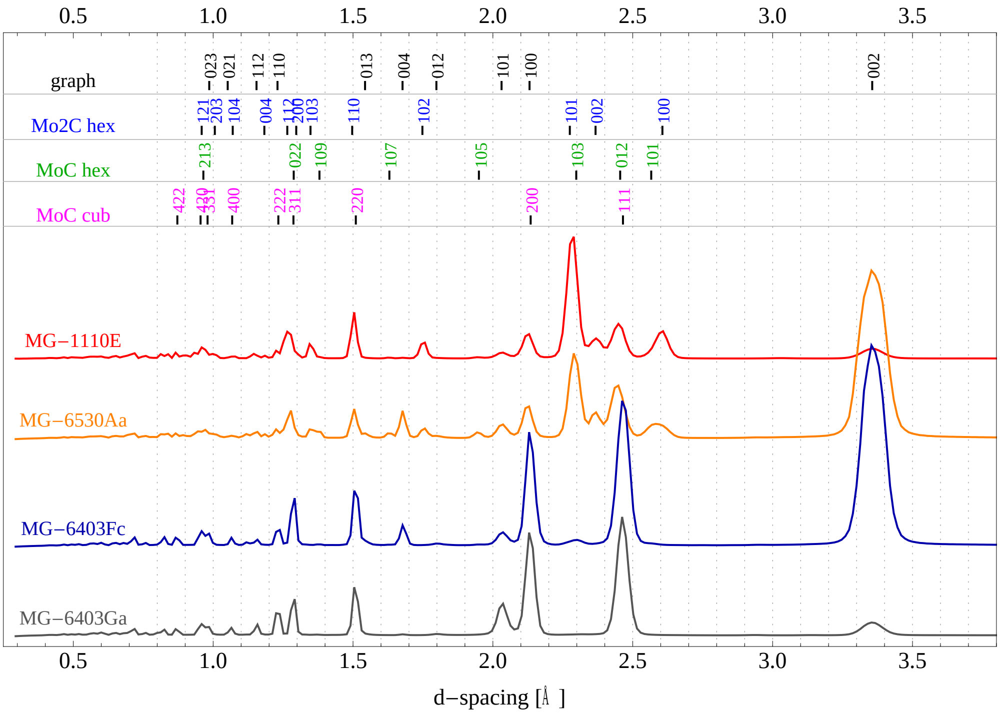

**Figure 5.30:** *XRD spectra of different MoGr grades using the synchrotron x-ray beam at BNL.*

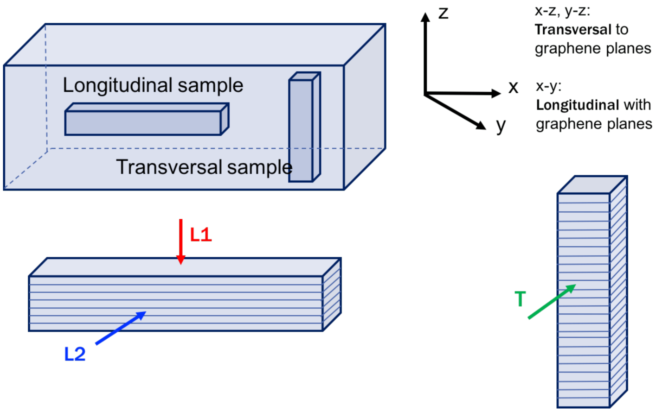

**Figure 5.31:** *Cutting orientation of MoGr and different x-ray irradiation directions.*

spectra of two grades (MG-6403Ga and Fc) that are, by composition, identical (only the atmosphere of the production cycle differs): as expected, the visible peaks in the diffraction pattern are the same. What it is interesting to notice is that in both cases the $L_2$ and $T$ patterns look very similar, almost superposed, while that of $L_1$ differs in some peaks, such as the C (002) and C (004) reflections. When the x-ray beam impacts the sample along $L_2$ or $T$, it passes in between the graphene planes, so the resulting diffraction patterns are expected to be very similar, since the incoming beam sees the same structure in both cases. When coming from $L_1$, the X-ray beam passes through the graphene planes and reflections of planes parallel to the basal plane, i.e. (00x), do not appear or have very low intensity. This is in line with the orthotropic nature of the composite. We recall that (002) and (004) graphite reflections correspond to that of two planes belonging to the same family of parallel planes {001} in equivalent lattice structures but with an out-of-phase distance between them in the vertical direction (third Miller index) of 1/2, for the (002), and 1/4, for the (004), of the interplanar spacing of the original (001).

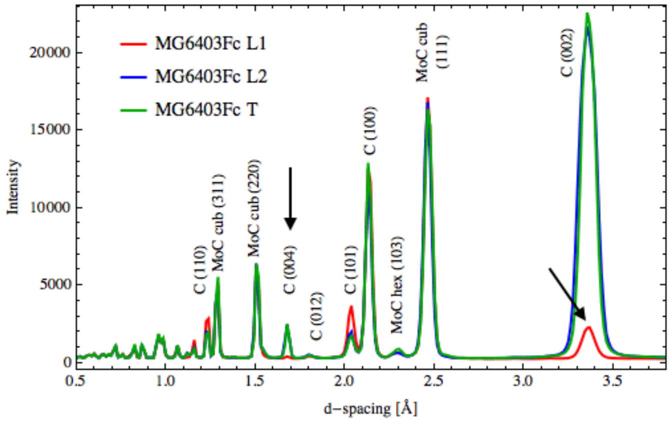

**Figure 5.32:** *XRD pattern of MG-6403Fc using synchrotron x-ray beam for different sample orientations.*

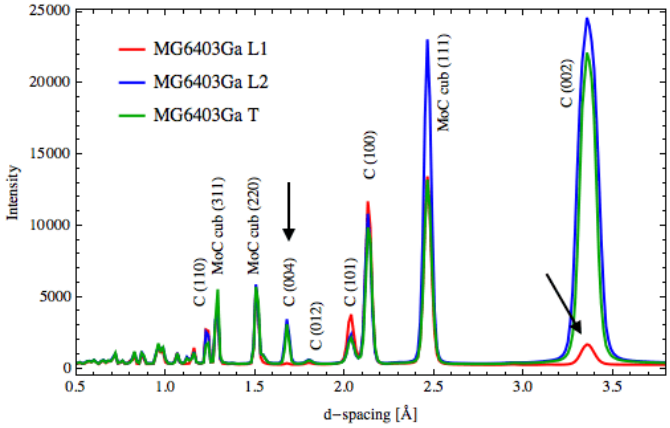

**Figure 5.33:** *XRD pattern of MG-6403Ga using with synchrotron x-ray beam for different sample orientations.*

Established that diffraction tests along $L_2$ or $T$ provide similar information, in Figure 5.34 the patterns of $L_1$ or $T$ orientated samples of MG-6530Aa grade are illustrated. The two diffraction spectra show large differences. For example, the intensity of the $Mo_2C$ peaks in the $T$ sample is generally higher than the $L_1$ case. This effect can be explained by the presence of carbides with a high degree of texture. In general, the term texture refers to the distribution of crystallographic orientations of a polycrystalline sample. If the orientations are fully random, the sample has no texture. If the crystallographic orientations are not random, but have some preferred orientation, then the sample has a certain degree of texture, depending on the percentage of crystals hav-

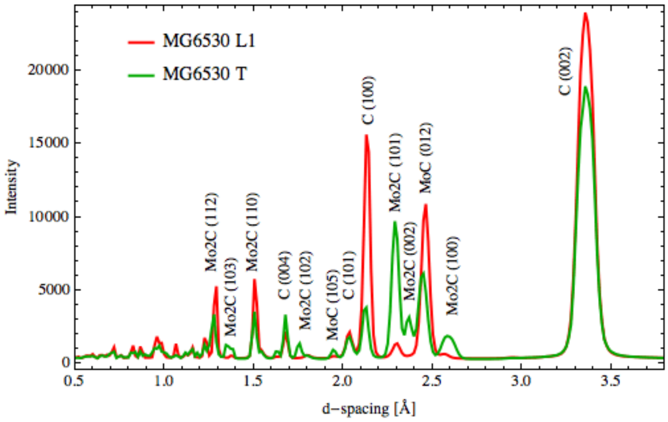

**Figure 5.34:** *XRD pattern of MG-6530Aa using synchrotron x-ray beam for different sample orientations.*

ing the preferred orientation. Graphite is known to orient in the space according to preferred directions. According to Ref [85, 86], in a crystalline structure hosting $Mo_2C$ and graphite, these carbides tend to arrange according preferred orientations with respect to graphite. A coherent interface arises when two crystals match perfectly at the interface plane so that the two lattices are continuous across the interface. If the graphite lattice bonds to the Mo2C crystal at about 19 °, there is an atomic match for every other graphite basal plane with the carbon sublattice. The evidence of texture in the diffraction spectrum of MG-6530Aa is a hint of the presence of coherent bonds between $Mo_2C$ and carbon atoms of graphite. Other types of Mo-carbides are less affected by this texture effect.

## 5.3 Experimental test of novel materials under high energy beam impact

The new concepts of primary and secondary collimators for HL-LHC upgrade are being reviewed to significantly reduce the impedance contribution from the collimation system, maintain, or possibly increase, the robustness of the present design and minimise the effect of high radiation doses. New jaw concepts mostly rely on the novel composite materials. However, the final material choices for the collimator upgrade require extensive characterisation campaigns of new materials under different beam irradiation regimes.

During accelerator operations, collimators are continuously exposed to irradiation, owing to their proximity to the circulating beams [87]. Long-term exposure to radiation has the potential to alter the microstructure of the materials, through formation of defects and trapping of gases. Degradation of material properties, reduced capacity of the device to perform its functions and premature failure can be envisaged as a result of collimator irradiation. On the other hand, collimator materials might also be exposed to short, high-intensity beam impacts, as a consequence of accidental scenarios: thermal effects caused by the direct energy deposition of the beam particles are thus induced to the material. Since the duration of the particle impact is in the order of microseconds or even shorter, the heating of the impacted material proceeds in time during which the heat conduction is negligible. Therefore mechanical stresses are created by this rapid non-uniform temperature increase [88, 89]. While effects from exposure to high radiation doses are extensively discussed in Chap. 6, we report here highlight results of impact tests from high intensity beams on the collimator materials.

Over the last 10 years, several beam-impact tests on collimators and collimator materials were performed to explore the consequences of failure scenarios on materials and equipment. At the LHC, the loss of a full injection batch is considered the most severe failure event for collimator survival. LHC injection error experiments were carried out in 2004 and 2006 on fully assembled jaws and validated the final design of the present primary and secondary collimators [70, 90]. In both tests, the CFC jaw blocks survived the impact of a full LHC injection train (288 bunches, 1.1 $\times 10^{11}$ p/b at 440 GeV with $\sigma$=0.35 mm). However, for HL-LHC operation, the injection train is expected to double its intensity with an even smaller emittance: the destructive potential of the injection error will then increase accordingly. In this respect, it is crucial to validate new collimator designs with beam experiments, along with novel designs, also existing secondary (or primary) collimator jaws to ascertain their robustness against High Luminosity beam parameters.

A recent experiment (called HRMT-23) was run in July 2015 to demonstrate the validity of the design of HL-LHC secondary collimator. The unique CERN HiRadMat facility [63] hosted the test: this facility provides high-intensity pulsed proton beam, extracted from the SPS, to an irradiation area where material samples and various accelerator devices can be tested. The test bench (Figure 5.35) is composed by a stainless steel vessel, under vacuum (pressure $> 10^{-3}$ mbar) to avoid potential contamination of the facility with the debris caused by the beam impacts. The vessel features six CFC-reinforced beryllium beam windows, three at the entrance and three downstream. It is equipped with radiation-hard optical glasses, to allow the visual inspection of the jaws during and after the experiment. An holder supports the three collimator jaws, which are:

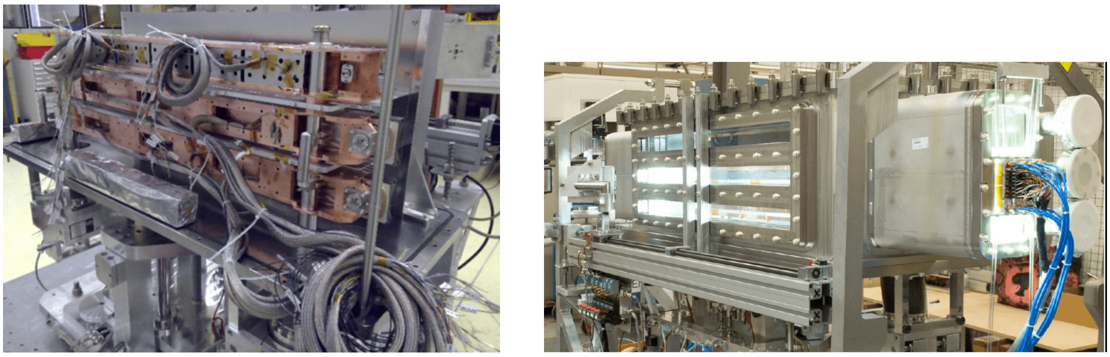

(a) Three-jaw stack.

(b) Assembly.

**Figure 5.35:** *Test bench of HRMT-23 experiment (a), allocating the three full collimator jaws (b).*

- HL-LHC Secondary Collimator Jaw (TCSPM) with 10 MoGr (grade MG-6530Aa) inserts of $100 \times 45 \times 25$ mm each (Figure 5.36(a)).

- HL-LHC Secondary Collimator Jaw (TCSPM) with 10 CuCD inserts of $100 \times 45 \times 25$ mm each (Figure 5.36(b)).
- TCSP jaw with one single block of $1054 \times 80 \times 25$ mm made of CFC AC-150K as active material (Figure 5.36(c)).

Each jaw is instrumented to allow as much complete as possible an online characterization, e.g. monitoring of temperature, residual strains and displacements, cooling water pressure spikes, etc.

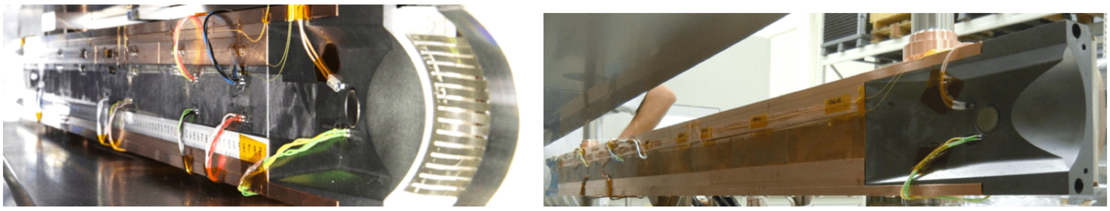

(a) MoGr jaw.

(b) CuCD jaw.

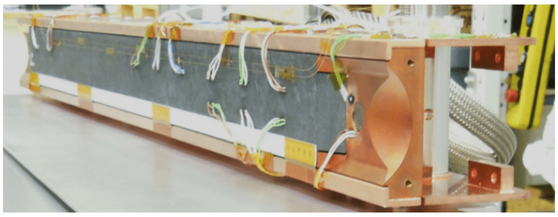

(c) CFC jaw.

**Figure 5.36:** *Collimator jaws instrumented for the HRMT-23 experiment.*

The HRMT-23 experiment was designed to assess the resistance of the HL-LHC jaws against two worst-case failure scenarios [91]:

- CuCD jaw, for tertiary collimators, against asynchronous beam dump resulting in 1 bunch at 7 TeV impacting the jaw,
- MoGr and CFC, for secondary collimators, against beam injection error implying the impact of 288 bunches at 450 GeV.

The beam energy and bunch population of the SPS cannot match the HL-LHC scenario. However, the threshold of damage in the absorbers depends more on the energy density rather than on the total deposited energy [92]. The energy densities of the above failure scenarios were achieved by reducing the beam size (e.g. from the 0.61 mm of the HL-LHC scenario to 0.35 mm at the maximum SPS intensity). A summary of the irradiation parameters is given in Table 5.4.

Up to 288 bunches (LHC injection batch), for a total intensity of $3.8 \times 10^{13}$ protons at 440 GeV, were extracted in a single kick and sent onto the jaws in CFC and MoGr to compare their robustness. The total pulse length was 7.8 $\mu$s. The CuCD jaw, instead, was exposed to impact of 24 bunch trains (roughly equivalent to one single LHC bunch at 7 TeV, reference scenario for TCT robustness evaluation [92]). Due to the high activation level, the opening of the tank was authorised by the radioprotection group only

**Table 5.4:** *HRMT-23 irradiation parameters.*

| Parameter | Unit | Value |
|---|---|---|
| Beam energy | [GeV] | 440 |
| Beam spacing | [ns] | 25 |
| Maximum beam intensity | [p] | $1.3 \times 10^{11}$ |
| Pulse intensity (1 to 288 bunches) | [p] | $1.3 \times 10^{11}$ to $3.8 \times 10^{13}$ |
| Beam size ($\sigma$) | [mm] | 0.35 to 1 |
| Impact depth | [mm] | 0.18 to 5 |
| Total pulses | [-] | 150 |
| Total bunches | [-] | 8450 |
| Total n. protons | [-] | $\sim 1 \times 10^{15}$ |

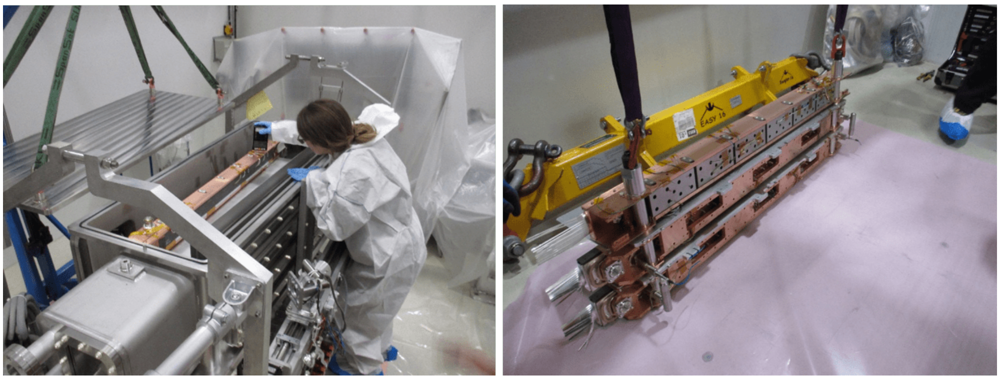

**Figure 5.37:** *Opening of the vacuum vessel of HRMT-23 and extraction of the three tested jaws.*

in November 2016, when the tank showed acceptable value of dose rate ($\sim 80\mu$Sv/h at contact). Figure 5.37 illustrates some phases of the dismounting procedure of the test bench and the extraction of the jaws. The status of the three jaws after the opening of the tank is illustrated in Figure 5.38. From a visual inspection of the jaws after the test, we can say that:

- CFC jaw looks undamaged: only some beam trace on the surface is visible, but no external sign of failure (Figure 5.38(a))
- MoGr jaw looks undamaged: there is a scratch provoked by the beam on the surface (10-20$\mu$m depth), but no sign of failure (Figure 5.38(b))
- CuCD jaw shows grooves, locally melted in the inside, generated by the higher-intensity beam impacts, as well as the evidence of a local fracture of the bulk material at the interface between adjacent blocks (Figure 5.38(c))

The test was definitely successful for both CFC and MoGr, which survived very satisfactorily the impact roughly corresponding to the HL-LHC beam injection error. CuCD jaw survived to the impact expected on TCTs during an asynchronous dump failure, although locally damaged. If this would happen in a real TCT jaws, the damage might be recovered by moving the jaw along the axis perpendicular to the collimation plane by up to 10 mm (so-called $5^{th}$ axis). This would allow to exposed a "fresh" undamaged portion of the jaw to the beam, replacing the damaged one. However,

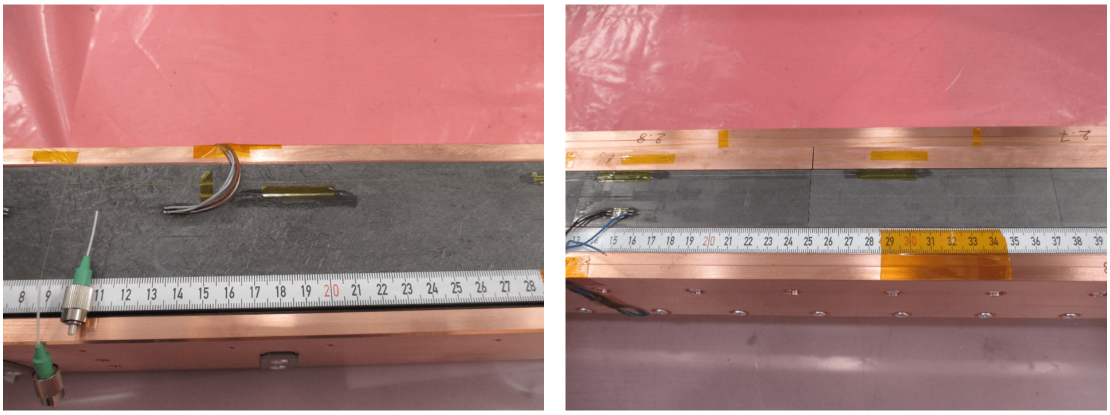

(a) CFC jaw. (b) MoGr jaw.

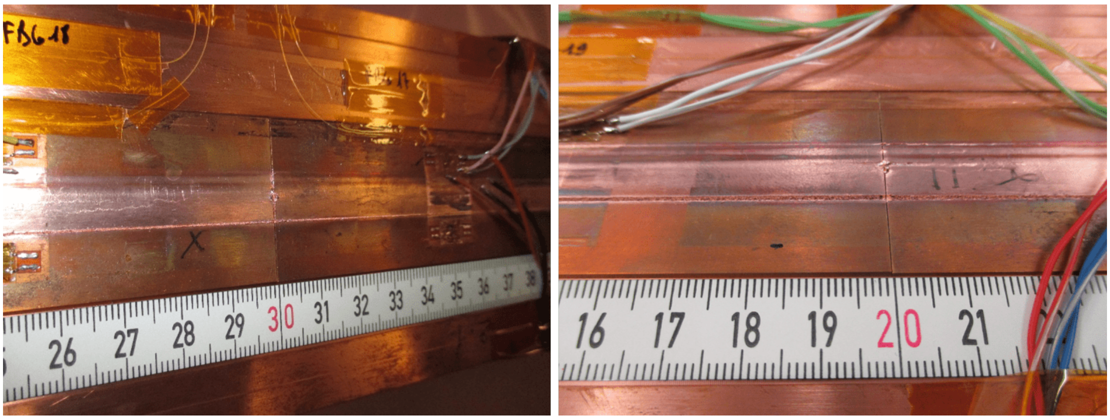

(c) CuCD jaw.

**Figure 5.38:** *Visual inspection of the three jaws after the HRMT-23 experiment.*

preliminary estimates indicate that a CuCD jaw is about 15 times more robust than the present IT-180 jaw, based on the experimental evidence that CuCD did not show large structural damage when hit by the same beam that caused catastrophic damage to IT-180 during HRMT-09 experiment [93].

A complete post-mortem analysis of the jaws has started to measure the change in the thermo-physical property of the impacted materials. It includes either non-destructive tests, such as profilometry to measure the groove depth, mapping of the electrical conductivity, etc, and destructive tests in a later stage. The thermal analyses, needed to compare the temperature probe response and useful as a first step for the structural simulations, are ongoing. Mechanical simulations, indeed, will aim at benchmarking the numerical models of the novel composites against the experimental data. Energy deposition studies will complete the picture of impact scenarios. Nevertheless, the immediate goals of the HRMT tests is the validation of the design of a low-impedance, high-robustness collimator prototype to be installed in the LHC in 2017.

# CHAPTER 6

# Radiation damage studies on collimator materials

The impact of radiation on equipment used in particle accelerators is a continuing concern. Due to their proximity to the beam, LHC collimator materials may experience aging, degradation and even failure after long-term radiation exposure. By now, very little is known about LHC collimator materials in terms of degradation of their functional properties after long-term irradiation. The increased need of predicting and understanding the effects of radiation on collimator materials is raising the interest of the international scientific community.

Within two EU-funded programs, namely EuCARD and EuCARD-2 projects, several irradiation campaigns were carried out over the last few years, to test the resistance of collimator materials against different particle beams and energies. Experiments involved a number of European and international partner institutions: at GSI Helmholtzzentrum (Germany), irradiations using swift heavy and light ions were performed; at Brookhaven National Laboratory (USA), using high energy protons and fast neutrons; at Kurchatov Institute (Russia), using low energy protons and carbon ions.

In this Chapter, several aspect of the post irradiation evaluation, including beam-induced changes in sample dimensions, thermo-mechanical properties and electrical resistivity, as well as X-ray diffraction and microscopy observations are discussed for some MoGr grades, CFC and CuCD.

## 6.1 Available literature on radiation damage in graphite composites

Carbon composites (C/C) are adopted in various fields, from aerospace applications to shielding for fission and fusion reactors, i.e. environment where the interaction with radiation is unavoidable. For this reason, the study of the behaviour of these materials in different irradiation conditions has always been of great interest for the scientific community.

Microstructural evolution of 3D-C/C composite materials irradiated by carbon ions at elevated temperatures was studied by Tsai et al. [94], leading to the conclusion that the composite exhibits a lower degree of graphitization than nuclear graphite and that modest irradiation levels of $7 \times 10^{21}\ \mathrm{p/cm^2}\ \mathrm{C^+/m^2}$ at temperatures of 600 °C led to macroscopical radiation damage as cracks and grain distortions in the matrix. The structural modifications of C/C composites under high temperature and ion irradiation (2 keV H of low flux $5 \times 10^{16}\ \mathrm{ions/m^2 s}$) were addressed by Paulmier et al. [95]. Their study also revealed that, even before irradiated, the microstructure of the C/C composites is strongly influenced by the manufacturing process and that 2D-C/C structures, in particular, exhibit increased disorder with elevated temperatures.

Comparative studies of irradiation-induced changes in the structure and the properties of 1D, 2D, and 3D C/C composite for fusion reactor applications were carried out by Burchell et al. [96]. Results indicated that the 3D C/C behaves more isotropically than the 2D and 1D composites, and that the thermal conductivity, severely degraded by neutron irradiation, can partially be recovered through annealing.

The effects of carbon-fiber orientation and graphitization on solid state bonding of a C/C composite to nickel were studied by Nishida [97]. In this study, C/C composites with the two types of carbon fiber orientations, heat-treated at two different temperatures, were used and the influence of both fiber orientation and graphitization at the joining of C/C composites to metals were investigated. Load-displacement tests revealed that carbon fibers undergoes slip deformation in the direction parallel to the planes due to crystallographic anisotropy. The response of C/C composites and other materials of interest for the next generation of high temperature reactors when operate in extreme conditions of radiation and temperature is discussed in Ref. [98].

For graphite-based materials [36,99], the mean free path of phonons can be sensibly reduced due to the presence of lattice defects and this may become the main cause of irradiation-induced degradation of the thermal conductivity, which can reduce by up to one order of magnitude with respect to the unirradiated value. In the case of ceramic materials, instead, the thermal conductivity can decrease by 5-14% almost regardless of the irradiation temperatures [99, 100].

The electrical resistivity of graphite may also be affected by radiation damage [101]. The mean free path of the conduction electron is relatively large, being limited only by crystallite boundary scattering. Irradiation introduces scattering centers, which reduce the mobility of the charge carrier, and electron traps, which decrease the carrier density. The overall effect is an increase of the electrical resistivity after irradiation.

Irradiations of 2D C/C for LHC collimators (namely AC-150K) were performed at BNL (USA) and Kurchatov Institute (Russia). The results have been published in a number of papers [87, 102, 103]. These were the first irradiation campaigns involving

LHC collimator materials. The successful results made us confident that the materials presently adopted in the system provide an overall good behaviour against irradiation, although indication of potential issue from radiation were outlined. The most relevant outcomes of these experimental studies are discussed in Chap. 6.4.

## 6.2 Experimental investigation of radiation damage in collimator materials

### 6.2.1 History of irradiation campaigns of collimator materials

Over the last ten years, several irradiation campaigns were conducted on present and future LHC collimator materials, in particular CFC, CuCD and MoGr. Table 6.1 contains a schematic history of the performed campaigns, which specifies the time, the institute hosting the experiments, the irradiated materials, the type and energy of the radiation used, and the maximum fluence achieved.

**Table 6.1:** *History of the irradiation campaigns performed over the last ten years on LHC collimator materials.*

| **Year** | **Materials** | **Institute** | **Beam** | **Energy** [MeV] |
|---|---|---|---|---|
| 2006 | CFC | Kurchatov | protons<br>$^{12}$C ions | 30 MeV<br>5 MeV |
| | | BNL | protons | 200 MeV |
| 2013 | CuCD | Kurchatov | protons | 30 MeV |
| | | BNL | protons<br>protons + neutrons | 200 MeV<br>200 MeV - spallation |
| | MoGr ($3^{rd}$ gen.) | BNL | protons<br>protons + neutrons<br>protons (Tandem) | 200 MeV<br>200 MeV - spallation<br>28 MeV (T$<$ 0°C) |
| 2014 – 2016 | CFC, CuCD,<br>MoGr ($4^{th}$-$7^{th}$ gen.) | GSI | $^{238}$U, $^{208}$Bi,<br>$^{197}$Au, $^{12}$C ions | 4.8 MeV/u |
| 2016 | CFC<br>MoGr ($6^{th}$-$7^{th}$ gen.) | BNL | protons | 160 MeV |

The main outcomes of these tests are been summarised in the following sections. The most recent tests, from 2014 to 2016, fell in the timeframe of this thesis work, and there was a directly participation in the setup of the experiments and the post-irradiation characterization analysis.

### 6.2.2 Facilities for irradiation tests

At BNL, irradiation experiments were carried out in two different facilities, BLIP and Tandem, as schematically shown in Figure. 6.1.

From the LINAC, a proton beam of energy up to 200 MeV can be directed towards the Brookhaven Linear Isotope Producer (BLIP) facility, where a special target station is installed with a multi-capsules setup to allow the exposure to radiation of several

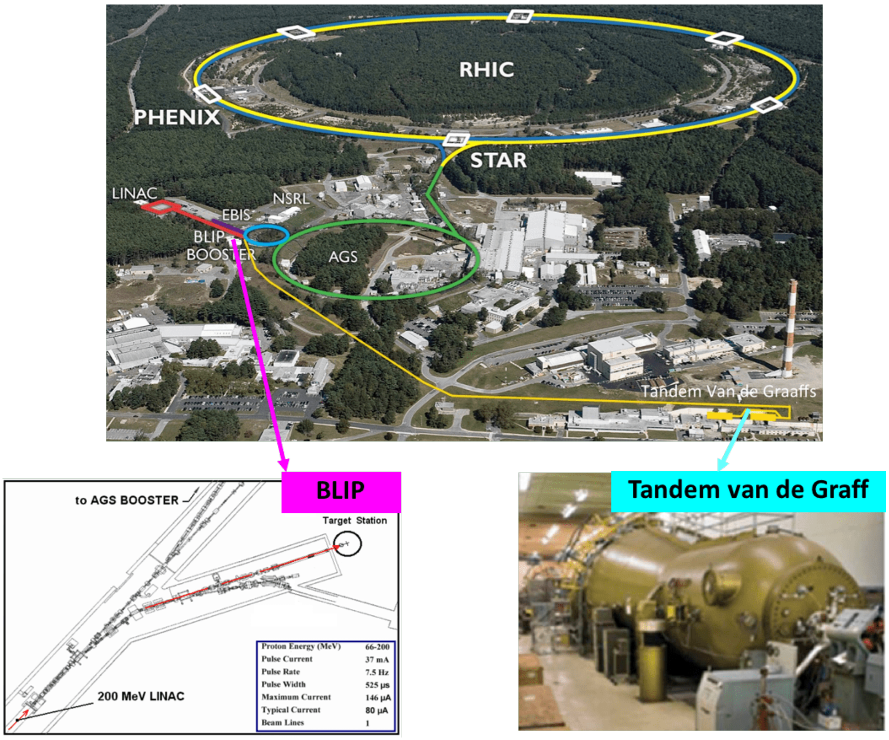

| | |
|---|---|
| Proton Energy (MeV) | 66-200 |
| Pulse Current | 37 mA |
| Pulse Rate | 7.5 Hz |
| Pulse Width | 525 μs |
| Maximum Current | 146 μA |
| Typical Current | 80 μA |
| Beam Lines | 1 |

**Figure 6.1:** *The BNL accelerator complex (top), then BLIP (bottom-left) and Tandem (bottom-right) experimental facilities used for material irradiation.*

materials at the same time. The schematic layout of the target array and the capsules is reproduced in Figure 6.2(a)-6.2(b). The atmosphere inside the capsules can be either vacuum or air. During the irradiaion, the outer faces of the capsules are continuously cooled down by water or gas (usually argon) that flows from the bottom to the top of the array. Irradiation of the target array (we will refer to the "LHC array" in the context

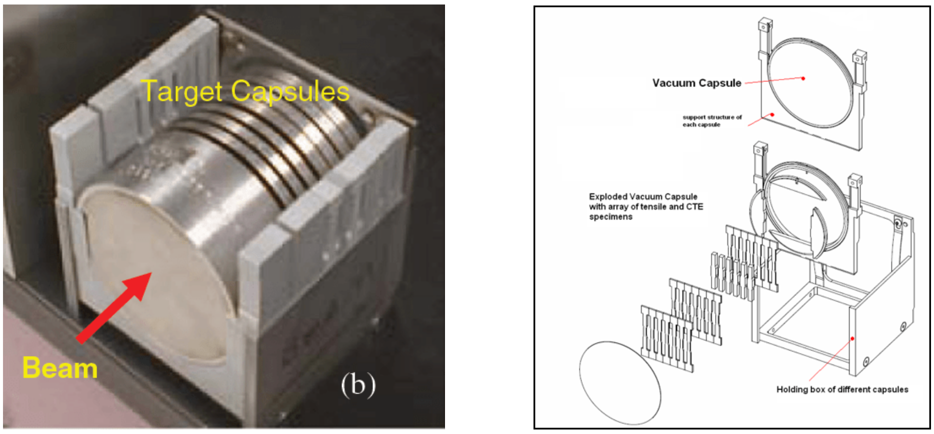

(a) Target array.

(b) Capsule assembly.

**Figure 6.2:** *Layout of the capsules used for material irradiation at BLIP.*

of the irradiation experiments with LHC collimator materials) is usually carried out in tandem with the isotope production. Two irradiation setups can be arranged: the target array can be placed as first in the station, directly facing the 200 MeV proton beam or it can be downstream of the isotope array (that sees the 118 MeV proton beam from the LINAC), being passively irradiated by spallation products, mainly fast neutrons. An example of the two operational modes at BLIP is illustrated in Figure. 6.3.

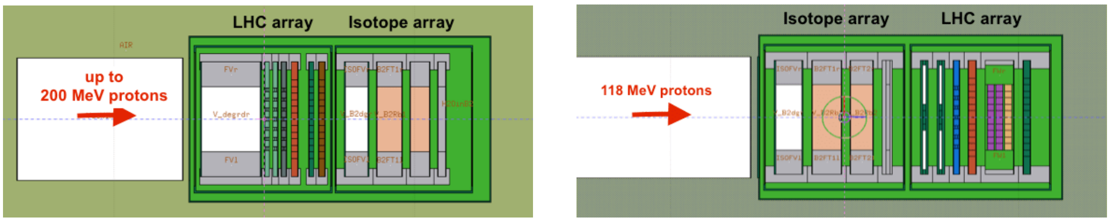

(a) Setup for 200 MeV proton irradiation. LHC material array is initially placed upstream of the isotope targets.

(b) Setup for 118 MeV proton irradiation. LHC material array is moved downstream of the isotope targets and sees the spallation neutron spectrum produced by the upstream array.

**Figure 6.3:** *Different setup during irradiation experiments at BLIP in 2013-2014 run.*

The BNL Tandem facility allows target irradiation with focused 28 MeV, 1 $\mu$A proton beam (Gaussian beam profile, $1.5 \times 1.75$ mm core size, plus tail). The ability of the Tandem facility to focus the 28 MeV primary proton beam down to few hundred micrometre beam spot is a great advantage in that proton irradiation of a small volume can be achieved enabling the accumulation of fluence that can trigger changes in the materials despite a limited irradiation time. Moreover, operating at low irradiation temperatures (LN2 cooling the copper blocks at 70 K) facilitates "freezing" of damage in the microstructure and the prevention of its annealing while materials are being irradiated. An example of the Tandem irradiation setup is given in Figure 6.4.

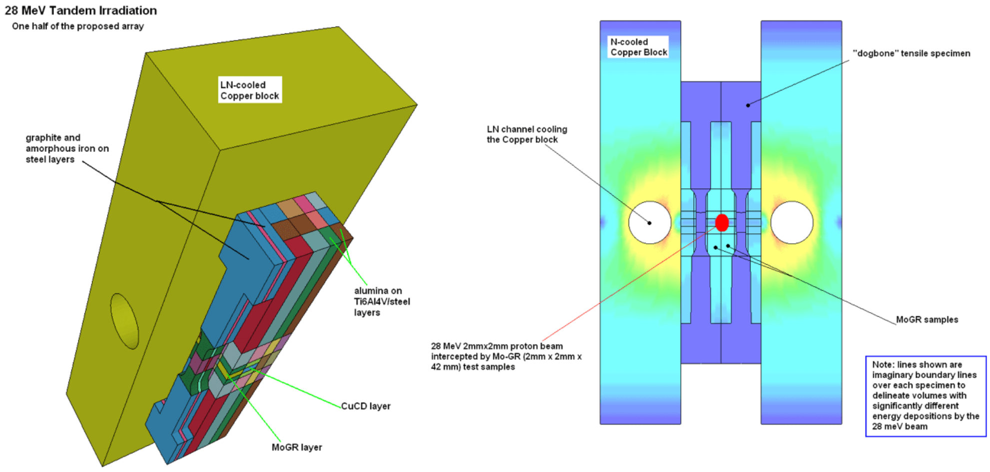

**Figure 6.4:** *Materials setup during irradiation experiment at Tandem in 2013-2014 run.*

The GSI accelerator facility consists of the linear accelerator UNILAC, the ring heavy ion synchrotron SIS and the experimental storage ring ESR, as shown in Figure 6.5. At the UNILAC, there are two ion sources that can provide ion species of several different elements. The energy delivered by the UNILAC is between 3.6 and 11.4 MeV/u. The UNILAC M-Branch facility (Figure 6.6) comprises of three beamlines. M1 branch is connected to a high resolution scanning electron microscope which allows the direct imaging of sample right after being irradiated. In the M2 beam-line, X-ray Diffraction analysis can be performed. M3 beam-line enables the control and recording of irradiation conditions, such as temperature through a thermal camera.

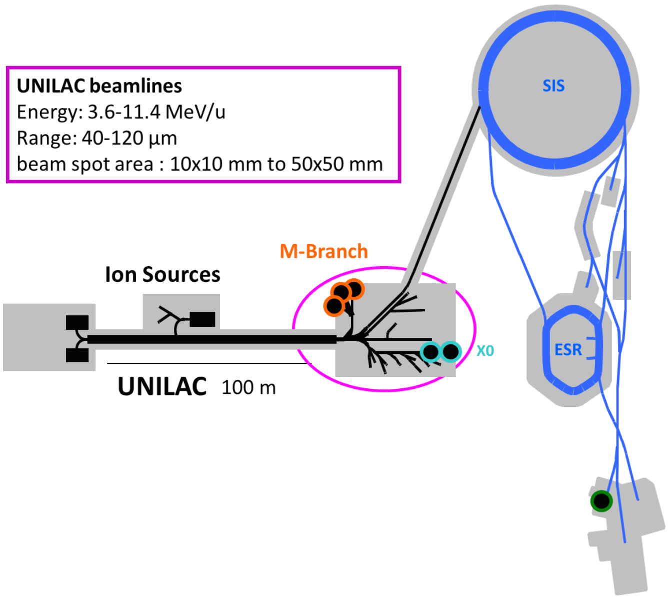

**Figure 6.5:** *GSI accelerator facility.*

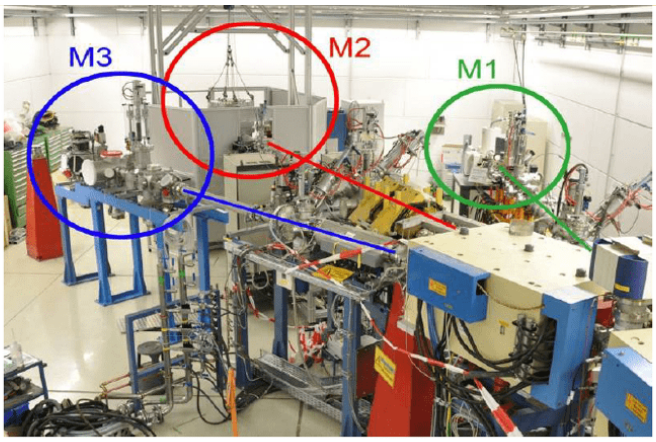

**Figure 6.6:** *M-branch irradiation facility at GSI.*

At Kurchatov Institute, irradiation tests are performed at the RRC-KI cyclotron, schematically illustrated in Figure 6.7. The cyclotron can operate with different types of beam (protons, helium, oxygen and carbon ions) at various energies. The beam extracted from RRC-KI isochronous cyclotron passes through the beam transport ion-optical system to the experimental hall, where the target unit is installed on the diagnostic device. A special cooling system and water-cooled target unit were developed for irradiation of LHC collimator materials with proton beam with energies up to 30 MeV with a maximum fluence of $10^{19}$ p/cm$^2$. The experimental setup works as it follow: a grid is placed between the incoming ion beam and the sample to be irradiated. Some regions of the sample are in the “shade” of the grid and thus are not irradiated. Therefore, any change in the irradiated zones is measured with respect to the zones that are not exposed to the beam. Moreover, visual inspections of the surface of the specimens after irradiation can be used to estimate the effect of irradiation erosion.

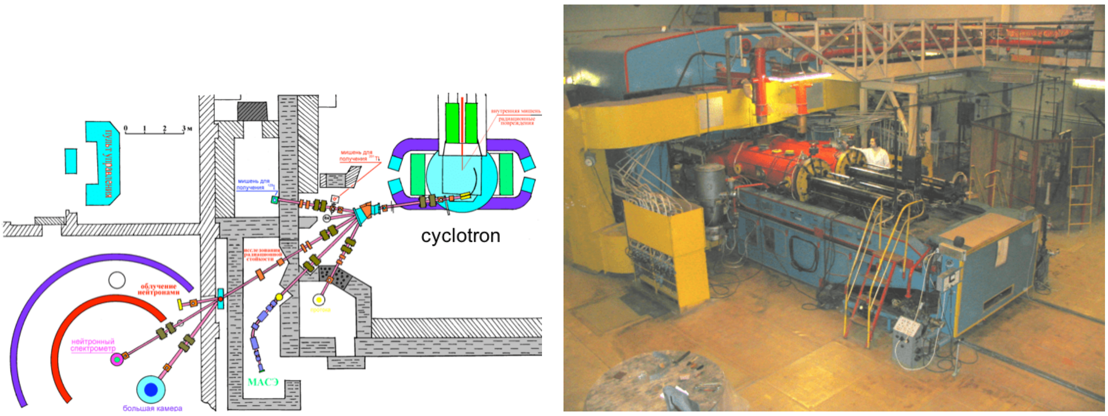

(a) Scheme of beam transportation from the cyclotron to different experimental halls.

(b) Picture of the cyclotron.

**Figure 6.7:** *RRC-KI cyclotron at Kurchatov Institute.*

## 6.3 Irradiation of MoGr composite

MoGr composite underwent important improvements of its properties over the years, leading to different "generations" of the material, as already discussed in Chap. 4. Irradiation experiments were conducted over several years, while the MoGr was evolving and improving. For this reason, at any campaign the most recent MoGr grade available at that time was tested . A schematic representation of the irradiation tests performed and the MoGr grades involved is given in Figure 6.8.

### 6.3.1 Evaluation of damage from heavy and light ion irradiation

Heavy ions have a much shorter stopping range in in the materials than light ions or protons do [34]. This means that the concentration of defects is much higher for the same kinetic energy, and the defects are more localized. At lower energies, it is possible that only the surface of the material might be damaged. At higher energies, recoil atoms are formed and the energy is transferred to the target nuclei, mainly owing to these secondary particles. Up to 1 GeV per nucleon, the Coulomb interaction is the most important interaction. Due to the dominant Coulomb interaction and the high charge, the damage cross-section of a U-ion, for example, is four orders of magnitude higher than

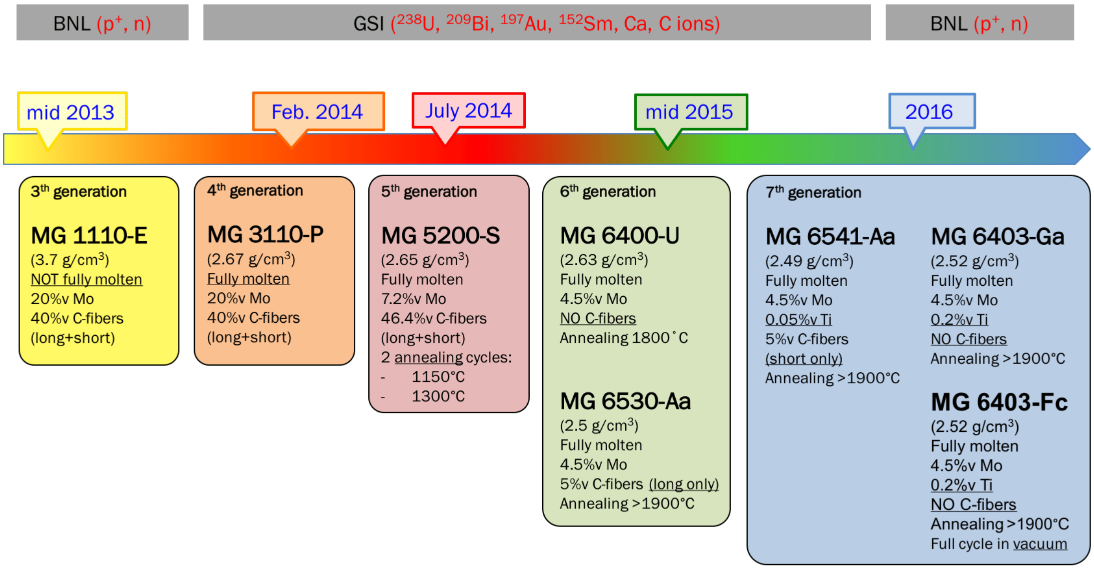

**Figure 6.8:** *Timeline of the irradiation campaigns performed on MoGr and relative grades tested.*

that of a proton at the same energy [34]. When swift heavy ions penetrate the matter, a large amount of energy is transferred to the matter through electronic excitation and electron-phonon coupling leading to local damage along the ion trajectory.

Irradiation tests were performed at M-branch beamlines at the UNILAC facility, GSI, where various grades of MoGr were exposes to different beam conditions, e.g. carbon ions of 5.9 MeV per nucleon (MeV/u), and 4.8 MeV/u calcium, bismuth, gold and uranium ions, with fluence ranging from $1 \times 10^{11}$ up to $5 \times 10^{13}\,\mathrm{i/cm^2}$.

The tests were performed at energies close to Coulomb barrier, which minimizes sample activation and allows fast characterization of the functional properties after irradiation. Therefore, the short characterization time allowed to perform several cycles of testing and optimization of MoGr radiation hardness. Ion-induced changes in the structure and functional properties of the irradiated materials were investigated using online and offline SEM, Raman spectroscopy and X-ray diffraction techniques (XRD). Moreover, profilometry, nanoindentation, online temperature monitoring and online electrical resistivity measurements were performed.

Samples of MG-3110P grade (see Chap. 4) were irradiated with 4.8 MeV/u $^{208}$Bi ion and 4.8 MeV/u $^{238}$U ion beams. Figure 6.9 clearly shows bending at fluence of $1 \times 10^{13}\,\mathrm{i/cm^2}$, perhaps already started at around $6 \times 10^{12}\,\mathrm{i/cm^2}$. Such a bending mainly involved transversal samples (i.e. where the graphite basal planes are oriented perpendicular to the surface). At a dose of $5 \times 10^{13}\,\mathrm{i/cm^2}$, all samples appear fractured. The ion beam only penetrates about 40 $\mu$m of the sample, inducing swelling of the irradiated layer. On the other hand, the non-irradiated substrate does not experienced any swelling and bends under the stresses between irradiated and non-irradiated layer. CFC samples, which were placed in the top row in the sample holder in Figure 6.9, did not show large deformation during irradiation. Raman spectroscopy and thermal conductivity measurements on MG-3110P showed disorder of graphitic structure as a result of irradiation [104]. In Figure.6.10, dynamic indentation tests revealed that the response of irradiated materials to pressure waves is worsened due to hardening and increased Young's modulus at higher fluence. MG-3110P suffered of residual stresses accumulated during the sintering process, which may have increased the grade of distortion of the grains. In order to release these stresses, post-production annealing at high temperature (e.g. 1150 °C or 1300 °C) was adopted on grade MG-5220S. Results after $^{197}$Au ion irradiation revealed that the radiation-induced deformation starts at fluence higher than $1 \times 10^{13}\,\mathrm{i/cm^2}$ when dealing with annealed samples. However, the accumulation of large doses can heavily affect the property and the microstructure of material.

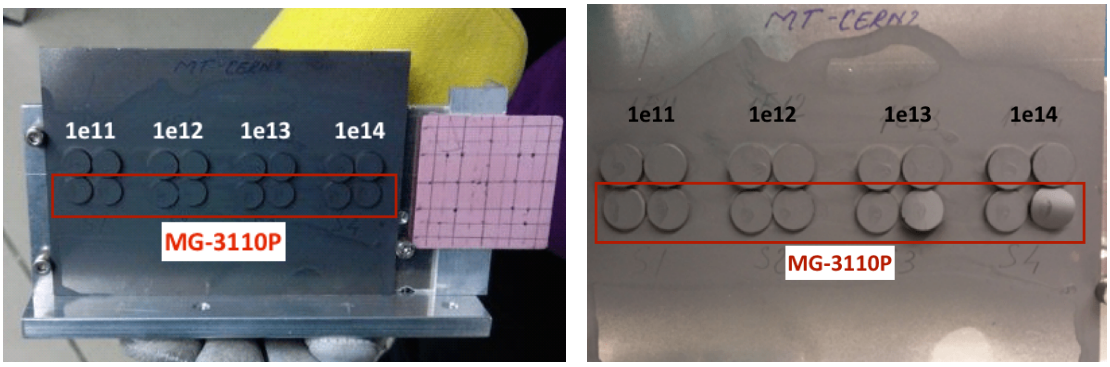

(a) Before irradiation. (b) After irradiation.

**Figure 6.9:** *Specimens of MG-3110P in the sample holder prior and after U ion irradiation. One longitudinal (on the left) and one transversal (on the right) sample were irradiated for each fluence. Courtesy of M. Tomut, GSI.*

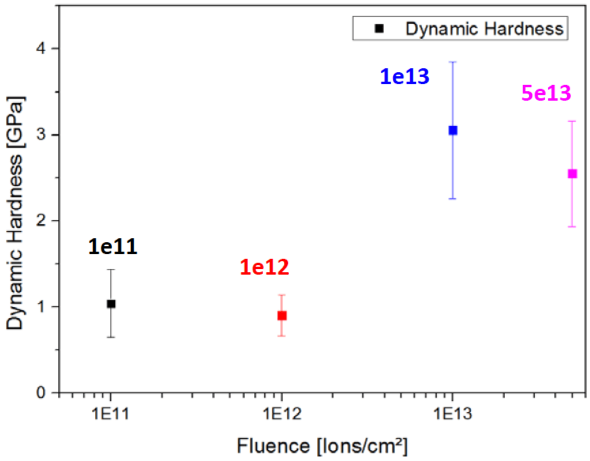

**Figure 6.10:** *Nano-indentation measurements performed on MG-3110P after $^{208}$Bi ion beam exposure. Courtesy of M. Tomut, GSI [105, 106].*

By SEM observations, the effects of radiation damage on the material microstructure was evaluated. Figure 6.11 shows the SEM images of the longitudinal samples of MG-5220S grade before and after irradiation. The white particles are the molybdenum carbides, while the black areas refer to the graphite matrix. After irradiation, no changes on molybdenum carbide surface were observed. But it is evident on the graphite matrix that the crystallite size decreases in the irradiated sample and new irregular grains form on the surface (Figure 6.11(b)), while the graphite surfaces of pristine sample are smoother (Figure 6.11(a)).

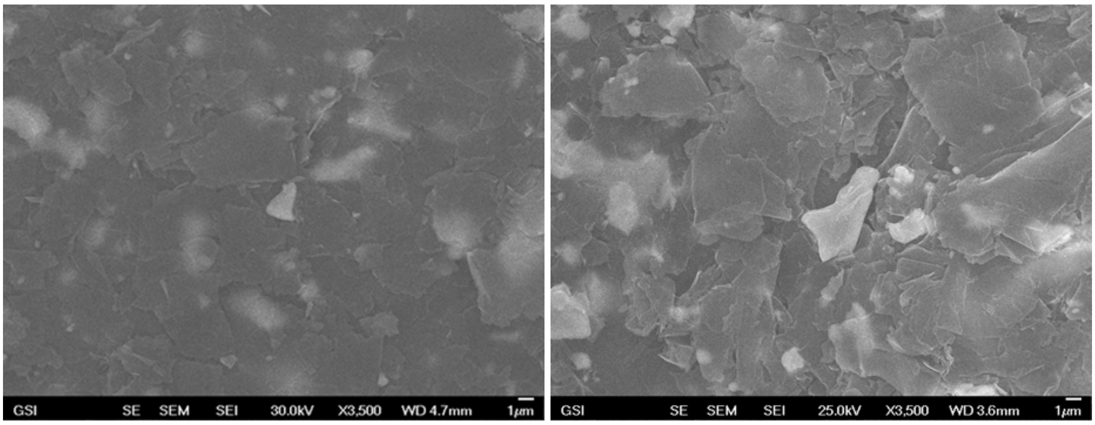

(a) Before irradiation.

(b) After irradiation with $1 \times 10^{12}\,\mathrm{i/cm^2 s}$.

**Figure 6.11:** *SEM images of longitudinal samples of MG-5220S, annealed at 1300° C. Courtesy of M. Tomut, GSI [106].*

Raman spectroscopy is a popular method to investigate the defects and disorder of carbon related materials. A Raman spectroscopy system (JOBIN YVON HOBIBA HR 800 UV) was used to investigate MG-5220S [106]. A perfect graphitic lattice would exhibit only the G ("Graphite") peak, which is responsible for the $\mathrm{sp}^2$-bonded carbons. A defect in the lattice can activate the D ("Defect") peak. The effects of the swift heavy ion induced on the samples can be explained by a set of parameters, such as the peak height ratio of D1 and G peaks, the intensity ratio or the integrated area ratio of those peaks, and the full width at half maximum of G peak. Ion irradiation is expected to lead to an increase in intensity of D1 peak and a decrease and broadening of band. From the analysis, it turned out that most of the parameters increased with increasing ion dose, which indicates the increasing disorder and the reduction of the in-plane grain size. These microscopic effects are the basic explanation for the change of the macroscopic properties, such as the thermal diffusivity (see plots in Ref. [104]) and the hardness.

The effects of Au-ion irradiation on MG-6400U, MG-6530Aa and MG6541Aa grades were also studied. As recalled in Figure 6.8, all these grades have high processing and post-processing cycle temperature. MG-6400U does not contain carbon fibers or additional dopant elements, while MG-6530Aa contains longer fibers but no dopants, and MG-6541Aa has short fibers and a small Ti addition. The result of profilometry measurements on these materials is illustrated in Figure 6.12: the damage continuously increases with the fluence for all the measured grades, the maximum bending is caused by swelling at fluence between $1 \times 10^{12}$ and $1 \times 10^{13}\,\mathrm{i/cm^2}$. At $1 \times 10^{13}\,\mathrm{i/cm^2}$, internal stresses in MG-6530Aa are released by means of the high temperature reached during the irradiation: cracks were indeed visible on the sample surface. The other grades, instead, experienced less bending at all fluencies.

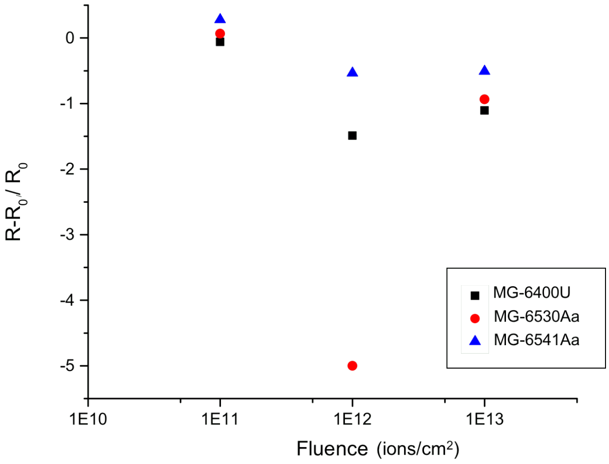

**Figure 6.12:** *Evolution of beam-induced radius of curvature of various MoGr grades as function of fluence. The samples were irradiated with 4.8 MeV/u Au ion beam. Courtesy of M. Tomut, GSI [105].*

The electrical resistivity degradation of these MoGr grades was monitored online by a 4-probe setup. The voltage drop across the sample was measured during the irradiation with calcium ions at low flux to avoid beam-induced heating. The change in resistivity of three MoGr grades is shown in Fig. 6.13, averaged over the sample thickness in the range of ion penetration ($\sim 50\,\mu$m). The defect accumulation and the reduction of the in-plane crystallite size result in a gradual increase of the resistivity: grade MG-6400U (no fibers) appears to be more prone to this effect after $4 \times 10^{13}\,\mathrm{i/cm^2}$, while grades with fibers show smaller resistivity degradation. In particular, MG-6530Aa (with long fibers) shows the lowest resistivity change of all analysed samples. The addition of carbon fibers seems to improve the material stability against ion-induced resistivity change. The longer the fibers, the stronger is their impact on the electrical charge transport.

### 6.3.2 Evaluation of damage from high-energy proton irradiation

At BNL, the first irradiation of MoGr composite (grade MG-1110E) was performed at the BLIP facility with 200 MeV proton beam in 2013-2014. The samples were encapsulated under vacuum in two capsules and exposed to protons as part of a multi-capsule, multi-material irradiation array. One capsule experienced long-term irradiation, which lasted about 8 weeks with a final accumulated fluence of $\sim 10^{21}\,\mathrm{p/cm^2}$: most of the samples experienced serious degradation and structural collapse at high fluence and therefore it was not possible to perform a complete post-irradiation characterization of thermo-mechanical and electrical properties. Another capsule of MoGr samples was exposed to $2.8 \times 10^{18}\,\mathrm{p/cm^2}$ followed by fast spallation neutron irradiation to $3.2 \times 10^{18}\,\mathrm{n/cm^2}$ (in the following, we refer to it as $\sim 6 \times 10^{18}\,\mathrm{(p+n)/cm^2}$ irradiation). It is important to notice that the level of $0.3\,$DPA reached during the high-dose irradiation is two orders of magnitude above the damage estimates for LHC primary collimators operating with protons at 7 TeV [107].

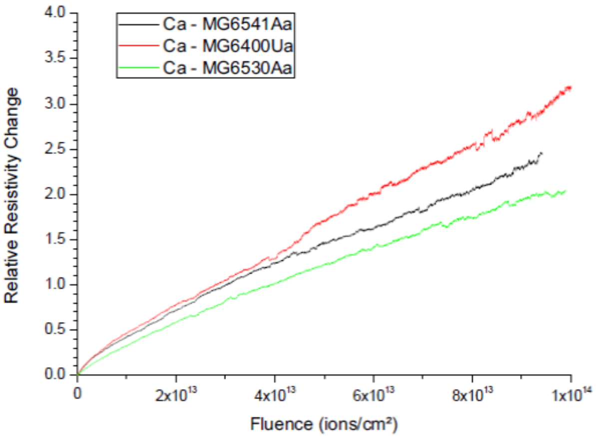

**Figure 6.13:** *Comparison of relative resistivity changes of various MoGr samples irradiated with 4.8 MeV/u Ca ions. Note that it can be estimated about* $10^{-4}$ *dpa generated in MoGr with a fluence of* $1 \times 10^{14}\,\mathrm{Ca/cm^2}$. *Courtesy of M. Tomut, GSI [105].*

A more recent test was committed and carried out at BLIP in 2016 with the main goal of identifying a "threshold" fluence at which the structural integrity of MoGr composite starts to be compromised, and then compare it with graphitic composites ($\sim 5 \times 10^{20}\,\mathrm{p/cm^2}$) [102, 108, 109]. This time, the irradiation experiment was performed in steps of fluence, from $\sim 5 \times 10^{19}$ to $\sim 2 \times 10^{20}\,\mathrm{p/cm^2}$. The total fluence was less than the one achieved in the previous irradiation due to a failure occurred in the downstream isotope production array that forced the premature end of the experiment. In this campaign, the most recent grades (MG-6530Aa, MG-6403Ga and MG-6403Fc) were irradiated. However, the post-irradiation characterisation of these grades has not been completed yet, due to the high level of activation of the samples that requires months (sometimes even years) of cooling down to stay within the limit of doses accepted by the post-irradiation test facilities. By now, it was only possible to perform X-ray diffraction tests on MG-6530Aa, irradiated at the lowest fluence step.

#### Visual inspection of irradiated capsules

The visual inspection of irradiated MG-1110E revealed that samples exposed to the maximum fluence of $1 \times 10^{21}\,\mathrm{p/cm^2}$ experienced serious degradation and structural collapse (Fig. 6.14). Samples that survived fluences of $6 \times 10^{18}\,\mathrm{(p+n)/cm^2}$ up to $\sim 2 \times 10^{20}\,\mathrm{p/cm^2}$ appeared, at least at a first look, structurally integer.

On the other hand, none of the capsules irradiated in 2016 showed signs of structural degradation up to the maximum achieved fluence (Fig. 6.15). MoGr seems to survive fluence up to $\sim 2 \times 10^{20}\,\mathrm{p/cm^2}$, thus the threshold of structural damage is above this value, reasonably expected to be not far from the $\sim 5 \times 10^{20}\,\mathrm{p/cm^2}$ found for carbon-carbon (C/C) composites.

#### Mechanical tests

Irradiation-induces changes in the microstructure of MoGr, leading to an increase of the ultimate tensile strength and Young's modulus, were studied through mechanical

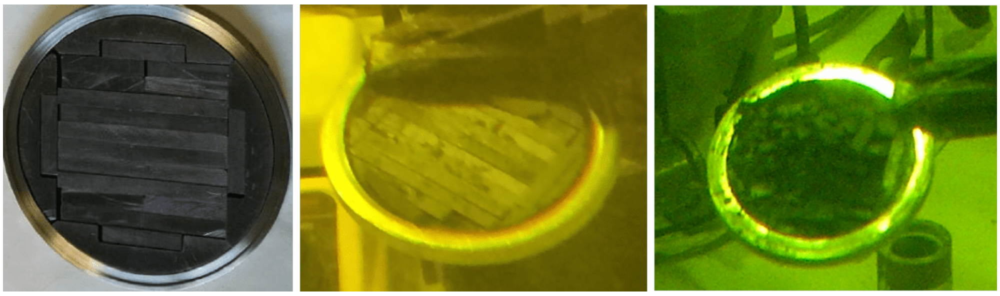

**Figure 6.14:** *Capsule of MoGr samples before irradiation (left). Observed structural degradation in MG-1110E samples after irradiation with exposure to* $2.8 \times 10^{18}\ \mathrm{p/cm^2}$ *at 200 MeV followed by fast neutron fluence of* $3.2 \times 10^{18}\ \mathrm{n/cm^2}$ *(center) and even more severe deterioration after* $1 \times 10^{21}\ \mathrm{p/cm^2}$ *by 200 MeV protons (right). Note that the two pictures of irradiated capsules have been taken through 8 cm thick lead glass of the hot cell where the samples were transported after the end of the irradiation to let them cool down. That is the reason of the pure quality of those pictures. Courtesy N. Simos, BNL [109].*

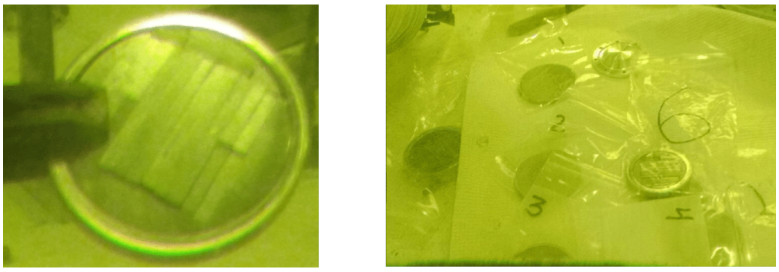

**Figure 6.15:** *Visual inspection of the MoGr capsules irradiated at BLIP in 2016. On the left side, MG-6530Aa capsule opened in the hot cell after exposure to a fluence of* $\sim 5 \times 10^{19}\ \mathrm{p/cm^2}$. *On the right, all capsules opened after the end of the experiment and none of them shows macroscopic signs of degradation at fluence in excess of* $2 \times 10^{20}\ \mathrm{p/cm^2}$. *Courtesy N. Simos, BNL [109].*

tests. Tests were conducted on the lowest-dose irradiated MG-1110E samples (fluence of $\sim 10^{18}\ \mathrm{p/cm^2}$) that did not shown any evidence of structural degradation during the irradiation. Bar-type specimens ($42 \times 4 \times 4$ mm) were used. The four-point bending test was performed (Figure 6.16(a)), which relates the load imposed to the sample, in a pure bending state, to the resulting deflection.

Fig. 6.16(b) shows load-deflection results for MG-1110E. The response of the unirradiated material looks similar to that of C/C composites [109] and graphite too [101, 110]: prior the irradiation, the application and removal of the load produces a large permanent deformation with a small elastic recovery. After irradiation, the stress-strain curve becomes more linear, the strain to failure is reduced, and the strength and elastic modulus are increased. On irradiation, there is a rapid rise in strength, typically 50% in graphite, which is attributed to dislocation pinning at irradiation-induced lattice defect sites. This effect is largely saturated at doses 1 dpa. Above such value, a more gradual increase in strength occurs because of the structural changes within the graphite. The strain behaviour of nuclear graphites subjected to an externally applied load is largely controlled by the shear of the component crystallites. As with strength, irradiation-induced changes in Young's modulus are the combined result of in-crystallite effects, due to dislocation pinning at low fluence that inhibit the dislocation motion, and superimposed structural change external to the crystallite [101].

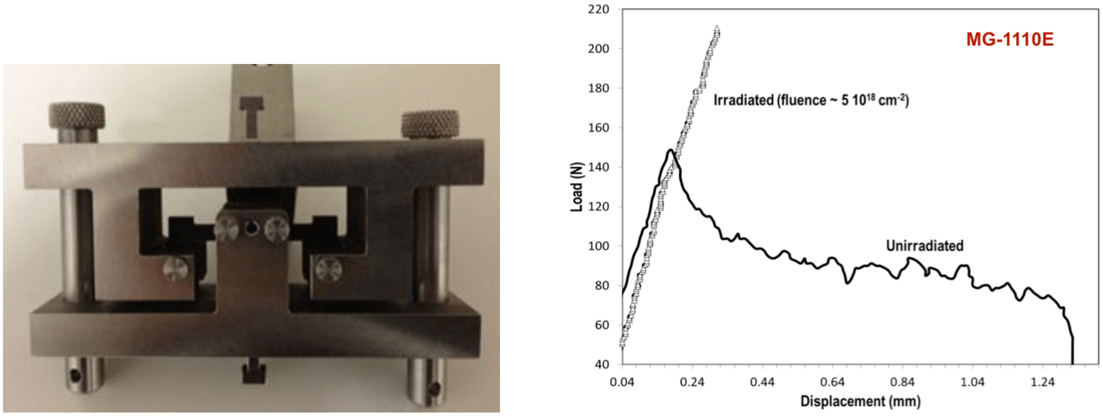

(a) Four-points-bending special fixture.

(b) Comparison of results of four-point-bending test of irradiated and unirradiated MG-1110E.

**Figure 6.16:** *Mechanical tests on MG-1110E performed at BNL before and after proton irradiation. Courtesy N. Simos, BNL [109].*

Furthermore, ultrasonic tests were performed before and after irradiation of MG-1110E (see Figure 6.17). The test revealed the anisotropy already existing in the pristine material due to the orientation of the carbon-fibers and the graphite basal planes in the compound: MoGr is indeed an orthotropic material. Measurements of ultrasonic velocities in the unirradiated sample show different velocities according to the measured direction: 1530 m/s in the transversal direction and 2956.5 m/s in the longitudinal one. Measurements on a low irradiated sample (fluence of$2.8 \times 10^{18}\,\mathrm{p/cm^2}$ and $3.2 \times 10^{18}\,\mathrm{n/cm^2}$) revealed an increase in the ultrasonic velocity ($\sim$30% along the transversal direction and by $\sim$20% along the longitudinal direction). It is clearly related to the change of the elastic constant induced by radiation, which further confirms the results obtained with the bending test.

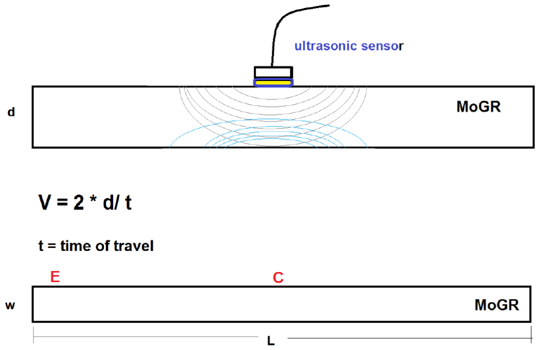

**Figure 6.17:** *Scheme of the ultrasound-based technique used to evaluate radiation-induced microstructural changes in MG-1110E. C indicates the central position and E the end-sample position during scanning test.*

**Thermal tests**

Thermal geometrical stability is very important for collimator materials, in order to guarantee the high beam cleaning efficiency required in operation.

Dilatometry studies have been carried out on unirradiated MG-1110E samples, and the dimensional change as a function of the temperature in the dilatometer furnace were measured. The samples were heated up to temperatures of $700\,°\mathrm{C}$. As shown in Figure 6.18(a)s, the inflection point of MoGr is at $\sim 500\,°\mathrm{C}$, about $100\,°\mathrm{C}$ less than isotropic graphite (IG) and two-dimensional carbon-fiber composite (2D-C/C). It means that the energy needed for interstitial atoms to move in the atomic structure of the MoGr is lower than that of the other two graphitic materials. Figure 6.18(b) shows dimensional changes of two irradiated MG-1110E samples, in comparison with irradiated annealed graphite and with unirradiated MoGr. The first MoGr sample was exposed to a fluence of $0.5 \times 10^{20}\,\mathrm{p/cm^2}$, while the second one to three times that fluence. TC-1 and TC-2 refers to annealing cycles up to $700\,°\mathrm{C}$ that followed the irradiation. The curves reveal that the annealing cycle seems to dimensionally stabilise the MoGr compound at levels below those of the pristine material. During post-irradiation annealing, in fact, a fraction of the irradiation-induced dimensional change is recovered. The annealing temperature above the irradiation temperature relates to the activation energy for radiation-induced defects.

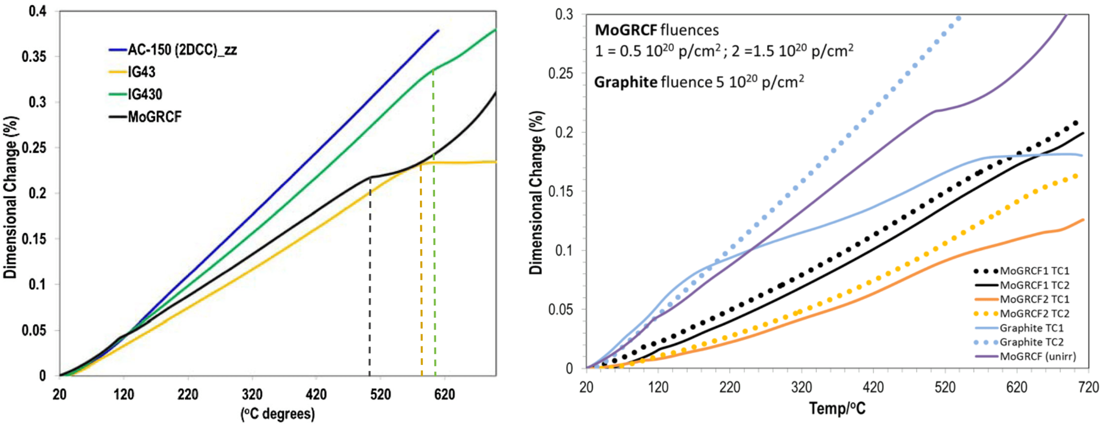

(a) Before irradiation.

(b) After irradiation.

**Figure 6.18:** *Dimensional change measured with dilatometer for different materials. Courtesy N. Simos, BNL [109].*

## 6.3.3 Microstructural evaluation of proton-irradiation-induced effects by X-ray Diffraction technique

As discussed in the previous sections, MG-1110E turned to be vulnerable to high-energy proton irradiation, experiencing brittle fracture already at low doses $\sim 6 \times 10^{18}\,(\mathrm{p+n})/\mathrm{cm^2}$ and severe extensive macroscopic damage at fluence of $\sim 10^{21}\,\mathrm{p/cm^2}$. The origin of such damage may come from the atomic displacement and defects in the lattice induced by radiation as well as from the uncontrolled release, under the combined effect of temperature and radiation, of internal stresses that were not released during the material production. The fact that more recent grades showed, from a visual inspection, no evident traces of macroscopical degradation may also be an indication of the beneficial effect of high-temperature annealing performed during the material manufacturing process.

Between 2014 and 2016, two X-ray Diffraction (XRD) campaigns were performed at the BNL National Synchrotron Light Source (NSLS). The main objective of the tests was the assessment of the microstructural evolution of the MoGr grades during irradiation, through a comparison of the diffraction spectra before and after irradiation, which could explain the vulnerability manifested as macroscopical structural degradation or modification of the thermo-mechanical properties of the compound. These measurements provided also the unique chance to characterise for the first time pristine sample of the novel composite materials under study for future HL-LHC collimators.

During the first campaign in 2014, monochromatic 70 keV X-ray beam and the polychromatic (“white”) 200 keV beam at the X17A and X17B1 beamline (respectively) of NSLS were used. The high flux/energy white beam of the X17 wiggler insertion device allows to produce energy dispersive X-ray diffraction (EDXRD) spectra that are collected by high-resolution energy-dispersive germanium detector downstream of the sample stage. In the second XRD experiment in 2016, a monochromatic 69 keV X-ray beam was used at the 28ID beamline of the new NSLS-II, which can provide X-rays up to 10000 times brighter than its forerunner.

The comparison of EDXRD spectra in Fig. 6.19 confirms the high level of graphitization of the pristine MG-1110E with respect to that of the commercial graphite and other carbon-carbon composites: graphite and fibers in MoGr are well crystallized (the 002 diffraction peak of graphite is narrower) and better than the counterparts shown. Specifically, the measured interplanar distances $d$ of the (002) planes for the three unirradiated material in Figure 6.19 are 3.351 Å for MoGr, 3.368 Å for graphite and 3.378 Å for 3D C/C composite. These results tend to exclude the possibility that the structural vulnerability shown by the material after irradiation comes from a poor graphitization during the fabrication process.

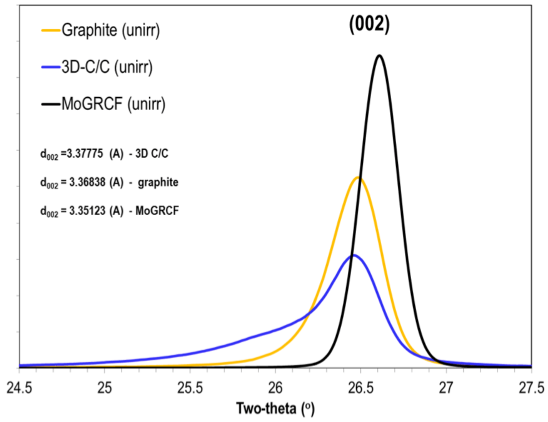

**Figure 6.19:** *EDXRD on MG-1110E: (002) reflection comparison with isotropic graphite (IG-430) and 3D C/C composite. Courtesy N. Simos, BNL [105].*

The 2D diffraction patterns of MG-1110E, pre and post irradiation, obtained by monochromatic 70 keV X-ray beam are shown in Figure 6.20. Figure 6.20(a) reveals an inhomogeneity with spots in the unirradiated material, possibly corresponding to the carbides phases. In Figure 6.20(b), an irradiation-induced transformation of intermediate phases towards the $Mo_2C$ phase accompanied by reduction of crystallinity can be observed.

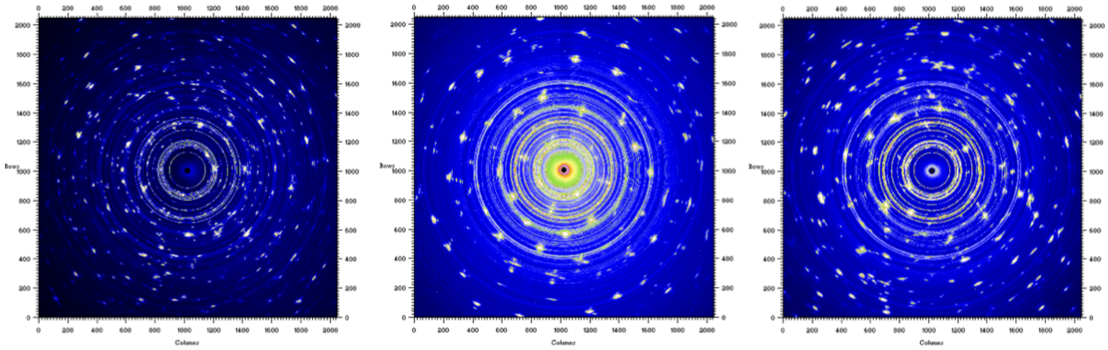

(a) Before irradiation.

(b) After irradiation at Tandem (low fluence, low temperature).

(c) After irradiation at BLIP (fluence of $\sim 6 \times 10^{18}\,(\mathrm{p+n})/\mathrm{cm}^2$).

**Figure 6.20:** *Diffraction images of MG-1110E collected by the 2D detector using monochromatic 70 keV X-ray beam at X17A beamline of NSLS. Courtesy N. Simos, BNL [109].*

Multiple scans on 2 mm thick samples, generated by polychromatic X-rays transmitted by the unirradiated material further support the indications from the monochromatic X-rays analyses. From the diffraction peaks in Figures 6.21(a) and 6.21(b), the inhomogeneous distribution of the Mo-carbide phases along the sample appears more evident. Additionally, plots of irradiated specimens at BLIP and Tandem seem to confirm the transformation of the metastable intermediate carbide phases into stable $Mo_2C$ (Figures 6.21(c) to 6.21(f) and Figure 6.22(a)).

Figure 6.22(b) shows the graphite (002) reflection in the unirradiated sample as well as in the BLIP and the Tandem irradiated ones. The plot reveals a larger increase in the d-spacing for the low-fluence and low-temperature Tandem-irradiated sample with respect to the BLIP-irradiated sample. These results would indicate that interstitial atoms (Figure 6.23) generated during Tandem irradiation between the basal planes of graphite have not annealed out because of the low temperature of 70 K (see Chap. 6.2.1) that inhibits the mobility of such defects. Noticeable is also the “shoulder” in the reflection of $Mo_2C$ (101) plane shown in Figure 6.24(a) after BLIP irradiation: it can be a sign of either amorphization or appearance of a new peak of carbide phases. This finding are being further investigated. Figure 6.24(b) shows a slight shift towards higher d-spacing of the reflection of the (004) graphite plane, which corresponds to a slight increase in interplanar distance induced by radiation. This is in line with the crystal growth seen for the reflection (002) in Figure 6.22(a).

MG-6530Aa grade irradiated in 2016 was tested with the XRD technique at NSLS-II. The high level of activation of the material at the time of the diffraction experiment allowed the access to the synchrotron of only one sample, which saw a fluence of

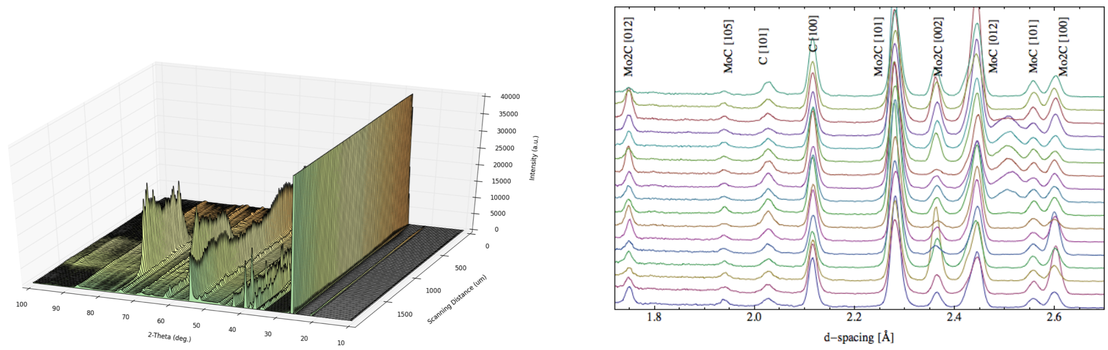

(a) 3D diffraction patterns, in 2-theta diffraction angle. Unirradiated MG-1110E. Courtesy N. Simos, BNL.

(b) 2D-diffraction patterns, in d-spacing. Selected interval. Unirradiated MG-1110E.

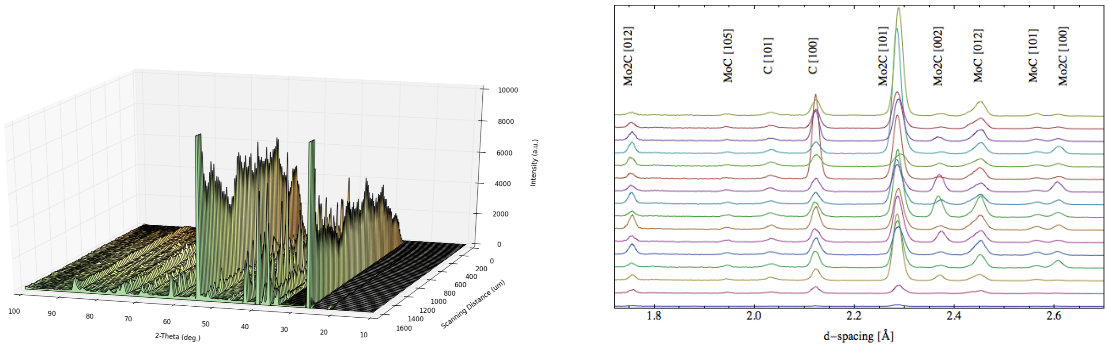

(c) 3D diffraction pattern, in 2-theta diffraction angle. MG-1110E irradiated at BLIP. Courtesy N. Simos, BNL.

(d) 2D-projection scan, in d-spacing. Selected interval. MG-1110E irradiated at BLIP.

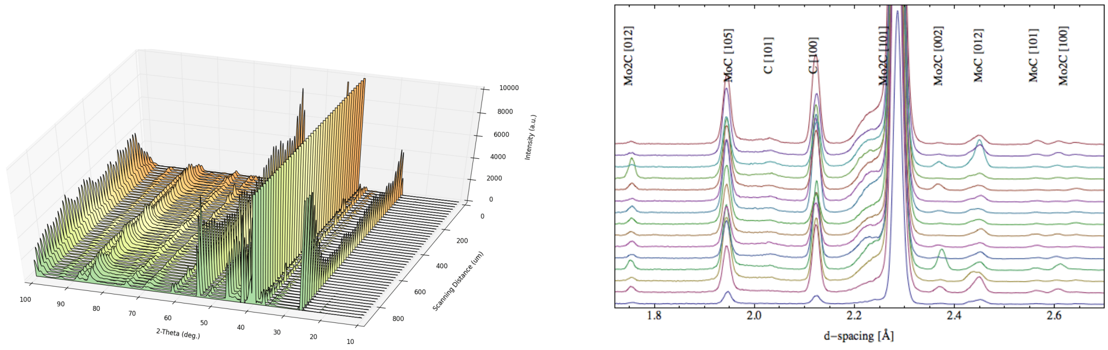

(e) 3D diffraction pattern, in 2-theta diffraction angle. MG-1110E irradiated at Tandem. Courtesy N. Simos, BNL.

(f) 2D-projection scan, in d-spacing. Selected interval. MG-1110E irradiated at Tandem.

**Figure 6.21:** *Multiple through-thickness scans of MG-1110E bar-type samples by means of 200 keV polychromatic X-ray beam from X17B1 beamline at NSLS I.*

$\sim 5\times10^{19}\,\mathrm{p/cm^2}$. However, this fluence was higher than that of the MG-1110E sample tested in the past. Figure 6.25(a) compares the spectra of MG-6530Aa before and after BLIP-irradiation: unlike the older MoGr grade, in this case the two spectra do not show relevant changes for what concerns appearance/disappearance of peaks. Looking at the detail of the (002) reflection of graphite (Figure 6.25(a)), a peak shift of about 1% toward higher d-spacing is a hint of small growth of the interplanar distance, due to

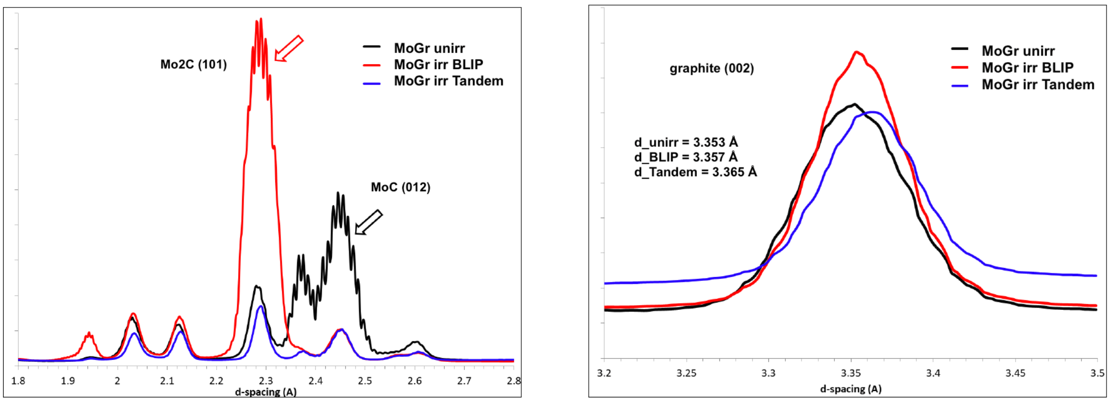

(a) Irradiation effects on MG-1110E. Wide d-spacing interval

(b) Irradiation-induced effects on (002) graphite reflection.

**Figure 6.22:** *Irradiation-induced changes in MG-1110E, extracted from the 2D detectors images in Figures. 6.20(a), 6.20(b), 6.20(c). Courtesy N. Simos, BNL.*

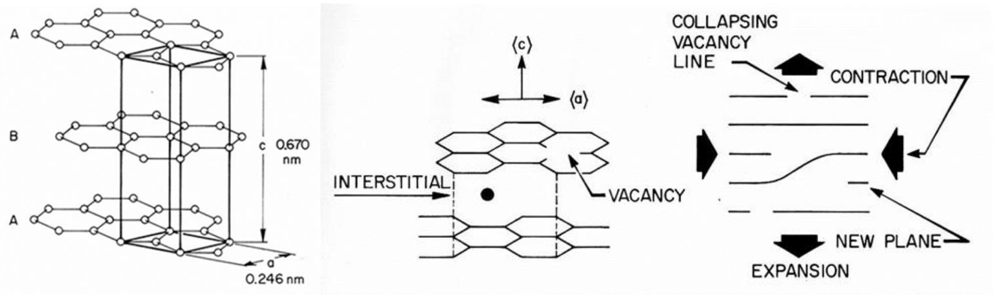

**Figure 6.23:** *Schematic of the damage process in graphite. Interstitial defects will cause crystallite growth perpendicular to the layer planes (c-axis direction) while coalescence of vacancies will cause shrinkage parallel to the layer planes (a-axis direction)*

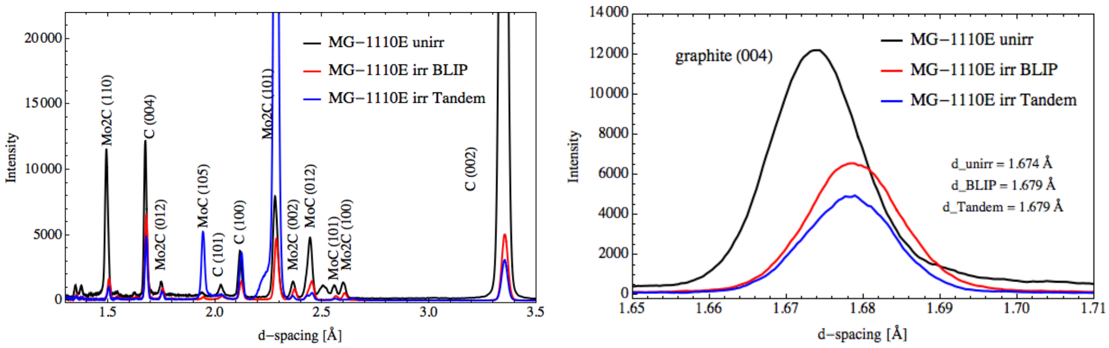

(a) Wide d-spacing interval.

(b) Irradiation-induced changes in (004) graphite reflection.

**Figure 6.24:** *Irradiation-induced changes in MG-1110E observed via 200 keV polychromatic X-ray beam of the X17B1 beam line at NSLS: comparison of unirradiated sample, BLIP-irradiated and Tandem-irradiated spectra.*

interstitial defects, seen also for MG-1110E.

From the visual inspection and these first XRD results, it seems that this new MoGr grade is more stable and resilient to radiation exposure than the previous one. A complete macroscopic characterisation, as well as more statistics for the diffraction tests, are required to fully confirm the improved behaviour under irradiation of the new generation of MoGr composite. This could not be carried out in the time frame of this thesis work because of the high activation level of the irradiated samples. Results are expected by end 2017, still on time for important feedback on the collimator production for the installation in the LHC planned for the Long Shutdown 2 (2018-2021).

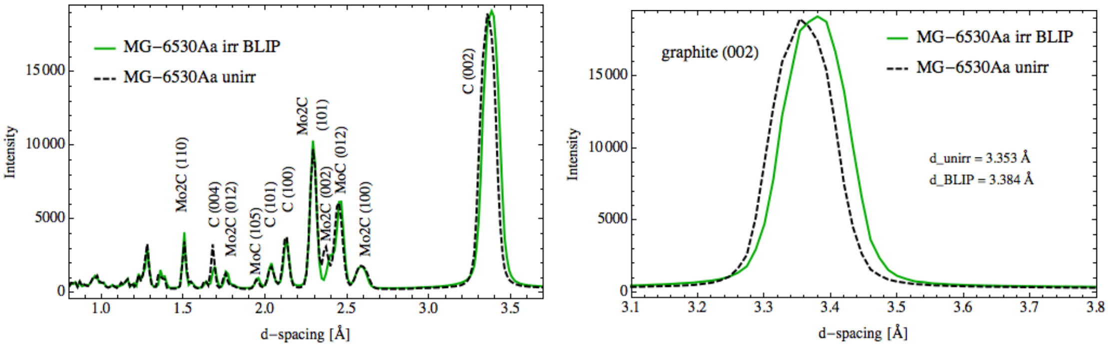

(a) Full d-spacing interval.

(b) Detail of (002) graphite reflection.

**Figure 6.25:** *Irradiation-induced changes in MG-6530Aa observed by 69 keV monochromatic X-rays 28ID beamline at NSLS II: diffraction spectra comparison between unirradiated sample and BLIP-irradiated one (fluence of* $\sim 5 \times 10^{19}\,\mathrm{p/cm^2}$.

## 6.4 Irradiation of CFC composite

Radiation exposure of carbon composite for LHC collimators (referred to as CFC, or 2D C/C, or AC-150K) was performed at BNL in 2006, when the material was irradiated with 200 MeV proton beam at BLIP [87, 109]. Unlike the capsule-enclosed setup used for later tests (like the ones that involved the MoGr), CFC's samples were cooled directly by the deionised water of BLIP (Figure 6.26(a)). The peak temperature recorded during the irradiation was about 120 °C. CFC was irradiated together with 3D-C/C composite and isotropic graphite (IG) for comparative purpose: as the main outcome of the campaign, all samples experienced serious structural degradation observed at fluence of $\sim 5 \times 10^{20}\,\mathrm{p/cm^2}$. However, the cooling made by direct contact with water might have played a role: radiolytic oxidation could have taken place as a result of the beam-induced radiolysis of the water, resulting then in free oxygen molecules that in turn react with the carbon atoms. This phenomenon contributes to the structural degradation of these carbon-based porous materials. CFC exhibited vulnerability to radiation especially along the "weak" direction: transversally cut sample with respect to carbon fibers planes appeared more severely damaged than their counterpart after the test (Figure 6.26(b)).

Because of the presence of the carbon fibers integrated in the graphite matrix and of the high degree of anisotropy, carbon-fiber-reinforced structures are more prone to experience dimensional change. The variation of the coefficient of thermal expansion (CTE) of unirradiated CFC as a function of the temperature is illustrated in Figure 6.27.

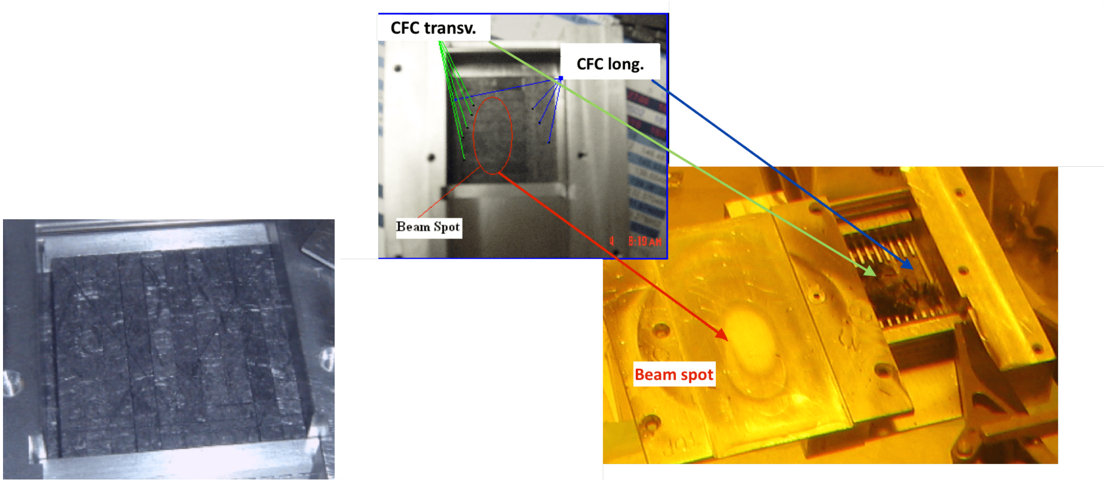

(a) Before irradiation.

(b) After irradiation.

**Figure 6.26:** *CFC capsule layout used for proton irradiation at BLIP. Disintegration of transversal specimens situated within* $1\sigma$ *of the beam is observed after irradiation. Courtesy of N. Simos, BNL.*

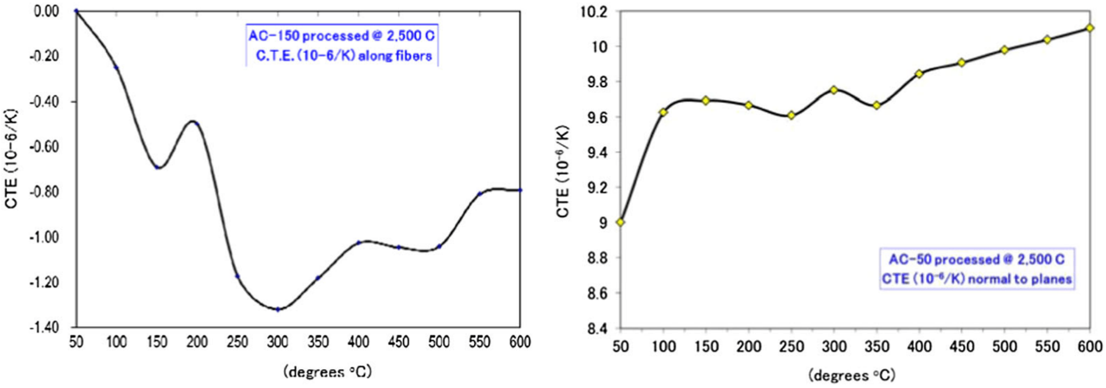

**Figure 6.27:** *Coefficient of thermal expansion (CTE) of unirradiated CFC along the two fiber orientations, longitudinal on the left and transversal on the right, given as a function of the temperature. Courtesy of N. Simos, BNL [109].*

The plot shows a significant variation of CTE with the temperature, different in the two directions, which demonstrates the anisotropy of the material: a negative CTE exists along the fibers, while it is increasingly positive normally to the basal planes. The volumetric changes in the CFC after thermal annealing cycles have also been studied. From Figure 6.28, it seems that the unirradiated structure stabilises after the thermal annealing in both the longitudinal and transversal orientations, which can be explained by a reduction of the initial porosity by thermal-induced growth into the preexisting pores of the material. Post-irradiation annealing performed on CFC irradiated with 200 MeV protons at fluence of $4.5 \times 10^{20}\ \mathrm{p/cm^2}$, showed the contraction in the direction normal to the fiber planes and the opposite effect along the planes occurring during the first thermal cycle at temperatures above the irradiation temperature (Figure 6.29). Above the irradiation temperature, in fact, radiation-induced defects mobilise and return to

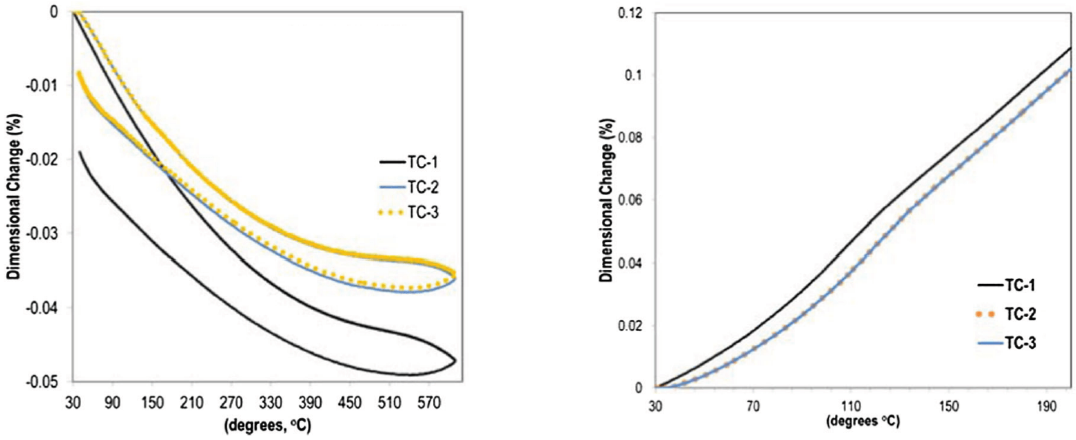

(a) Unirradiated CFC. Orientation parallel to carbon fibers.

(b) Unirradiated CFC. Orientation transversal to carbon fibers.

**Figure 6.28:** *Dilatometry test after thermal annealing of unirradiated CFC along the two sample cut orientations: parallel to fibers (left), transversal to fibers (right). Courtesy of N. Simos, BNL [109].*

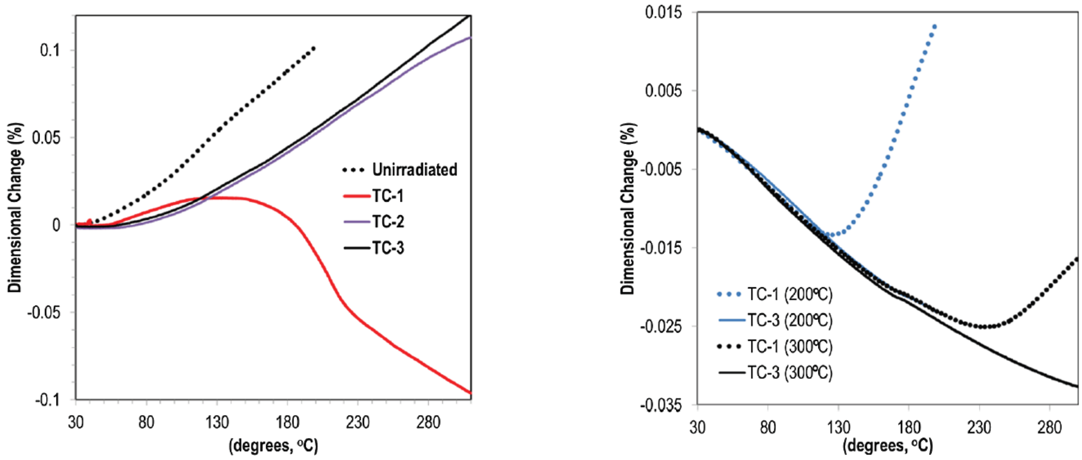

(a) Irradiated CFC. Orientation parallel to carbon fibers.

(b) Irradiated CFC. Orientation transversal to carbon fibers.

**Figure 6.29:** *Dilatometry test after thermal annealing of irradiated CFC (fluence of* $4.5 \times 10^{20}\ \mathrm{p/cm^2}$*) along the two sample cut orientations: parallel to fibers (left), transversal to fibers (right). Courtesy of N. Simos, BNL [109].*

their original position in the lattice of the graphite matrix.

A more recent irradiation of CFC was carried out at BLIP in 2016, together with new grades of MoGr, to allow a direct comparison between the two materials irradiated in the same conditions (no direct water cooling of CFC samples as in the first campaign). A proton beam of 200 MeV was delivered against the material placed in a capsule sealed under vacuum. The good response of all irradiated materials was shown in Figure 6.15, where the absence of a direct contact with the cooling water may also have reduced the radiation-induced radiolysis on CFC with respect to the experiments in 2006.

Diffraction tests were performed at NSLS-II facility on CFC sample irradiated at fluence up to $\sim 10^{20}\,\mathrm{p/cm^2}$ in three different points on the sample (top, middle, bottom) and then compared with the unirradiated patter, as depicted in Figure 6.30(a). First of all, the spectra taken in the different positions appear almost superposed in the three cases, which means that the irradiation along the sample was pretty uniform, also thanks to the use of a rasterised proton beam. The comparison with the pristine sample shows a similar peak intensity before and after irradiation. However, peak shifting clearly appears for some of the most relevant reflection of graphite (Figures 6.30(b) and 6.30(c)). Peaks shifted towards larger d-spacing as a consequence of the irradiation generally means a lattice growth due to defects generated by the radiation.

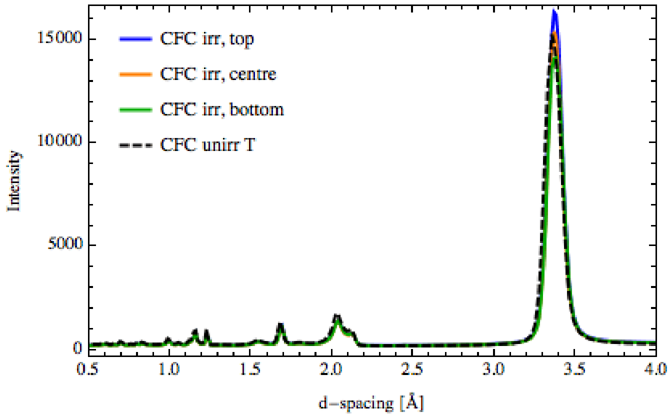

(a) Full d-spacing interval.

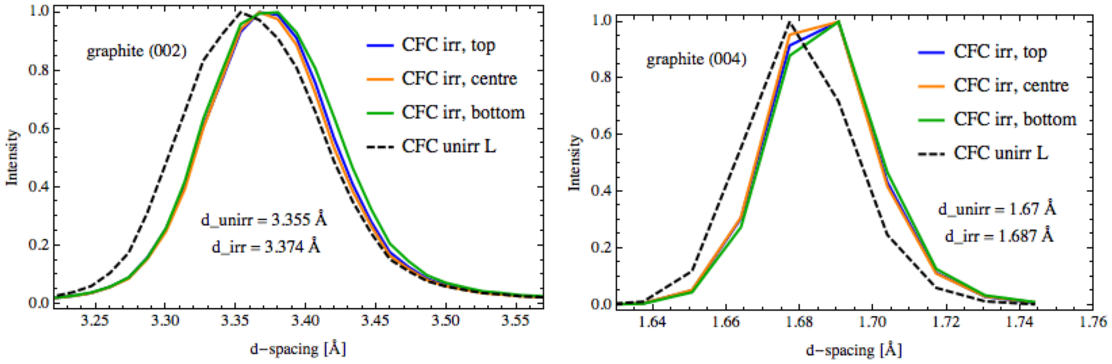

(b) Reflection of (002) graphite plane. Normalised peak.

(c) Reflection of (004) graphite plane. Normalised peak.

**Figure 6.30:** *Irradiation-induced changes in CFC observed by 69 keV monochromatic X-rays 28ID beamline at NSLS II: diffraction spectra comparison between unirradiated sample and BLIP-irradiated (fluence of* $\sim 10^{20}\,\mathrm{p/cm^2}$.

Post-irradiation macroscopic characterisation of the CFC samples irradiated in 2016 is still on-going. However, the available results would confirm the good response of this material, as well as the 3D-C/C composite and the isotropic graphite, to proton irradiation up to fluence of $\sim 10^{20}\,\mathrm{p/cm^2}$, while structural vulnerability has been proved for fluence of $\sim 5\times10^{20}\,\mathrm{p/cm^2}$.

During the period 2006-2007, CFC was also exposed to 30 MeV proton irradiation from the RRC cyclotron at Kurchatov Institute (Russia). First of all, an extensive measurement program was carried out to determine the physical and thermo-mechanical properties of the samples before irradiation. Notably, the effect of temperature on various CFC properties up to approximately 700 °C was studied: it was found that below 100 °C, i.e. in the operational range of LHC collimators, CFC has a negative thermal expansion coefficient. This feature has been thus considered in the collimator jaw design to compensate the expansion of the back copper plate in case of a jaw heating.

Changes od the physical and thermo-mechanical properties of CFC were investigated in a range of radiation doses from $10^{17}\,\mathrm{p/cm^2}$ until dose $3.1 \times 10^{19}\,\mathrm{p/cm^2}$. For 30 MeV protons, the penetration length in carbon is about 7 mm, which ensured a uniform irradiation over the volume of the 4 mm thick samples provided for the test. The results, reported in more detail in Ref. [103], demonstrate that the properties of CFC follow the general behaviour of carbon-based materials under irradiation: in particular, increased strength, increased resistivity, decreased thermal conductivity are found. However, in such anisotropic composites, the properties may vary significantly depending on the sample cutting direction with respect to the basal planes. In CFC, the stronger degradation of the properties as function of the irradiation dose was observed along the direction parallel to the basal planes. A sharp increase in the volume of the samples (up to 1.5%) was found, together with an increase in Young's modulus (50%), in electrical resistivity (up to 350%), and a reduction of the thermal conductivity (by 70-80%). In particular, electrical resistivity and thermal conductivity experience a stiffer change in the initial stage of irradiation, followed by a saturation. Property changes were observed in several bulk specimens, which confirms the reliability of the results.

At Kurchatov Institute, irradiation tests on CFC were also performed using 5 MeV 12-carbon ion beams from the cyclotron [103]. The data analysis showed that the deformation due to a fluence of $3\times10^{17}\,\mathrm{ion/cm^2}$ is approximately 2 $\mu$m for CFC samples. This value becomes not so small if compared to 5 $\mu$m penetration depth of carbon ions in graphite. From a visual inspection of the sample surfaces after irradiation, it was found that craters and caves not present before beam exposure were induced by irradiation. In some cases, also the carbon fibres present in the composite appeared broken.

## 6.5 Irradiation of CuCD composite

Copper-Diamond composite was tested in several irradiation experiments. At BNL, CuCD samples were exposed in the BLIP facility to 200 MeV proton beam (peak fluence of $\sim 1 \times 10^{21}\,\mathrm{p/cm^2}$) and some of the samples saw a mix spectrum of protons and spallation neutron (fluence of $\sim 6 \times 10^{18}\,(\mathrm{p+n})/\mathrm{cm^2}$). From a first visual inspection of the capsule containing the irradiated samples (Figure 6.31), the material successfully survived the tests. A darker zone is visible, which can be associated to the area that saw the beam within the first 1 or 2 $\sigma$ size. Local plastic deformation due to the irradiation temperature might be the cause of such discolouration.

Figures 6.32(a) and 6.32(c) reproduce the multiple diffraction spectra performed with 200 MeV X-rays by scanning along the thickness of the BLIP-irradiated and Tandem-irradiated CuCD samples. The peak distribution tends to remain very similar over the whole scanned length, without relevant widening or shifting of the main peaks. In Figures 6.32(b) and 6.32(d), a comparison with the unirradiated CuCD is done: it has been

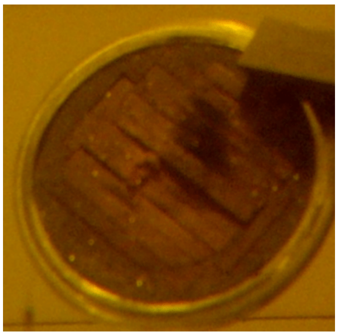

**Figure 6.31:** *Visual inspection of the CuCD capsule irradiated with 200 MeV protons at BLIP. Courtesy N. Simos, BNL.*

compared the lines from the center of the scanned profile, where the major effects from the impact of the proton beam are expected. In both cases, there is a good reproducibility of the pattern before and after irradiation as well as a good matching of the peaks.

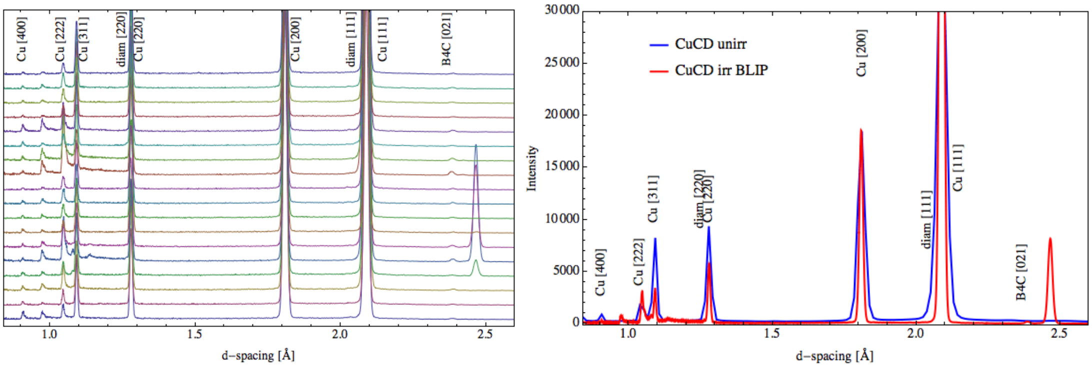

(a) 2D-projection scans. BLIP-irradiated CuCD.

(b) Comparison with unirradiated CuCD.

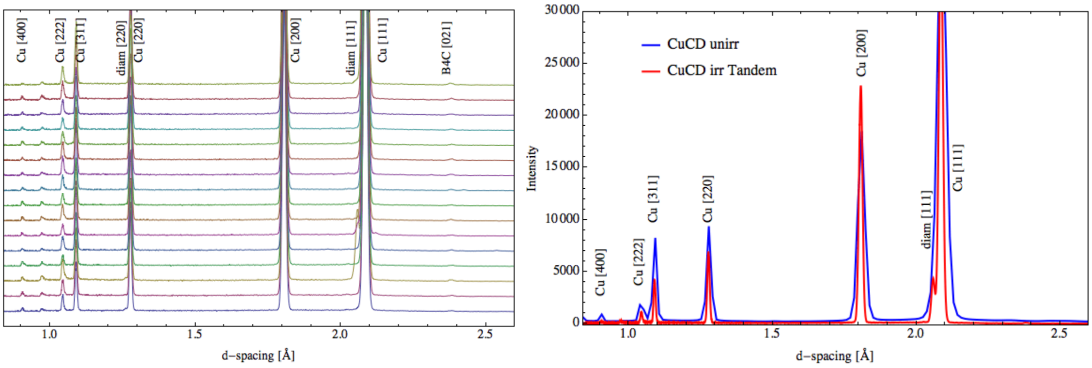

(c) 2D-projection scan.Tandem-irradiated CuCD.

(d) Comparison with unirradiated sample.

**Figure 6.32:** *Multiple through-thickness scans of CuCD samples irradiated at BLIP and Tandem, by mean of the 200 keV polychromatic X-ray beam of the X17B1 beam line at NSLS I.*

Waiting for the full post-irradiation characterisation to be completed, based on the first outcomes of the diffraction experiment we can preliminarily say that, so far, CuCD showed a good response to radiation tests with high energy protons.

Some samples of CuCD were irradiated at Kurchatov Institute with protons at the energy of 30 MeV, reaching a maximum fluence up to $\sim 10^{18}\,\mathrm{p/cm^2}$. The detailed report on these activities was published in Ref. [111]. Measurements showed that the density remains unchanged even at high fluence, as well as the electrical resistivity that however experienced a 10% increase at the maximum fluence. Thermal expansion coefficient (CTE) of CuCD samples changes almost linearly with the temperature increase. The experiments showed that, after first irradiation at $10^{17}\,\mathrm{p/cm^2}$, CTE increases by 5-7%, and by 35-40% after second irradiation at $10^{18}\,\mathrm{p/cm^2}$. Furthermore, thermal conductivity seemed to strongly reduce for all the measured samples after irradiation. SEM observations were performed to investigate possible changes in the material at the level of the microstructure. It was found that cracks, not present before irradiation, are formed at the interface between the copper matrix and the diamond particles at fluence of $\sim 10^{17}\,\mathrm{p/cm^2}$ and then progressively propagate in the matrix. Finally, by means of Transmission Electron Microscopy, a high density of dislocations and intrinsic stacking faults were observed in the diamond crystals closer to the surface and irradiated at high fluence.

In 2014, bismuth and uranium ion irradiation performed at GSI on CuCD: samples did not show any evidence of structural degradation and the composite turned to be very stable to ion beam irradiation.

## 6.6 Conclusions on irradiation tests and outlook

Radiation hardness of different grades of MoGr was tested using swift ions at GSI and high energy protons and fast neutrons at BNL. Ion irradiation performed at GSI revealed that the early grades exhibited an accentuated beam-induced dimensional changes and deformation. A continuous optimisation of the MoGr processing cycle and composition was carried on, in order to improve the radiation stability of the material. High temperature sintering, annealing and Ti addition have shown to reduce the deformation of the material at high doses. Carbon fibers can reduce the radiation-induced hardening and the degradation of electrical and thermal conductivity. However, the anisotropic swelling enhanced by the presence of the fibers can contribute to the matrix deformation. Therefore, the addition of short pitch fiber seems to be a good compromise solution. BNL irradiation experiments seem to confirme the improved radiation resistance of MoGr composites of the last generation.

The carbon-fiber-composite CFC, used in the present LHC collimators, showed similar behaviour of other carbon materials under proton irradiation at Kurchatov and BNL, i.e. increased mechanical strength, increased electrical resistivity, and decreased thermal conductivity. From the macroscopic point of view, the material did not show evidence of structural damage except for very high proton fluence ($\sim 5 \times 10^{20}\,\mathrm{p/cm^2}$), which is in line with the finding of damage threshold for other graphite composites. Diffraction experiments with synchrotron X-rays demonstrate that no relevant change in the microstructure of CFC occurs, either in the phase and in the lattice. Moreover, CFC turns to resist well also against ion beam irradiation.

Irradiation tests on CuCD proved its resistance to radiation-induced degradation of physical and thermo-mechanical properties, as a consequence of exposure to either proton or ion beams. At Kurchatov, modifications of few percents in the electrical conductivity, thermal diffusivity and CTE were measured after irradiation. No change in the phases present or in the interplanar spacing were observed at BNL by means of XRD technique.

The results collected from the several irradiation campaign performed so far are quite promising for assessing the overall good radiation resistance of the studied materials. However, it is very important to understand how the experimental results with low-energy and high-fluence beams can be scaled to the LHC case. The LHC collimators operate in a rather different radiation environment, owing to the smaller proton fluence but the much larger energies, which are concentrated in a relatively small fraction of the jaw volume (due to the small size of the secondary particle shower induced by the high energy beams). The issue has not been fully addressed yet: dedicated simulation studies are being launched, and are currently ongoing, in the attempt to find useful correlations between the experimental results and scenarios expected in the machine.

CHAPTER 7

# Simulation tools for new collimation materials

In this Chapter, simulation tools for collimation studies and a validation strategy are presented, which covered an important part of this PhD work. SixTrack is a well established beam dynamics code for accelerators, which features a dedicated implementation to model the interaction of beam particles with collimators. The need to evaluate the collimation performance of HL-LHC with newly developed composites has required an extended version of the present collimator material routine, which so far included only mono-element materials. The composite material model in SixTrack was successfully benchmarked with other simulation codes. Furthermore, a specific feature for fast beam failure simulations has been fully validated for the first time, through a detailed comparison of simulation results and direct measurements with the LHC beam, at energy close to that foreseen for the HL-LHC.

## 7.1 SixTrack code for collimation studies

SixTrack is a symplectic tracking code built for long term beam dynamics studies in high-energy rings [6–8]. It allows to compute the trajectories of single charged particles using six-dimensional vectors of coordinates ($x$, $x'$, $y$, $y'$, $s$, $E$) in circular accelerators. It has also a magnet system model which takes into account non-linearities up to the $20^{th}$ order.

A special version of SixTrack was developed to model also the interaction with collimators: this setup is currently used at CERN as standard tool for collimation studies [112]. With this routine, the dynamics of a large number of protons that populate the beam halo can be studied throughout the simulated ring, which is accurately described by a detailed LHC aperture model, and the interaction of the particles with the collimator materials, which generates different scattering mechanisms, can be also simulated. Moreover, to efficiently optimise the system, it is extremely important to collect sufficient statistics to reproduce in simulation the locations where losses are expected to occur in the machine.

In a SixTrack simulation, particles are tracked through the lattice element by element and their coordinates are transformed according to the type of element using a map derived from the electromagnetic field [113]. The machine optics, i.e. the sequence of beam line elements and and magnet strength, is read in from the output of the MAD-X code [114]. The so-called *thin lens* model is used to define the lattice: according to this approximation, magnetic elements are divided into an adequate number of slices. The main advantage of this formalism is to reduce the CPU computing time that would occur as a results of a standard thick-lens tracking. This approximation becomes extremely important when large machines, like the LHC, has to be studied.

In order to start a SixTrack simulation, a set of external input files are required [8]. Optics and lattice information are stored in a file called *fort.2*. A collimator database (*CollDB*) contains the details of each collimator, such as name, aperture, material, length, etc. The main tracking parameters, i.e. number of protons to run, number of turns, proton energy, initial distribution, etc, are collected in the *fort.3* data file. After providing SixTrack with such information, any machine and collimation configuration can be simulated.

When a particle hits a collimator jaw, it can undergo a number of different physical interactions (see Section 7.1.1 for additional details), until an inelastic events occur. At this point, SixTrack considers this particle “absorbed” at the location of the event and it is removed from the tracking. The hadronic and electromagnetic showers developed by the inelastic processes are not accounted for in SixTrack. Separated codes are used to model secondary particle showers. The main focus of SixTrack is, indeed, to simulate the dynamics of the beam halo in the the ring, reproducing accurate particle trajectories.

In addition to the losses on collimators, the simulation setup is also optimised to identify loss locations around the ring, in particular in the superconducting (cold) magnets. This is done by a dedicated program, *BeamLossPattern* [54], that follows the halo particles and compares their transverse amplitude to the LHC aperture. In the simulated ring, about 270000 points, one every 0.1 m step, are checked to identify the loss location in the machine. Then, another post-processing program, *CleanInelastic*, identifies the particle intercepted by the collimators only after touching the beam pipe and remove them from the count of collimator losses.

The final output of SixTrack simulations consists of detailed beam loss maps, which indicate the locations in the ring where the particles are lost. Simulated loss patterns from SixTrack, resulting from regular beam cleaning, have shown a good agreement with LHC data [115].

### 7.1.1 Particle-matter interactions in SixTrack

Before going into the details of the material implementation adopted by SixTrack, it can be useful to briefly recall the main scattering processes that a proton can undergo when interact with the matter. Scattering mechanisms in SixTrack are modelled by a

Monte-Carlo code, which derives from the K2 scattering routine [116], that has been recently reviewed and improved [117]. The scattering routine allows to simulate a set of proton-matter interactions in the collimator jaw, which can be classified in:

- *Continous interactions*, that include ionization, multiple Coulomb scattering and Rutherford scattering.
- *Point-like nuclear interactions*, that include nuclear elastic, inelastic and inelastic-diffractive scattering.

#### Ionization

When a charged particle collides against the atomic electrons along the path of the traversed material, the energy transferred from the incoming particle to the electrons can be high enough to put them in motion, and then ionising the material. The energy loss along the path, commonly called stopping power, is expressed by the Bethe-Bloch equation [118]:

$$-\frac{dE}{dx} = Kz^2\frac{Z}{A}\frac{1}{\beta_{rel}^2}\left[\frac{1}{2}\ln\frac{2m_ec^2\beta_{rel}^2\gamma^2T_{max}}{I^2} - \beta_{rel}^2 - \frac{\delta}{2}\right] \tag{7.1}$$

where $Z$ and $A$ are respectively the atomic number and the atomic mass of the material, $m_e$ is the electron mass while $z$, $\beta_{rel}^2$ and $\gamma$ are respectively the charge, the velocity and the relativistic factor of the incident particle. $I$ is the mean excitation energy, $T_{max}$ is the maximum kinetic energy that an electron can gain in one single collision and finally $\delta$ is a correction term depending on the density of the material. $K/A$ is a constant, equal to $(4\pi N_A r_e^2 m_e c^2)/A = 0.307075$ MeV g$^{-1}$ cm$^2$ for $A = 1$ g mol$^{-1}$. The energy loss per unit length (in MeV g$^{-1}$ cm$^2$) given as a function of the particle energy in any material varies very slowly for $E >$100 TeV [119]. In SixTrack, $dE/dx$ at the reference energy of 450 GeV/c was initially used to estimate the energy lost by ionization in both the injection and the top energy case. However, to more accurately estimate $dE/dx$, the revised version of the scattering routine [117] now computes Eq. 7.1 for protons of any given energy. This calculation requires information on atomic parameters, such as $Z$, $A$, $I$, as well as on the material density, needed for the conversion to metric units (GeV/m).

#### Multiple Coulomb Scattering (MCS)

When a charged particle traverses a medium, it faces many small angle deflections, most of them caused by Coulomb scattering from the nuclei, so the origin of its name. According to Moliere's theory [120], the rms of the deflection angle $\theta$ after crossing a thickness $s$ of material is given by:

$$\theta(s) = \frac{13.6MeV}{\beta_{rel}cp}z\sqrt{\frac{s}{X_0}}\left[1 + 0.038\ln(\frac{s}{X_0})\right] \tag{7.2}$$

where $p$ is the momentum of the incident particle. $X_0$ is the radiation length of the material and indicates the mean length of the medium that the particle has to traversed to reduce its energy by $1/e$.

### Rutherford scattering

This mechanism takes place when the incoming proton passes very close to a nucleus and is deflected away with a large scattering angle by the repulsive force due to the positive charge of the nucleus. It is still considered as Coulomb scattering, but with a finite cross section defined as:

$$\frac{d\sigma_{ruth}}{dt} = 4\pi\alpha^2(\hbar c)^2 \left(\frac{Z}{t}\right)^2 e^{-0.856\times10^3 tR^2} \tag{7.3}$$

where $a = 1/137$, $(\hbar c)^2 = 0.389$ GeV$^2$mbarn and $Z$ is the atomic number. The factor proportional to $1/t^2$ is the classical Rutherford formula for Coulomb scattering near a point charge. The exponential term is the nuclear form factor that accounts for the finite size of the nucleus. $R$ is the radius of the nucleus that, if not measured, is calculated by $R = 2\hbar c\sqrt{b}$. $b$ is the slope factor of the angular distribution for proton-nucleus elastic interaction, which is correlated to the mass number of the material by the formula $b = 14.1A^{2/3}$.

### Point-like interactions

Unlike the previous mechanisms that occur over a certain length of the material, proton-matter interaction can also involve an incoming proton and one of the components of the atomic structure of the traversed material (like nucleons, i.e. protons or neutrons, or the entire nucleus). The proton-nucleon interactions can be elastic, inelastic or inelastic-diffractive. The implementation of such scattering mechanisms in SixTrack has been extensively discussed in Ref. [117, 121].

In *nuclear elastic* scattering, the beam particle survives to the event it underwent, changing direction and energy according to the two-body kinematics. With a look at the LHC, nuclear elastic scattering, together with ionisation and MCS, plays a major role in diluting the beam particles and reducing their energy when they survive to the impact onto a collimator.

In *nuclear inelastic* scattering the incoming particle do not come out from the material (and therefore considered lost there), and generate new (secondary) particles. These events are extremely important in the design of beam intercepting devices, as they provide an estimation of the beam attenuation.

Moreover, *single-diffractive* (SD) scattering also exists. The momentum transferred during the collision can excite a nucleon of the medium, that have enough energy to travel some distance through the medium. However, the probability that the incoming proton survives without being lost is null. From here the reason why SD scattering is considered a quasi-elastic mechanism. This process is very important for LHC collimation because part of the betatron halo is converted into an off-momentum halo, due to the larger variation in energy of the particles after the event.

### Particle mean free path

Point-like interactions and Rutherford scattering are mechanisms with a finite probability to take place once the incoming particle has travelled a certain characteristic length inside the material, which is called *mean free path*. In other words, this quantity corresponds to the average distance a particle can travel in the medium without undergoing any collision event with another particle or nucleus. The mean free path $\lambda_i$ of each process $i$ mentioned above is inversely proportional to the cross section of the process itself and it can be expressed through the formula:

$$\lambda_i = \frac{1}{\sigma_i} \frac{A}{\rho N_A} \tag{7.4}$$

where $\sigma_i$ is the cross section of the process, $\rho$ and $A$ are respectively the material density and the atomic weight, and $N_A$ is the Avogadro number. A *total collision length* is also defined as:

$$\frac{1}{\lambda_{tot}} = \frac{\rho N_A}{A} \sigma_{tot} = \frac{\rho N_A}{A} \left(\sigma_{el} + \sigma_{SD} + \sigma_{inel} + \sigma_{ruth}\right) \tag{7.5}$$

that takes into account all the possible elastic, quasi-elastic and inelastic collisions, as well as the Rutherford scattering events, that can occur along the path. In the LHC, the *inelastic collision length* $\lambda_{inel}$ is particularly important for the collimator design, as it expresses the average length needed to achieve an attenuation of $1/e$ of the primary particle, by nuclear inelastic events.

## 7.2 Collimator material routine in SixTrack

A dedicated database embedded in SixTrack stores the material properties required by the scattering routine to simulate the different scattering processes. Some of the input parameters are:

- Atomic and mass number,
- Material density,
- Radiation length,
- Mean excitation energy,
- Cross sections of the point-like interactions,
- Rutherford scattering cross section.

So far, only pure materials were implemented in the code, which are i.e. aluminium, beryllium, carbon, copper, lead, and tungsten. The values of the material properties were directly taken from Ref. [119] or used in the formulas discussed in Section 7.2.1 to calculate the desired parameters. However, the need to study future LHC configurations with novel collimator materials has required an upgrade of such routine to also include composite materials.

### 7.2.1 Implementation of composite materials

Composite materials, already used in the present LHC collimators or being considered for the HL-LHC collimation upgrades, have been added to the existing material database in SixTrack. The newly implemented materials are:

- Molybdenum-Graphite composite (MoGr, grade MG-6530Aa),
- Copper-Diamond composite (CuCD),

- Tungsten Heavy Alloy Inermet-180 (IT-180),
- Glidcop.

The material routine in SixTrack treats mono-element materials. In the presented approximation, composite materials are dealt with by calculating off-line the input parameters required by the code, starting from the material composition. The result is a "composite" nucleus weighted on the constituent nuclei. The approximation considers an “averaged” composite material, which is not detailed described at the atomic level. In simulation, this approach can affect the scattering processes that occur locally in the material. However, we remind that collimators are bulk devices, whose final properties are anyway averaged over the full size of the collimator. Therefore, we expect that the approximations done in our implementation are consistent and can reproduce the properties of the composite materials without large errors. Comparative simulation studies were also performed with the aim of quantifying the error of this approximation by comparing the results with that of a more "physical" material approach used by other codes. The main outcomes of the study are discussed in Chap. 7.2.2.

A description of how the values of each parameter required by the database have been calculated for composite materials is provided below. The atomic number $Z$ and atomic weight $A$ of each compound material was calculared as average weighted on the atomic fraction of their components $i$:

$$p = \sum_i at_i \cdot p_i, \quad \text{(i = 1, 2,...)} \tag{7.6}$$

where $p$ is the property of the compound to be computed, $p_i$ are the values of the property, extracted from the Particle Data Group database [119], for the i-th element present in the material and $at_i$ the atomic content of each element in the composite.

The mean ionization energy $I$ and the radiation length $\chi_0$ must be provided to SixTrack to calculate the energy lost by ionization and correctly simulate the MCS events. According to [119], for a composite material, these parameters can be approximated by:

$$\frac{1}{p} = \sum_i \frac{wt_i}{p_i}, \tag{7.7}$$

where $wt_i$ is the mass fraction of the i-th element in the compound. Once more, $p_i$ refer to values in [119].

The incoming protons can interact with the nuclei of the material in different ways. Each process is characterized by its cross section ($\sigma$), that gives the probability for the scattering process to occur in a specific material. The total nuclear cross section ($\sigma_{\text{tot}}$) and the nuclear inelastic cross sections ($\sigma_{\text{inel}}$) at 450 GeV were implemented in SixTrack, calculated as follows:

$$\sigma = \frac{A}{N_A \rho \lambda}, \tag{7.8}$$

with $N_A$ Avogadro’s number, $A$ and $\rho$ the average atomic weight and the density of the material, respectively. For composite materials, the collision length ($\lambda_{\text{tot}}$) and the inelastic length ($\lambda_{\text{inel}}$) are calculated as in Eq. (7.7). The Rutherford scattering cross section $\sigma_{ruth}$ was derived through Eq. 7.3. In particular, the radius $R$ and the slope factor $b$ were computed by using the average mass weight for the "composite" nucleus, calculated as in Eq. 7.6.

Table 7.1 lists the most important parameters, along with the composition, of the materials considered in the implementation. The properties of CFC are also reported in the table for comparison, although the material was already coded in SixTrack as pure carbon.

**Table 7.1:** *Summary of the properties of the new composite materials added in SixTrack: average atomic number $Z$, average atomic weight $A$, density $\rho$, electrical conductivity $\sigma_{\mathrm{el}}$, composition by atomic fractions, radiation length $\chi_0$, collision length $\lambda_{\mathrm{tot}}$ and inelastic scattering length $\lambda_{\mathrm{inel}}$ for 200 GeV/c protons.*

| | $Z$ | $A$ (g/mol) | $\rho$ (g/cm$^3$) | $\sigma_{\mathrm{el}}$ (MS/m) | **at. content** (%) | $\chi_0$ (cm) | $\lambda_{\mathrm{tot}}$ (cm) | $\lambda_{\mathrm{inel}}$ (cm) |
|---|---|---|---|---|---|---|---|---|
| **CFC** | 6 | 12.01 | 1.67 | 0.14 | 100 C | 25.57 | 35.45 | 51.38 |
| **MoGR** | 6.653 | 13.532 | 2.5 | 1 | 2.7 $Mo_2C$, 97.3 C | 11.931 | 24.84 | 36.42 |
| **CuCD** | 11.898 | 25.238 | 5.4 | 12.6 | 25.7 Cu, 73.3 CD, 1 B | 3.162 | 13.56 | 20.97 |
| **Glidcop** | 28.823 | 63.149 | 8.93 | 53.8 | 99.1 Cu, 0.9 $Al_2O_3$ | 1.442 | 9.42 | 15.36 |
| **IT-180** | 67.657 | 166.68 | 18 | 8.6 | 86.1 W, 9.9 Ni, 4 Cu | 0.385 | 6.03 | 10.44 |

The composite materials implementation in SixTrack has been validated and is now part of the official release of the code.

### 7.2.2 Comparison of SixTrack composite material implementation with other simulation codes

SixTrack and MERLIN [122] are simulation tools commonly used for particle tracking and collimation studies. However, the two codes use different approaches to treat composite materials. In SixTrack point-like scattering are performed from an imaginary composite nucleus (which is the weighted average of the constituent nuclei). In Merlin, when a point-like scattering occurs, an elementary constituent nucleus of the material is randomly selected and the proton scatters from the constituent nucleus with corresponding cross sections and all other properties. MERLIN can also reproduce a similar approach to the SixTrack one by enabling point-like scattering from the composite nucleus instead of the constituent nuclei. The two approaches have been compared in order to quantify the errors [123]. In the following, the former method will be called MERLIN-method, the latter MERLIN-6T-method.

The case of a pencil beam ($6.4 \times 10^6$ protons) impacting on 1 cm long block of material has been considered. Figure 7.1 shows the change in polar angle $\theta$ and particle momentum $dp$ for particles that undergo single diffractive (SD) events in the material block (either MoGr or CuCD): the distribution of $\theta$ and the spread in energy loss are larger in MERLIN, while SD events resulting in small energy loss are more frequent in SixTrack. The simulations of MCS and ionisation events is based on the same approach in the two codes. As expected, the distributions in Figure 7.2 appear identical.

From a first comparison, SixTrack and MERLIN results have shown small differences in spite of the different approaches of the two codes in treating composite materials. For the purpose of our tracking studies, we consider these differences small enough to reliably used the simplified approach implemented in SixTrack.

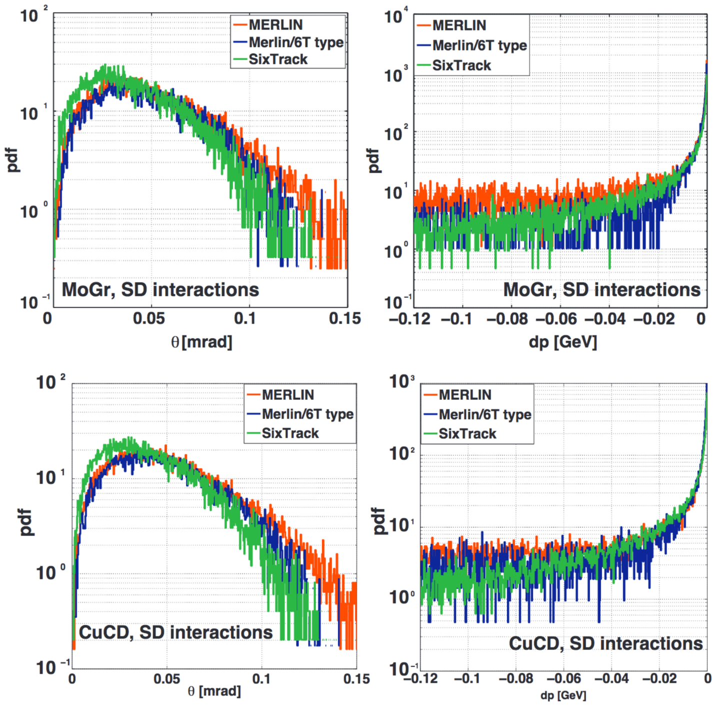

**Figure 7.1:** *Comparison of simulation results using MERLIN-method, MERLIN-6T-method and SixTrack. Distribution of polar angle θ (left) and energy loss dp (right) for single diffractive events in MoGr (top) and CuCD (bottom) block. Courtesy of A. Valloni [123].*

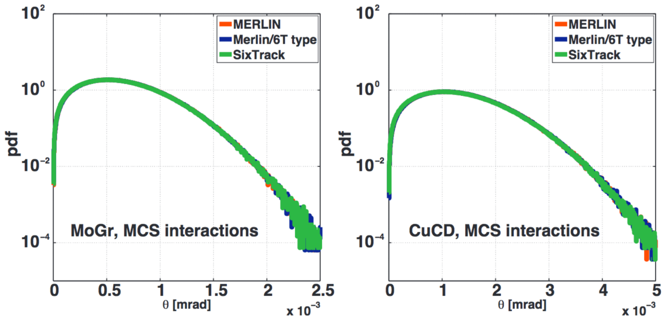

**Figure 7.2:** *Comparison of simulation results using MERLIN-method, MERLIN-6T-method and SixTrack. Distribution of polar angle θ for multiple Coulomb scattering and ionisation events in MoGr (left) and CuCD (right) block. Courtesy of A. Valloni [123].*

## 7.3 SixTrack simulations for fast failure scenarios

To dynamically simulate beam failure scenarios in the LHC (see Chap. 2.2.2 for reference), the setup of SixTrack simulations was adapted, as detailed in Refs. [124–126]. In practice, a dynamic kick is applied to the beam particles when they arrive at any of the 15 beam extraction kickers (MKD) in IR6. The kick angle received by each proton bunch in simulation is a function of the rise time of the MKD's magnetic field. A Gaussian bunch profile of SixTrack macro-particles is tracked for 3 turns: when the particles pass the MKDs at the second turn, they receive an intermediate kick, which risks to kick them onto the machine aperture. At the third turn, the MKDs have reached their full field and all remaining particles are extracted. These simulations are performed with the full LHC collimation system in place.

SixTrack simulations were performed for the case of an asynchronous beam dump (ABD), where all the dump kickers misfire simultaneously, for different optics deployed in the LHC Run II at 6.5 TeV. In Chap. 7.3.1, simulation results will be compared with experimental measurements with the LHC beams. A train of 6.5 TeV protons with 25 ns spacing between consecutive bunches was simulated for both LHC proton beams. In simulations were taken into account only the bunches belonging to the zone of angles not caught by the IR6 collimators and still in a range that can hit the TCTs before seeing the full field at the third turn (grey band in Figure 7.3) .

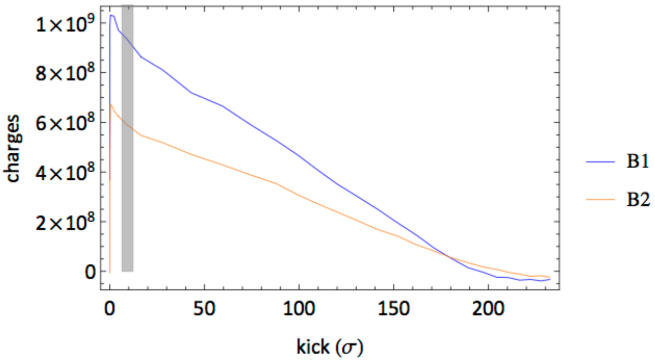

**Figure 7.3:** *Abort gap population, measured by the abort gap monitors during the asynchronous dump test with tight collimator settings and* $\beta^*$ *= 80 cm for both beams, giving as a function of total kick in* $\sigma$ *summed over all MKDs.*

Three machine configurations of the LHC 2015 proton run at 6.5 TeV were considered: for the first one, the injection optics ($\beta^*$= 11 m) is used, while in the other two the optics is squeezed to $\beta^*$= 80 cm and the collimators are set either to nominal settings [127] or tighter settings as in a special study [128]. The experimental procedure to validate the machine protection settings against asynchronous beam dump foresees adding bumps at IR6 collimators to account for orbit drift. In simulation, this was reproduced by further retracting the TCDQs and TCSP by the corresponding amount. The deployed collimator settings used in simulations are listed in Table 7.2.

The distribution of particles lost in the ring as simulated by SixTrack for the three considered cases is shown in Figures 7.4(a), 7.5(a) and 7.6(a). The losses at collimators and magnets were summed over all bunches considered in the simulation. Simulations of TCDQ losses are multiplied by a factor 7 to take into account not simulated bunches that however in measurement are absorbed by this collimator. As expected, in all cases the main loss location is in IR6, but high loss peaks stick out also from collimators in IR7. Losses at IP1/5 TCTs increase when tightening the settings, while the peak in IP8, not visible at flat top when collimators are still opened, appears for squeezed optics. On the other hand, IR3 decreases looking from flat top to squeeze, maybe because particles

**Table 7.2:** *Collimator settings used for SixTrack simulations at 6.5 TeV in various machine configurations. The values are expressed in units of standard deviation [$\sigma$] of the beam size, calculated for a normalized emittance of 3.5 $\mu$m rad.*

| Location | Collimator Families | Flat top ($\beta^*$= 11 m) | OP squeeze ($\beta^*$= 80 cm) | MD squeeze ($\beta^*$= 80 cm) |
|---|---|---|---|---|
| IR7 | TCP/TCSG/TCLA | 5.5 / 8 / 14 | 5.5 / 8 / 14 | 5.5 / 8 / 14 |
| IR3 | TCP/TCSG/TCLA | 15 / 18 / 20 | 15 / 18 / 20 | 15 / 18 / 20 |
| IR6 | TCSP - TCDQ | 9.1 + 2.4 | 9.1 + 2.4 | 9.1 + 2.4 |
| IP1/5 | TCT | 37 | 13.7 | 10.7 |
| IP2/8 | TCT | 37 / 37 | 37 / 15 | 37 / 15 |

are caught by IP5.

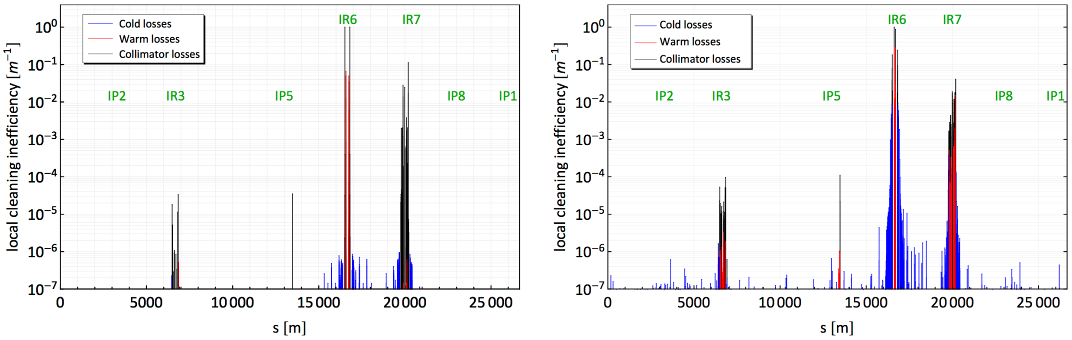

(a) SixTrack simulation.

(b) Measurement performed on 6.9.2015 at 10:59:13.

**Figure 7.4:** *Loss distribution in the ring following asynchronous beam dump at 6.5 TeV with injection optics ($\beta^*$ = 11 m).*

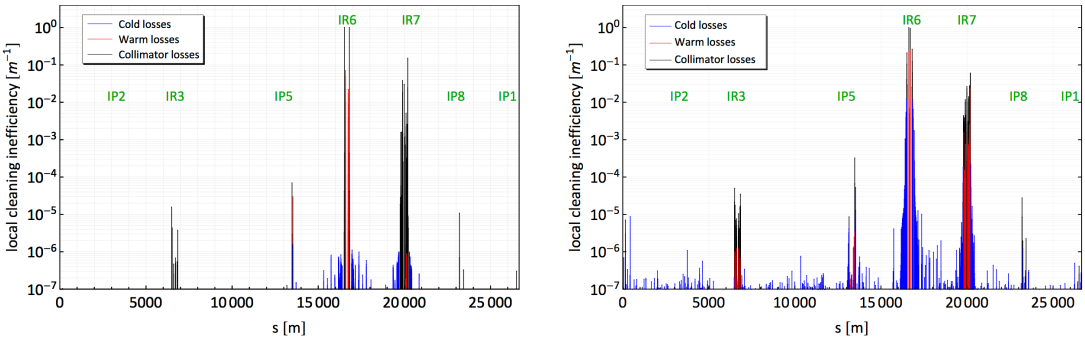

(a) SixTrack simulation.

(b) Measurement performed on 4.7.2015 at 15:43:26.

**Figure 7.5:** *Loss distribution in the ring following asynchronous beam dump at 6.5 TeV with squeezed optics ($\beta^*$ = 80 cm).*

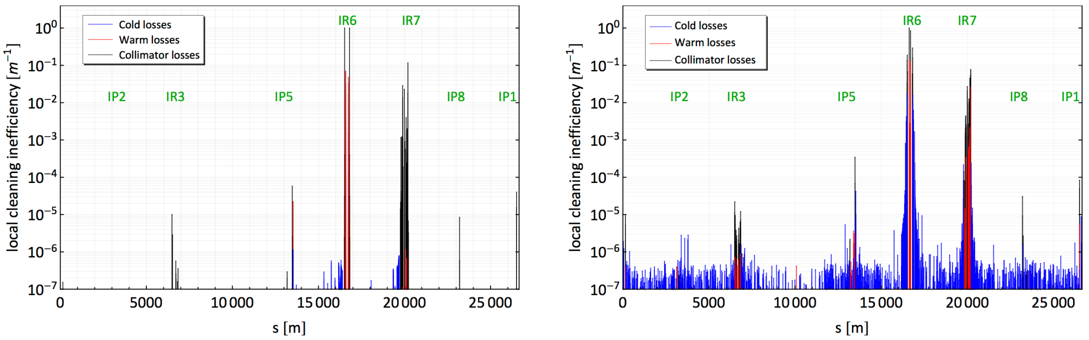

(a) SixTrack simulation.

(b) Measurement performed on 9.10.2015 at 07:13:26.

**Figure 7.6:** *Loss distribution in the ring following asynchronous beam dump at 6.5 TeV with squeezed optics ($\beta^*$ = 80 cm) and tighter TCT settings in IP1/5.*

### 7.3.1 Measurements with LHC beams at 6.5 TeV

It is fundamental to benchmark SixTrack simulations for beam failure scenarios to have a reliable tool that could predict the response of the LHC collimators in future machine configurations and beam parameters. Measurements of fast beam losses performed in 2015 are used to benchmark SixTrack results.

Asynchronous beam dumps in the LHC were mimicked by first turning off the RF system to induce a debunching of a bunch in a bucket next to the abort gap. Once a sufficient abort gap population was reached, a standard beam dump was triggered. Examples of the abort gap distribution at the moment of the dump are shown in Figure 7.3. Loss data at flat top and squeeze with nominal collimator settings were taken during asynchronous dump tests performed in a standard LHC configuration, while a dedicated measurement session (MD) was devoted to test the squeezed optics with tighter collimator settings [128]. The signals were recorded by ionising chambers (BLMs) and then normalized to the highest value. The signals with an integration time of 1.3 s are collected in Figures 7.4(b), 7.5(b) and 7.6(b) for the cases in analysis.

A detailed quantitative comparison between simulated and measured loss patterns is made more difficult by the fact that the presented simulation chain produces lost protons on the aperture, while the BLM signal is mainly caused by the shower particles created by the impact and could be simulated by energy deposition tools. However, a good qualitative agreement can be stated for the three scenarios: the level of normalised losses estimated in simulations in IR6 and IR7 is well reproduced by the measurement, as also the higher contribution to the losses in IR7 from Beam 2 (right side of the insertion) due to the worst phase advance with respect to Beam 1. The same trend is visible in IR3, although the discrepancy between simulations and measurements is slightly higher than the other IRs. Reproducing the measured losses in IP1, IP5 and IP8 within factors 3-4 is a very good result considering that showers are not included in SixTrack. The upstream showers are also very likely responsible for the high warm losses in IR3, IR6 and IR7, which are absent in the simulations as shown in [115]. The blue spike sticking out from IP2 in Figure 7.6(b) is noise recorded by a single BLM upstream of IP2 that can be reasonably discarded when compared with simulation.

### 7.3.2 Comparison of simulation results and measurements

The fraction of the total abort gap population impacting on the horizontal tertiary collimators in IP1 and IP5 measured during the ABD is compared with SixTrack simulations for the same collimators in all the configurations considered for this study. In order to have a meaningful comparison, the BLM signals were converted from Gy/s to the estimated number of protons impacting the TCT, with a procedure detailed in [126], and then normalised to the abort gap population at the time of the dump. It should be also noted that the simulated bunches were all equally populated, while the population was not fully homogeneous during the measurement (Figure 7.3). Therefore, each simulated bunch was normalised to the measured population profile of the abort gap over the corresponding 25 ns interval and in the end the losses at the TCTs were summed over all bunches and normalised to the total abort gap population.

By looking at the ratio for single TCTs in Figure 7.7, it can be stated that the overall accuracy of the simulations with respect to the measurements is good: all results are within the expected uncertainties except for TCTPH.4R1.B2, which should be investigated more in detail. Possible explanations for the discrepancy could be errors on the BLM placement or electronics, causing a different BLM response, or errors on the assumed collimator setting.

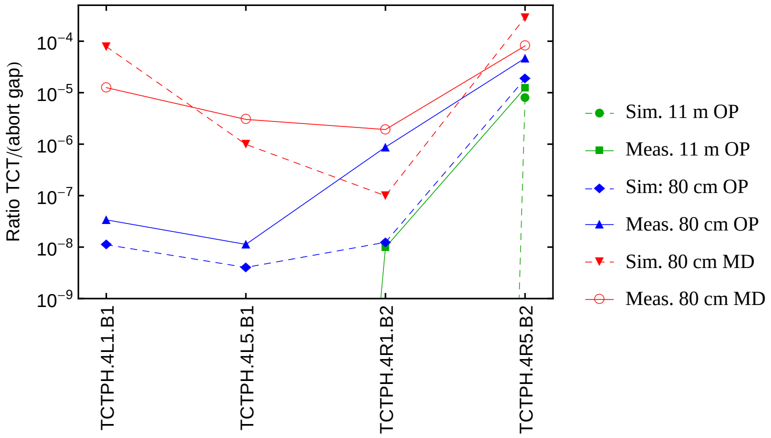

**Figure 7.7:** *Fraction of the total abort gap population impacting on the TCTs in IP1/5 during the asynchronous dump in simulation and measurement for the cases discussed.*

## CHAPTER 8

# Methods for collimator material choice validation at HL-LHC

The achievement of the HL-LHC beam parameters strongly relies on a upgraded collimation system, based on novel collimator materials and design. The final choice of materials requires the evaluation of the performance of the new collimation system under either nominal operation and accidental conditions. This chapter presents the results of simulation studies perform during this PhD work to finalise the material choices for the collimator families more involved in the upgrade, i.e. secondary collimators, tertiary collimators and dispersion suppressor collimators.

## 8.1 Secondary collimator materials

New materials are considered to replace the present CFC jaws of primary (TCP) and secondary (TCSG) collimators aiming at reducing their large contribution to the electromagnetic impedance, while preserving the robustness of the device against either single-turn and steady-state losses.

### 8.1.1 Cleaning performance with low-impedance collimators

To study the effect of new collimator materials on the cleaning efficiency of the collimation system, SixTrack simulations were performed for the two beams and in the two planes of the halo distribution. The accelerator ring simulated in SixTrack was configured as 7 TeV HL-LHC machine, with optics squeezed to $\beta^* = 15\,\text{cm}$. The full collimation system was simulated and the collimator openings were set according to Table 8.1: a $2\,\sigma$ retraction between primary and secondary collimators in IR7 was used [129], where $\sigma$ is the local betatronic beam size at the collimator assuming a nominal normalized emittance of 3.5 $\mu$m and the design $\beta$-function.

**Table 8.1:** *Collimator settings used for the SixTrack simulation. The values are expressed in units of standard deviation of the beam, calculated for a normalized emittance of 3.5 $\mu$m rad.*

| **Collimator Families** | **Settings** [$\sigma$] |
|---|---|
| IR7 TCP / TCSG / TCLA | 5.7 / 7.7 / 10 |
| IR3 TCP / TCSG / TCLA | 15 / 18 / 20 |
| IR6 TCSG / TCDQ | 8.5 / 9 |
| IP1/5 TCTs | 10.9 |
| IP2/8 TCTs | 30 |

In simulations, present IR7 primary or secondary collimators made of CFC were replaced with new collimator jaws, in either MoGr or CuCD. To do so, the updated material implementation described in Chap. 7.2.1 was used. The combinations of collimator replacements considered in simulation are listed below:

**Case 1** : all IR7 secondary collimators in MoGr

**Case 2** : all IR7 secondary collimators in CuCD

**Case 3** : all IR7 primary collimators in MoGr

**Case 4** : all IR7 primary collimators in CuCD

In a preliminary approach, simulated beam losses in collimators and magnets around the LHC ring were studied for the cases of interest. Figure 8.1 illustrates the loss distribution of Beam 1 horizontal halo for Case 1 (a-b) in comparison with the results for Case 4 (c-d). As most of the first interaction of the protons with the IR7 collimators occur in the TCP and given the higher density of CuCD than that of CFC, we would expect a pattern in Case 4 with some differences with respect to the other cases. However, it is hard from such overviewing plots to catch similarities and differences in the simulated cases. For this reason, the analysis below focuses on specific portions of the simulated ring, i.e. the two blocks of the superconducting magnets in IR7, the secondary collimators in IR7 and other collimators of particular interest in other locations. However, as future reference, a complete set of loss maps for the two beams and two planes in the Cases 1 to 4 can be found in the Appendix A.

We look at the losses in the dispersion suppressor (DS) magnets in the two clusters, of about 30 m long each, downstream of IR7 (from now on, called DS1 and DS2 respectively). These are by now the highest loss locations in the layout of the present collimation system. However, for the new HL-LHC baseline, the installation of up to two collimators per beam, one in front of each clusters, is currently under consideration: these collimators should efficiently catch such losses, preventing to reach the DS magnets. The simulation results presented below are a case study, which considers a pessimistic scenario where no DS collimators are installed, therefore the effects of the change in the collimator material on the losses in the DS can be isolated. The following

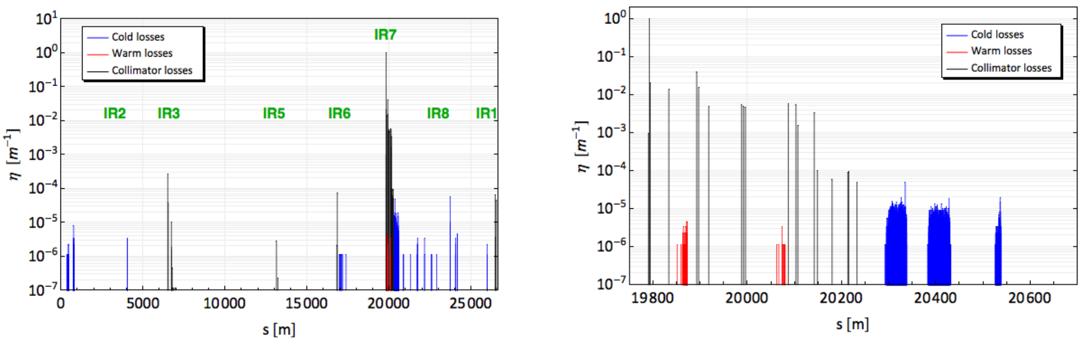

(a) Case 1. Full ring.

(b) Case 1. Betratron cleaning insertion IR7.

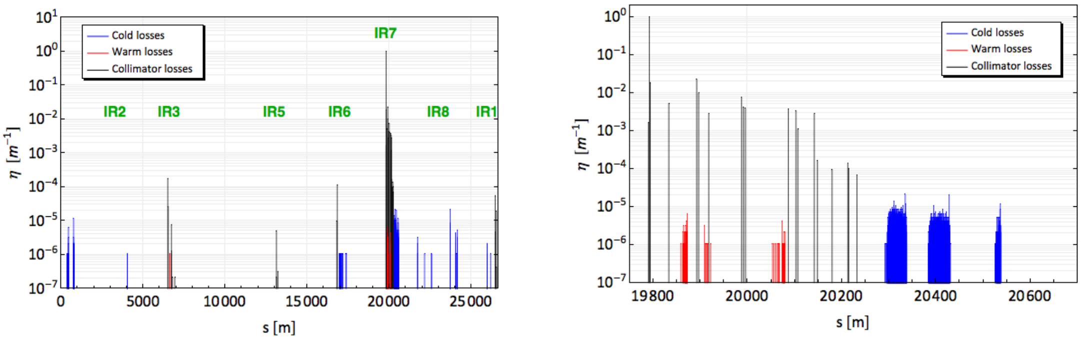

(c) Case 4. Full ring.

(d) Case 4. Betratron cleaning insertion IR7.

**Figure 8.1:** *Simulated beam loss map at 7 TeV of the HL-LHC machine for Case 1-4, Beam 1 horizontal halo.*

formula was applied to calculate the cleaning inefficiency in the DS clusters:

$$\eta_i = \frac{N_{loss\,DS_i}}{l_{DS_i} \times N_{abs}}, \qquad (i = 1, 2) \tag{8.1}$$

where $N_{loss\,DS_i}$ is the sum of the losses occurred within the length $l_{DS_i}$ =30 m, and $N_{abs}$ is the total particles absorbed by the collimators.

The results of the cleaning inefficiency calculated in the two DS clusters for different materials of the IR7 secondary collimators are illustrated in Figure 8.2. In the first cluster, we find about 40% higher inefficiency in B2 H than in the other cases, already when CFC's collimators are used. The replacement of the collimator jaw with novel material slightly improves the cleaning performance in all the simulated scenarios of about a factor 3-4, depending whether MoGr or CuCD (higher-Z) is used. In the second cluster, B1 V turns out to be the worse case for the cleaning, but the change in the secondary collimator material would improve by 10-12%. However, one has to be taken into account that the statistics of the particle lost in this cluster is quite poor, as indicated by the larger error bars. As expected, the losses in the DSs are not affected in a relevant way by the material choice of the TCSGs. Particles that reach the DS magnets are indeed generated by single diffraction events that take place in the primary collimators [130].

In Figure 8.3, the effect of the replacement of the primary collimator material is

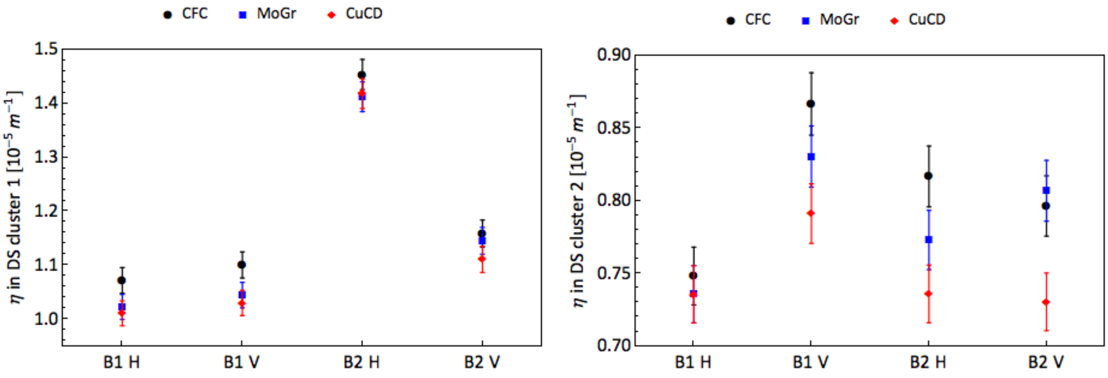

(a) IR7 DS cluster 1.

(b) IR7 DS cluster 2.

**Figure 8.2:** *Simulated cleaning inefficiency in the two clusters of the IR7 DS when different materials of secondary collimators are used. Results are shown for Beam 1 and Beam 2, horizontal and vertical halo.*

shown in the DS. As expected, when TCPs are changed with a denser material than CFC, a large improvement up to 50% in the cleaning efficiency is found in both clusters.

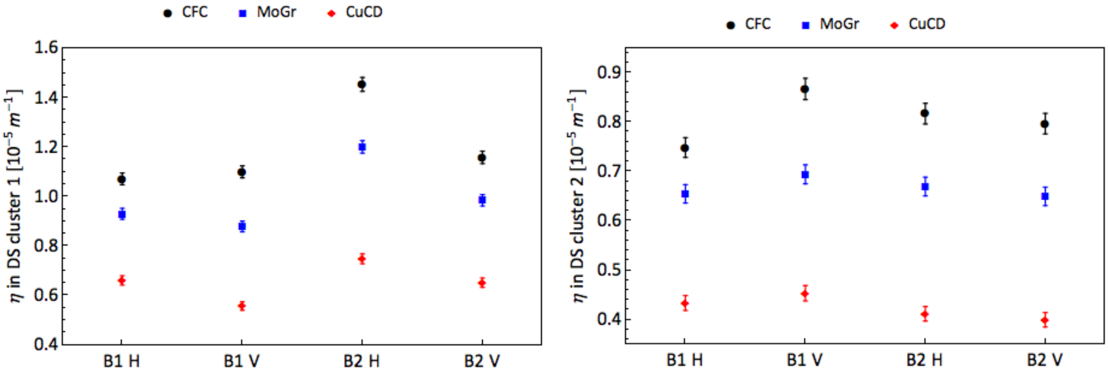

(a) IR7 DS cluster 1.

(b) IR7 DS cluster 2.

**Figure 8.3:** *Simulated cleaning inefficiency in the two clusters of the IR7 DS when different materials of primary collimators are used. Results are shown for Beam 1 and Beam 2, horizontal and vertical halo.*

We now discuss the loss sharing between the IR7 collimators, by looking at the number of the inelastic interactions occurring in the jaw volume, collimator by collimator. Since the loss profiles in the IR7 collimators look very similar for the simulated beams and planes, only the case of Beam 1 horizontal halo is discussed. The losses on all secondary collimators are depicted in Figure (a) for the Cases 1-2 in comparison with the reference CFC case. The plot reveals that the first two TCSG downstream of the primary collimators are progressively more loaded as the effective $Z$ of the composites increases, in the worst case up to 8% increase in Case 1 and 14% in Case 2 (Fig (b)). These are the secondary collimators that intercept the products of the scattering with the TCPs, and also a larger $Z$ value has a direct impact on the absorption of particles. Differences in losses at the TCSGs further downstream are less apparent and, if any, indicate a lower load in the new materials than in the present CFC. This is mainly caused by a larger fraction of secondary halo that is absorbed by the first two TCSGs. It is very important to stress that an increase in beam losses leads to a simultaneous increase of the energy deposited by the particles in the matter. Simulations of the energy density and the thermo-mechanical response on the new secondary collimators have been recently performed to confirm whether the structural integrity of the composite material jaws will not be compromised by the increased energy deposited. Preliminary results are presented in Chap. 9.2.1. The distribution of the particles lost along the length of the two jaws of the most loaded secondary collimator (TCSG.B5L7) for Case 1-2 is plotted in Figure 8.5: as expected, it shows an exponential decrease due to inelastic scattering events along the jaw length and the slope looks steeper for CuCD and MoGr, materials with higher density and therefore shorter inelastic length, than the case of CFC.

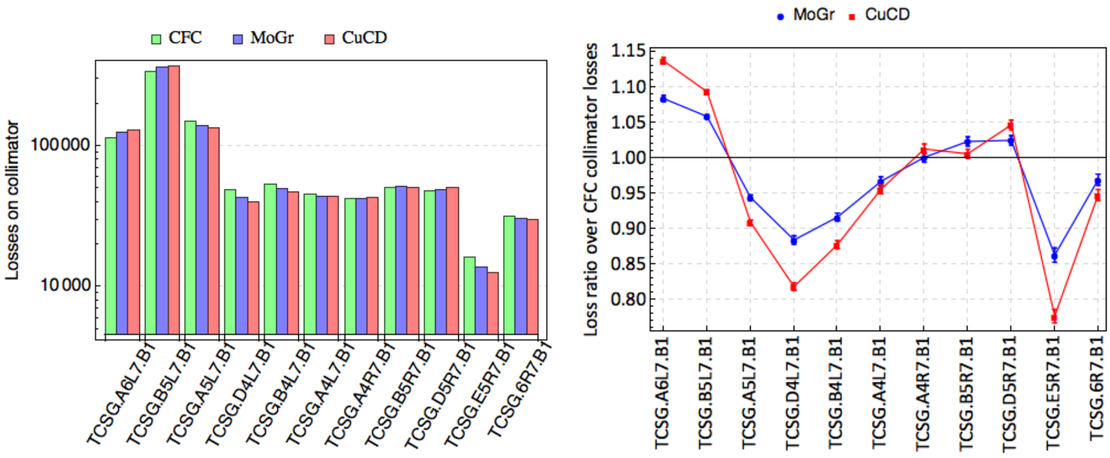

(a) Simulated losses on TCSGs in IR7 for different jaw materials.

(b) Loss ratio over the reference CFC case.

**Figure 8.4:** *Simulation results for Case 1 and Case 2.*

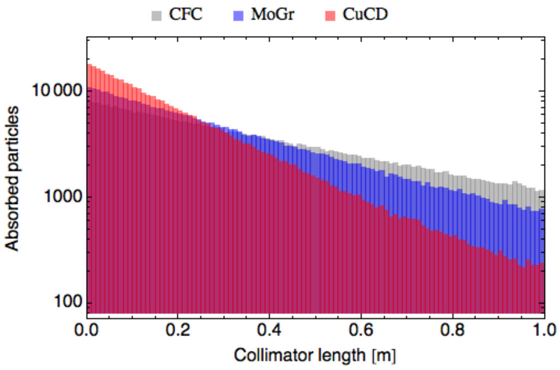

**Figure 8.5:** *Distribution of particles lost along the length of the most loaded TCSG in IR7 for Case 1-2.*

On the other hand, when advanced materials are used to replace the primary collimators as in Case 3-4, a 10% loss increase occurs in the most impacted primary collimator, i.e. TCP.C6L7.B1, with horizontal halo, with a consequent reduction of the particles that reach the TCSGs downstream, up to 20% at the first TCSG in Case 3 and 50% in Case 4 (Figure 8.6). The spike at the horizontal secondary collimator TCSG.B4L7.B1 can be related to a scattering effect due to the different material in the primary collimators. Protons that experienced single diffractive event in a primary collimator may come out with different momentum depending on the material traversed: for example, the denser the material, the smaller the momentum of the outcoming particle. A different momentum can bring such particle to impact the collimators downstream, with an higher probability to hit the first horizontal collimator. Nevertheless, the number of destructive interactions underwent by the primary protons is not the dominant factor to understand the beam losses on a collimator. The energy lost by ionization during the trajectory in the material and the generation of secondary particle shower from nuclear inelastic interactions contribute for the largest part to the total energy deposited in the collimator. Therefore, results of tracking simulations must be complemented by energy deposition and thermo-mechanical studies to have a more complete picture of the effect of beam losses on a beam-intercepting device.

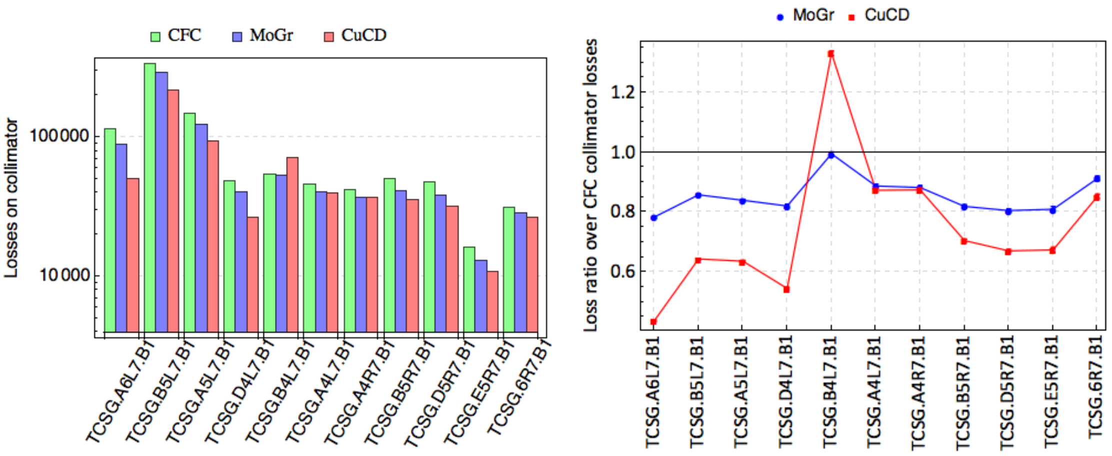

(a) Simulated losses on TCSGs in IR7 for different jaw materials.

(b) Loss ratio over the reference CFC case.

**Figure 8.6:** *Simulation results for Case 3 and Case 4.*

The number of protons lost in the tertiary collimators located upstream of the high luminosity experiments in IP1 and IP5 has been also evaluated, as a function of the material used in the IR7 collimators. The higher are the losses at the TCTs, the higher is the probability that large secondary particle shower comes out from the jaw and ends up on the experimental detectors, generating a unwanted background noise signal. In Figure 8.7, the losses in IP1/5 tertiary collimators are shown for all beams and planes, in the simulated Case 1-2. As general observation, by changing the material of the secondary collimators, the losses tend to decrease in all the analysed locations of the ring. In particular, if we look at the tertiary collimators in cell 4 of IP1 and IP5 for Beam 1 and Beam 2 respectively, which are the collimators sitting closer to the IP, we see that TCTPH.4L1.B1 is impacted by the same amount of primary protons, regardless of the material used in IR7's. A 30% loss reduction is achieved in this collimator in the case of B1 V, while very few losses are counted for the vertical counterpart. Looking at Beam 2, instead, we have very low statistics even for the most exposed collimators, i.e. TCTPH.4R2.B2 and TCTPV.4R2.B2, already when CFC is used. Advanced collimators would significantly reduced the losses, in some cases down to zero. Similar conclusions can be derived for the simulated Case 3-4, illustrated in Figure 8.8. Horizontal collimators of Beam 1 experience a general loss reduction when moving from CFC to MoGr and CuCD. Vertical collimators, instead, show similar behaviour regardless of the material. In Beam 2, the losses on tertiary collimators are much lower than Beam 1, and the material replacement does not largely change the number of particle lost. From simulation results, the use of materials else than CFC in IR7 primary and secondary collimators would positively affect also the tertiary collimators, which see a general reduction of the local beam losses. As expected, the material choice of low-impedance primary/secondary collimators in IR7 do not affect the background noise

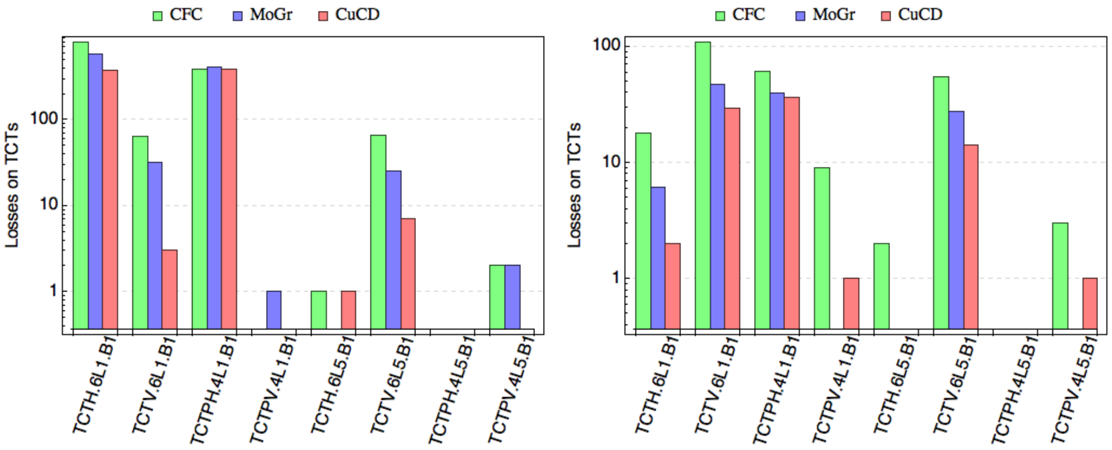

(a) Beam 1, horizontal halo.

(b) Beam 1, vertical halo.

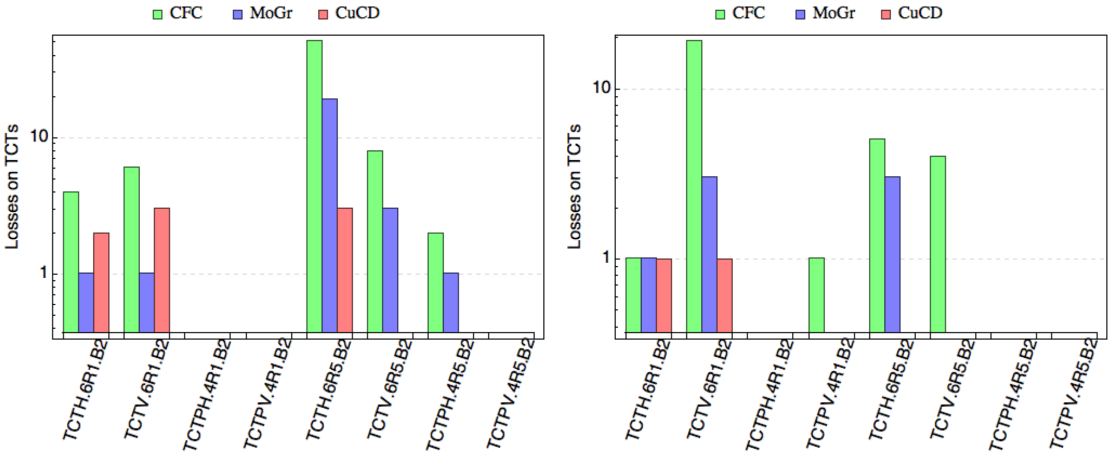

(c) Beam 2, horizontal halo.

(d) Beam 2, vertical halo.

**Figure 8.7:** *Simulated losses on the tertiary collimators in IP1 and IP5 for Case 1-2.*

signal at the experiments. Background studies can be complemented by shower simulations. However, there is no strong reason to expect a-priori that fewer impacts on TCTs should not translate into a lower background.

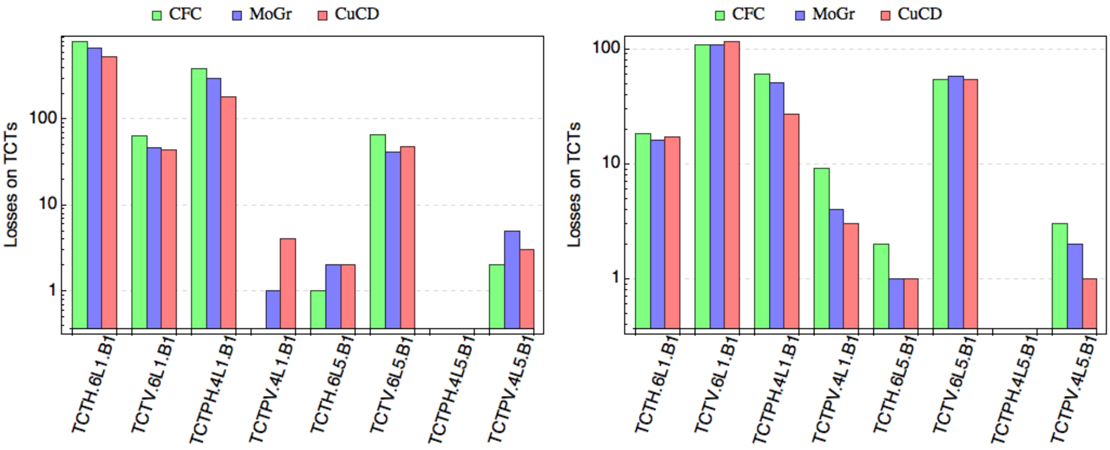

(a) Beam 1, horizontal halo.

(b) Beam 1, vertical halo.

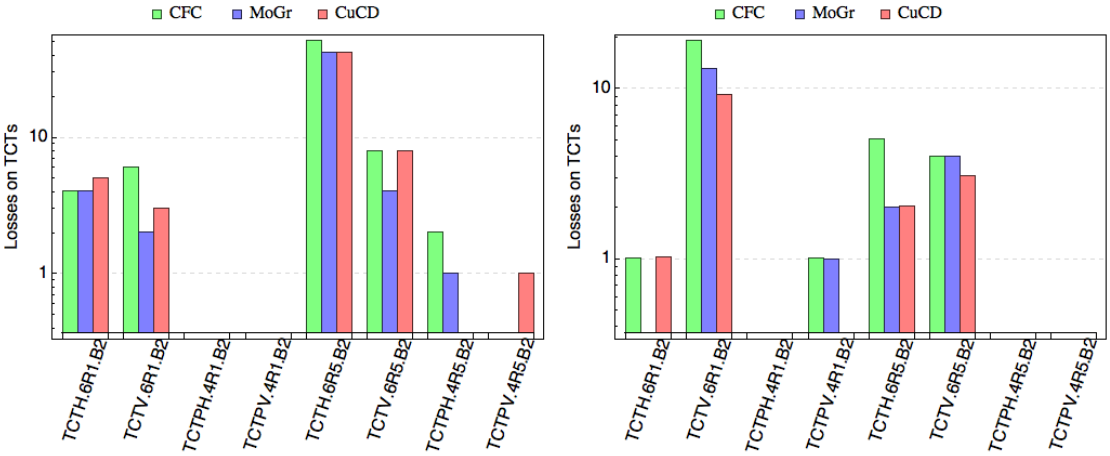

(c) Beam 2, horizontal halo.

(d) Beam 2, vertical halo.

**Figure 8.8:** *Simulated losses on the tertiary collimators in IP1 and IP5 for Case 3-4.*

## 8.2 Systematic method of damage limits calculation for tungsten collimators

In modern high-energy hadron machines, it is crucial to have a reliable way of estimating the onset of beam-induced damage to accelerator components, such as collimators, to ensure safe operation. A new method to calculate such damage has been developed based on a three-step simulation approach. This method consists of tracking studies to determine beam impact conditions for design failure cases, which was the part mainly covered by this PhD work, energy deposition studies and thermo-mechanical analysis of the dynamic response of the material to pressure waves propagation inside its structure.

We applied the method to the study of possible damage of tungsten tertiary collimators in the LHC, if they are hit by miskicked beam during a beam extraction failure. Several possible scenarios with different optics and beam conditions have been investigated and are presented below.

### 8.2.1 Definition of damage criteria

In order to quantify whether the material is damaged after beam impacts, we use three levels of damage for different types of structural changes in the tungsten collimators, similarly to Ref. [92].

Below the first damage level (threshold 1) it is assumed that the induced deformation can be almost fully recovered upon removal of the load. The material remains fully elastic or an equivalent plastic strain of no more than 0.2% is produced. In this case, the expected deformation along the transversal direction is less than few tens of microns: this damage does not compromise the flatness of the collimator jaw and its cleaning functionality can still be guaranteed. Beyond threshold 1, the material enters in its plastic regime, where it deforms permanently over larger volumes.

Above threshold 2, tungsten fragments are ejected, generating a groove on the jaw surface. In this regime, the cleaning functionality of the collimator risks to be severely jeopardized. However, this might be recovered by moving the jaw along the axis perpendicular to the collimation plane by up to 10 mm (so-called $5^{\mathrm{th}}$ axis [1, 92]). In this way, a “fresh", undamaged portion of the jaw is exposed to the beam, replacing the damaged one. Nevertheless, the ejected tungsten fragments can pollute the vacuum tank of the collimator and the beam pipe downstream, which could risk to have effects on operation in terms of vacuum quality and beam losses. If the ejected fragments have to be cleaned, they will result in downtime of the machine.

Finally, if the beam intensity is above threshold 3, the impact leads to severe damage that cannot be recovered even using the $5^{\mathrm{th}}$ axis: the plastic deformation in the material is equal or greater than 2% with a cylindrical groove of 8 mm diameter [92]. In these conditions, the integrity of the material is fully compromised and the collimator must be replaced.

As a general design principle, collimator settings and machine configurations are chosen with the aim to minimize the risk of beam losses beyond threshold 1.

### 8.2.2 Overview of simulated cases

The worse case scenario of erratic beam dump caused by the pre-firing of the most downstream kicker in the dump line (MKD.A) was reproduced in simulation for both LHC beams. A palette of several cases was simulated to cover a broad range of operational scenarios with different impacts on the TCTs, i.e. various optics versions with varying betatron phase advance between the MKDs and TCTs, and different TCT settings. In this way, comparing several scenarios and assessing the spread in damage thresholds between them, the results can be more reliably extrapolated to other possible configurations.

**Table 8.2:** *Betatron phase advances (module expressed in 360 degrees) between MKDs and horizontal TCTs in front of the high-luminosity experiments (ATLAS in IP1 and CMS in IP5). Note that the cases listed in bold in the table corresponds to the ones simulated for this study.*

| | IP | **Nom. LHC** $\beta^*$=55 cm | **HL-LHC 1.0** $\beta^*$=15 cm |
|---|---|---|---|
| **Beam 1** | | | |
| **TCTH.4L1.B1** | 1 | **56** | 209 |
| TCTH.4L5.B1 | 5 | 47 | 245 |
| **Beam 2** | | | |
| TCTH.4R1.B2 | 1 | 198 | 140 |
| **TCTH.4R5.B2** | 5 | **176** | **104** |

The machine configurations considered for this study are the nominal LHC optics with $\beta^* = 55$ cm and the upgraded HL-LHC optics with $\beta^* = 15$ cm. The collimator openings (Table 8.1) are set according to a $2\,\sigma$ retraction between the TCP and TCSG in IR7 [129], where $\sigma$ is the local betatronic beam size at the collimator assuming a nominal normalized emittance of 3.5 $\mu$m and the design $\beta$-function. In all simulated cases, a normalised emittance of 3.5 $\mu$m was used, instead of 2.5 $\mu$m, which is the HL-LHC baseline, in order to account for larger tails. Losses at the TCTs are dominated by particles belonging to the core of the beam and losses from the tails are expected to decrease if 2.5 $\mu$m is used: therefore, a pessimistic case was considered in this study. However, non-Gaussian overpopulated tails could slightly increase the losses over a small range around the opening of the dump protection collimators [131].

SixTrack simulations were performed for a perfect machine, without errors on optics, apertures and collimators. However, in operation several errors occur, such as orbit drifts, collimator misalignments or optics errors. For example, a beta-beating of +20% would correspond to an increase in beam size by 10%. Such an optics error applied to a collimator at $10\,\sigma$ would correspond to a reduction of the effective cut by $1\,\sigma$. In simulations, the combination of possible errors that could make the losses worse is accounted for by moving the TCTs closer than the nominal settings (see Table 8.1).

The betatron phase advance from the MKDs to downstream protection collimators (TCSG6 and TCDQ) is by design close to 90°, so that the kicked beam is at its maximum displacement, while the phase advance to the TCTs varies between optics versions, and the different studied TCTs. Phase advance is shown in Table 8.2 for the nominal and HL optics, for both beams, and different tertiary collimators. Higher losses are expected if the phase advance from the MKDs is close to 90° or 270°. TCTH.4L1.B1 appears as the most critical TCT in the nominal optics for Beam 1, while TCTH.4R5.B2 is critical for the HL-LHC optics for Beam 2.

In operation, the TCTs should always be shadowed by the TCDQ, however, imperfections could jeopardize this so that the TCTs may experience large primary proton losses and consequent damage. A first set of SixTrack simulations was performed with low statistics ($6.4\times10^3$ macro-particles per bunch) for nominal LHC and HL-LHC optics, scanning over different TCT settings to mimic imperfections. The resulting losses in the TCTs, summed over the simulated bunches and normalised by a bunch population of $1.3\times10^{11}$ protons/bunch for nominal LHC and $2.2\times10^{11}$ protons/bunch for

HL-LHC, are shown in Figure 8.9, where we show the most critical TCTs.

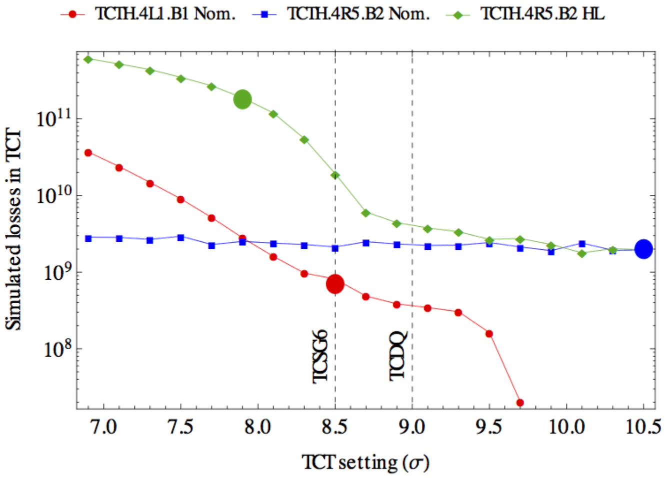

**Figure 8.9:** *Losses at TCTs as function of collimator retraction for different beam optics. Each coloured line refers to the most impacted TCT in the three simulated optics cases. The bigger markers are the scenarios selected for the study.*

Because of the complexity and the time required, three cases were selected to be further studied with higher statistics in the full simulation chain. These cases are summarised in Table 8.3. They were selected in order to have a range of different impact distributions on the TCT jaw. Case 1 (blue dot in Figure 8.9) corresponds to setting-independent losses intercepting the TCT even when the settings are open enough to be well shadowed by the dump protection. It is therefore important to verify that those unavoidable losses are not dangerous for the integrity of the collimator jaws. A realistic scenario of losses can occur when TCT is moved at the same settings of TCSG6 [72] (Case 2, red dot), where the TCTs start to be exposed and losses rise with decreasing TCT setting. Finally, a very pessimistic case is simulated for Case 3 (green dots), where the effective TCT settings are tight and, consequently, the impacts on the jaw are very high. SixTrack simulations were repeated for these cases using 6.4×$10^6$ macro-particles per bunch in order to have a better statistics for the subsequent simulation steps.

**Table 8.3:** *Summary of scenarios selected for simulation studies.*

| | **Beam energy** [TeV] | **Optics** | **Beam** | **Bunch intensity** [$\times10^{11}$ p/b] | $\beta^*$ [cm] | **TCT halfgap** [$\sigma$] |
|---|---|---|---|---|---|---|
| Case 1 | 7 | Nom-LHC | B2 | 1.3 | 55 | 10.5 |
| Case 2 | 7 | Nom-LHC | B1 | 1.3 | 55 | 8.5 |
| Case 3 | 7 | HL-LHC | B2 | 2.2 | 15 | 7.9 |

In the following, a detailed analysis of each simulated scenario will be presented and the resulting damage thresholds will be discussed.

**Case 1: Nominal LHC optics, Beam 2**

In this case, nearly constant losses occur at the TCTH.4R5.B2 for any settings, even when the TCT is completely shadowed by the dump protection collimators (see Figure 8.9). Because of the good phase advance between the MKD and the TCT in this optics (see Table 8.2), it is extremely unlikely that the TCT is directly hit by the mis-kicked beam. Protons that reach the TCT have instead previously been intercepted by the TCDQ or TCSG6, from where they scattered back into the beam with a spread in angles and hence large amplitudes. These particles are referred to as secondary protons, to be distinguished from the primary ones that hit directly a TCT without having interacted with any other collimator upstream. Since most secondary protons are scattered to large amplitudes, the number of TCT hits is only weakly dependent on the TCT settings in the studied range (see Figure 8.9).

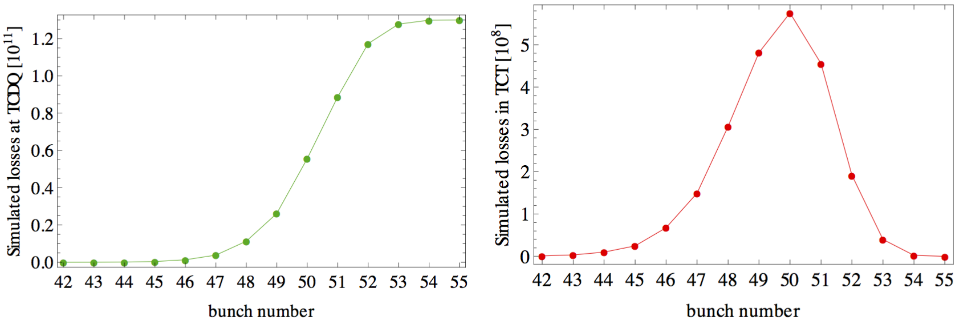

(a) Particles intercepted by TCDQ.

(b) Particles lost in TCTH.4R5.B2.

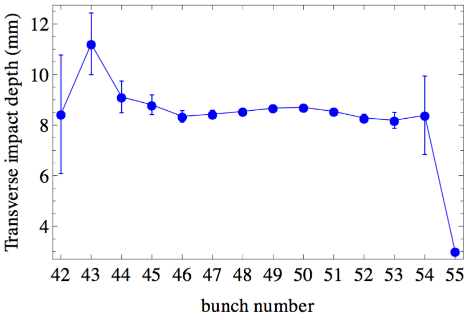

(c) Average impact depth at TCTH.4R5.B2.

**Figure 8.10:** *Losses and impact parameter as function of bunch number for Case 1. A bunch population of 1.3*$\times 10^{11}$ *p/b has been considered for nominal LHC scenario to scale up the simulated losses on the TCT to a full physics beam.*

IIn case of an SMPF, the total kick amplitude increases with time and hence with increasing bunch number. With a bunch spacing of 25 ns, about 140 bunches can be fitted in the time it takes before all MKDs have reached full field, where we define bunch number 1 to pass at the moment of the misfire. However, the first 40 bunches passing by the MKDs receive a very small kick and are dumped in the next turn; particles in bunch numbers greater than 55 are kicked to an amplitude larger than the TCDQ/TCSG6 aperture and are almost all absorbed in the protection collimators. Only a few bunches, from

42 to 55, contribute to the losses in the TCT (Figure 8.10(a)). These bunches produce about 98% of the total number of the impacting protons. Single bunch contribution to losses in TCTH.4R5.B2 is shown in Figure 8.10(b). An average impact parameter of about 8 mm is found over the simulated bunches (Figure 8.10 (c)). The transverse distribution of the inelastic interactionsalong the full jaw length is shown for Case 1 in Figure 8.11. The plot shows the transversal coordinate $x$ and the longitudinal one $s$, while the third coordinate $y$ has been integrated. A customised bin size of 2 cm is used in s, and 20 $\mu$m in x. In the left jaw (up), losses are found within the first 20 mm, while in the right one within 30 mm. Both left and right jaws see the highest density of losses in the first 10 mm. Along the longitudinal coordinate $s$, most of the inelastic events occur within the first few centimetres. The incoming proton interact with the TCT jaw, made of high density and high-Z material (IT-180). This composite features a nuclear inelastic length, i.e. the mean free path that the particle travels in the material before undergoing a nuclear inelastic event, of about 10 cm [132], which is in line with the longitudinal profile in Figure 8.11.

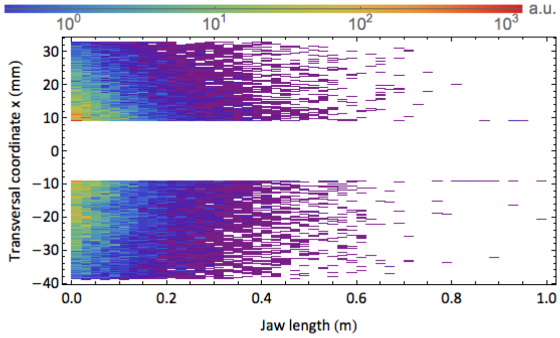

**Figure 8.11:** *Density histogram of inelastic nuclear events in the TCTH.4R5.B2 jaws for Case 1. A customised bin size of 2 cm is used in s, 20 $\mu$m in $x$, and losses are integrated along $y$. The TCT settings (10.5 $\sigma$ is Case 1) is shown with its value in millimetres, i.e. 9.03 mm from the beam centreline to the edge of the collimator jaw.*

The coordinates of inelastic interactions within the TCT volume were used by FLUKA for energy deposition calculations, and the resulting energy deposition map is shown in Figure 8.12, sampling from all bunches. Figure 8.13 shows the peak energy density profile per lost proton along the length of the TCT jaws for Case 1. From the plot, the profile of the left jaw (referred to as "Positive Jaw") turns to be the highest. The density of inelastic interactions simulated in SixTrack is quite similar between the two jaws, with a slightly higher density in the left jaw. However, the energy deposited in each jaw from the shower of secondary particles emerging from the other jaw also contributes to the energy density.

Thresholds of damage, from the thermo-mechanical simulations of the structural response of the collimator, are shown in Figure 8.14 in comparison with the losses expected at the TCT for the scenario simulated in Case 1 during a single MKD prefiring failure. The blue curve of the protons lost in the TCT lies a factor 15 below the value leading to plastic deformation of the material, regardless of the TCT settings used. This means that, for the loss profile per bunch in Figure 8.10(b) and the respective

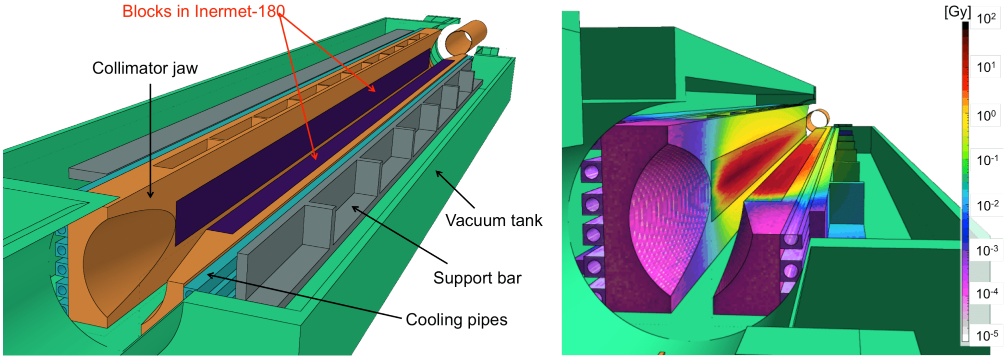

**Figure 8.12:** *TCT geometry as modelled by FLUKA (left) and map of energy deposited by all the impacting proton bunches on the TCT jaws for Case 1 (right).*

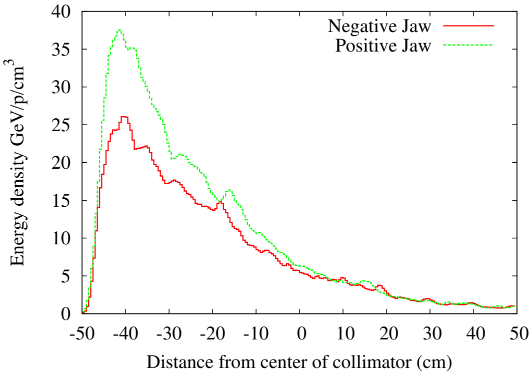

**Figure 8.13:** *Map of dose deposited by all the impacting proton bunches on the TCT jaws, obtained by FLUKA simulations, for Case 1.*

impact distribution, we can conclude that the onset of damage in the collimator jaw is expected only with a bunch population 15 times higher.

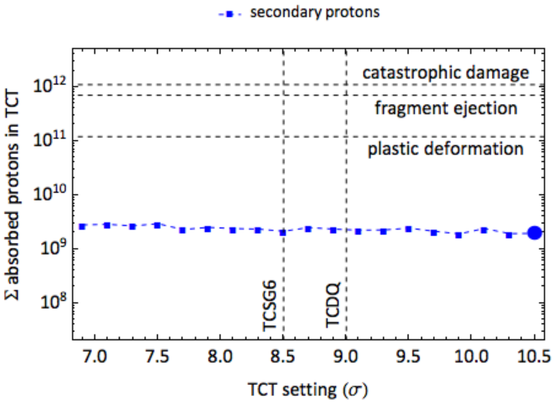

**Figure 8.14:** *Losses expected at the TCT in comparison with estimates of damage of the tungsten jaw for Case 1. The losses are estimated assuming a bunch population of 1.3*$\times 10^{11}$ *p/b.*

### Case 2: Nominal LHC optics, Beam 1

We now focus on the losses on the TCTH.4L1.B1 for the nominal LHC optics. Because of the phase advance of $56^\circ$ from the MKDs, this collimator is more exposed to beam losses in case of dump failure. In particular, for the setting considered in Case 2, the TCSG6 is at the same level as the TCT, therefore, both primary and secondary protons contribute to losses in the collimator. This is clear in Figure 8.15 where the impact distribution in the jaw is shown: primary protons interact on average at $100\,\mu$m from the edge of the collimator, while the secondary particles coming from the upstream collimators show an impact profile which is more spread-out inside the jaw, with an average impact parameter of about 500 $\mu$m. The overall distribution of the inelastic interactions along the depth and the length of the jaw is shown in Figure 8.16: simulated losses mainly concentrate in one jaw, only few particles are lost in the opposite jaw, therefore neglected in the plot.

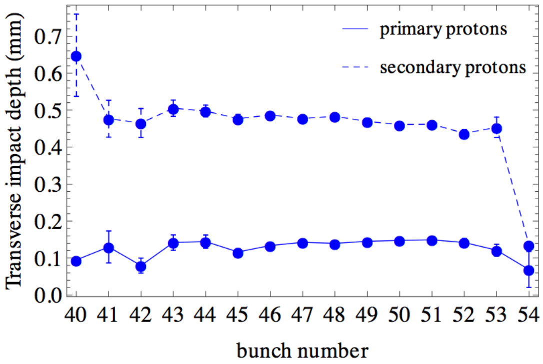

**Figure 8.15:** *Average transverse depth of impact from the edge of the collimator jaw given as function of bunch number for Case 2. A bunch population of 1.3$\times10^{11}$ p/b has been considered.*

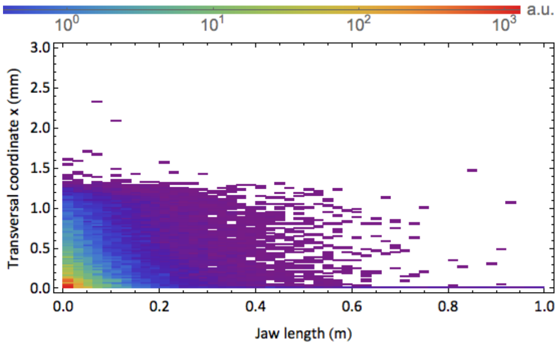

**Figure 8.16:** *Density of inelastic interactions in the TCTH.4L1.B1 jaw for Case 2. Only the left jaw is shown: few particles are lost in the opposite one, therefore losses in that jaw were neglected in the plot. A customised bin size of 2 cm is used in $s$, 20 µm in $x$, and losses are integrated along $y$. In this case, the collimator halfgap in millimetres, 7.3 mm, has been already subtracted to the transversal coordinate, so the edge of the jaw is set at $x$=0.*

The energy density deposited by the protons in the collimator differs between the left and the right jaw (Figure 8.17): the highest peak of lost protons occurs at the right, while the left jaw mainly sees the shower particles which are spread out over the collimator length.

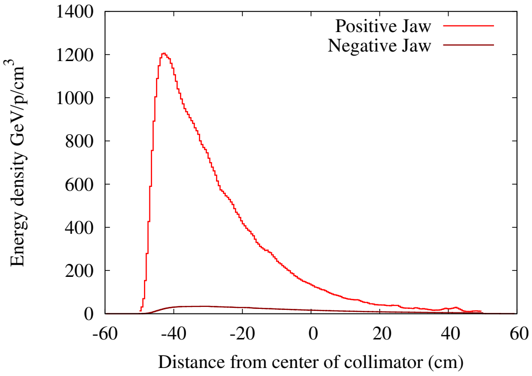

**Figure 8.17:** *Peak deposited energy profile along the TCTH.4L1.B1 jaws for Case 2.*

In Figure 8.18, we show the losses at the TCT (in red) as a function of the TCT settings, together with the damage limits that were calculated for Case 2 with Autodyn. In grey, the separated contributions to the losses from primary and secondary protons, solid and dashed curve respectively, are shown. Secondary proton impacts dominate as long as the TCT is in the shadow of the dump protection collimators. Much tighter openings will likely expose the TCT to primary protons that may induce permanent deformation of the jaw (see Figure 8.19) and eventually provoke ejection of tungsten fragments from the surface and contaminate the vacuum of the collimator tank. However, the movement of the jaw along the 5th axis would still allow to recover of the damage generated also at very tight settings.

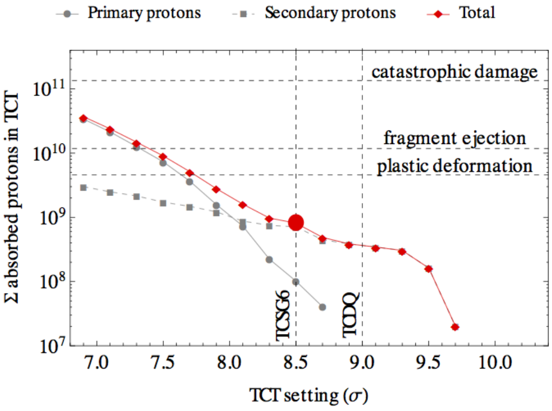

**Figure 8.18:** *Simulated losses expected at the TCT compared with the estimates of damage for Case 2. The contribution of primary and secondary protons is shown in grey. The losses are estimated assuming a bunch population of 1.3$\times 10^{11}$ p/b.*

### Case 3: HL-LHC v1.0 optics, Beam 2

A very pessimistic scenario is considered in Case 3: TCTH.4R5.B2 is closed to 7.9 $\sigma$, further in with respect to the protection collimators of IR6. This is a setting not foreseen

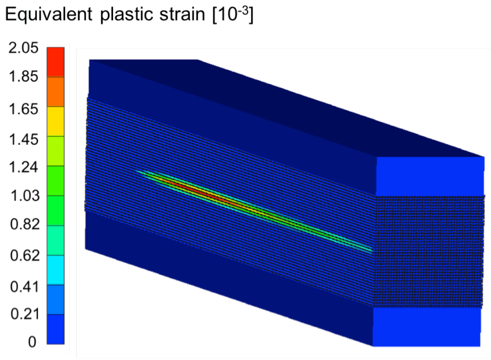

**Figure 8.19:** *Plastic deformation in TCTH.4L1.B1 simulated by Autodyn for Case 2. The picture shows the plastic strain profile corresponding to the onset of permanent damage in the jaw (threshold 1), reached after the impact of the last proton bunch.*

for standard operation, but it would represent a catastrophic configuration where large orbit drift or other errors may occur at the same time of the dump failure.

In Figure 8.20-a the peak loss in the TCT is slightly shifted to higher bunch numbers compared to previous cases. This is mainly due to the different $\beta$-function at the MKDs for this optics which determines a different amplitude of the kick angle experienced by the bunches. As shown in the loss density profile in Figure 8.21, the impacts occur in one jaw because they are dominated by primary protons. In fact, in this case losses from primary beam are concentrated in the first few hundred $\mu$m of the jaw, while a tail of secondary particles with lower intensity extends to about 3.5 mm on average (Figure 8.20-b). Figure 8.22 shows that the energy density deposited by the protons in the collimator differs between the left and the right jaw and the same explanation adopted for Case 2 applies also here.

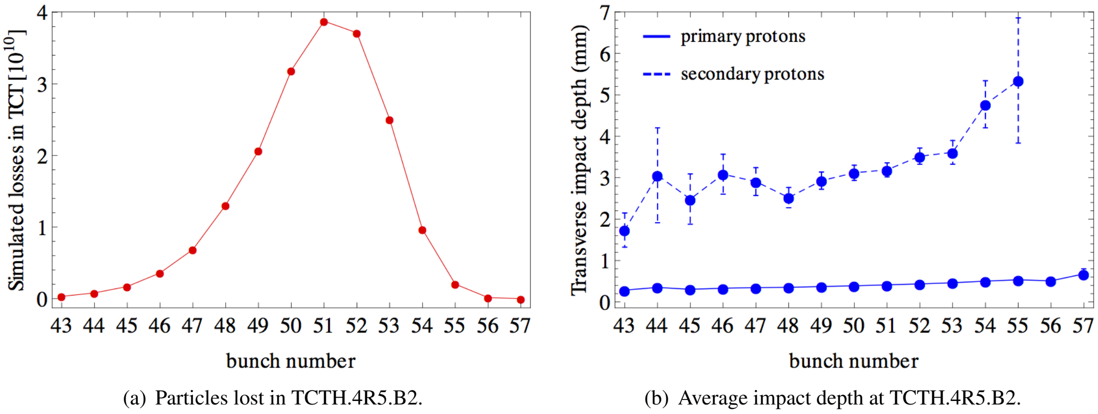

(a) Particles lost in TCTH.4R5.B2. (b) Average impact depth at TCTH.4R5.B2.

**Figure 8.20:** *Losses and impact parameter given as function of bunch number for Case 3. A bunch population of* $2.2\times10^{11}$ *p/b has been considered to estimate the losses on the TCT.*

The simulation chain was completed and the thresholds of material damage calculated for Case 3. Figure 8.23 shows the phenomenon of spallation when threshold 3 is reached in the TCT jaw. After the impact of the beam against the collimator jaw,

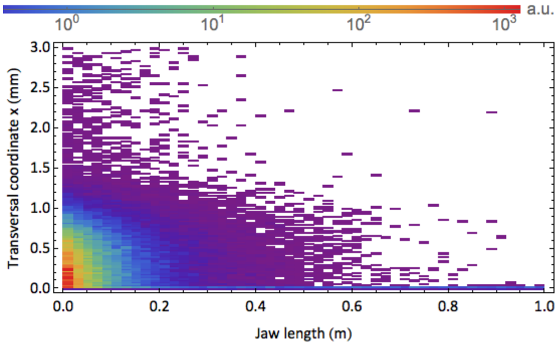

**Figure 8.21:** *Density of inelastic interactions in the TCTH.4R5.B2 jaw for Case 3. Simulated losses concentrate in the left (positive) jaw, only few particles are lost in the opposite jaw, therefore neglected in the plot. A customised bin size of 2 cm is used in $s$, 20 $\mu$m in $x$, and losses are integrated along $y$. In this case, the collimator halfgap in millimetres, 11.9 mm, has been already subtracted to the transversal coordinate, so the edge of the jaw is set at $x$=0.*

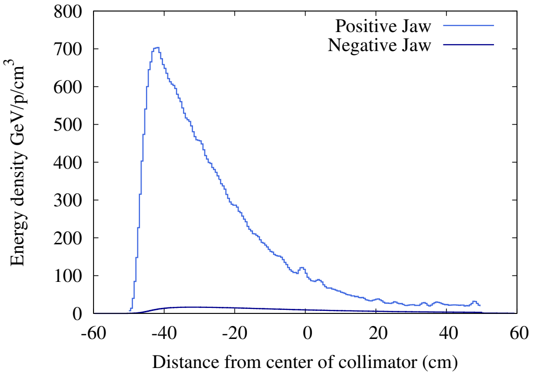

**Figure 8.22:** *Peak deposited energy profile along the TCTH.4R5.B2 jaws for Case 3.*

a shock wave of compression starts to propagate from the point of the impact to the free surface and the bulk of the jaw. When the wave reaches the free surface, it reflects, changes sign and imposes a tensile stress to the material. In solid mechanics, a spallation process occurs when fragments of material (spalls) are ejected from a body subjected to a tensile stress wave with amplitude higher than the spall strength of the material. The spall strength is defined as the ultimate strength under hydrostatic tension. In the studied scenarios, a simplified failure model was used: first of all the spall strength is considered constant throughout the simulation, while studies made by [133] showed that it changes as a function of density and flow stress. Additionally, the spall strength in the simulation has been defined as equal to the ultimate strength of a material under uniaxial stress. This is typically a good approximation for brittle materials, for which the Rankine yield criterion apply [134]. However, due to the beam impact, the material experiences a temperature increase above the brittle-to-ductile transition temperature, and exhibits ductile failure. In any case, assuming that the spall strength of a ductile material is equal to the ultimate tensile strength measured with a uniaxial test is a conservative hypothesis, as the first quantity is always higher than the second one [133]. In Inermet-180, the fragments are a mixture of a solide-liquide phase from the low-melting Cu-Ni matrix (melting point of 1400°C) and a solid phase of W, which would melt above 3400°C. In the strength model defined with Autodyn, the melting temperature of IT180 was defined as the lowest melting temperature of its constituents, thus that of the Cu-Ni matrix. If the temperature after the impact is locally higher than that of the low-melting phase, the material becomes a fluid and it cannot stand a tensile stress state. In the model, this is equivalent to a failure, as the yield stress of the material becomes null. When below the melting temperature, instead, the matrix remains solid and the code considers the ultimate strength value to evaluate the mechanical resistance of the body. As explained, this assumption is conservative.

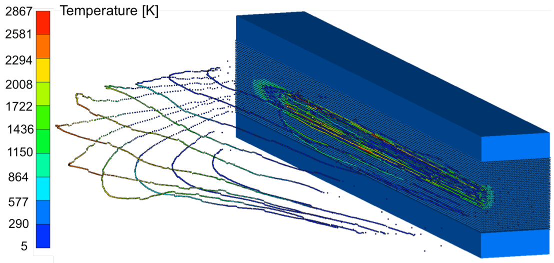

**Figure 8.23:** *Temperature profile in TCTH.4R5.B2 for Case 3 reached when TCT jaw is deeply damaged and no longer recoverable (threshold 3). The traces outside the jaw block are projections of material fragments.*

By looking at Figure 8.24, the level of losses due to primary protons would be already so high to irremediably damage the tungsten jaw. However, as pointed out at the beginning of this section, Case 3 represents an extreme scenario which should not be used for normal operation. While, operating at the nominal 10.9 $\sigma$ setting for HL-LHC, the losses at the TCT would be dominated by secondary protons, for which the limits are consistently higher (see Figure 8.14). Therefore, a strict limit is imposed on the acceptable orbit drifts during HL-LHC operation. If the combined loss in margin between the TCT and the TCDQ would be more than about 2 $\sigma$, there is a non-negligible risk for significant damage if an SMPF would occur.

### 8.2.3 Calculation of material damage for tungsten collimators

Table 8.4 shows a summary of the damage thresholds calculated using the 3-step method for the study cases presented in this paper.

**Table 8.4:** *Damage limits calculated for tungsten collimator jaw for the three cases discussed in the study.*

| Material damage | Thresholds (n. protons) | | |
|---|---|---|---|
| | Case 1 | Case 2 | Case 3 |
| Plastic deformation | $1.2 \times 10^{11}$ | $4.6 \times 10^{9}$ | $6.9 \times 10^{9}$ |
| Fragment ejection | $7 \times 10^{11}$ | $1.8 \times 10^{10}$ | $2.6 \times 10^{10}$ |
| Catastrophic damage | $1.1 \times 10^{12}$ | $1.4 \times 10^{11}$ | $1.7 \times 10^{11}$ |

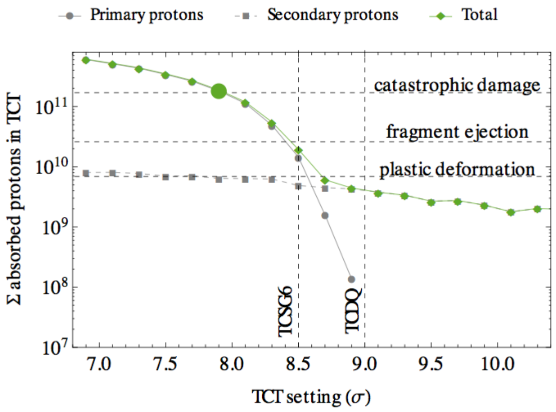

**Figure 8.24:** *Simulated losses expected at the TCT compared with the estimates of damage for Case 3. The contribution of primary and secondary protons is shown in grey. The losses are estimated for a bunch population of* $2.2\times10^{11}$ *p/b.*

The number of impacting protons needed to damage the TCT jaw in Case 1 is about a factor 20 higher than in Case 2 and 3. The reason of this difference is explained by the transverse impact distribution of primary and secondary protons at the front face of the TCT for the bunch with the largest fraction of particles impinging on the collimator in each simulated case. In Case 1, hits from secondary protons dominate and the impact distribution is quite spread along several millimetres over the width of the jaw (Figure 8.25(a)). The impact profile in Figure 8.25(b) shows that for Case 2 a significant contribution to the losses comes also from primary protons which are lost in the first 1 mm from the edge, with an average of 100 $\mu$m. Secondary losses still dominate but they occur in the first 1.5 mm: this is because, between the dump line and the TCTH.4L1.B1, there is a betatron collimation insertion in IR7 that cuts off the secondary particles generated in IR6 above a certain amplitude. Finally, primary losses clearly dominates in Case 3 up to 1.5 mm (Figure 8.25(c)), however a tail of secondary particles impacts the TCT up to about 15 mm. By comparing the profiles for the three cases, Case 2 turned out to be the most critical one because the loss profile is very narrow. As an example, it can be noticed that the secondary proton distribution in Case 2 is even narrower than that of primary proton distribution of Case 3.

In the past simulations, estimates of material damage were calculated by assuming pessimistically that one LHC bunch impacts on the TCT jaw with a fixed impact parameter, without underlying particle tracking studies [92]. The bunch intensity was scaled to identify the value that corresponds to the onset of damage. If we compare threshold 1 ($5 \times 10^9$) in Ref. [92] with the value calculated for Case 1, there is more than a factor 20 difference, while the damage limits calculated for Case 2 and 3 are similar, because of the similar distribution of the protons impacting the TCT. This shows the importance of accounting for the real impact distribution when determining the damage limit.

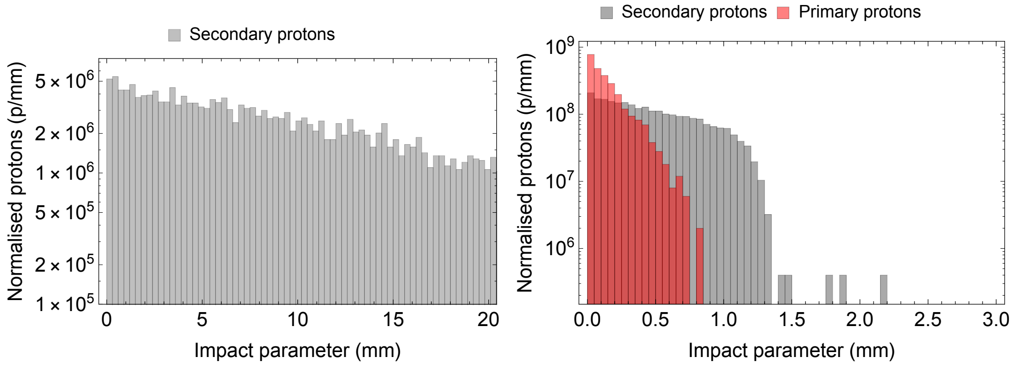

(a) Case 1, TCTH.4L5.B2, bunch 49

(b) Case 2, TCTH.4L1.B1, bunch 49

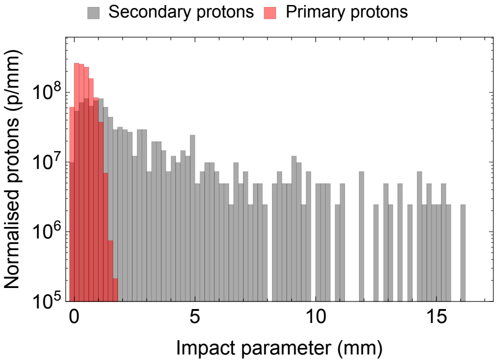

(c) Case 3, TCTH.4R5.B2, bunch 52

**Figure 8.25:** *Transverse impact distribution at the face of the TCT for the most impacting bunch in different simulated scenarios. In each case, the histogram bars are normalised to the bin size and to the total number of protons lost. Losses are calculated considering a bunch population of* $1.3 \times 10^{11}$ *for Nominal LHC optics (Case 1 and 2), and* $2.2 \times 10^{11}$ *for HL-LHC optics (Case 3).*

## 8.3 Dispersion suppressor collimator materials

The mitigation of local off-momentum losses in the dispersion suppressor (DS) magnets in IR7, and the consequent reduction of magnet quench probability, will rely on the addition of new collimators, the so-called TCLD[1] [5]. TCLD jaw material and operational settings are still an open question and need to be defined as part of the HL-LHC baseline. The baseline choice of TCLD material will be finalised based on SixTrack simulation results for failure scenarios as well as nominal operation conditions, presented in the following sections.

### 8.3.1 Failure scenarios at the LHC with TCLDs

Particle tracking simulations have been carried out to assess whether the protection of TCLD from fast beam losses would add constraints on the settings that can be deployed in operation. In this study, two TCLDs for each beam are considered, one collimator located in cell 8 (called TCLD.8R7 for Beam 1 and TCLD.8L7 for Beam 2), and one

---

[1] TCLD: Target Collimator Long absorbers in Dispersion suppressor region

collimator in cell 10 (called TCLD.10R7 for Beam 1 and TCLD.10L7 for Beam 2). As recalled in Chap 7.3, fast failure losses expected at a collimator, for instance in the case of a SMPF event, are closely related to the difference in betatron phase between the collimator itself and the kicker magnets in IR6. The phase advance at the TCLDs for both beams is listed in Table 8.5 and is compared with that of the dump protection collimator (TCSP), which generally have the worst phase advance from the kickers (90° or integer multiples). Due to a phase advance close to 270°, TCLD.10L7.B2 is the collimator where we expect more particles lost during an SMPF failure.

**Table 8.5:** *Fractional betatron phase advances (expressed in degrees) between MKDs and IR7 TCLDs and IR6 TCSP.*

| **Collimator** | **Phase advance** [°] |
|---|---|
| **Beam 1** | |
| TCSP.A4R6.B1 | 92 |
| TCLD.8R7.B1 | 37 |
| TCLD.10R7.B1 | 145 |
| **Beam 2** | |
| TCSP.A4L6.B2 | 92 |
| TCLD.8L7.B2 | 149 |
| TCLD.10L7.B2 | 255 |

SixTrack simulations were performed using the special setup for SMPF, discussed in Chap 7.3, for the HL-LHC v1.2 optics configuration. Consecutive Gaussian bunches of protons, spaced by 25 ns, with an energy of 7 TeV were simulated. The case of horizontal beam halo was considered with a statistics of about $2.3 \times 10^5$ simulated particles. Simulations were performed for a perfect machine, without errors on optics, apertures and collimators. To mimic such imperfections, a scan over different TCLD settings (from $12\sigma$ to $7.5\sigma$) was done. The collimator settings listed in Table 8.1 were used for the other collimators.

The benefits of the presence of TCLD collimators during a SMPF are clear from Figure 8.26, where the distribution along the ring of the losses is shown for Beam 1, with and without TCLD. For example, with a TCLD at $10\,\sigma$ settings, Figure 8.26(b), losses are no longer seen in the DS magnets downstream of IR7 as well as in IP3, IP5 and IP8. Losses in IP1 are instead reduced by a factor 5. Figure 8.26(c) shows that the level of the losses in IR7 complies with the collimation hierarchy: about one order of magnitude difference in losses between the highest TCP peak and the TCSG, and a factor 17 less losses than the TCSG in the two TCLDs, which in this configuration share a similar amount of losses.

In Beam B2, the cleaning of DS losses is very efficient already for TCLDs at $12\,\sigma$ (Figure 8.27). However, when the TCLD settings are reduced to $7.5\,\sigma$ (Figure 8.28(a)-8.28(b), the losses at TCLD.10L7.B2 increase significantly, about a factor 8 above the TCSG and more than 3 orders of magnitude with respect to the $12\,\sigma$ case.

Figure 8.29 gives an overview of how collimator settings would affect the losses caught by TCLDs during an SMPF failure. The plot also shows for reference the damage thresholds for tungsten collimators [135] calculated in Chap. 8.2.3, where the con-

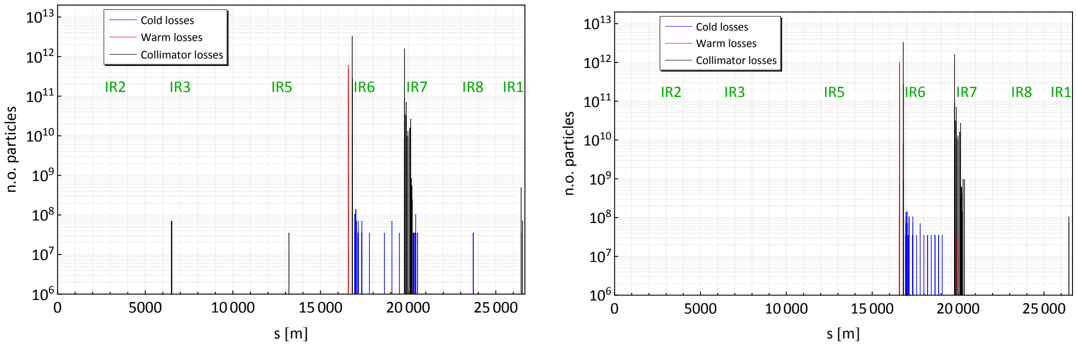

(a) No TCLD installed.

(b) TCLD at $10\,\sigma$ settings.

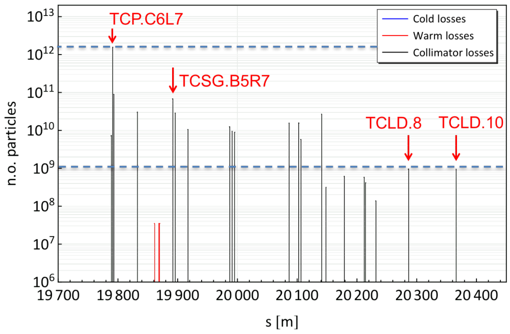

(c) TCLD at $10\,\sigma$ settings. Zoom in IR7.

**Figure 8.26:** *Simulated losses in the ring due to SMPF failure for Beam 1 at 7 TeV.*

tribution to damage from primary and secondary protons is distinguished. Most of the simulated TCLDs are hit by protons already scattered out from IR6 collimators (therefore labelled as "secondary protons") and the losses are still below the damage level. However, due to the worse phase advance from the kickers (Table 8.5), TCLD.10L7.B2 may be exposed to primary beam losses (dashed red line in Figure 8.29), which increase significantly when the settings are tighten below $10\,\sigma$. In these loss conditions, the damage of the tungsten jaw may not be negligible: more robust materials that could stand such beam loads might be needed and CuCD could be also a viable option for TCLDs. On the other hand, the onset of significant primary losses starts at settings below $10\,\sigma$ that are probably excluded by other operational constraints, as the effective momentum cut at the TCLDs. In fact, the $i-th$ collimator must satisfy the requirement:

$$\frac{\delta p}{p}|_i > \frac{\delta p}{p}|_{TCP} \tag{8.2}$$

$$\frac{N_i \times \sigma_i}{D_i} > \frac{(N \times \sigma)_{TCP}}{D_{TCP}}, \tag{8.3}$$

where $p$ is the momentum of the particle, $N$ is the collimator setting in unit of $\sigma$, i.e. the beam size, and $D$ is the dispersion function at that location. Therefore, the cut in momentum at the IR3 TCP must be always smaller than any other location in the ring, in order to avoid that such location becomes the primary stage of collimation for the

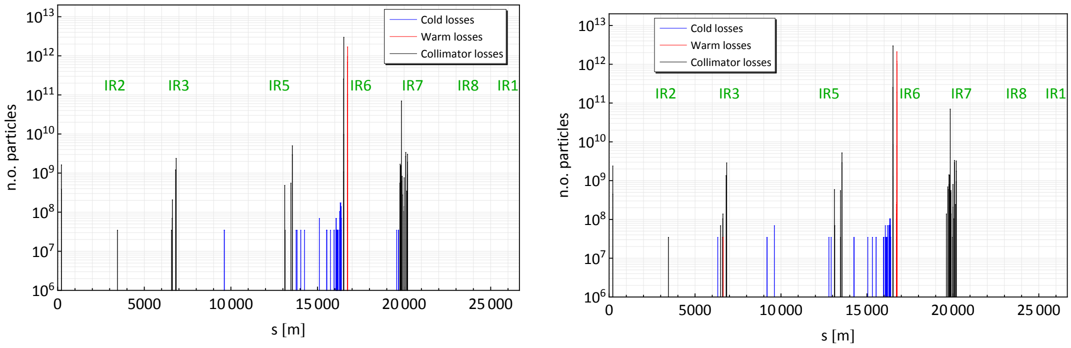

(a) No TCLD installed.

(b) TCLD at 12 $\sigma$ settings.

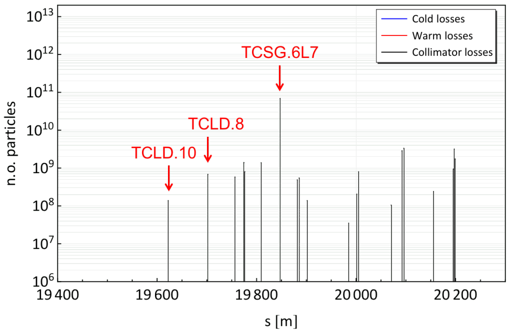

(c) TCLD at 12 $\sigma$ settings. Zoom in IR7.

**Figure 8.27:** *Simulated losses in the ring due to SMPF failure for Beam 2 at 7 TeV.*

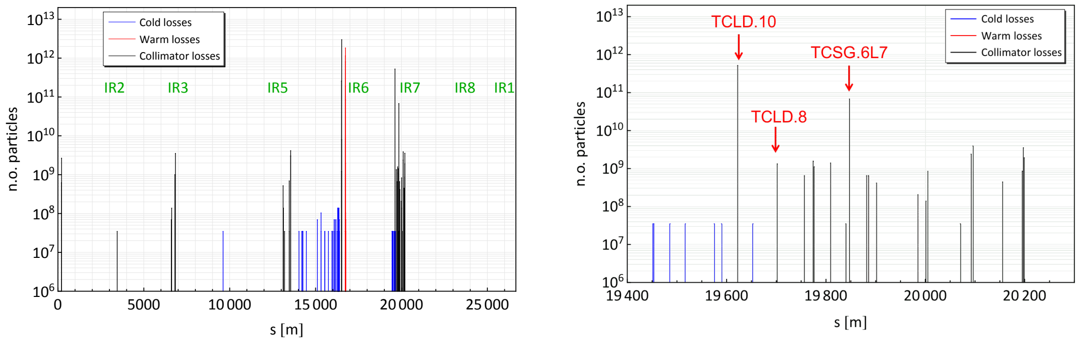

(a) Full ring.

(b) Zoom in IR7.

**Figure 8.28:** *Simulated losses in the ring due to SMPF failure for Beam 2 at 7 TeV and TCLD settings at* $7.5\,\sigma$.

off-momentum particles.

The calculation of the off momentum cut at each TCLD as well as at the IR3 TCP for different collimator settings is listed in the tables of Figure 8.30(a). By comparing the values in Figure 8.30(b) and Figure 8.30(c), one can say that for the present baseline of IR3 TCP at 15 $\sigma$, TCLDs in cell 8 would be safe for both beams, while limitations may come for TCLDs in cell 10, in particular for settings below 11 $\sigma$ in Beam 1 and

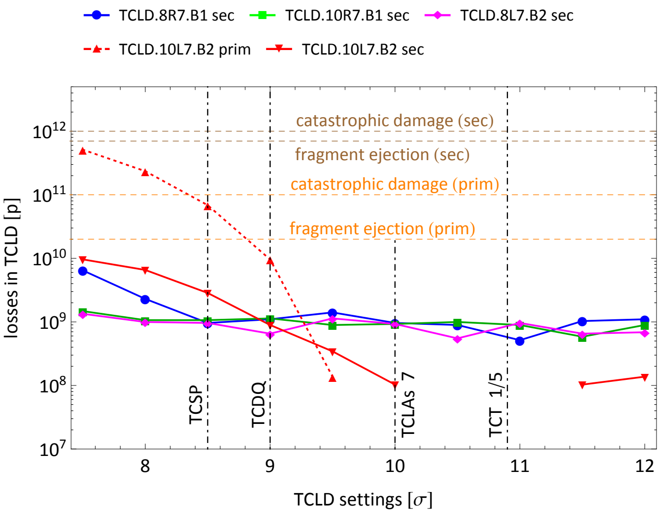

**Figure 8.29:** *Simulated losses at TCLDs, following SMPF failure, as function of collimator settings. Nominal TCLD settings are assumed at the level of the TCLA in IR7.*

$10\,\sigma$ in Beam 2.

Based on the considerations in the case of beam failure, TCLDs in IT-180 can safely operate for settings larger than $9\,\sigma$. However, the high dispersion and the coupling with momentum collimation in IR3 may constraint the smaller achievable halfgap for TCLDs in cell 10 not below $11\,\sigma$.

### 8.3.2 Cleaning performance with TCLDs

Cleaning simulations were performed for horizontal Beam 1 ($6.4 \times 10^6$ particles) at 7 TeV, with the collimator settings in Table 8.1. Different TCLD settings were considered in simulations, according to Table 8.6, and, in a first approach, IT-180 was used as material for the jaw. A comparison of the loss distribution over the full LHC ring, normalised to the highest collimator loss, is shown in Figure 8.31, for the case without any DS collimator (Figure 8.31(a)) and with two TCLDs set at $20\,\sigma$ settings (Figure 8.31(b)) By comparing the Figures, it is evident how the losses in the DS downstream of IR7 (identified by the two blue blocks in Figure 8.31(a)) are largely cured, down to the level of single particle contribution, thanks to the installation of one TCLD upstream of each cluster.

**Table 8.6:** *TCLD settings used for SixTrack simulations with HL-LHC v1.2 optics ($\beta^* = 15\,$cm). The values are expressed in units of standard deviation of the beam, calculated for a normalized emittance of 3.5 $\mu$m rad. TCLD settings of $300\,\sigma$ mean that the collimator is fully open, as it was not installed.*

| **Collimator** | **Settings** [$\sigma$] | | | | |
|---|---|---|---|---|---|
| TCLD cell 8 | 10 | 12 | 15 | 20 | 300 |
| TCLD cell 10 | 10 | 12 | 15 | 20 | 300 |

The cleaning efficiency $\eta_i$ for DS1 and DS2, calculated according to Eq. 8.1, given as function of the simulated settings, is shown in Figure 8.32. By setting the TCLDs

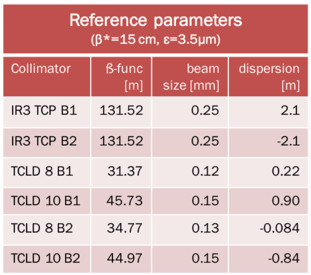

| Reference parameters<br>(β*=15 cm, ε=3.5μm) | | | |
|---|---|---|---|
| Collimator | ß-func [m] | beam size [mm] | dispersion [m] |
| IR3 TCP B1 | 131.52 | 0.25 | 2.1 |
| IR3 TCP B2 | 131.52 | 0.25 | -2.1 |
| TCLD 8 B1 | 31.37 | 0.12 | 0.22 |
| TCLD 10 B1 | 45.73 | 0.15 | 0.90 |
| TCLD 8 B2 | 34.77 | 0.13 | -0.084 |
| TCLD 10 B2 | 44.97 | 0.15 | -0.84 |

(a) Optics parameters.

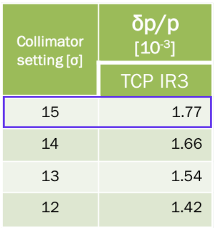

| Collimator setting [σ] | δp/p [10⁻³]<br>TCP IR3 |
|---|---|
| 15 | 1.77 |
| 14 | 1.66 |
| 13 | 1.54 |
| 12 | 1.42 |

(b) IR 3.

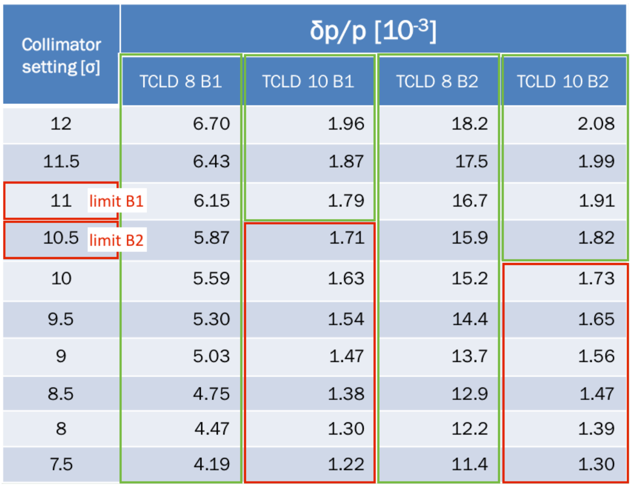

| Collimator setting [σ] | δp/p [$10^{-3}$] | | | |
|---|---|---|---|---|
| | TCLD 8 B1 | TCLD 10 B1 | TCLD 8 B2 | TCLD 10 B2 |
| 12 | 6.70 | 1.96 | 18.2 | 2.08 |
| 11.5 | 6.43 | 1.87 | 17.5 | 1.99 |
| 11 limit B1 | 6.15 | 1.79 | 16.7 | 1.91 |
| 10.5 limit B2 | 5.87 | 1.71 | 15.9 | 1.82 |
| 10 | 5.59 | 1.63 | 15.2 | 1.73 |
| 9.5 | 5.30 | 1.54 | 14.4 | 1.65 |
| 9 | 5.03 | 1.47 | 13.7 | 1.56 |
| 8.5 | 4.75 | 1.38 | 12.9 | 1.47 |
| 8 | 4.47 | 1.30 | 12.2 | 1.39 |
| 7.5 | 4.19 | 1.22 | 11.4 | 1.30 |

(c) TCLDs in IR 7

**Figure 8.30:** *Calculation of momentum cut for IR3 TCP and IR7 TCLDs at 7 TeV for HL-LHC v1.2 optics.*

at $10\,\sigma$, the efficiency improves more than 2 orders of magnitude in the first DS cluster with respect to the case of no TCLD installed. A gain of a factor 70 can be already obtained at $20\,\sigma$ settings. Losses in the second cluster are considerably reduced and only few particles are lost when TCLDs are in.

Same exercise was done using the CuCD composite as replacement of IT-180 in the TCLD jaws: this option is also under consideration to improve the collimator robustness against fast beam losses. The cleaning performance using two different materials is compared in the DS1 (Figure (a)) and in DS2 (Figure (b)). The collimation system is clearly less efficient, roughly a factor 10 less, when a lighter composite, as CuCD, replaces IT-180: the lower density of the material lets more particles escape from the collimator and eventually reach the machine aperture. This is also confirmed by Figure 8.34 which shows the origin of the particles lost in the DS clusters, i.e. were the particle underwent its last interaction before being lost in the DS. With TCLD in IT-180 (Figure (a)), the last interactions mostly occurred in the collimators else than the TCLDs (mainly IR7 TCPs and TCSGs): when the particle hits the IT180 jaws, inelastic interactions likely occur and the particle is absorbed. On the other hand, scattering events are dominant in CuCD jaws (Figure (b)), therefore they contribute to the losses in the DS. In Figure 8.35, losses in TCLDs are compared in the case of IT-180 and CuCD, given as function of the simulated TCLD settings. As expected, with IT-180 the losses on the TCLD in cell 8 and 10 are higher than when CuCD is used. A peak of $10^{-3}$ losses in cell 10 is reached for $10\,\sigma$ TCLD settings, and it can be reduced by 20% by opening the settings to $20\,\sigma$.

The best scenario would be to have two TCLDs, one upstream of each DS cluster. However, a recent baseline change was made, which considers only one TCLD

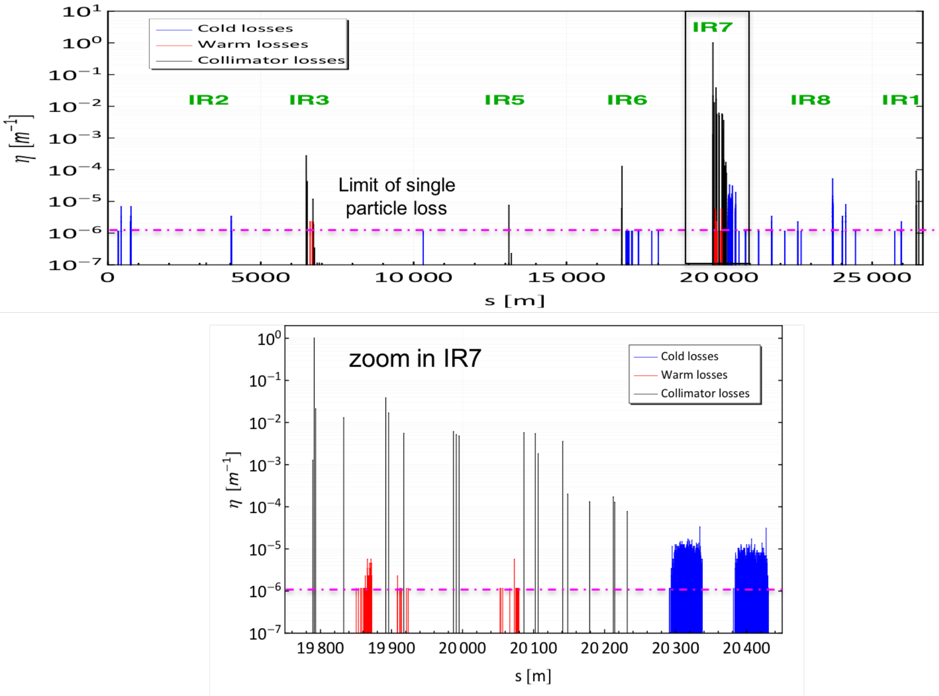

(a) No TCLDs installed. Zoom in IR7 insertion (top) and full ring (bottom).

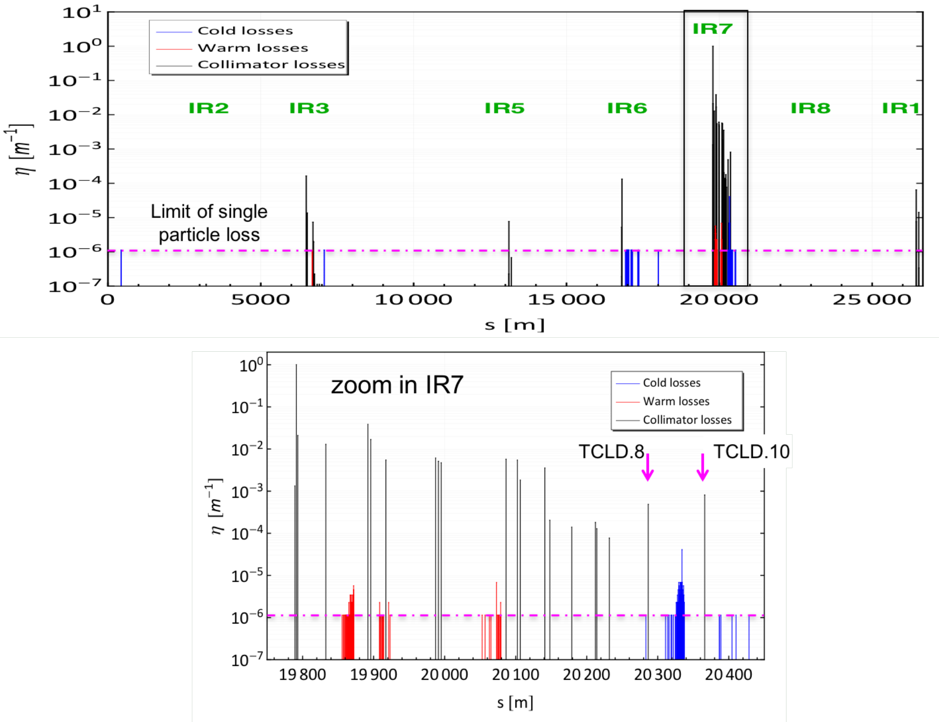

(b) TCLDs at 20 $\sigma$. Zoom in IR7 insertion (top) and full ring (bottom).

**Figure 8.31:** *Standard simulated loss pattern for Beam 1 at 7 TeV, with and without TCLDs in IR7.*

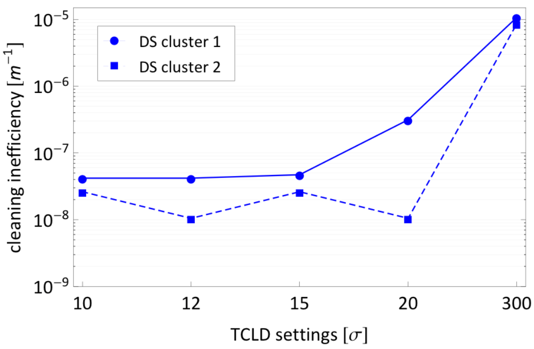

**Figure 8.32:** *Cleaning efficiency calculated over 30 m length in the two DS clusters for different TCLD settings. The dot-dashed magenta line represents the limit of single particle loss (*$\sim 5 \times 10^9$ *particles in the simulated case).*

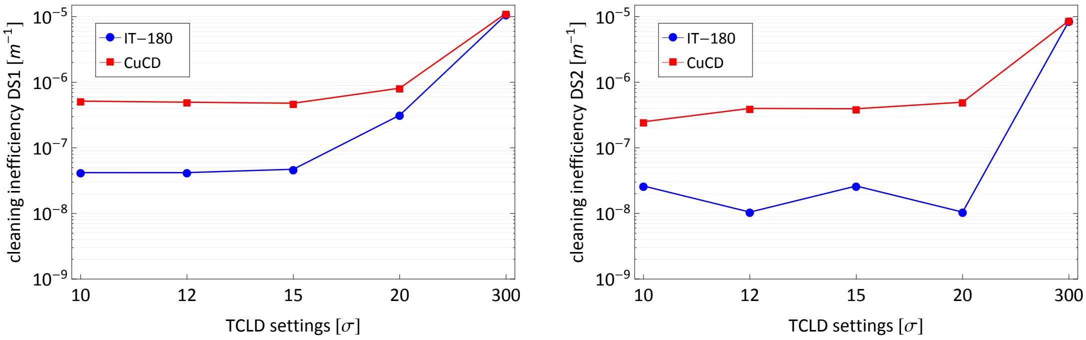

(a) Cleaning efficiency in DS1

(b) Cleaning efficiency in DS2.

**Figure 8.33:** *Comparison of cleaning performance in the DS clusters when different TCLD materials are used.*

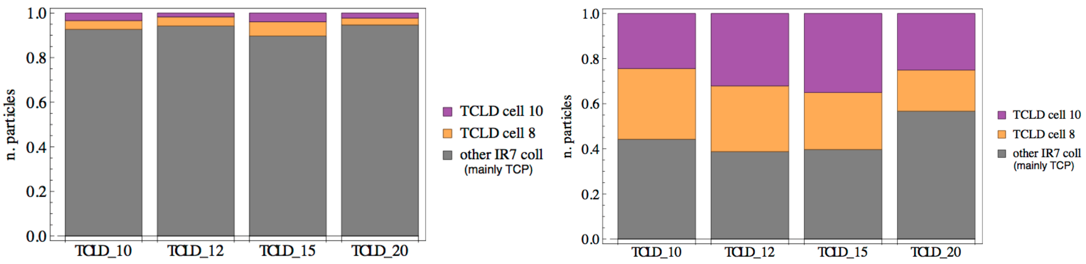

(a) TCLDs in IT-180

(b) TCLDs in CuCD.

**Figure 8.34:** *Location of the last interaction of the simulated particles before being lost in the DS.*

per beam. Therefore, cleaning simulations were performed with only TCLD8 in. The choice of this collimator is made to protect the downstream magnets, which are considered to be the most exposed to the quench [136]. In Figure 8.36, the cleaning efficiency in the two DS clusters is shown and the results with both TCLDs and only the one in cell 8 are compared for different simulated TCLD settings. As expected, no changes are found in the first clusters (Figure 8.36(a)), while in the DS2 (Figure 8.36(b)) the in-

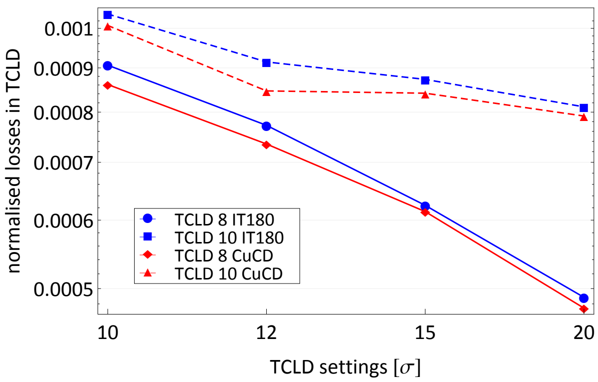

**Figure 8.35:** *Comparison of the losses in TCLDs for the case of IT-180 and CuCD collimator jaw.*

efficiency increases of 2 orders of magnitude with respect to the case of both TCLD in. However, there is a factor 2 gain in cleaning efficiency than the case with all TCLD out. This corresponds to about a factor 5 reduction in energy deposited in the DS2 magnet coils [137], which should be safe enough to prevent quench during proton operation, while similar studies for ions are ongoing [138].

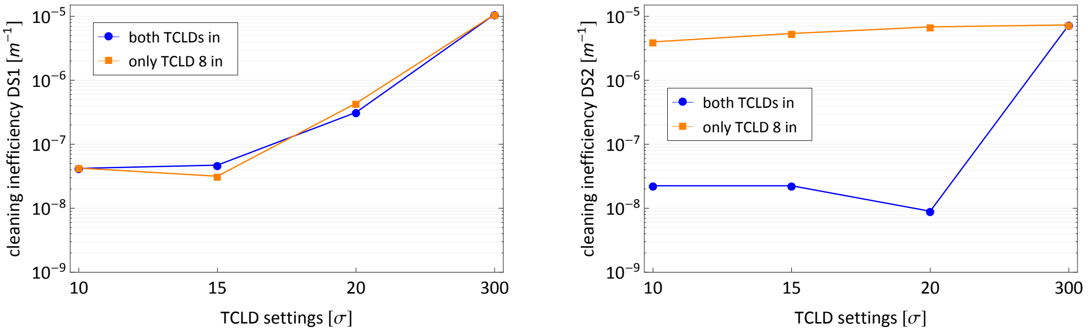

(a) Cleaning efficiency in DS1

(b) Cleaning efficiency in DS2.

**Figure 8.36:** *Comparison of cleaning performance in the DS clusters when 1 or 2 TCLDs are installed.*

In order to have a more complete picture of the cleaning performance with DS collimators, a summary of the results of cleaning simulations performed for both beams and both halo planes is illustrated in Figure 8.37, where the contribution to the cleaning efficiency is the two DS clusters was separated and plotted as function of the TCLD settings. For DS1 (Figure (a)), B2 H appears as the most critical case, with the higher cleaning inefficiency. However, by closing the TCLD 8 to $12\,\sigma$ settings, we can gain a factor 10 in efficiency. For DS2 (Figure (b)), TCLD 10 is already effective at $20\,\sigma$ in all the beams and halo planes. Moreover, this settings would guarantee no limitations in terms of fast losses and momentum cut. We can thus propose a strategy of "asymmetric" settings for TCLDs, which foresees TCLD 8 at $10 - 12\,\sigma$ and TCLD 10 at $15 - 20\,\sigma$. At the moment, IT-180 remains the best choice of material for TCLD jaws. However, CuCD can provide more robustness to TCLD 10 if operation at tighter settings, e.g. $10\,\sigma$, will be required. In that case, the configuration would be about 10 times less efficient than IT-180 but the gain in efficiency will be still significant than without any DS collimator.

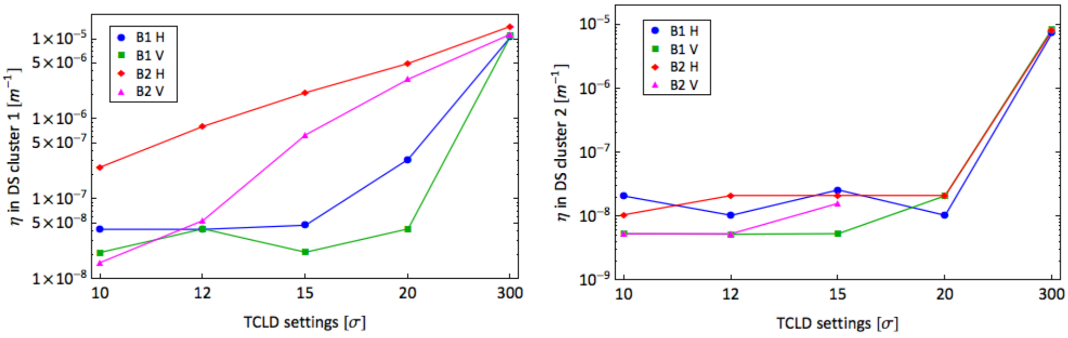

(a) Cleaning efficiency in DS1

(b) Cleaning efficiency in DS2.

**Figure 8.37:** *Cleaning performance in the DS clusters when 2 TCLDs are installed. Results for both beams and halo planes are compared.*

## CHAPTER 9

# The HL-LHC collimation system upgrade

Several functionalities of the present LHC collimation system must be upgraded in order to cope with the challenging HL-LHC beam parameters. The material R&D for the future collimator jaws addressed key issues of the present system and of the HL-LHC upgrade, in particular the reduction of the beam coupling impedance contribution, the improvement of the mechanical robustness, and the high cleaning performance. In this Chapter, the baseline layout of the HL-LHC collimation layout is presented: the main novelties of the collimation upgrade are discussed and the cleaning performance of the proposed system are evaluated in simulations.

## 9.1 Overview of HL-LHC collimation upgrades

The present baseline of HL-LHC collimation system foresees a staged upgrade that will extend over the next two Long Shutdowns (LSs) of the LHC: the first phase will take place during the LS2 (2019 - 2021) and new collimators will operate starting from Run III (2021- 2024), the second one will be in preparation to the HL-LHC operation and will be covered during the LS3 (2024 - mid 2026). Table 9.1 shows the baseline for the two phases of the upgrade as well as the collimation layout of the present Run II for reference. In particular, region of installation, collimator name, jaw material and number of collimators installed in each phase are listed in the table.

As a summary, the HL-LHC baseline foresees the installation of:

- TCSPM[1]: secondary low-impedance collimators in IR7, with jaws made of MoGr coated with 5 $\mu$m molybdenum layer, and embedded BPMs.

---

[1] TCSPM: Target Collimator Secondary with Pick-up and Metallic jaws

- TCPPM[2]: primary collimators in IR7, with jaws made of MoGr and BPMs.
- TCLD: collimators made of IT-180, one installed upstream from the first cluster of DS magnets in IR7, and one located in the missing cryostat of IP2.

---

[2] TCPPM: Target Collimator Primary with Pick-up and Metallic jaws

**Table 9.1:** *Baseline layout of the LHC collimation system during different phases of the upgrade (Run III and HL-LHC). The configuration of the present machine (Run II) is reported as reference.*

| | **Location** | **Collimator** | | | **Run II** | **Run III** | **HL-LHC** |
|---|---|---|---|---|---|---|---|
| | | **Name** | **Acronyms** | **Material** | (present) | (post LS2) | (post LS3) |
| CLEANING INSERTIONS | IR 7 | Primary | TCP | CFC | 3 | 1 | 1 |
| | | | TCPPM | MoGr | - | 2 | 2 |
| | | Secondary | TCSG | CFC | 11 | 7 | - |
| | | | TCSPM | MoGr | - | 4 | 11 |
| | | Shower absorber | TCLA | IT-180 | 5 | 5 | 5 |
| | | Dispersion suppr. | TCLD | IT-180 | - | 1 | 1 |
| | IR 3 | Primary | TCP | CFC | 1 | 1 | - |
| | | | TCPPM | MoGr | - | - | 1 |
| | | Secondary | TCSG | CFC | 4 | 4 | 4 |
| | | Shower absorber | TCLA | IT-180 | 4 | 4 | 4 |
| EXPERIMENTS | IP 1 | Tertiary | TCTP4 | IT-180 | 2 | - | - |
| | | | TCTPX | CuCD | - | 2 | 2 |
| | | | TCTP6 | CuCD | - | 2 | 2 |
| | | Debris absorber | TCL4 | Cu | 1 | - | - |
| | | | TCLX | Cu | - | 1 | 1 |
| | | | TCL5 | Cu | 1 | - | - |
| | | | TCLP5 | IT-180 | - | 1 | 1 |
| | | | TCL6 | IT-180 | 1 | - | - |
| | | | TCLP6 | IT-180 | - | 1 | 1 |
| | IP 5 | Tertiary | TCTP4 | IT-180 | 2 | - | - |
| | | | TCTPX | CuCD | - | 2 | 2 |
| | | | TCTP5 | CuCD | - | 2 | 2 |
| | | Debris absorber | TCL4 | Cu | 1 | - | - |
| | | | TCLX | Cu | - | 1 | 1 |
| | | | TCL5 | Cu | 1 | - | - |
| | | | TCLP5 | IT-180 | - | 1 | 1 |
| | | | TCL6 | IT-180 | 1 | - | - |
| | | | TCLP6 | IT-180 | - | 1 | 1 |
| | IP 2 | Tertiary | TCTP | IT-180 | 2 | 2 | 2 |
| | | Dispersion suppr. | TCLD | IT-180 | - | 1 | 1 |
| | IP 8 | Tertiary | TCTP | IT-180 | 2 | 2 | 2 |
| DUMP | IR 6 | Secondary | TCSP | CFC | 1 | 1 | 1 |
| | | Diluiter | TCDQ | graphite | 1 | 1 | 1 |

- TCTP[3]: 2 additional tertiary collimators, with CuCD jaws and embedded BPMs, at protection of the triplets in IP1 and IP5.

## 9.2 Low-impedance collimators

Collimator impedance reduction is required to cope with the higher bunch population and with the additional sources of impedance (e.g. crab cavities) foreseen by the upgrade. The impedance contribution of different LHC collimators have been recently studied for the present machine configuration and the results have been successfully benchmarked with measurements in the LHC [139].

Figure 9.1 shows the estimates of the tune shift (see Chap. 1.1.4 for the definition of the tune shift) for Beam 1 primary and secondary collimators in IR7 at 7 TeV. In each bar, the contribution to the horizontal and vertical tune shift are stacked, if both present. The values for collimators in Beam 2 are not reported because very similar to the other beam. The highest peaks in a single plane are found in the first two primary collimators, oriented vertically and horizontally, respectively. However, the high number of secondary collimators and, for some of them, the high tune shift make the TCSGs the first objects to be replaced with low-impedance collimators to guarantee the HL-LHC beam stability.

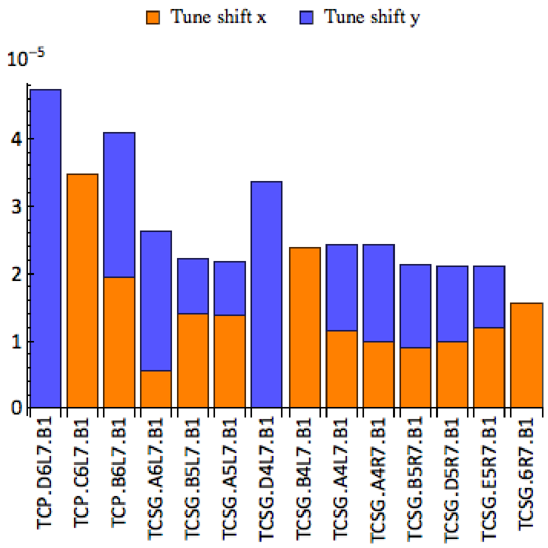

**Figure 9.1:** *Tune shift of primary and secondary collimators in IR7 Beam 1.*

According to the present HL-LHC collimation baseline, new low-resistivity secondary collimators in MoGr (referred to as TCSPM), will replace the present TCSGs in IR7. For its outstanding electrical conductivity with respect to the present CFC, MoGr is being considered as an alternative to minimise the impact on the impedance budget of the CFC collimators. The current baseline foresees 5 $\mu$m coating layer of pure molybdenum (high electrical conductor) on top of the MoGr bulk in the jaw. This additional highly conductive layer would further reduce the resistive wall impedance seen by the

---

[3] TCTP: Target Collimator Tertiary with Pick-up

particle beam. However, due to the higher density of the material used, increased beam losses are expected in the most exposed TCSPMs, with a redistribution of the thermal load on the downstream collimators. The thermo-mechanical effect of such losses in the TCSPM jaws has been recently studied and are discussed in Chap. 9.2.1.

In the staged approach of the upgrade, it is planned to install up to 4 TCSPM per beam in IR7 during LS2 and the replacement of all the TCSGs will be completed during LS3. If no constraints are added by the robustness of the MoGr jaws, the choice of collimators to replace can be only based on the single-collimator impedance contribution, according to Figure 9.1. In such a case, candidate secondary collimators to be replaced can be:

- TCSG.D4L7.B1 (vertical) and TCSG.A6L7.B1 (skew), with the largest tune shift in the vertical plane;
- TCSG.B4L7.B1 (horizontal), TCSG.B5L7 (skew) and/or TCGS.6R7, with the tune shift in the horizontal plane.

Additional margins on the beam stability could be achieved if low-impedance primary collimators were installed. This will be addressed by the consolidation project: it foresees the installation of TCPPM with BPM buttons and jaws in MoGr, in light of the excellent results of the recent experimental tests at the HiRadMat (see Section 5.3). The overall cleaning performance would benefit of the new TCPPMs, with a reduction of the losses in the DS up to 15%, as shown in Figure 8.3. Up to 2 TCPPM could be installed in the LHC already during LS2 (see Table 9.1), to further reduced the impact of beam collimation on the total impedance budget of the Run III machine.

### 9.2.1 Robustness studies on low-impedance collimators

Preliminary studies to assess the robustness of the new secondary collimator design have been recently carried out. These studies required a joint effort from several teams at CERN. In particular, the results of particle tracking simulations for the scenario labelled as Case 1 in Chap. 8.1.1 provided the distribution of the beam losses in the collimator jaw, which was used as input for energy deposition calculations; then, thermo-mechanical assessment of the structural behaviour of the collimator also followed.

Two loss scenarios were considered: the continuous beam losses with 1 h beam lifetime (Scenario 1) and the 10 s transient losses with 0.2 h beam lifetime (Scenario 2). In both cases, simulations were performed for 7 TeV protons, Beam 1 horizontal halo, with the HL-LHC machine optics and the collimator settings set as in Table 8.1. A total of $6 \times 10^{14}$ protons were lost in the full collimation system, meaning a loss rate of $1.68 \times 10^{11}$ p/s for Scenario 1 and $8.34 \times 10^{11}$ p/s for Scenario 2. From Figure 8.4, TCSG.A6L1.B1 is the secondary collimator most exposed to losses when CFC jaws are replaced with MoGr. The study thus focused on this collimator.

Table 9.2 contains the breakdown of the energy per proton deposited in the collimator (left and right jaws, and vacuum tank) as well as the corresponding power for both the studied scenarios. In Scenario 1, about 9 kW are deposited on each jaw (slightly higher on the right jaw than on the left one), and 2 kW in the tank. The total power in the collimator is close to 21 kW, which is a factor $\sim$4.7 higher than the 4.5 kW calculated for CFC collimator design (TCSG) and nominal LHC machine [140] (see Table 9.3 for the detailed comparison). There is thus a factor 2 from the increased beam intensity between nominal LHC and HL-LHC machine, plus an additional factor $\sim 2.7$ owing to the higher density of the jaw material.

**Table 9.2:** *Estimated energy and power deposited by 7 TeV proton beam in the most loaded low-impedance secondary collimator with jaws in MoGr (TCSPM), for the case of 1 h and 0.2 h beam lifetime (BLT).*

| **Collimator component** | **Energy deposited** [GeV/p] | **Power deposited** [kW] | |
|---|---|---|---|
| | | 1 h BLT | 0.2 h BLT |
| Tank | 86.35 | 2.03 | 10.15 |
| Left jaw | 395 | 9.30 | 46.5 |
| Right jaw | 398.4 | 9.38 | 46.9 |

**Table 9.3:** *Comparison of the thermal load generated by 7 TeV proton beam in the most loaded TCSG (CFC jaws) [140] or TCSPM (MoGr jaws), for the case of 1 h and 0.2 h beam lifetime (BLT).*

| **Loss case** | **BLT** | **TCSG** (from [140]) | **TCSPM** |
|---|---|---|---|
| Steady state | 1 h | 4.5 | 20.7 |
| 10 s transient | 0.2 h | 22 | 103.5 |

The energy deposition profile on the collimator, simulated with FLUKA, is depicted in Figure 9.2, which shows that the thermal load is not symmetric on the jaw. Thermo-mechanical simulations could not exploit the symmetry of the jaw, therefore the entire jaw was considered in simulations.

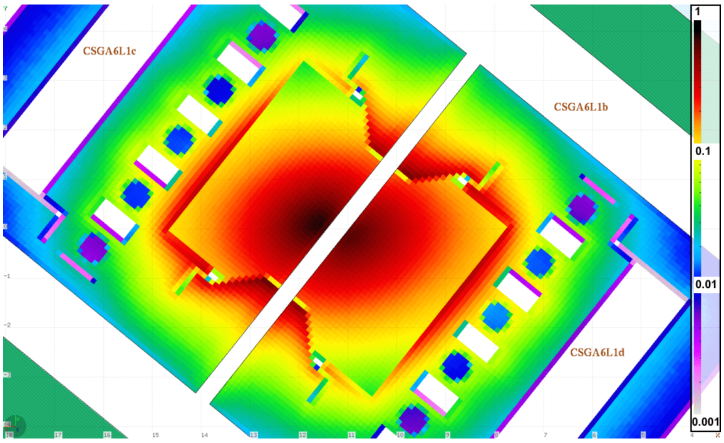

**Figure 9.2:** *Energy deposition map (in GeV cm$^{-1}$p$^{-1}$), obtained from FLUKA simulations, on the most loaded secondary collimator for the HL-LHC machine, 7 TeV proton beam and 1 h beam lifetime. Courtesy of E. Skordis.*

The result of the thermal analysis on the right collimator jaw is illustrated in Figure 9.3, where the temperature profile along the entire jaw and a selected section is shown. High temperature, up to 127° C, is reached in the last two MoGr blocks, more than in the rest of the jaw. If one compares the front face of the block with the rear one, a temperature gradient of about 70° C is found within the block itself.

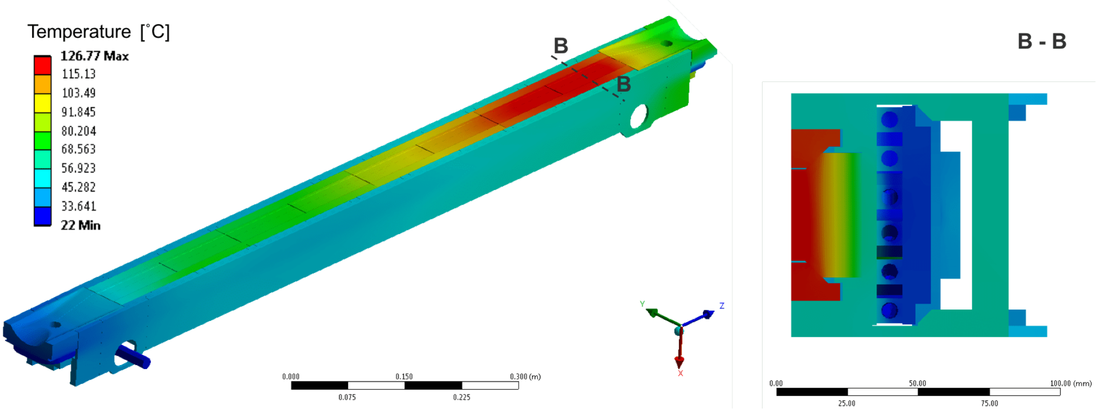

**Figure 9.3:** *Simulated temperature profile, obtained from AUTODYN code, of the right jaw of TCSG.A6L1.B1, for the HL-LHC machine, 7 TeV proton beam and 1 h beam lifetime. The profile is shown for the entire jaw (left) as well as for the section B-B (right). Courtesy of F. Carra and G. Gobbi.*

The effect of the thermal load on the deformation of the jaw was also studied. A total deflection at the beam axis of 79.5 $\mu$m was calculated, which takes into account the self-weight of the jaw, the thermally-induced deflection, and the mechanical tolerances. If compared with the collimator design specification, which allows a maximum deflection of 100 $\mu$m, the estimated deformation is within the limit, with a 20% margin. The deformation of the TCSPM turns to be slightly lower than that calculated in the past [140] for the TCSG design, i.e. 82.5 $\mu$m, in spite a thermal load of about 5 times higher.

For Scenario 2, a total power deposition of 103.5 kW in the TCSPM jaw was calculated (Table 9.2), value that has to be compared with 22 kW of the CFC's case [140]. Thermo-mechanical simulations are currently ongoing to estimate the structural deformation.

To summarise, according to the preliminary simulation results for the case of steady-state losses, 1 h beam lifetime and 2 $\sigma$ retraction settings (between secondary and primary collimators), the increased load on TCSPM due to the beam impact, accounting also for an additional factor 2 from the HL-LHC beam intensity, appears to be compatible with the present estimates of dynamic deformation limits during beam losses. Therefore, for the simulated scenario, the new low-impedance secondary collimator design with MoGr jaws is robust and not concerned by structural issues. However, for a full validation of the TCSPM design, the study must be complemented with the calculation (ongoing) of the thermally-induced deformation in the jaw in the case of transient beam losses (0.2 beam lifetime), as well as for the beam injection error (by benchmarking the results from the HRMT-23 experiment) and the asynchronous beam dump (although for secondary collimators is expected to be less critical than the injection failure). If the simulations will confirm that the new collimator design is robust to either nominal and failure conditions, the choice of the positions where to install the TCSPMs in IR7, if a limited number of slots is available in the first stage of the upgrade, will only be based on impedance considerations: those collimators with the highest contribution to impedance will be replaced first.

## 9.3 Improved protections in the experimental regions

In the present LHC collimation layout, two tertiary collimators (we call them TCT4) are installed in cell 4 upstream of each experimental region, in order to protect the local aperture bottlenecks, found in the triplet when $\beta^*$ is squeezed to small values, from both regular operation losses and accidental losses during beam failures, in particular during an ABD. However, during HL-LHC the critical aperture bottlenecks to be protected will no longer be only in the triplet [141], which in any case are planned to be replaced to allow a much larger aperture. The $\beta$-functions upstream of the TCT4 will indeed be significantly larger than in the nominal configuration, which could potentially introduce new bottlenecks, in particular in cells 4-5, therefore additional protection are being considered. The installation of two additional TCTs, one per plane, in between cell 6 and cell 5, referred to as TCT6, may therefore protect the downstream cells 4-5.

To assess the need of an additional protection in the IP's, SixTrack simulations with 7 TeV protons were performed with the same method explained in Chap. 7.3, but artificially reducing the aperture of the magnets in Q4 and Q5 to mimic possible imperfections of the machine. The HL-LHC optics lattice (version 1.0) with $\beta^*$ squeezed at 15 cm was used and $2\sigma$-retraction collimator settings in IR7, according to in Table 8.1. Figure 9.4 shows the integrated losses in the quadrupoles of cells 4-5 (Q4-Q5). Without TCT6 and with a large magnet aperture value in the IP (above $20\,\sigma$), we already see losses in Q4-Q5. On the other hand, the introduction of TCT6 upstream of Q4-Q5 seems to cure the losses as long as collimator settings are smaller than the aperture to protect. For reference, in the baseline scenario with $\beta^* = 15$ cm, the minimum aperture of these magnets for the round beam optics is set to $21.2\,\sigma$ and for the non-baseline flat optics scenario it is reduced to $16.6\,\sigma$ [142, 143].

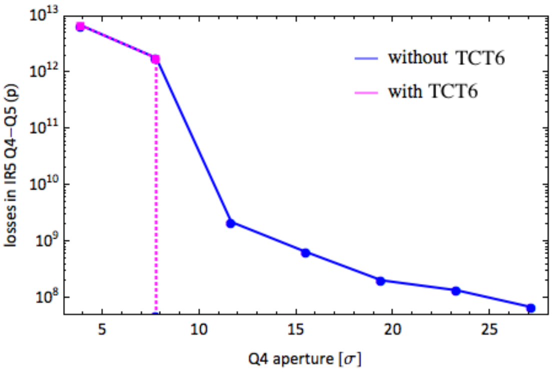

**Figure 9.4:** *Integrated beam losses in Q4-Q5 magnets of IP5 for Beam 2 during an ABD, as a function of the normalised aperture. In simulation, TCTs settings are kept constant at 10.5 $\sigma$, while TCSP and TCDQ in IR6 are at 8.5 $\sigma$ and 9 $\sigma$, respectively.*

As discussed in Chap. 8.2, tertiary collimators might be exposed to large losses from an ABD with possible damage of the jaws. Losses expected in the most impacted TCTs for both Beam 1 and Beam 2 were simulated for the HL-LHC machine configuration and collimator settings as listed in Table 8.1. As explained in Chap. 8.2.2, possible errors and orbit drift on top of the dump kicker misfiring were accounted for by scanning down tertiary collimator positions in IP1 and IP5 around their nominal settings. In Figure 9.5, simulated losses in the TCTs are compared with damage limits for tungsten collimators calculated for the HL-LHC scenario (Case 3 in Chap. 8.2.3).

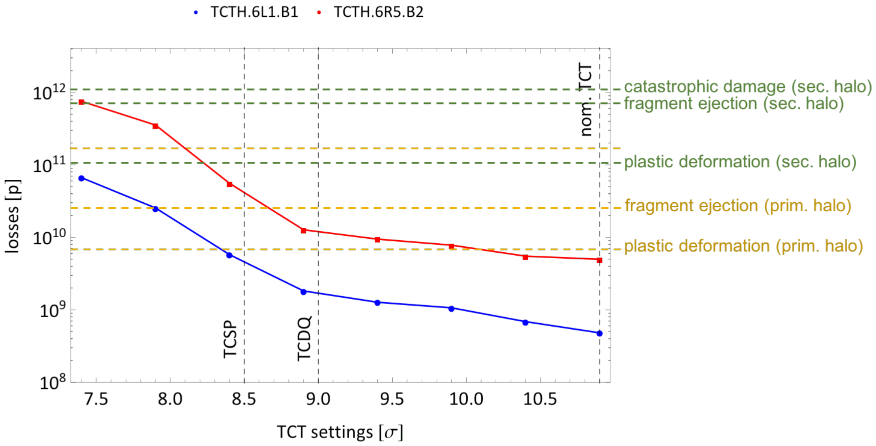

**Figure 9.5:** *Losses at the most loaded TCT in IP1 and IP5 as function of collimator settings. Damage thresholds as calculated in Chap. 8.2.3 for Case 3 are added for comparison.*

In order to ensure safe machine operation conditions with sufficient margins to accommodate possible errors (either in machine optics or collimator settings) at least 2 $\sigma$ margin is required [72], with the standard bunch population in each specific machine configuration. The present HL-LHC collimation baseline foresees TCTs in IP1 and IP5 set to $10.9\ \sigma$. As shown in Chap. 8.2.2, for these settings secondary particle losses dominate and damage limits calculated for secondary halo are at least a factor of 15 higher than the losses expected in Beam 2's TCT, which are the highest if compared with the other beam. Going down to tighter settings, below the protection collimators in IR6 and in particular below the level of the TCSP, the losses in the TCT increase owing to the contribution of the primary proton losses. The damage estimates are much lower for primary halo and therefore TCTH.6R5.B2 may be likely exposed to damage. For Beam 1, the losses are generally expected to be lower than the Beam 2 case, due to a more favourable phase advance of the TCT from the kickers. Therefore, we can conclude that operation at nominal settings for TCTs would guarantee the required margin during HL-LHC, also accounting for errors.

However, smaller $\beta^*$ and tighter collimator settings must be carefully evaluated. A limitation of bunch population might be imposed unless TCTs are upgraded with a more robust design. The limited robustness of the present tertiary collimators will be addressed by the HL-LHC upgrade program [73]. CuCD jaws are indeed under consideration for the new TCTPM[4] design, to replace the present jaws in IT-180. Recent tests, discussed in Section 5.3, were performed at the CERN HiRadMat facility to as-

---

[4] TCTPM: Target Collimator Tertiary with Pick-up and new Material jaws

sess the robustness of CuCD and IT-180 collimator jaws. In these tests, a CuCD jaw, hit by a 450 GeV proton beam the caused the serious structural damage of Figure 3.4 to a IT-180 jaw, remained almost intact (Figure 5.38(c)). The experience gained from the HiRadMat tests reveals that a CuCD jaw appears about 15 times more robust than one in IT-180. [71, 93]. It should be also noted that, owing the reduced absorption capability of materials lighter than tungsten, the elements downstream of the TCTs might be more exposed to losses. While this seems acceptable for the magnets in the present LHC machine [144], the HL-LHC scenario, in particular in terms of background signal to the experimental detectors [145, 146], is being evaluated.

A possible alternative to reduce the losses on tertiary collimators during beam failure would be to rematch the machine optics in the area of interest to have a more favourable phase advance between the dump kickers and the TCTs [147]. In this case, the present layout with TCTs in IT-180 would still be optimal to guarantee IP's protection and low background to the experiments. This was studied for the operation in 2016 with very good results [72]. However, we consider that more robust, CuCD-based, tertiary collimators should be used until similar optics solutions are found also for the HL-LHC machine.

## 9.4 Beam cleaning performance with HL-LHC collimation layout

In order to evaluate the cleaning performance of the HL-LHC machine (post LS3 configuration, see Table 9.1) expected to become operative starting from 2024, SixTrack simulations have been performed. The considered collimation configuration features 2 IR7 TCPPM with MoGr jaws, all IR7 TCSPM with CuCD jaws, 1 TCLD in cell 8 of IR7 and 2 TCT6 in both IP1 and IP5, with jaws in IT-180. Optics parameters and collimator settings used in simulations are listed in Table 9.4.

**Table 9.4:** *Machine parameters and collimator settings used in simulations of HL-LHC (post-LS3) scenario.*

| **Machine parameters** | |
|---|---|
| Optics version | HL-LHC v1.2 |
| Beam energy | 7 TeV |
| Normalised beam emittance | 3.5 $\mu$m rad |
| $\beta^*$ | 15 cm |
| **Collimator Families** | **Settings** $[\sigma]$ |
| IR7 TCPPM / TCSPM / TCLA / TCLD 8 | 5.7 / 7.7 / 10 / 12 |
| IR3 TCP / TCSG / TCLA | 15 / 18 / 20 |
| IR6 TCSP / TCDQ | 8.5 / 9 |
| IR1/5 TCTPs | 10.9 |
| IR2/8 TCTPs | 30 |

The resulting loss distribution along the full ring for Beam 1 horizontal halo is illustrated in Figure 9.6(a). The beneficial contribution of the installation of the TCLD 8 is clear in Figure 9.6(b) that shows an enlarged view of the IR7 region: the TCLD strongly reduces the losses caught by the superconducting magnets of the first DS cluster, bringing the peaks down to the limit of the single-particle resolution. By comparing the results of the two clusters for all the simulated beams and planes (Figure 9.7), one can quantify the difference in the losses in more than two orders of magnitude between the clusters. Figures 9.8(a-b) illustrate the cleaning inefficiency in the two DS clusters for the case of HL-LHC machine optics, by comparing the“old” collimation layout (black dots), i.e present LHC collimator materials and without TCLD, with the “new” collimation system simulated for the post-LS3 scenario. From Figure 9.8(a) more than one order of magnitude in efficiency is gained in DS1 with the new system in all the simulated cases. The second cluster, in Figure 9.8(b), benefits from the new collimation layout of up to 70% loss reduction in Beam 1 and 40% in Beam 2. From discussions in Chap. 8.3, we can estimate that the contribution to the efficiency from new primary and secondary collimator material is no more than 30%, while it is the installation of the TCLD that plays the major role in reducing the losses in the DS.

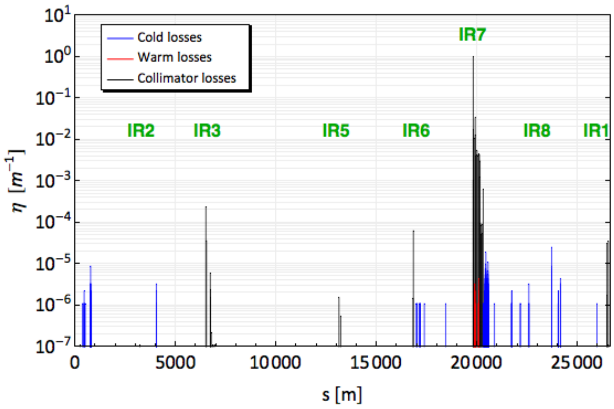

(a) Full ring

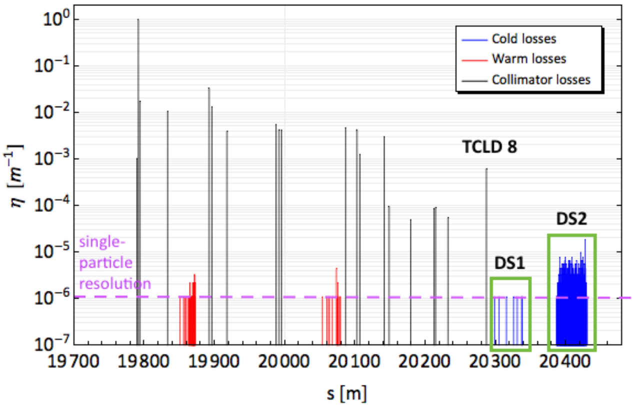

(b) Betratron cleaning insertion IR7

**Figure 9.6:** *Simulated beam loss map at 7 TeV and post LS3 for the case of Beam 1 horizontal halo.*

In Figure 9.9, the losses on the most impacted tertiary collimators, for each beam and plane, are compared between the “old” collimation layout (in gray) and the post-LS3 one (in magenta). In the latter, a significant reduction of the losses is generally

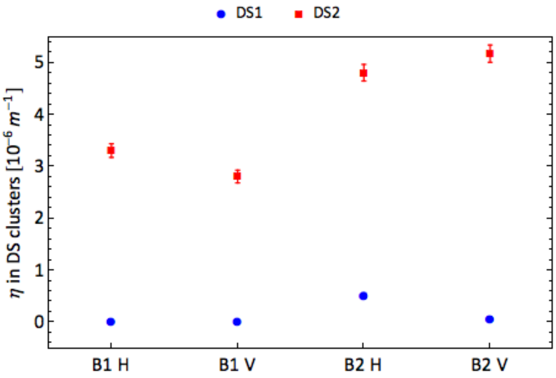

**Figure 9.7:** *Simulated cleaning inefficiency in the IR7 DS clusters for the HL-LHC (post LS3) scenario, according to Table 9.1. Values are shown for Beam 1 and Beam 2, horizontal and vertical halo.*

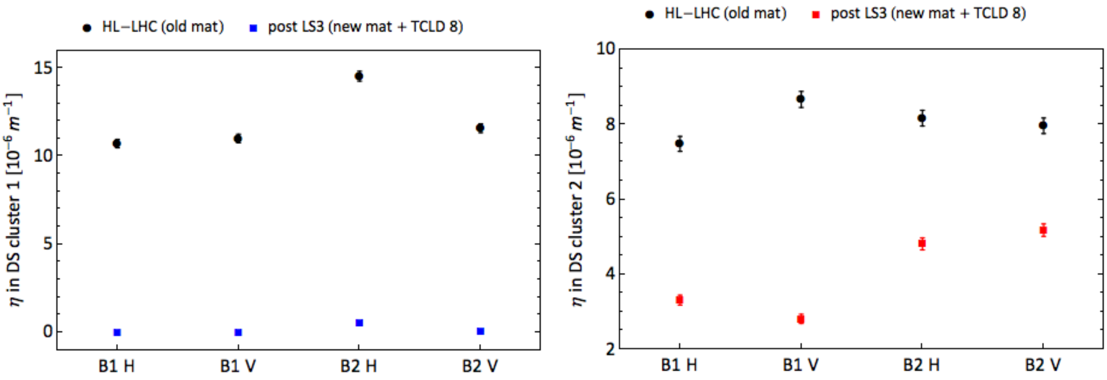

(a) IR7 DS cluster 1.

(b) IR7 DS cluster 2.

**Figure 9.8:** *Cleaning inefficiency in the two clusters of the IR7 DS, calculated according to Eq. 8.1, for the HL-LHC (post LS3 machine). A comparison is shown between the case when present collimator materials and layout are used and the case with the new TCPPM, TCSPM and one TCLD. Results are shown for Beam 1 and Beam 2, horizontal and vertical halo.*

found in all the selected collimators. If compared with Figures 8.7 and 8.8, where a relatively small loss reduction in the TCTs is achieved if advanced low-impedance collimators are used in IR7, there is the evidence that the TCLD drastically reduces the losses not only locally in the DS magnets, but also in the further downstream TCTs, with a consequent beneficial effect on the background to the experiments.

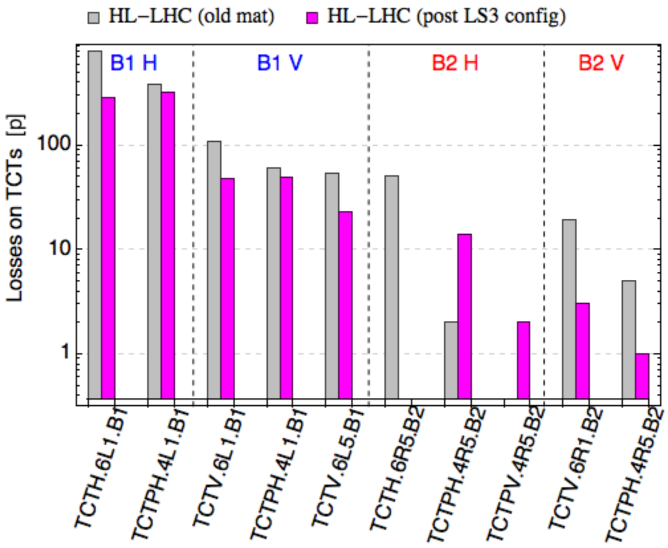

**Figure 9.9:** *Losses at the most impacted tertiary collimators for each beam and plane. The results are compared for the 7 TeV HL-LHC machine with present collimator material (in grey) and the post LS3 scenarios (in magenta) that includes the new TCPPM, TCSPM and the TCLD 8.*

# CHAPTER 10

# Conclusions

THE High-Luminosity upgrade of the Large Hadron Collider (HL-LHC), planned for the next years, aims at further expanding the physics discovery reach of the LHC, by increasing the luminosity of the machine. In order to achieve this goal, it is necessary to push various operational parameters of the machine, including the stored beam energy, beyond the design values. These challenging HL-LHC beam parameters have an impact on several parts of the collider. In particular, the beam collimation system turns out to be one of the bottlenecks for the achievement of the upgraded performance. Therefore, important upgrades of the overall collimation system layout are required. In particular, various limitations have been identified that call for an improvement of the materials used in various collimator types.

Accordingly, the upgrade of collimator materials has been a hot topic in the LHC collimation studies over the last decade, triggering several international programmes under the CERN coordination. This included two EU-funded programmes, a new one being about to start. Moreover, dedicated collaborations were established with international laboratories: for example, several irradiation tests on LHC collimator materials were performed at Kurchatov Institute (Russia), BNL Brookhaven National Laboratory (USA) and GSI Helmholtz Centre for Heavy Ion Research (Germany).

This PhD thesis work was performed at an exciting time when several of the cited studies approached the end of the R&D phase to enter the critical phase of design finalisation and production of prototypes of new collimators. Indeed, the collimation system upgrade within HL-LHC will start in the LHC long shutdown 2 (LS2) between 2019 and 2020: between 15 and 20 collimators based on new designs and materials will be produced and installed in LS2. This will follow a staged upgrade for significant performance improvement in the LHC Run III (2021-2024), that will precede the full deployment of HL-LHC.

In this context, the main goal of this thesis was to propose new collimator materials for HL-LHC and give a solid validation of the collimation performance with the upgraded system. This goal was pursued along two main lines: a comprehensive experimental characterisation, by several techniques, of the new composite materials developed to address the more challenging collimator requirements, and a detailed simulation study to evaluate the performance of the upgraded system. Clearly, this is a multi-disciplinary effort that requires the interaction with different teams, and the collection of information coming from various types of expertise. The organisation of the different aspects into a consistent framework is one of the key contributions of this work.

The experimental characterisation of novel composite materials has been performed both in normal and in extreme conditions, such as under high doses or shock beam impacts. The outcome of these characterisation measurements provided an important feedback to the material development. In particular, several X-ray diffraction experiments were performed on collimator material samples at BNL's synchrotron light source, which provided for the first time a systematic and comparative microscopic characterisation of these materials in their unirradiated and irradiated status. A strong effort was required to make these activities possible in the timeline of the thesis, owing to the induced radioactivity of some specimens. The outcome of these analyses has an important role in the finalisation of the new collimator material choice.

Two novel composite materials are the most promising candidates for the new HL-LHC collimators: i.e. Molybdenum carbide-Graphite composite (MoGr) and Copper-Diamond composite (CuCD). It has to be noticed that these materials were developed a few years before this thesis work started. However, the evolution and optimization of their properties is still ongoing, and this work could contribute to the finalization of the materials that will be used for imminent production.

MoGr features a factor of 5 higher electrical conductivity than the present Carbon-Fiber-Carbon composite (CFC) used in primary and secondary collimators. The use of such composite would reduce the single-collimator contribution to the machine impedance by about 90%. Moreover, the addition of a thin coating layer of pure molybdenum or titanium-nitride on top of the bulk material can further improve the electrical conductivity with a consequent reduction of the impedance. Beam impact tests proved the good robustness of MoGr collimators against the worst expected beam loss scenarios in the LHC. The results of irradiation campaigns demonstrated that recent and more optimised MoGr grades possess good radiation resistance to both proton and ion beams, with a threshold of structural degradation not far from that of graphitic materials.

CuCD is being considered as an alternative for more robust tertiary collimators. Based on the successful outcome of recent impact tests on CuCD jaws, preliminary estimates would indicate that a tertiary collimator in CuCD is about 15 times more robust than the present one in Inermet-180 (IT-180): CuCD did not show large structural damage when hit by the same beam that caused catastrophic damage to IT-180 during a previous experiment. Moreover, CuCD turns to have a very good response to radiation: it showed high resistance to damage at both macroscopic and microscopic level.

Simulation studies have also been carried out to validate the choice of materials and layout of the HL-LHC collimation system. The simulations were performed with the SixTrack code, the standard tool for collimation performance studies at the LHC. A new collimator material implementation has been developed, which includes a model for composite materials. This implementation was successfully benchmarked with other simulation codes and found to be fully adequate for the scope of this work. Furthermore, an existing tool that allows the dynamic simulation of beam failure scenarios in the LHC was validated for the first time against new measurements in the machine at top energy, in conditions closer to that expected for HL-LHC. A comparative study was performed with an overall good agreement between simulated and measured losses on tertiary collimators following an asynchronous beam dump test for different machine configurations adopted in 2015. The main conclusion of this work is that the developed simulations tools are adequate for the simulation of the new HL-LHC collimation layout. The new tools can be consistently used for all future performance assessment.

Simulations discussed in this work confirmed that collimation cleaning efficiency is only slightly improved by the new low-resistivity secondary collimators. This result was not unexpected, since the main goal was the reduction of beam coupling impedance, and not the cleaning efficiency. However, new primary collimators, built from a denser material (MoGr instead of CFC) may improve the cleaning efficiency. On the other hand, the use of denser materials than CFC (e.g., MoGr) increases the number of destructive events that occur between the beam particles and the material; consequently, it increase the energy deposited in the collimators, which may eventually deform the jaws under the effect of increased thermal load and have an impact on the jaws roughness, which for collimators is allowed only within certain tolerances. Preliminary results of thermo-mechanical studies, which were triggered by the new results of cleaning simulations and used those results as input, showed that the thermal load produced on MoGr secondary collimators from continuous beam losses is compatible with the estimated limits of dynamic deformation of collimator jaws. However, the complete validation of new collimator choice for primary and secondary collimators requires further studies for fast loss scenarios, which was not possible to finalise in the timeframe of this thesis. Full experimental assessment could only be performed in Run III (from 2021, after the beam injectors upgrade), but present results are sufficient to start the new collimator production for LS2.

A new method to reliably calculate the onset of beam-induced material damage to accelerator components was presented. It consists of a three-step approach: particle tracking studies to determine beam impact conditions for design failure cases (this aspect was covered by this PhD work), energy deposition studies and thermo-mechanical analysis of the dynamic response of the material to the impact (provided from a joint collaboration with other groups at CERN). The results showed that, in HL-LHC operation, large losses are expected on tertiary collimators with the risk for the tungsten jaws to experience permanent deformation. CuCD jaws to replace those in IT-180 have been proposed as a viable solution to mitigate the robustness constraints for tertiary collimators. Although it is outside the scope of this thesis, the effect on the elements downstream, in particular on the experimental detectors, of the reduced absorption of tertiary collimator, due to a material lighter than tungsten, must be evaluated for HL-

LHC beam conditions. Since the upgrade of the interaction regions is planned for LS3, these studies were not pursued with very high priority.

The addition of one collimator (TCLD) in front of each Dispersion Suppressor (DS) beam loss cluster in IR7 significantly reduces the expected high losses in the downstream magnets, considered to be the limiting factor to the cleaning performance. From cleaning simulation results, an increase in cleaning efficiency up to two orders of magnitude can be obtained if IT-180 is used for TCLD jaws as foreseen by the present baseline. If replaced with CuCD, TCLD would be 10 times less efficient than the baseline case but, on the other hand, higher structural robustness of the collimator in case of accident would be achieved. A recent change in the baseline allows the installation of only one TCLD per beam. It was proposed to install it in cell 8, in front of the first DS cluster, as magnets that are most likely expected to quench are those just downstream.

In conclusion, the studies carried out in this PhD thesis pose a solid basis for the choice of materials for the HL-LHC collimation upgrade. In particular, MoGr is considered as viable option for the first production of low-impedance secondary collimators; CuCD has been fully validated as material for new tertiary collimators (with only the study of leakage to the experiments pending); IT-180 is still a valid material choice for DS collimators. These material choices are being part of the HL-LHC collimation baseline layout, whose performance has been assessed in this thesis.

A prototype of a new low-impedance secondary collimator, featuring MoGr jaws with two coating options has been recently produced. It will be installed in the LHC as of mid 2017 and will be tested in operation during the next machine run. Dedicated beam tests are required to confirmed the effectiveness of MoGr to reduce the collimator impedance contribution, also when tighter collimator settings are used. Beam tests at the HiRadMat facility are planned for 2018, to experimentally verify the robustness against beam losses of different coating options for collimators. Nevertheless, a simulation effort is still needed for a full validation of the new collimator. The SixTrack-FLUKA coupling code, a recently-developed tool that merges the particle tracking features of SixTrack with physical particle-matter interactions models of FLUKA, can be used in the future to perform cleaning studies with more complex collimator geometry, as for the case of coated jaws, or for dose and DPA calculation.

# Acknowledgements

And, finally, the end of this manuscript...
My poor neurones slowly unload of all scientific thoughts and feel strangely light, as they have not been for long time. Looking back, I clearly gather in my mind all the people who were at my side during the years of my “PhD journey”, and now I would like to thank.

Stefano and Alessandro, they were my guides in this exciting, but sometimes difficult, journey. At the beginning, there was a big junction in front of me: *accelerators* was marked on one way, *materials* on the other. I thought the two paths could never cross each other, many times I was about to give up and get down from the mountain, which appeared too high for me. Instead, my mentors led me by the hand along one of the two ways and, finally, we met together at the top. So, my first thanks goes to them.

Thanks also to professor Beghi for his endless willingness to step beside me in this journey, discussing about any of my doubts and welcoming all my new ideas.

A special thanks goes to Roderik, who taught me that determination and exactness are the keys to succeed in every field. Many thanks to all my CERN colleagues in MME group and LHC Collimation team, for helpful inputs and several fruitful discussions. I would like to thank someone in particular: Adriana and Alessio, not only for your support at work, but mainly for your humanity; Jorge and Fede, for those times I came to you asking trivial questions, to which you always answered with pleasure and a smile; Nikos, for his enthusiasm at work as in life; and the “Canederli”, with whom I shared many lunches at CERN’s restaurant.

I feel to say a great thank to Nick Simos and Marilena Tomut: they introduced me to the amazing world of material sciences and radiation studies: I was not just a a spectator, but they gave me the chance to get my hands dirty! Thanks for the unique opportunities that I lived over the past years and that you made possible.

Stripping me of English clothes, I switch now to Italian, as many other people deserved “un immenso grazie”.

Il primo, un po’ commosso, va ai miei nonni, quelli che mi sostengono quotidianamente e mi rifocillano il cuore e la mente con ogni loro parola, e quelli che vegliano su di me da più lontano...

Quando ero piccola, uno dei primi disegni con cui riempivo i fogli bianchi riproduceva uno uomo alto con il gel sul cappelli, una cravatta variopinta e una valigetta in mano; accanto una donna dai capelli neri vaporosi e un lungo abito da sera; in mezzo uno scricciolo di bambina, vestita come un'eroina dei cartoni animati, che li tiene per mano. I bambini viaggiano lontano con al fantasia, eh?! Ma qualcosa va al di là della fantasia ed è solo lo specchio della realtà: quelle mani unite sono il simbolo di un'unione tra un figlio e i suoi genitori che sono per lui sempre presenti e lo tengono per mano in ogni momento della vita. Sono loro, mamma e papà, che devo ringraziare se sono diventata la persona che sono, nel bene...e a volte anche un po' nel male! :)

Davide, tu sei la stella che ha illuminato questo mio duro percorso e che non ha mai smesso di brillare. Ogni giorno accogli con immensa pazienza le mie arrabbiature, facendomi capire che a tutto c'è soluzione. Condividi con me ogni gioia e sai come rendere speciale i momenti trascorsi insieme. Da te ho imparato tanto in questi anni: che è con il sudore e la perseveranza che si raggiungono gli obiettivi, ma soprattutto che è la felicità il primo vero obiettivo di ogni persona.

Un grazie particolare va a Claudia per tanti bei momenti che abbiamo condiviso e le nostre "pausette caffè", e ad Irene per avermi supportato in tante occasioni, come una sorella maggiore. Last but not least, grazie a Roberto e alla nostra promettente attività di scambio no-profit di pasticciotti leccesi con torte al pistacchio di mamma Mirella.

# APPENDIX A

# Loss maps of HL-LHC machine at 7 TeV

This appendix contains the loss maps of Beam 1 and Beam 2, horizontal and vertical halo, for the case of the HL-LHC machine configuration at 7 7 TeV, discussed in Chap. 8.1.1. The first section show the results of the replacement of only IR7 secondary collimators with either MoGr or CuCD (Case 1-2), while the second section illustrate the scenarios with replaced IR7 primary collimators (Case 3-4).

# A.1 Material replacement of IR7 secondary collimators only

### IR7 secondary collimators in MoGr - Beam 1

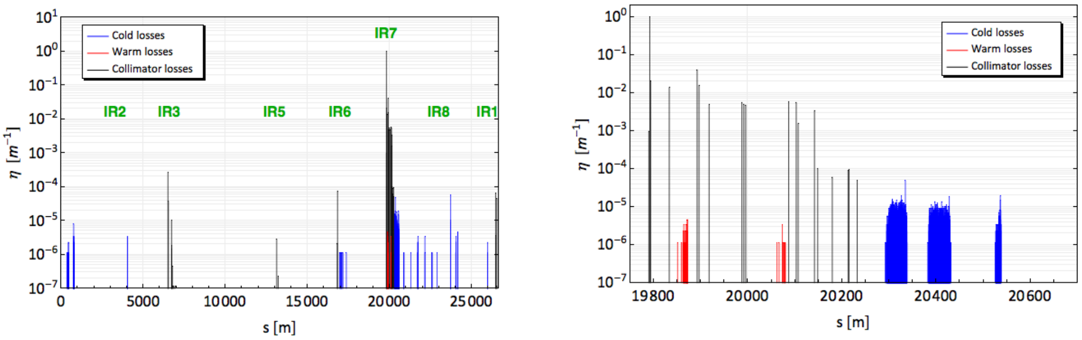

(a) Full ring

(b) Betratron cleaning insertion IR7

**Figure A.1:** *Simulated beam loss map at 7 TeV of the HL-LHC machine for the case of Beam 1 Horizontal halo.*

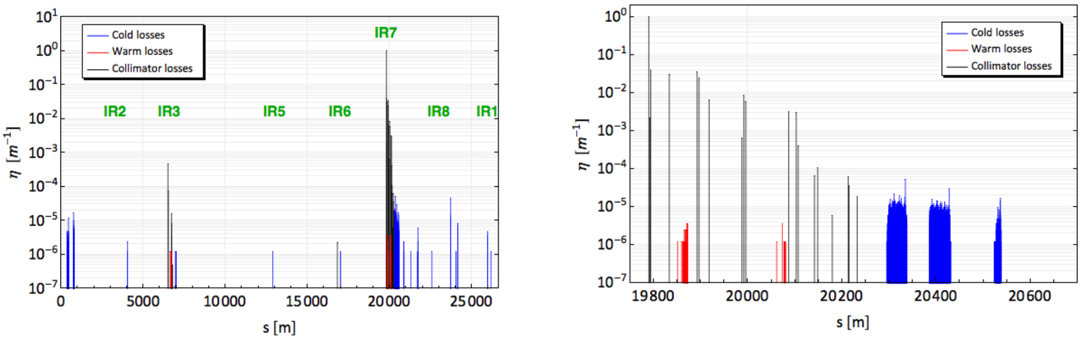

(a) Full ring

(b) Betratron cleaning insertion IR7

**Figure A.2:** *Simulated beam loss map at 7 TeV of the HL-LHC machine for the case of Beam 1 Vertical halo.*

### IR7 secondary collimators in MoGr - Beam 2

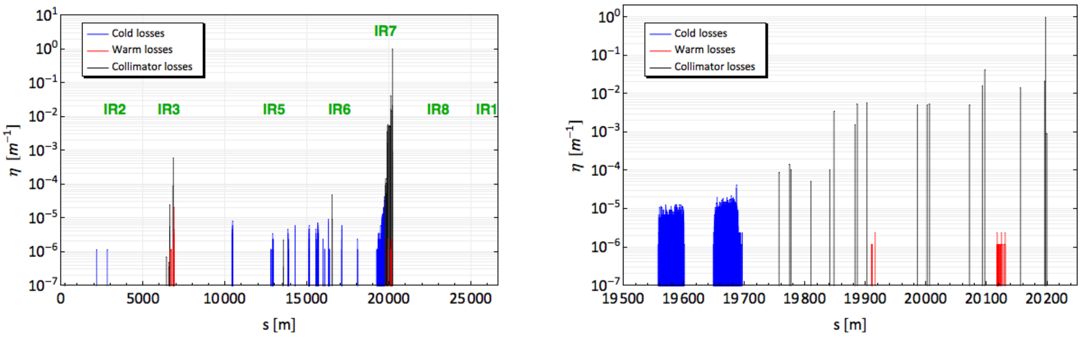

(a) Full ring

(b) Betratron cleaning insertion IR7

**Figure A.3:** *Simulated beam loss map at 7 TeV of the HL-LHC machine for the case of Beam 2 Horizontal halo.*

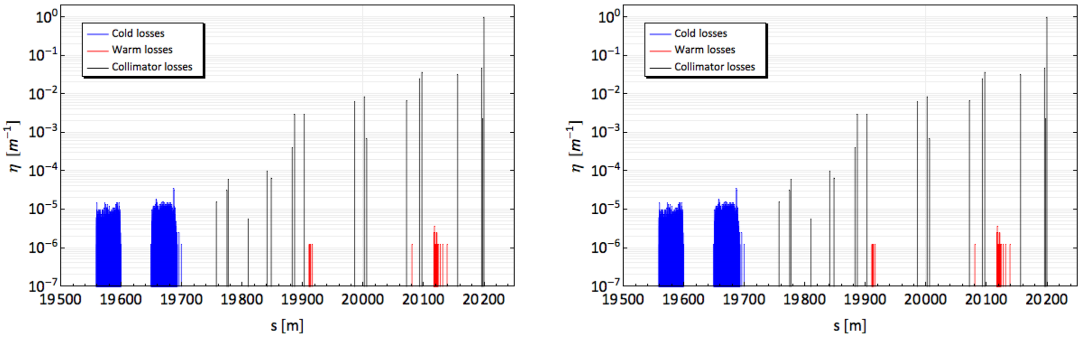

(a) Full ring

(b) Betratron cleaning insertion IR7

**Figure A.4:** *Simulated beam loss map at 7 TeV of the HL-LHC machine for the case of Beam 2 Vertical halo.*

### IR7 secondary collimators in CuCD - Beam 1

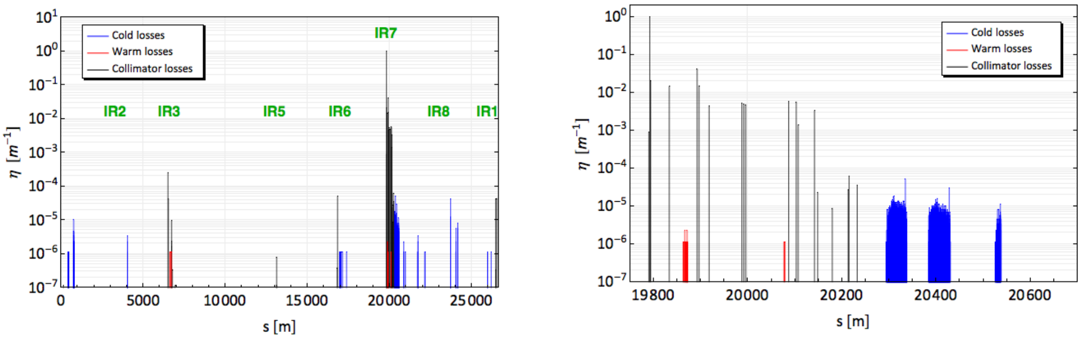

(a) Full ring

(b) Betratron cleaning insertion IR7

**Figure A.5:** *Simulated beam loss map at 7 TeV of the HL-LHC machine for the case of Beam 1 Horizontal halo.*

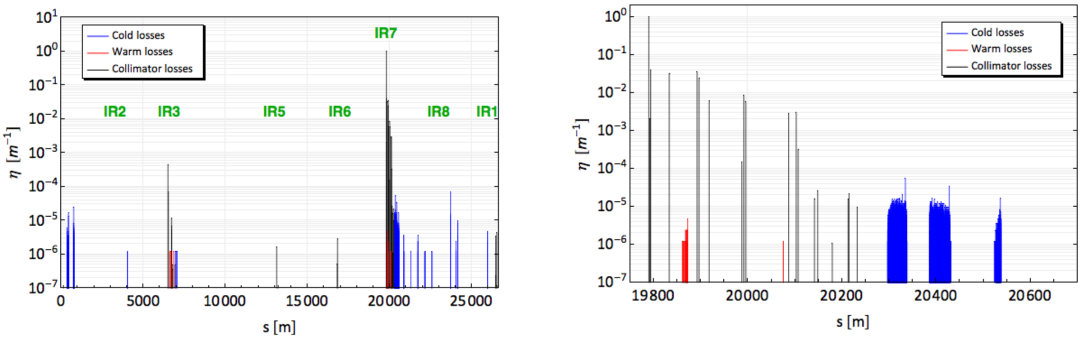

(a) Full ring

(b) Betratron cleaning insertion IR7

**Figure A.6:** *Simulated beam loss map at 7 TeV of the HL-LHC machine for the case of Beam 1 Vertical halo.*

### IR7 secondary collimators in CuCD - Beam 2

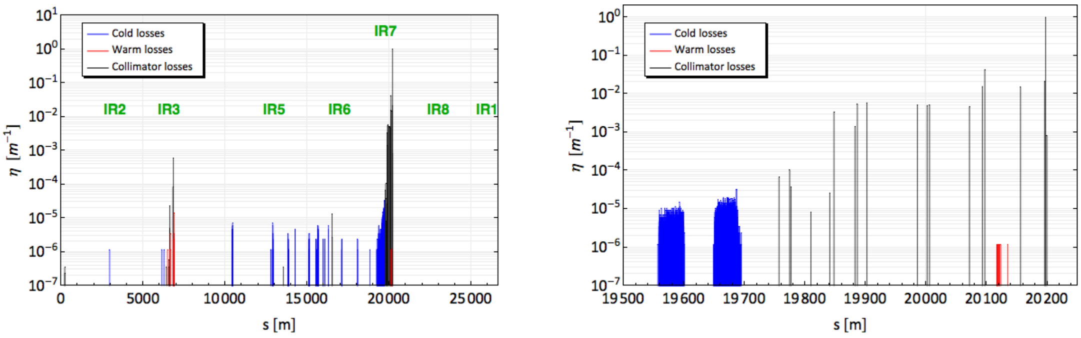

(a) Full ring

(b) Betratron cleaning insertion IR7

**Figure A.7:** *Simulated beam loss map at 7 TeV of the HL-LHC machine for the case of Beam 2 Horizontal halo.*

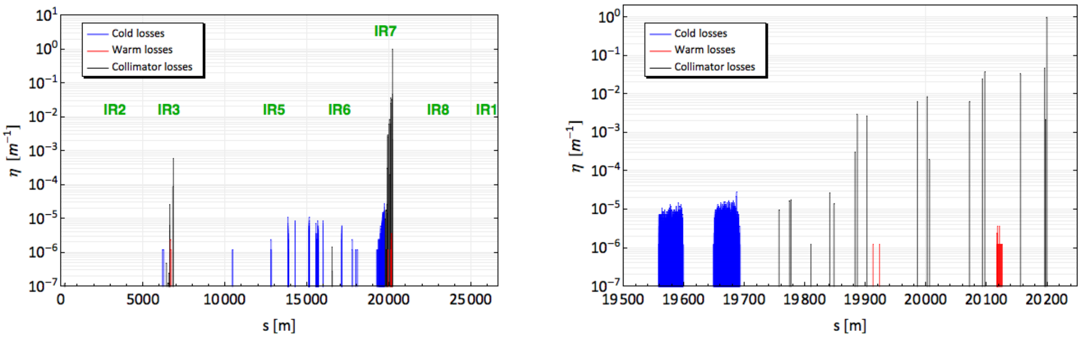

(a) Full ring

(b) Betratron cleaning insertion IR7

**Figure A.8:** *Simulated beam loss map at 7 TeV of the HL-LHC machine for the case of Beam 2 Vertical halo.*

## A.2 Material replacement of IR7 primary collimators only

### IR7 primary collimators in MoGr - Beam 1

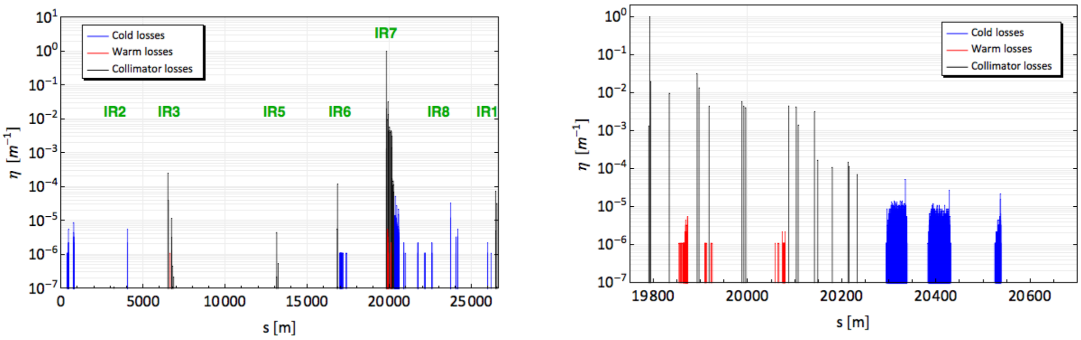

(a) Full ring

(b) Betratron cleaning insertion IR7

**Figure A.9:** *Simulated beam loss map at 7 TeV of the HL-LHC machine for the case of Beam 1 Horizontal halo.*

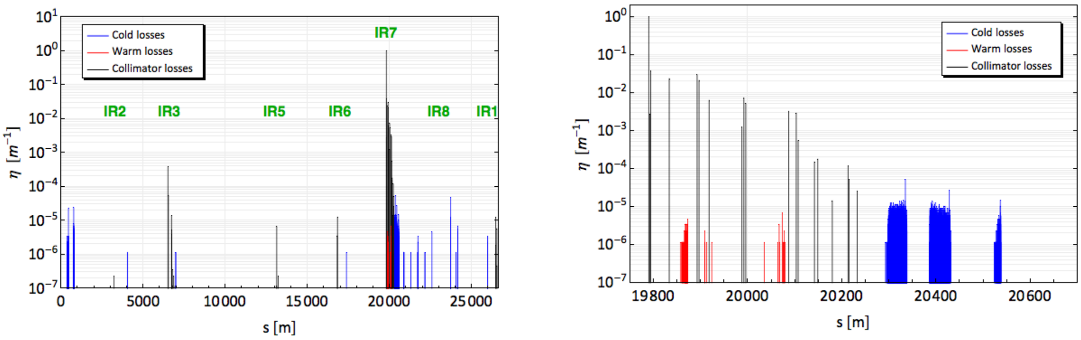

(a) Full ring

(b) Betratron cleaning insertion IR7

**Figure A.10:** *Simulated beam loss map at 7 TeV of the HL-LHC machine for the case of Beam 1 Vertical halo.*

### IR7 primary collimators in MoGr - Beam 2

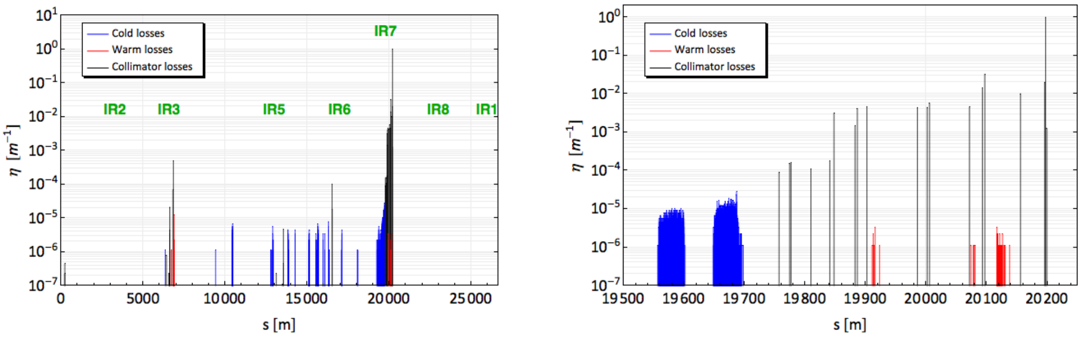

(a) Full ring

(b) Betratron cleaning insertion IR7

**Figure A.11:** *Simulated beam loss map at 7 TeV of the HL-LHC machine for the case of Beam 2 Horizontal halo.*

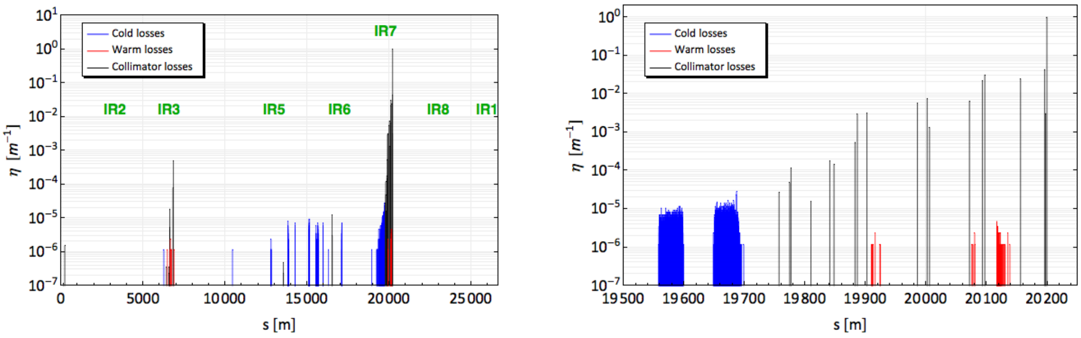

(a) Full ring

(b) Betratron cleaning insertion IR7

**Figure A.12:** *Simulated beam loss map at 7 TeV of the HL-LHC machine for the case of Beam 2 Veertical halo.*

### IR7 primary collimators in CuCD - Beam 1

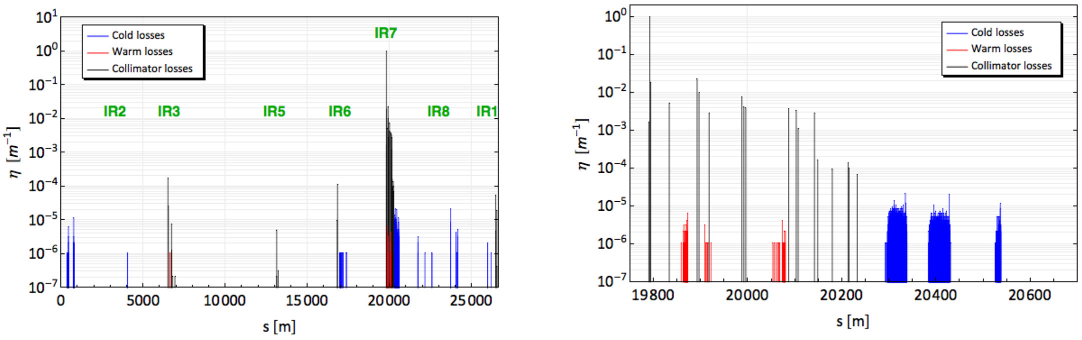

(a) Full ring

(b) Betratron cleaning insertion IR7

**Figure A.13:** *Simulated beam loss map at 7 TeV of the HL-LHC machine for the case of Beam 1 Horizontal halo.*

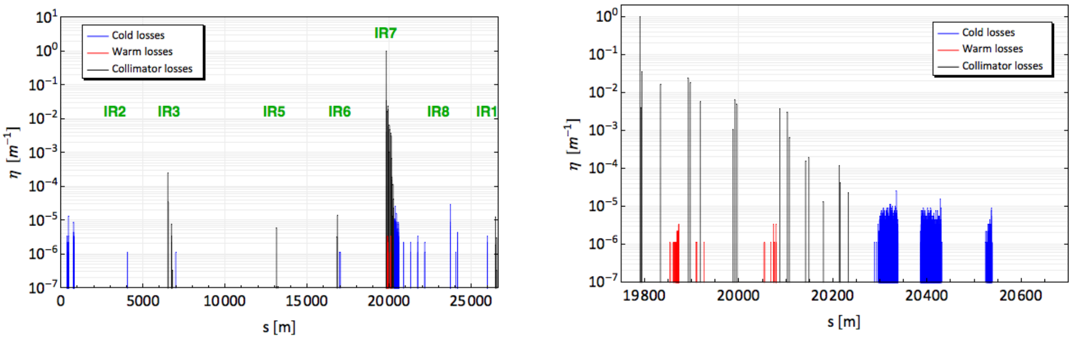

(a) Full ring

(b) Betratron cleaning insertion IR7

**Figure A.14:** *Simulated beam loss map at 7 TeV of the HL-LHC machine for the case of Beam 1 Vertical halo.*

### IR7 primary collimators in CuCD - Beam 2

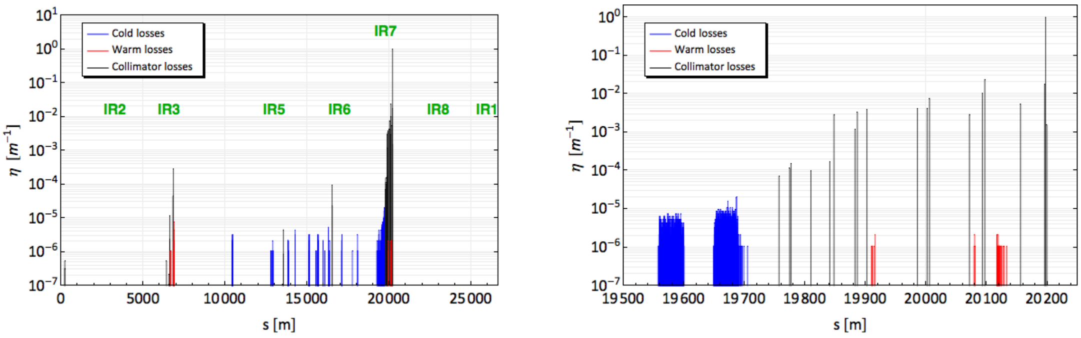

(a) Full ring

(b) Betratron cleaning insertion IR7

**Figure A.15:** *Simulated beam loss map at 7 TeV of the HL-LHC machine for the case of Beam 2 Horizontal halo.*

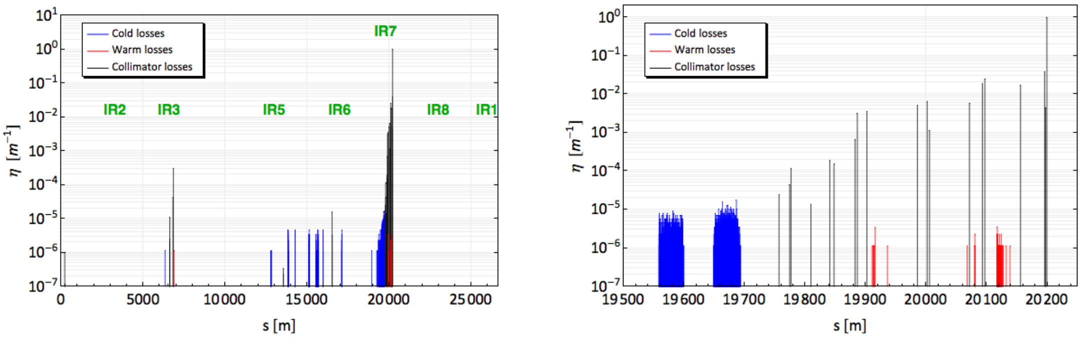

(a) Full ring

(b) Betratron cleaning insertion IR7

**Figure A.16:** *Simulated beam loss map at 7 TeV of the HL-LHC machine for the case of Beam 2 Vertical halo.*

## APPENDIX B

# Loss maps of post-LS3 machine configuration at 7 TeV

This appendix contains the loss maps of Beam 1 and Beam 2, horizontal and vertical halo, for the case of post LS3 machine configuration at 7 TeV. The parameters used in simulations are discussed in Chapter 9.4.

### Beam 1

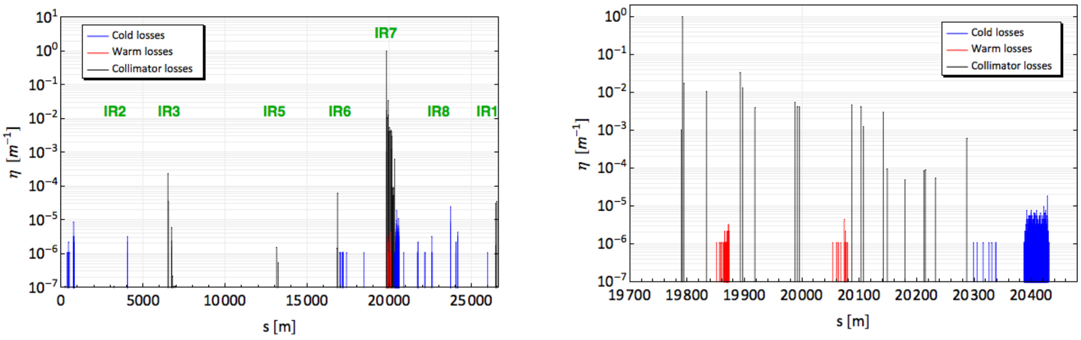

(a) Full ring

(b) Betratron cleaning insertion IR7

**Figure B.1:** *Simulated beam loss map at 7 TeV and post LS3 for the case of Beam 1 Horizontal halo.*

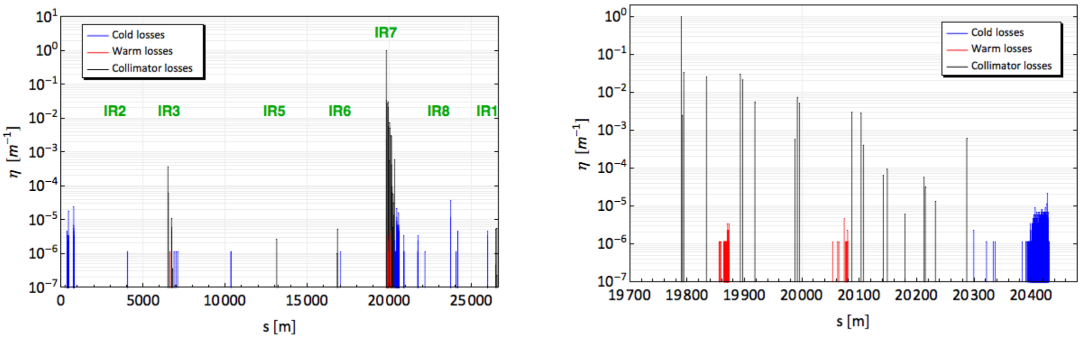

(a) Full ring

(b) Betratron cleaning insertion IR7

**Figure B.2:** *Simulated beam loss map at 7 TeV and post LS3 for the case of Beam 1 Vertical halo.*

## Beam 2

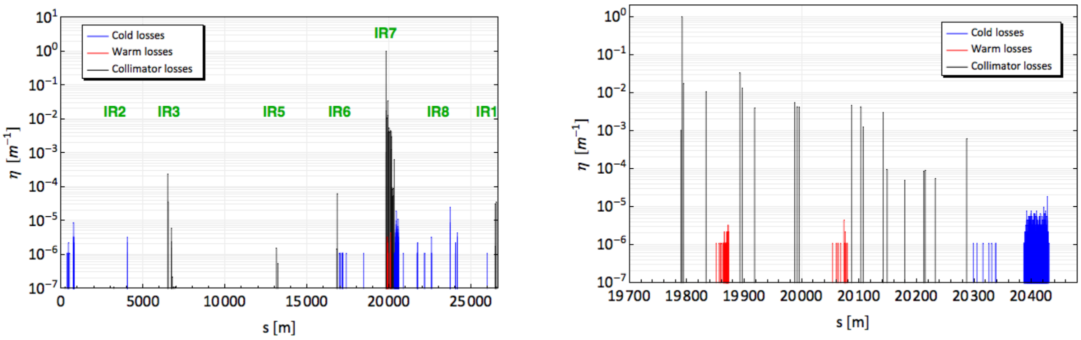

(a) Full ring

(b) Betratron cleaning insertion IR7

**Figure B.3:** *Simulated beam loss map at 7 TeV and post LS3 for the case of Beam 2 Horizontal halo.*

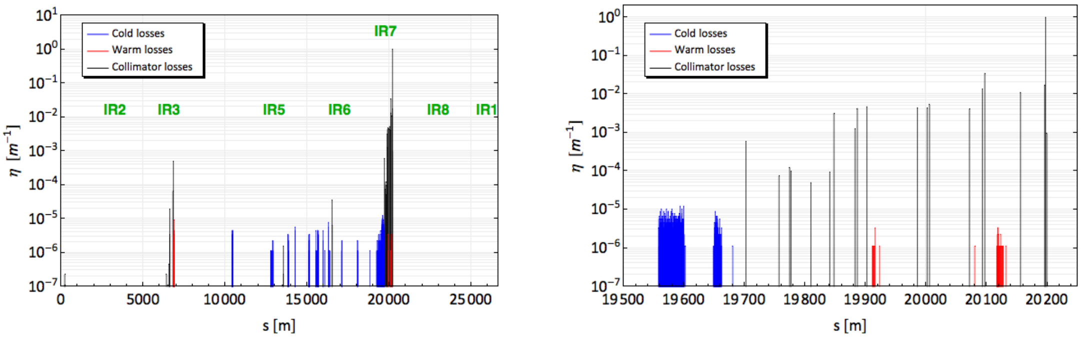

(a) Full ring

(b) Betratron cleaning insertion IR7

**Figure B.4:** *Simulated beam loss map at 7 TeV and post LS3 for the case of Beam 2 Vertical halo.*

# Bibliography

[1] Brüning, O., LHC Design Report Vol.1: The LHC Main Ring, 2004.

[2] I. Bejar Alonso *et al.*, HiLumi LHC Technical Design Report, Technical report, CERN-ACC-2015-0140, 2015.

[3] R.W. Assmann *et al.*, The final collimation system for the LHC, *EPAC06, Edimburgh, Scotland*, 2006.

[4] E. Metral *et al.*, Machine settings and operational scenario from stability considerations for HL-LHC, *4th Annual Meeting of HL-LHC, KEK, Japan*, 2014.

[5] D. Mirarchi, *et al.*, Cleaning Performance of the Collimation System of the High Luminosity Large Hadron Collider, in: Proc. of International Particle Accelerator Conference (IPAC'16), Busan, Korea, May 8-13, 2016, number 7 in International Particle Accelerator Conference, pages 2494–2497, JACoW, Geneva, Switzerland, June 2016, ISBN 978-3-95450-147-2, doi: doi:10.18429/JACoW-IPAC2016-WEPMW030.

[6] F. Schmidt, SIXTRACK version 1.2: user's reference manual, *CERN/SL/94-56-AP*, 1994.

[7] Sixtrack, `http://sixtrack.web.cern.ch/SixTrack/`.

[8] R. De Maria *et al.*, Recent Developments and Future Plans for SixTrack, *IPAC13, Shanghai, China*, 2013.

[9] A. Ball *et al.*, Future Circular Collider Study. Hadron collider Parameters, Technical Report FCC-ACC-SPC-0001, CERN, Geneva, Switzerland, 2014.

[10] M. Fiascaris *et al.*, First design of proton collimation system for 50 TeV FCC-HH, *IPAC16, Busan, Korea*, 2016.

[11] M. Martini, An introduction to transverse beam dynamics in accelerators, *CERN/PS 96-11*, 1996.

[12] M. Sands, The physics of electron storage rings, *SLAC report 121*, 1970.

[13] H. Wiedermann, Particle Accelerator Physics, Springer, 3rd edition, 2007, ISBN 978-3-540-49043-2.

[14] K. Wille, The Physics of Particle Accelerators, an introduction, OXFORD University Press, first edition, 1996.

[15] A. W. Chao, Physics of Collective Beam Instabilities in High Energy Accelerators, Wiley Series in Beam Physics and Accelerator Technology, Wiley-VCH, 1993.

[16] K. J. Ng, Coupling Impedances and Beam Instabilities in Accelerator Rings, US Accelerator School, Hampton, Virginia, January 2015.

[17] S. Peggs *et al.*, ESS Technical Design Report, Technical report, ESS-doc-274-v15, 2013.

[18] R. Ronningen, in: 46th ICFA Advanced Beam Dynamics Workshop on High-Intensity and High-Brightness Hadron Beams (HB2010), Morschach, Switzerland, page 662, 2010.

[19] J.M. Conrad, *et al.*, The DAE$\delta$ALUS Experiment, *Nuclear Physics B Proceedings Supplement*, 2010.

[20] G. F. Knoll, Radiation Detection and Measurement, D. Fowley, 2010.

[21] K. E. Holbert, Radiation Effects and Damage, Academic notes.

[22] R. A. Knief, Nuclear Energy Technology, McGraw-Hill, 1981, pp. 72.

[23] J. Koutsky, Radiation damage of structural materials, McGraw-Hill, 1981.

[24] M.J. Norgett, M.T. Robinson, I.M. Torrens, A proposed method of calculating displacement dose rates, *Nuclear engineering and design*, 33, pages 50–54, 1975.

[25] G.H. Kinchin and R.S. Pease, The Displacement of Atoms in Solids by Radiation, *Reports on Progress in Physics*, 18, pages 1–51, 1955.

[26] Primary Radiation Damage in Materials, Technical report, OECD/NEA, 2015.

[27] S. O. Kucheyev, *et al.*, Effect of ion species on the accumulation of ion-beam damage in GaN, *Phys. Rev. B*, 64, page 035202, Jun 2001, doi: 10.1103/PhysRevB.64.035202.

[28] P. A. Karaseov, *et al.*, Density of displacement cascades for cluster ions: An algorithm of calculation and the influence on damage formation in zno and gan, *Semiconductors*, 43(6), pages 691–700, 2009, ISSN 1090-6479, doi: 10.1134/S1063782609060013.

[29] H. Föll, Defects in crystals, Academic notes, University of Kiel, Faculty of Engineering.

[30] G. Was, Fundamentals of radiation materials science, Springer, Berlin, 2007.

[31] M. Li, Moving from Dpa to Changes in Materials Properties, in: Radiation Effects in Superconducting Magnet Materials (RESMM12), February 14, 2012 Fermilab, USA, 2012.

[32] M. P. Surth, Moving from DPA to Change in Material Properties, in: Proceedings of Radiation Effects in Superconducting Magnet Materials (RESMM12), Fermilab, USA, 2012.

[33] S. Maloy, *et al.*, The effect of 800 mev proton irradiation on the mechanical properties of tungsten at room temperature and at 475° c, *Journal of Nuclear Materials*, 343(1), pages 219–226, 2005, ISSN 0022-3115, doi: http://dx.doi.org/10.1016/j.jnucmat.2004.12.018, proceedings of the 6th International Workshop on Spallation Materials Technology.

[34] D. Kiselev, Activation and radiation damage in the environment of hadron accelerators, Paul Scherrer Institute, Viligen, Switzerland.

[35] T.M. Tritt, Thermal Conductivity: Theory, Properties, and Applications, Kluwer Acvademic / Plenum Publishers, New York, 2004.

[36] T. Maruyama *et al.*, Neutron Irradiation Effects on the Thermal Conductivity and Dimensional change of graphite Materials, *Journ. Nucl. Mat.*, 195, pages 44–50, 1992.

[37] E. E. Bloom, The challenge of developing structural materials for fusion power systems, in: Conf. on Fusion Reactor Materials, ICFRM-8, Sendai, Japan, 26-31 October 1997, pages 258–263, 1998.

[38] D. L. Porter, F. A. Garner, Irradiation creep and embrittlement behavior of aisi 316 stainless steel at very high neutron fluences, *Journal of Nuclear Materials*, 159, pages 114–121, 1988, ISSN 0022-3115, doi: http://dx.doi.org/10.1016/0022-3115(88)90089-X.

[39] H. Rauh *et al.*, Hydrogen concentrations near cracks in target materials for high-power spallation neutron sources, *Journal of Nuclear Materials*, 295(1), pages 109–120, 2001.

[40] P. Hurh *et al.*, Radiation damage study of graphite and carbon composite target materials, *IPAC13, Shangai, China*, 2013.

[41] L. K. Mansur, Fundamentals of Void Swelling in Metal Alloys, in: Workshop on Characterization of Advanced Materials under Extreme Environments for Next Generation Energy Systems, Brookhaven National Laboratory, September 25, 2009 , 2009.

[42] R. Alemany, M. Lamont, S. Page, LHC modes, Technical Report LHC-OP-ES-0005, CERN, 2007.

[43] M.N. Wilson, Superconducting Magnets, Oxford Univeristy Press, 1987.

[44] The ATLAS Collaboration, The ATLAS Experiment at the CERN Large Hadron Collider, *J. Instrum.*, 2008.

[45] The CMS Collaboration, The CMS Experiment at the CERN Large Hadron Collider, *J. Instrum.*, 2008.

[46] Statement by the ATLAS collaboration about findings of the Higgs Boson at the CERN LHC, 2012.

[47] Statement by the CMS collaboration about findings of the Higgs Boson at the CERN LHC, 2012.

[48] The LHCb Collaboration, The LHCb Detector at the CERN Large Hadron Collider, *J. Instrum.*, 2008.

[49] The ALICE Collaboration, The ALICE Experiment at the CERN Large Hadron Collider, *J. Instrum.*, 2008.

[50] M. Meddahi *et al.*, LHC Injectors Upgrade (LIU) Project at CERN, *IPAC15, Richmond, VA, USA*, 2015.

[51] S. Fartoukh *et al.*, An Achromatic Telescope Squeezing (ATS) scheme for the LHC upgrade., *IPAC11, San Sebastian, Spain*, 2011.

[52] B. Dehning *et al.*, The LHC beam loss measurement system, *PAC07, New Mexico, USA*, 2007.

[53] E. B. Holzer *et al.*, Beam Loss Monitoring System for the LHC, *CERN-AB-2006-009*, 2005.

[54] S. Redaelli, R.W.Assmann, G. Robert-Demolaize, LHC aperture and commissioning of the collimation system, in: J. Poole (Editor), Proceedings of the LHC Project Workshop - Chamonix XIV, Chamonix, France, pages 268–277, 2005.

[55] R. Schmidt *et al.*, Protection of the CERN Large Hadron Collider, *New J. Phys. 8, 290*, 2006, doi: 10.1088/1367-2630/8/11/290.

[56] R. W. Assmann *et al.*, Requirements for the LHC collimation system, *EPAC02, Paris, France*, page 1326, 2002.

[57] R. W. Assmann *et al.*, The Consequences of Abnormal Beam Dump Actions on the LHC Collimation System, *LHC Project Note 293, CERN*, 2002.

[58] A. Dallocchio *et al.*, LHC collimators with embedded beam position monitors: a new advanced mechanical design, in: IPAC11 (Editor), IPAC11, San Sebastian, Spain, 2011.

[59] G. Valentino *et al.*, Performance of the LHC collimation system during 2015, in: G. Valentino *et al.* (Editor), Evian 2015 Workshop on LHC Commissioning, Evian-les-Bains, France, 15 - 17 Dec 2015, volume B. Goddard, S. Dubourg, pages 157–162, 2015.

[60] B. Salvachua*et al.*, Collimation System Performance, in: Chamonix 2014: LHC Performance Workshop, Chamonix, France, 25 - 28 January 2016, 2016.

[61] G. Valentino *et al.*, First operational experience with embedded collimator BPMs in the LH, *IPAC16, Busan, Korea*, 2016.

[62] F. Carra *et al.*, Mechanical engineering and design of novel collimators for HL-LHC, *IPAC14, Dresden, Germany*, 2014.

[63] I. Efthymiopoulos *et al.*, HiRadMat: a new irradiation facility for material testing at CERN, in: IPAC11, San Sebastian, Spain, 2011.

[64] N. Mounet *et al.*, Collimator impedance measurements in the LHC, *IPAC13, Shanghai, China*, 2013.

[65] N. Mounet, First estimates of intensity limitations from HL-LHC transverse impedance, 2014.

[66] R.W. Assmann *et al.*, Summary of MD on nominal collimator settings, *CERN-ATS-Note-2011-036 MD*, 2011.

[67] N. Mounet, The LHC Transverse Coupled-Bunch Instability, CERN-THESIS-2012-055, EPFL Lausanne, 2012.

[68] N. Biancacci *et al.*, Update on the HL-LHC impedance budget, *4th Annual Meeting of HL-LHC, KEK, Japan*, 2014.

[69] R. Bruce *et al.*, Is collimation still a limitation for HL-LHC?, Presentation at LHC Performance Workshop, Chamonix, January 23-27, 2016.

[70] A. Dallocchio, Study of thermo-mechanical effects induced in solids by high energy particle beams: analytical and numerical methods, CERN-THESIS-2008-140, Politecnico of Turin, 2008.

[71] A. Bertarelli, Beam-Induced Damage Mechanisms and their Calculation, in: R. Schmidt (Editor), Proceedings of the Joint International Accelerator School: Beam Loss and AcceleratorProtection, Newport Beach, USA, volume 159, pages 159–227, 2014, doi: http://dx.doi.org/10.5170/CERN-2016-002.

[72] R. Bruce *et al.*, Calculations of safe collimator settings and $\beta^*$ at the CERN Large Hadron Collider, *Phys. Rev. ST Accel. Beams 18, 061001*, 18(6), page 061001, 2015, doi: 10.1103/PhysRevSTAB.18.061001.

[73] E. Quaranta, *et al.*, Towards Optimum Material Choices for the HL-LHC Collimator Upgrade, in: Proc. of International Particle Accelerator Conference (IPAC'16), Busan, Korea, May 8-13, 2016, number 7 in International Particle Accelerator Conference, pages 2498–2501, JACoW, Geneva, Switzerland, June 2016, ISBN 978-3-95450-147-2, doi: doi:10.18429/JACoW-IPAC2016-WEPMW031, doi:10.18429/JACoW-IPAC2016-WEPMW031.

[74] E. Skordis, FLUKA estimation of DPA for ion irradiation and update on IR7 DPA calculations for LHC operations, Presentation at Eucard-2 WP11 Topical Meeting, Malta, April $29^{th}$, 2016 .

[75] N. Mariani, Development of novel advanced Molybdenum-based composites for high energy physics applications, CERN-THESIS-2014-363, Politecnico di Milano, 2014.

[76] A. Daoud *et al.*, Anisotropy effects on the tensile and fatigue behaviour of an oxide dispersion strengthened copper alloy, *Materials Science and Engineering A*, 534, pages 640–648, 2012.

[77] GlidCop, Technical report, SCM Metal Products, inc, 2008.

[78] J. D. Brooks and G. H. Taylor, Chemistry and Physics of Carbon, Marcel Dekker, New York, 1968.

[79] J. L. White and J. M. Pontelandolfo, Graphite-carbide materials prepared by hot-working with a dispersed liquid-carbide phase, *Carbon*, 4, pages 305–314, 1966, doi: https://doi.org/10.1016/0008-6223(66)90043-1.

[80] J. Guardia-Valenzuala *et al.*, Development and properties of high thermal conductivity molybdenum carbide-graphite composites, *To be published in Carbon*, 2017.

[81] C. Accettura *et al.*, TCSPM components outgassing test update, Presentation at HiColDEM, HL-LHC Collimators: Design, Engineering and Prototyping, CERN, March $16^{th}$, 2017.

[82] N. Biancacci *et al.*, HL-LHC collimator impedance studies for IP7 and IP3, *ColUSM Meeting 08 May 2015, CERN*, 2015.

[83] W. J. Parker *et al.*, Flash Method of Determining Thermal Diffusivity, Heat Capacity and Thermal Conductivity, *Journal of Applied Physics*, 32, pages 1679–1684, 1961.

[84] ASTM C1161-02c, Standard Test Method for Flexural Strength of Advanced Ceramics at Ambient Temperature, 2002.

[85] R. B. Matthew, Deformation and strengthening in molybdenum carbide-natural graphite composite materials, Ph.D. thesis, 1970.

[86] R. B. Matthews and G. M. Jenkins, The high temperature interaction molybdenum graphite, *Journal of Material Science*, 10, 1975.

[87] N. Simos *et al.*, Studies of material properties under irradiation at BNL Linear Isotope Producer (BLIP), *Fermilab-Conf-10-480-APC, November 2010*, 2010.

[88] N. Charitonidis, Design Optimisation of a High Intensity Beam Facility and Feasibility Experiment of a Solid Fragmented Target, CERN-THESIS-2014-067, École Polytechnique Fédérale de Lausanne, Lausanne, Switzerland, 2014.

[89] P. Sievers, Elastic Stress Waves in Matter due to Rapid Heating by an Intense High-Energy Particle Beam, Technical report, CERN, Geneva, Switzerland.

[90] A. Bertarelli *et al.*, Permanent Deformation of the LHC Collimator Jaws Induced by Shock Beam Impact: An Analytical and Numerical Interpretation, in: EPAC06, Edimburgh, 2006.

[91] A. Bertarelli et al., Mechanical Design for Robustness of the LHC Collimators, in: PAC05, Knoxville, 2005.

[92] A. Bertarelli *et al.*, Updated robustness limits for collimator material, in: M. Jonker (Editor), Proceedings of the LHC Machine Protection Workshop, Annecy, France, CERN-ACC-2014-0041, pages 108–112, 2013.

[93] M. Cauchi *et al.*, High energy beam impact tests on a LHC tertiary collimator at the CERN high-radiation to materials facility, *Phys. Rev. ST Accel. Beams*, 17(2), page 021004, 2014, doi: 10.1103/PhysRevSTAB.17.021004.

[94] S. C. Tsai *et al.*, Microstructural evolutions of three-dimensional carboncarbon composite materials irradiated by carbon ions at elevated temperatures, *Prog. Nucl. Energy*, 57(32), 2012.

[95] T. Paulmier *et al.*, Structural modifications of carbon-carbon composites under high temperature and ion irradiation, *Appl. Surf. Sci.*, 243(376), 2005.

[96] T. D. Burchell, in: Proceedings of the 39th SAMPE Symposium, volume 39, pages 2423–2436, 1994.

[97] T. Nishida *et al.*, Effects of carbon fiber orientation and graphitization on solid state bonding o f C/C composite to nickel, *Mater. Trans., JIM*, 44(148), 2003.

[98] N. Simos *et al.*, Composite Materials under Extreme Radiation and Temperature Environments of the Next Generation Nuclear Reactors, Intech, Rijeka, 2011, 2011.

[99] L.L. Snead, T.D. Burchell, Thermal Conductivity Degradation of graphite due to Neutron Irradiation at Low Temperature, *Journ. Nucl. Mat*, 1995.

[100] M. Akiyoshi *et al.*, Thermal Conductivity of Ceramics during Irradiation, *Fusion Eng. Des.*, 81, pages 321–325, 2006.

[101] T. D. Burchell, Radiation effects in graphite and carbon-based materials, *MRS Bulletin*, 22(4), pages 29–35, 1997, doi: 10.1557/S0883769400033005.

[102] N. Simos *et al.*, Experimental studies of targets and collimators for high intensity beams, in: 39th ICFA Advanced Beam Dynamics Workshop: High Intensity High Brightness Hadron Beams (HB 2006,Tsukuba, Japan), 2006.

[103] A. I. Ryazanov, The effects of high-energy proton beams on LHC collimator materials, Technical report, Russian Research Centre "Kurchatov Institute", 2008.

[104] M. Tomut *et al.*, Heavy ion induced radiation effects in novel molybdenum-carbide graphite composite materials, *GSI Report 2015-1, 266 p.*, 2015.

[105] E. Quaranta *et al.*, Radiation-induced effects on LHC collimator materials under extreme conditions, *IPAC16, Busan, Korea*, 2016.

[106] M. Tomut *et al.*, Present results on material damage from irradiation. Milestone MS70, Technical report, EuCARD-2 Enhanced European Coordination for Accelerator Research and Development, 2016.

[107] A. Lechner *et al.*, DPA calculations with FLUKA, *2nd EuCARD2 ColMat-HDED annual meeting, GSI, Germany*, 2014.

[108] N. Simos *et al.*, Target material irradiation studies for high intensity accelerator beams, *Nucl. Phys. B, Proc. Suppl.*, 149, 2005.

[109] N. Simos *et al.*, Radiation damage and thermal shock response of carbon-fiber-reinforced materials to intense high-energy proton beam, *Phys. Rev. ST Accel. Beams*, 19(111002), 2016.

[110] J. H. W. Simmons, Radiation Damage in Graphite, Elsevier, 1965.

[111] A. I. Ryazanov, Experimental and theoretical studies of the effects of high-energy proton beams on LHC collimator materials, Technical report, Russian Research Centre "Kurchatov Institute", 2013.

[112] G. Robert-Demolaize *et al.*, A new version of SixTrack with collimation and aperture interface, *PAC05, Knoxville, USA*, 2005.

[113] G. Robert-DÃ©molaize, Design and Performance Optimization of the LHC Collimation System, CERN-THESIS-2006-069, Joseph Fourier U., Grenoble, 2006.

[114] Madx, `http://cern.ch/mad/`.

[115] R. Bruce *et al.*, Simulations and measurements of beam loss patterns at the CERN Large Hadron Collider, *Phys. Rev. ST Accel. Beams 17, 081004*, 2014.

[116] T. Trenkel and J. Jeanneret, K2, a software package evaluating collimation systems in circular colliders., CERN-SL-Note-94-105-AP, 1994.

[117] C. Tambasco, An improved scattering routine for collimation tracking studies at LHC, CERN-THESIS-2014-014, Università La Sapienza, Roma, Italy, 2014.

[118] K. Nakamura *et al.*, Passage of particles through matter, *JPG 37, 075021*, 2010.

[119] K.A. Olive *et al.*, Particle Data Group, 2014.

[120] H. A. Bethe, Moliere's theory of multiple scattering, *Physical Review*, 89, pages 1256–1266, 1953.

[121] N. Catalan Lasheras, Transverse and Longitudinal Beam Collimation in a High-Energy Proton Collider (LHC), CERN-THESIS-2000-019, Zaragoza, 1998.

[122] Merlin, `https://github.com/MERLIN-Collaboration/MERLIN`.

[123] A. Valloni *et al.*, MERLIN cleaning studies with advanced collimator materials for HL-LHC, *IPAC16, Busan, Korea*, 2016.

[124] L. Lari *et al.*, Accelerator physics studies on the effects from an asynchronous beam dump onto the LHC experimental region collimators, *IPAC12, New Orleans, Louisiana, USA*, 2012.

[125] L. Lari *et al.*, MOPWO046, *IPAC13, Shangai, China*, 2013.

[126] R. Bruce *et al.*, Collimation with tighter TCTs at $\beta^*$=40 cm, *CERN-ACC-2015*, 2015.

[127] R. Bruce *et al.*, Baseline LHC machine parameters and configuration of the 2015 proton run, in: M. Draper (CERN) (Editor), Proceedings of Chamonix 2014: LHC Performance Workshop, Chamonix, France, CERN-2015-002, pages 100–106, 2014.

[128] C. Bracco *et al.*, LHC MD292: TCDQ-TCT retraction and losses during asynchronous beam dump, *CERN-ACC-NOTE-2016-0017*, 2016.

[129] R. Bruce *et al.*, Parameters for HL-LHC aperture calculations and comparison with aperture measurements, *CERN-ACC-2014-0044*, 2014.

[130] C. Bracco, Commissioning Scenarios and Tests for the LHC Collimation System, CERN-THESIS-2009-031 ; EuCARD-DIS-2009-004, EPFL Lausanne, 2008.

[131] R. Bruce *et al.*, Parameters for aperture calculations at injection for HL-LHC, *CERN-ACC-2016-0328*, 2016.

[132] E. Quaranta *et al.*, Collimation cleaning at the LHC with advanced secondary collimator materials, *IPAC15, Richmond, Virginia*, 2015.

[133] D. E. Grady, The spall strength of condensed matter., *J. Mech. Phys. Solids*, 36(3), pages 284–353, 1987.

[134] W. Rankine, On the stability of loose earth., *Philosophical Transactions of the Royal Society of London*, 147, 1857.

[135] P. Gradassi *et al.*, Updated TCT Damage Limits for Asynchronous Dump Cases, *CWG Meeting 08 June 2015, CERN*, 2015.

[136] B. Salvachua *et el.*, Collimation quench test with 6.5 TeV proton beams, *CERN-ACC-NOTE-2016-0015*, 2016.

[137] E. Skordis, Updated power deposition simulations for DS collimators in IR7, presentation to ColUSM, January 30, 2015.

[138] P. D. Hermes, Heavy-Ion Collimation at the Large Hadron Collider: Simulations and Measurements, CERN-THESIS-2016-030, Westfalischen Wilhelms University of Munster, Germany, 2016.

[139] N. Biancacci *et al.*, Collimator impedance: are tighter settings allowed for impedance?, Presentation at Collimation Working Group, CERN, 7th November 2016.

[140] A. Dallocchio *et al.*, Finite Element Methods for the thermo-mechanical analysis of the Phase I Collimators , in: Workshop on Materials for Collimators and Beam Absorbers , 2006.

[141] M. Fitterer *et al.*, Optics considerations for PIC and US1scenarios for HL-LHC in the framework of the RLIUP review, *CERN-ACC-NOTE-2014-0031*, 2014.

[142] H. G. Morales *et al.*, Beam cleaning of the incoming beam in experimental IRs in HL-LHC, *To be published in CERN ATS- Note-2017*, 2017.

[143] R. De Maria *et al.*, HL-LHC aperture update, 67th Collimation Upgrade Specification Meeting, CERN, February 5th, 2016.

[144] P. Ortega *et al.*, Triplet energy deposition in case of asynchronous dump, 2015.

[145] R. Bruce *et al.*, Source of machine-induced backgroung in the ATLAS and CMS detectors at the CERN Large Hadron Collider, *Nucl. Instrum. Methods Phys. Res. A*, (729), pages 825–840, 2013.

[146] M. Guthoff *et al.*, Effects of beam losses to CMS and ATLAS, *5th Annual Meeting of HL-LHC, CERN*, 2015.

[147] R. Bruce *et al.*, 2016 LHC configuration: can we get to $\beta^* = 40$ cm?, in: B. Goddard, S. Dubourg (Editor), Evian 2015 Workshop on LHC Commissioning, Evian-les-Bains, France, CERN-ACC-2015-376, 2015.